AI-AEC-13093
NASA-CR-121222

DESIGN AND ANALYSIS OF THE RADIATOR STRUCTURE FOR SPACE POWER SYSTEMS

AEC Research and Development Report

(NASA-CR-121222) DESIGN AND ANALYSIS OF THE RADIATOR STRUCTURE FOR SPACE POWER SYSTEMS (Atomics International) 211 p HC $12.75 CSCL 22B
N73-26892
Unclas
G3/31 08327

Atomics International Division
Rockwell International

P.O. Box 309
Canoga Park, California 91304

AI-AEC-13093
SNAP REACTOR
SNAP PROGRAM
M-3679-R69
C-92b
NASA-CR-121222

DESIGN AND ANALYSIS OF THE RADIATOR STRUCTURE FOR SPACE POWER SYSTEMS

W. H. DAUTERMAN
L. D. MONTGOMERY

with contributions by

R. V. ANDERSON
J. W. CARROLL
R. VAN HOUTEN

Atomics International Division
Rockwell International

P.O. Box 309
Canoga Park, California 91304

CONTRACT: AT(04-3)-701
ISSUED: JUNE 22, 1973

FOREWORD

The work described here was done at the Atomics International Division of Rockwell International Corporation, under the direction of the Space Nuclear Systems Division, a joint AEC-NASA office. Project management was provided by NASA-Lewis Research Center and the AEC-SNAP Project Office.

DISTRIBUTION

This report has been distributed according to the category "Systems for Nuclear Auxiliary Power (SNAP) Reactor — SNAP Program," as given in the Standard Distribution for Classified Scientific and Technical Reports, M-3679, and according to the NASA Supplementary Report Distribution List at the end of this report.

CONTENTS

CONTENTS

CONTENTS

TABLES

FIGURES

FIGURES

FIGURES

FIGURES

FIGURES

FIGURES

ABSTRACT

The design, analysis, fabrication, and development of the 5-kwe radiator structure are shown. Thermal performance, meteoroid protection, structural capability during launch, development testing and space operation, material evaluation, and the configuration selection are described. The fin-tube development program depends on the relative values of the thermal coefficients of expansion. The initial selection of aluminum fins and Type 316 stainless-steel tubes was based on previous experience; however, the large differential in their expansion rates showed that an alternate, more compatible, combination was needed. Copper, stainless-steel-clad copper, boron-impregnated aluminum, and an independent radiator with a titanium structure were all considered as alternate materials. The final selection was Lockalloy fins with Type 304 stainless-steel "D" tubes.

I. INTRODUCTION

The radiator is one of the major components of the 5-kwe thermoelectric space power system. The design, analysis, fabrication, and development was predicated on using established techniques of brazing aluminum fins to stainless-steel tubes and using these assemblies to fabricate an integral heat rejection and structural support radiator.

As the analysis and development progressed, major limitations on this material combination became evident. A major problem with joining the dissimilar materials was concerned with the formation of a brittle intermetallic compound between the aluminum silicon braze and the nickel in the stainless steel. A major difficulty with the aluminum-fin and stainless-steel-tube assembly selected initially is the large differential thermal expansion mismatch between the two materials. This mismatch leads to relatively large stresses being induced within the materials and at the bond interface. The stresses generated are in excess of the yield and/or creep strength of the fin and can cause progressive deformation (thermal ratcheting) with each thermal cycle.

An efficient thermal heat transfer path must be achieved between the highly conductive fin and NaK-containing tube; therefore, a metallurgical bond between the two is normally required. The very high stresses on the bond area resulted in separation during thermal cycling of small test samples. This bimetallic effect also required that a symmetrical fin-tube cross section be used to prevent axial bowing of each assembly.

As a result of the delamination of the aluminum and stainless-steel joints in the thermal cycling tests, and the pessimistic stress analysis results, a search for other material combinations was made and Lockalloy (Be-38% Al) was selected as an alternate to the 3003 aluminum alloy. The light weight Lockalloy potentially solves the differential thermal expansion mismatch problem, since its expansion closely matches that of stainless steel.

Several other fin materials considered were copper, copper-stainless steel, and beryllium-nickel. All of these were acceptable from the standpoint of the thermal expansion mismatch; however, other problems caused their abandonment.

The coppers would necessitate considerable weight increase and there was a potential problem associated with application of the AI-93 emissivity coating. The beryllium is extremely notch sensitive and would have required extending the state of the art to fabricate the radiator.

It was therefore concluded that the Lockalloy fin represented the optimum design for this system and was the reference design at the time this project was closed out.

II. SUMMARY

The development of the radiator structure was based on the use of established techniques for its design, analysis, and fabrication. It was to be fabricated by brazing aluminum fins to stainless-steel tubes and edge riveting these assemblies to form an integral heat rejection and structure support radiator. Joining of aluminum to stainless steel had apparently been successfully achieved by several fabricators. It was found, however, that the major problem with joining the dissimilar metals was the formation of the brittle Al_3Ni intermetallic compound between the aluminum-silicon braze and the nickel in the stainless steel. Formation of a zone greater than 0.0002-in. in thickness typically resulted in bond failure during thermal cycling. During the normal type of brazing, the assembly would be at the braze melt temperature of 1000°F for approximately 15 min, and a relatively thick zone would be formed. The formation of this compound can be inhibited or prevented by controlling the time at the melt temperature or the use of a diffusion barrier over the stainless steel. At lower temperatures (<600°F) the inter-diffusion between aluminum and stainless steel is sufficiently small that growth of a diffusion zone to the critical thickness would not occur for this application.

The approach used by one fabricator was to tin the stainless-steel tube with aluminum-silicon braze alloy prior to puddle brazing. This method was performed by hand and it required considerable skill just to melt the brazing alloy and yet flow the metal without overtemperaturing. The process resulted in a minimum time at temperature. Wetting was achieved by wire brushing the stainless-steel tubes to remove oxides as it was tinned. Another vendor employed a titanium plating on the stainless-steel tubes to act as a diffusion barrier and to enhance wetting. The titanium was electrolytically applied in a fused salt bath at 1550°F. In this process, interstitials in the stainless steel must either be stabilized or low in concentration to prevent a brittle zone developing between the titanium and stainless steel. Aluminum silicon braze and flux was then placed between the titanium-coated stainless steel and aluminum fins, and the whole assembly was furnace brazed. A possible problem with this approach is the formation of titanium silicides at the braze-titanium barrier interface, although at 600°F, it appears that the inter-diffusion rates are very low.

Other processes considered included casting of the aluminum around water-chilled, stainless-steel tubes; explosive bonding concentric tubes of aluminum and stainless steel; co-extrusion of bimetal tubing; and diffusion bonding. Available equipment for pressurized die casting aluminum around stainless-steel tubes was limited to 3-ft lengths and modifications to make longer lengths (15 ft) were deemed too expensive. Samples obtained by explosive bonding were radially cracked at the interface between the aluminum and stainless steel, and the process was not pursued further. Co-extrusion of the two materials was precluded because the melting point of aluminum is far below the extrusion temperature for stainless steel. Diffusion bonding was considered a possible backup approach.

The process of titanium-plating tubes followed by brazing was selected as the reference approach for further development. It was selected primarily because the available data indicated a barrier was required for achieving a high integrity bond, and brazing was the most economical and most easily scaled up to the longer lengths, of the various processes.

Two approaches have been investigated by one vendor, both using the titanium-plated, stainless-steel tubes. One approach used preplaced aluminum-silicon braze and flux in an argon atmosphere furnace. The second used pressure and resistance heating to melt preplaced braze alloy. This latter process did not use a flux to remove oxides since the oxide surfaces were disrupted by the mechanical work.

A. THERMAL CYCLE TEST RESULTS

Examination of samples received from the fabricator indicated that the titanium plating had separated from the stainless steel during brazing on some of the samples. This was attributed to the formation of TiC at the interface since normal Type 304 stainless-steel tubing had been used instead of Type 304L stainless steel. One-inch samples were cut off the ends of the approximately 6-in.-long specimens, and the short lengths were thermally cycled between 600°F and room temperature by placing them in and out of a furnace. All specimens showed delamination with from one to ten thermal cycles. Tests on small specimens from the other vendor also delaminated upon one thermal cycle application.

B. THERMAL STRESS ANALYSES

Concurrent with the above materials and process development effort, stress analysis was being performed on the fin and tube assembly. A basic problem with the bonded aluminum and stainless steel lies with the large differential in their thermal expansion rates.

The aluminum will contract about 0.25% more than the stainless steel on cooling from 600°F to room temperature. This amounts to approximately 0.5 in. of mismatch over the total length of the radiator.

A two-dimensional stress analysis code was used to model the fin and tube assembly and calculate effective stress and strain over the cross section. The code was capable of handling both plastic and elastic properties of the materials. The results of this analysis indicated that yielding of one or both of the materials would occur on every thermal cycle. Although the code results predicted that the aluminum could be made to yield and recover in a stable manner (i.e., always returning to the same position) if the stainless steel were thick enough, differential yielding and creep of the fin from root to tip would probably cripple it as a load-carrying member. The residual stresses imposed on the stainless-steel tubes and aluminum sections would be nearly impossible to analyze since the local yielding of the aluminum would depend upon local temperatures and the direction of the ripples being formed.

With the disappointing thermal cycling tests and the detailed stress analysis results, it was evident that the aluminum and stainless-steel radiator design was the wrong approach. A search for alternate materials combinations was made to alleviate the differential thermal expansion mismatch problem.

After an extensive literature survey, a Lockalloy (Be-38% Al)-Type 304L series stainless-steel combination was selected for further evaluation since a nearly perfect match in thermal expansions was obtained. The Lockalloy compared to 3003 aluminum has lower density, higher stiffness, and higher strength which make it suitable as a radiator fin material. Although its conductivity is higher than that of 3003 aluminum at room temperature, it is lower at 600°F.

Stress analysis of the Lockalloy and stainless steel fin and tube assembly showed that both materials remained in the elastic range through thermal cycling.

The maximum residual elastic strain in the Lockalloy was 0.01% and in the stainless steel 0.07%, which occurred during cooldown from the brazing operation. These materials eliminated the stress problems resulting from differential thermal expansion since, during subsequent thermal cycling, both materials remained in the elastic range.

Discussions with Kawecki Berylco, Inc.; Lockheed; Solar; and Rockwell-International, Columbus Division, all indicated that the material was available at approximately the same cost as beryllium. However, the Lockalloy could be machined, drilled, and riveted by techniques approaching standard aluminum and magnesium alloys. Rockwell International is presently using Lockalloy for stringers in a riveted missile application, and no special procedures are followed except that all chips are picked up with a vacuum cleaner during drilling of holes.

A design goal was to keep the cross sectional fin-tube geometry simple to reduce machining cost of the Lockalloy. As a result of the survey, some question was raised on the variation of the properties of Lockalloy as a function of extrusion and rolling direction. Indications are that elongation in the direction of rolling will be 7% or higher, while in the transverse direction, the elongation could be as low as 1 to 2%. However, tensile strengths are approximately the same in either direction. These values and their effect on riveting procedures initiated an evaluation of the fracture characteristics of Lockalloy. Initial results looked promising. The transverse ductility of Lockalloy sheet material can be increased to about 7% if cross rolling is used in the final processing operations; however, the maximum length obtainable is 24 in. The design was based on this maximum length.

The survey showed that Lockalloy had been successfully bonded to aluminum, beryllium, and itself using aluminum-silicon braze alloys.

Indications are that the problems associated with bonding Lockalloy to stainless steel using the aluminum silicon braze alloy will involve the same considerations as bonding aluminum to stainless steel; that is, the formation of brittle intermetallics to critical depths must be avoided. Also, any braze alloy used to join Lockalloy must have a melting point below the 1193°F aluminum-beryllium eutectic melting point.

In addition to the Lockalloy stainless steel, other materials combinations considered were copper-stainless steel and boron-filament-impregnated aluminum. Both of the above combinations essentially solved the thermal expansion mismatch problem, and indications were that the bonding problems could be readily solved. However, the copper fins would result in a significant weight penalty, and handling of the thin annealed copper would be difficult during assembly. Also, the application of the AI-93 emissivity coating to copper is more of an unknown than applying it to aluminum or Lockalloy, since continued oxidation of the copper during radiator operation could result in spalling of the coating. The boron aluminum appeared to be too far in advance of the state of the art and the cost would be excessive. Both these latter approaches were abandoned.

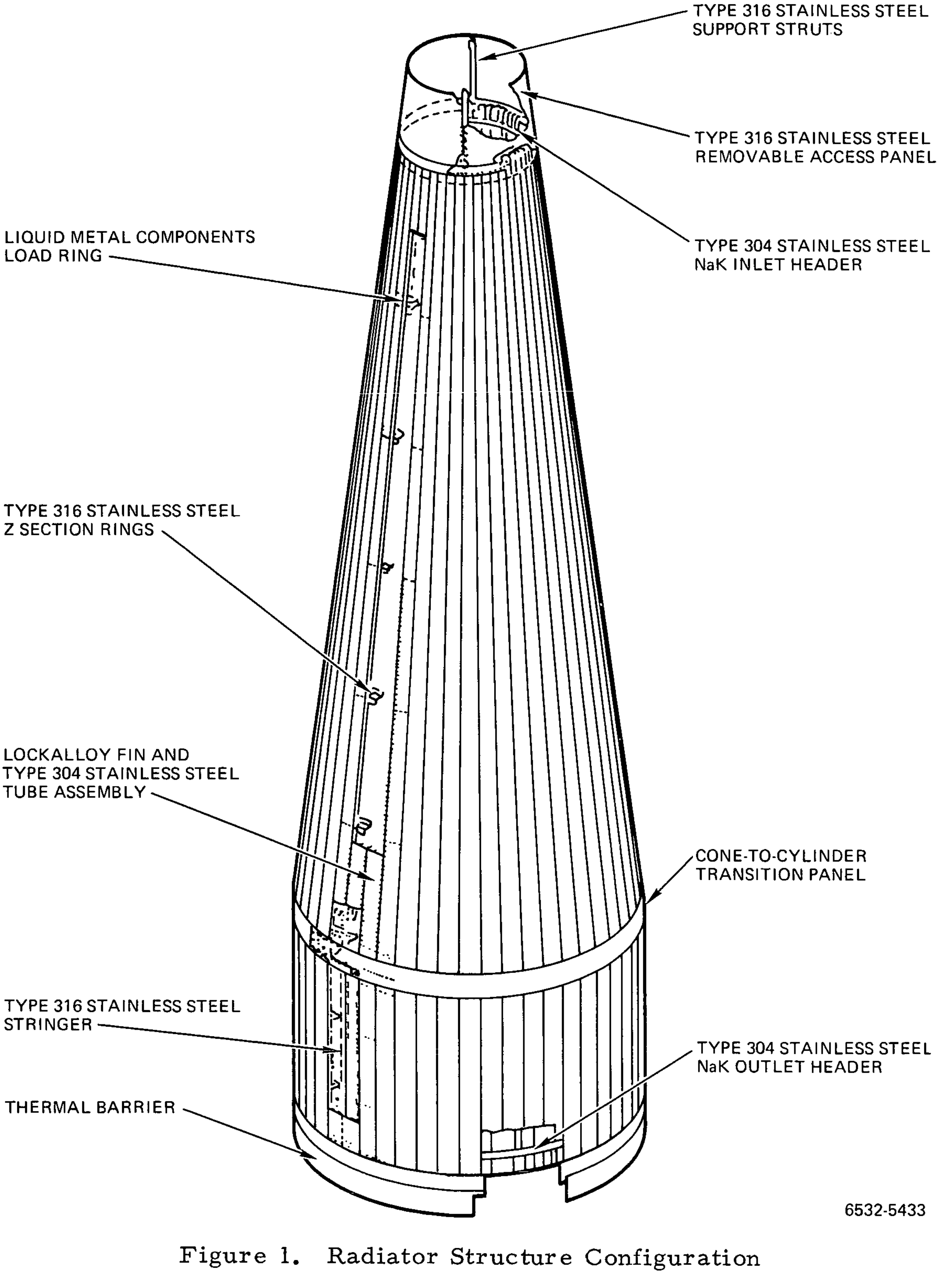

Figure 1. Radiator Structure Configuration

III. CONFIGURATION

The reference design of the 5-kwe thermoelectric system radiator is shown in Figures 1 and 2. The evolution of the basic configuration and its components is described in the following sections. As shown, the configuration consists of a section of a cylinder and a frustum of a cone. The radiator is a dual function component serving as a heat rejection device and the structure for the system. The large diameter at the lower end of the cylinder is attached to the forward end of the space device. The reactor and radiation shield are to be mounted at the small diameter of the cone. Internal components such as the thermoelectric converters, pumps, and expansion compensators are mounted on the inner surface of the radiator.

Figure 3 shows the final design of the 5-kwe thermoelectric system. The reactor and shield are both joined and attached to the forward end of an access panel array. The radiator structure extends from Station 215.3 to 5.5. The forward end of the radiator is the conical section between Stations 74.7 and 215.3 with the small diameter 30.0 inches. The lower cylindrical section between Stations 5.5 and 74.7 is 72.0 inches in diameter. The total radiator area is 266.8 ft^2.

A. CONE OR CONE-CYLINDER CONFIGURATION SELECTION

The configuration selection was performed within the constraints imposed by system performance requirements and launch vehicle integration limitations. However, in that no system application or mission has been defined to date, dimensional requirements were not established. The radiator configuration selection was, therefore, performed under the following assumptions.

1) The design should be such to maximize the reactor-to-spacecraft separation distance within the constraints imposed by system total weight.
2) The design should provide an integral functional and structural unit.
3) The design should allow shadow shielding (neutrons and gammas) of at least the base spacecraft interface plane.
4) The design should be compatible with all probable launch vehicles and spacecraft.

Two design concepts were investigated: all conical and conical-cylindrical. Analytic techniques were employed to calculate the total 5-kwe Reactor Thermoelectric System weight and envelope (geometry) as a function of the radiator design parameters. Those parameters investigated included configuration (conical or conical-cylindrical), conical section half-angle, and base diameter. Radiator area was an independent variable determined by the system thermal performance requirements.

The system design point configuration selection was conical-cylindrical. The all-conical system exhibits minimum weight for a specific area (and performance). However, the system weight penalty associated with the conical-cylindrical selection is approximately 0.5% (of the total system weight). Additionally, the envelope reduction which results from this selection includes a 3% decrease in system height (as compared to a similarly performing conical system), and a 10% decrease in system base diameter. The conical-cylindrical system thus offers the best compromise between minimization of system weight and system envelope. Utilization of this geometry also provides a shadow shielded area at the spacecraft mating plane which is larger than the system base area (because the shielded angle includes the entire radiator conical section).

The system design point conical half angle selection was 8.5°. Design studies indicated that the minimum conical-cylindrical system weight occurred with a 7.5° half-angle. The design point selection was again a compromise between minimum weight and minimum envelope. Utilization of the 8.5° angle provides a 2.5% reduction in total height for an 0.5% increase in total weight. Additionally, the resultant larger volume for internal component placement near the shielding allows increased power conversion system packing densities to be realized.

The cylindrical section base diameter for the 5-kwe system was selected as 6 ft. This selection was made on a weight minimization basis; however, the resultant system exhibits excellent compatibility to launch vehicles and potential spacecraft.

Page intentionally left blank

Page intentionally left blank

B. MATING PLANE ATTACHMENT

The mating plane attachment is the interface between the 5-kwe thermoelectric system and the space device. Its function is to maintain structural integrity between the two systems during launch and space operation and at the same time to restrict the heat flow from the radiator to the spacecraft.

It is desirable to keep the interface short; however, the thermal gradient increases inversely with length which then affects the thermal stresses.

This attachment was considered as a relatively low priority item and did not receive the degree of analysis as did other structural and functional components. It was concluded, however, that a high strength, heat resistant, low conductive metal should be used for the attachment. Titanium meets these requirements. The alloy was not selected but 6Al-4Va-Ti was tentatively selected. It would be a thin shell, 0.040-in. wall, 72 in. diameter, and 5.5 in. long. To accommodate the axial thermal gradient and the thermal expansion mismatch with the radiator, the attachment would have a series of axial slots around the periphery and oriented from the radiator end towards the space device.

C. SHIELD ATTACHMENT

The neutron shield is composed of a stainless steel shell in which lithium hydride is cast under a hydrogen environment. The shell serves as a major structural component with the gamma shield, reactor, and reactor control mechanisms mounted on it. The shield shell sustains all loads on these components and transmits them into a skirt at the lower outer diameter. The skirt is 15 in. forward of the upper end of the radiator which has a corresponding skirt at its forward end.

The intermediate structure is composed of six longitudinal struts equally spaced around the periphery and six panels which are bolted in place. This allows structural continuity with access to the internal piping system for the final steps of the system assembly

The forward skirt of the radiator is to have sufficient axial depth to provide a rigid load path to spread the load in the six struts over the 48-tube and fin assembly.

D. RINGS AND STRINGERS

The rings, or frames, are major structural components that have a double function. They maintain a circular cross section for the radiator and provide end support for the column segments. The ring spacing determines the column length and since column strength is a function of length, the load capacity of the radiator is partially determined by the frames. The rings will be fabricated of sheet metal and will have a "Z" cross section with cutouts and scallops on their outer diameter to conform with the inner surface of the radiator.

The stringers will run axially on the inner radiator surface and will be the fin splice material. The cross section will be a chevron and will be fabricated of sheet metal. It was originally intended to have "T" section stringers but sufficient strength could be attained by having the tubes serve as stringers.

E. COMPONENT BRACKETRY

The pump, thermoelectric array, and expansion compensators, are major components that will be supported on the radiator. The bracketry will be of conventional aerospace configuration, however, provision will be made for thermal mismatch. Both temperatures and coefficients of expansion of the radiator and these components will be different from each other. Therefore, the radial growth differentials will be accommodated by slotted holes with shanked bolts. Axial mismatch, where it is significant, will be accommodated by flexure of the bracket.

F. EMITTANCE COATING SELECTION

The radiator fin surface requires a coating system which is effective in rejecting internal heat and reflecting solar input. The coating must operate in the temperature region 500 to 700°F for 5 years. The environmental requirements for the system thermal radiator coating are given in Table 1.

During the SNAP 10A program, two thermal coatings were considered for use on the system radiator, Z-93 and AI-93. Z-93 is a zinc oxide coating with a potassium silicate binder. AI-93 consists of a top coat of stannic oxide, a subcoat of chromium-cobalt nickel, and a binder of aluminum phosphate.

TABLE 1

COATING ENVIRONMENTAL REQUIREMENTS

Parameter	Requirement
Duration	5 yr
Vacuum	10^{-5} to 10^{-6} torr (ground test)
Temperature	650°F Maximum
Nuclear Irradiation	TBD* nvt (fast) TBD* R
Ultraviolet and Proton Irradiation	5 yr
Dynamic Load	(See Table 2)

Early screening tests(1,2) were made which included many of the basic metal oxides, with particular interest devoted to the white oxides. These tests were begun with an evaluation of the spectral reflectance and total normal emittance of candidate metallic oxides including the oxides of barium, cesium, antimony, silicon, titanium, zinc, and zirconium.

From this study it was found that:

1) The thermal emittance at 600°F for coatings with the aluminum phosphate binder was consistently 3 to 5% higher than coatings with the potassium silicate binder.

2) The solar absorption for coatings with the aluminum phosphate binder was consistently 10 to 20% higher than coatings with the potassium silicate binder.

3) The white pigment which exhibited the highest thermal emittance at 600°F was stannic oxide.

In that the optimum thermal effectiveness of the radiation control coating is determined primarily by the thermal emittance, further coating experimentation emphasized use of the stannic oxide pigment and an aluminum phosphate binder. Total hemispherical emittance measurements of the stannic oxide coating system yield a value of $\epsilon = 0.88$ at 600°F.

---

*TBD - To be determined.

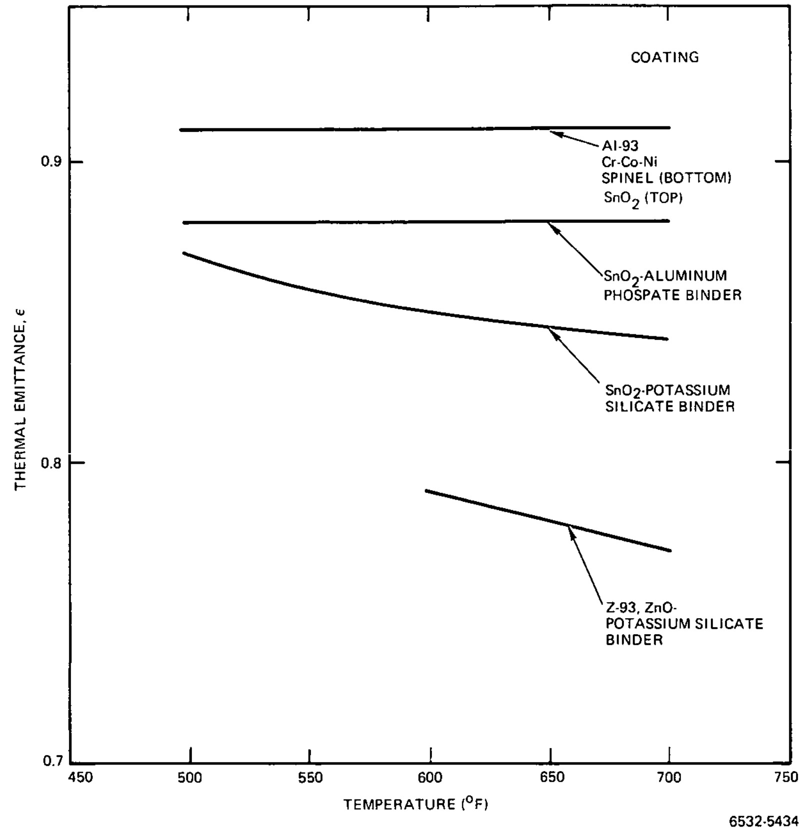

Figure 4. Thermal Emittance of Candidate Coating Systems vs Temperature

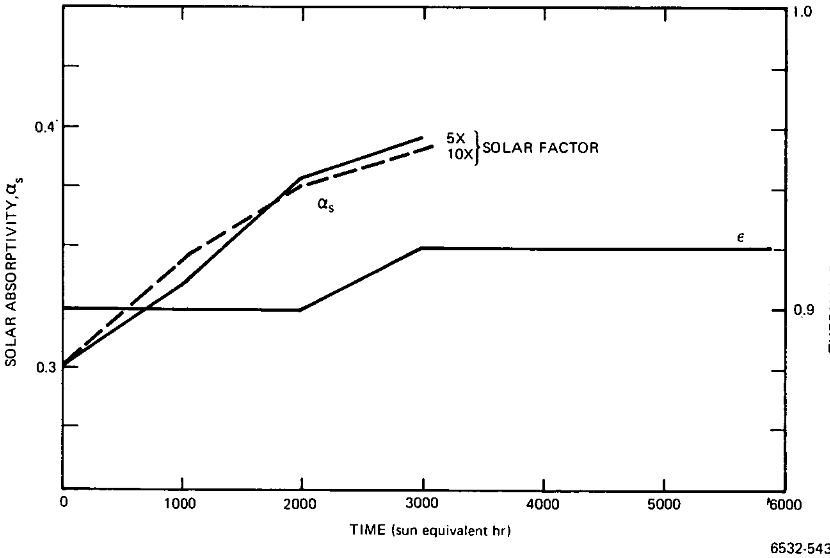

Figure 5. AI-93 Stability in High Vacuum (10^{-7} torr) at 600°F and Ultraviolet Exposure

Many black coatings have a high thermal emittance in the short wavelength infrared region (1 to 4 μ). To further increase the bulk emittance, a composite coating system was devised in an effort to maximize the spectral emittance throughout the infrared region. This was accomplished by utilizing a high thermal emittance, black subcoat and the stannic oxide as a topcoat. Total hemispherical emittance measurements of the two layer composite coating (AI-93) yielded a value of $\epsilon = 0.91$ at 600°F.

The thermal emittance values of the candidate coating systems are shown in Figure 4 as a function of temperature.(3)

Long-term emittance stability tests of AI-93 were made at 600°F in vacuum. Prior to the test, the emittance of the tailored coating as adaptable to aluminum substrates was 0.90. Subsequent to the 4900-hr test, the emittance of the sample was 0.92.

The results of these tests, taken at 10^{-5} torr, are shown in Figure 5 as a function of time.(3)

Three-thousand-hour stability tests of the AI-93 coating system in a simulated space ultraviolet environment resulted in a 50% increase in solar absorptance.(3) The tests were performed utilizing an AH6 mercury lamp for exposure and the vacuum attained during irradiation was 10^{-7} torr. Samples were irradiated at two various solar factors, 5 and 10. Degradation results were similar for each of these accelerated exposures. These tests were also run at 600°F. The results of both exposure factors tests are also shown in Figure 5 as functions of time.

IV. LOADING REQUIREMENTS

The loads which have an influence on the structural characteristics of the radiator exist throughout the life of the radiator and begin with its fabrication. Both mechanical and thermal loads are imposed on the system. Aside from a 1-g axial load in conjunction with the ground test and pre-launch thermal environment, the mechanical and thermal loads do not occur simultaneously. With this one exception, the loads can be treated separately.

The most significant mechanical loads occur during the launch. Although a payload and corresponding mission were not established, a probable flight was assumed. The payload was estimated to weigh 1350 lb and have a length of 12 to 14 ft with a diameter equal to that of the 5-kwe system radiator. It was assumed that the orbit would be polar, circular, and at 600 nautical miles. Then with a system of approximately 1850 lb, the total orbital weight would be about 3200 lb and would require a Titan launch vehicle.

The launch induced loads can be categorized as follows:(4)

1) Low frequency and sustained accelerations
2) Acoustic
3) Shock
4) Thermal.

Non-launch induced thermal loads are results of system operating characteristics.

A. MECHANICAL LOADING

1. Ground Handling Loads

These loads occur while moving the various segments of the radiator during the fabrication phase and moving the completed radiator and system. In plant movements, shipment to the launch site and handling at the launch site up to the time of lift-off were included. Packaging, handling, and hoisting equipment shall be designed in such a manner that ground handling loads shall not exceed 2 g's in any direction and therefore, do not govern the structural design of the system or its components. Ground handling loads, therefore, are not considered in the following structural evaluation of the radiator.

2. Launch Accelerations

The most probable launch vehicle was selected as the Titan-IIIB with Burner II. However, to accommodate potential variations in payload weight and system weight, the Titan-IIIB and the Titan-IIIC with Transtage Burner were also considered.

The accelerations of design significance occur during the maximum qα transonic phase, first stage burnout, and second stage burnout. Table 2 shows the anticipated accelerations associated with these three conditions. An ultimate factor of safety of 1.25 is used in conjunction with the design loads. These levels are also shown.

TABLE 2

LAUNCH ACCELERATIONS

Case	Design Acceleration (g)		Ultimate Acceleration (g)	
	Axial	Transverse	Axial	Transverse
Maximum qα Transonic	6.0	1.6	7.5	2.0
Uncontrolled First Stage Burnout	8.0	1.0	10.0	1.25
Second Stage Burnout	13.0	0.5	16.25	0.625

The maximum qα transonic accelerations are generated from combined engine and aerodynamic vibrations which induce low frequency missile vibrations in the axial and transverse direction. This condition excites the maximum transverse vibration.

The first stage burnout accelerations are due to an uncontrolled engine shutdown. When the supply of fuel is exhausted and burning tends to be sporadic, axial mode vibrations are induced at approximately 20 Hz.

The sustained accelerations are dependent on system mass and the engine thrust. The engines of the Titan system provide nearly constant thrust during each stage. It is obvious, then, that maximum axial accelerations will occur at the end of the burn for each stage when the mass is at a minimum.

$$A = W/T$$

where

A = Acceleration (g)
W = Flight weight (lb)
T = Engine thrust (lb).

Figure 6 shows the axial accelerations of the potential launch vehicles as a function of time from lift-off. A Titan system without a Stage III and with a low mass payload can reach 13.25 g at the end of Stage II burn. The acceleration of Stage II with a 3200-lb payload can reach 12.6 g. With a Burner II and a 3200-lb payload, the Stage II maximum acceleration is 9.1 g.

The loading in the radiator from the launch environment is a function of the system weight distribution and the configuration. For a system of 1800 lb, 72-in.-diameter cylinder, 236 in. from the base of the neutron shield to the base of the reactor and 8.5° cone, Table 3 shows the panel loads for the radiator. The panel loads are derived from the shear (thrust) and moment curves (Figure 7) by the following relationships.

$$N_a = \frac{V}{2\pi R}$$

$$N_b = \frac{M}{\pi R^2}$$

$$q = \frac{V}{\pi R}$$

and $N = N_a G_a \pm N_b G_t$

where

V = 1-g shear or thrust
M = 1-g moment
R = Radius
N_a = Panel membrane load due to thrust
N_b = Panel membrane load due to bending
G_a = Axial acceleration
G_t = Transverse acceleration
q = Panel shear flow.

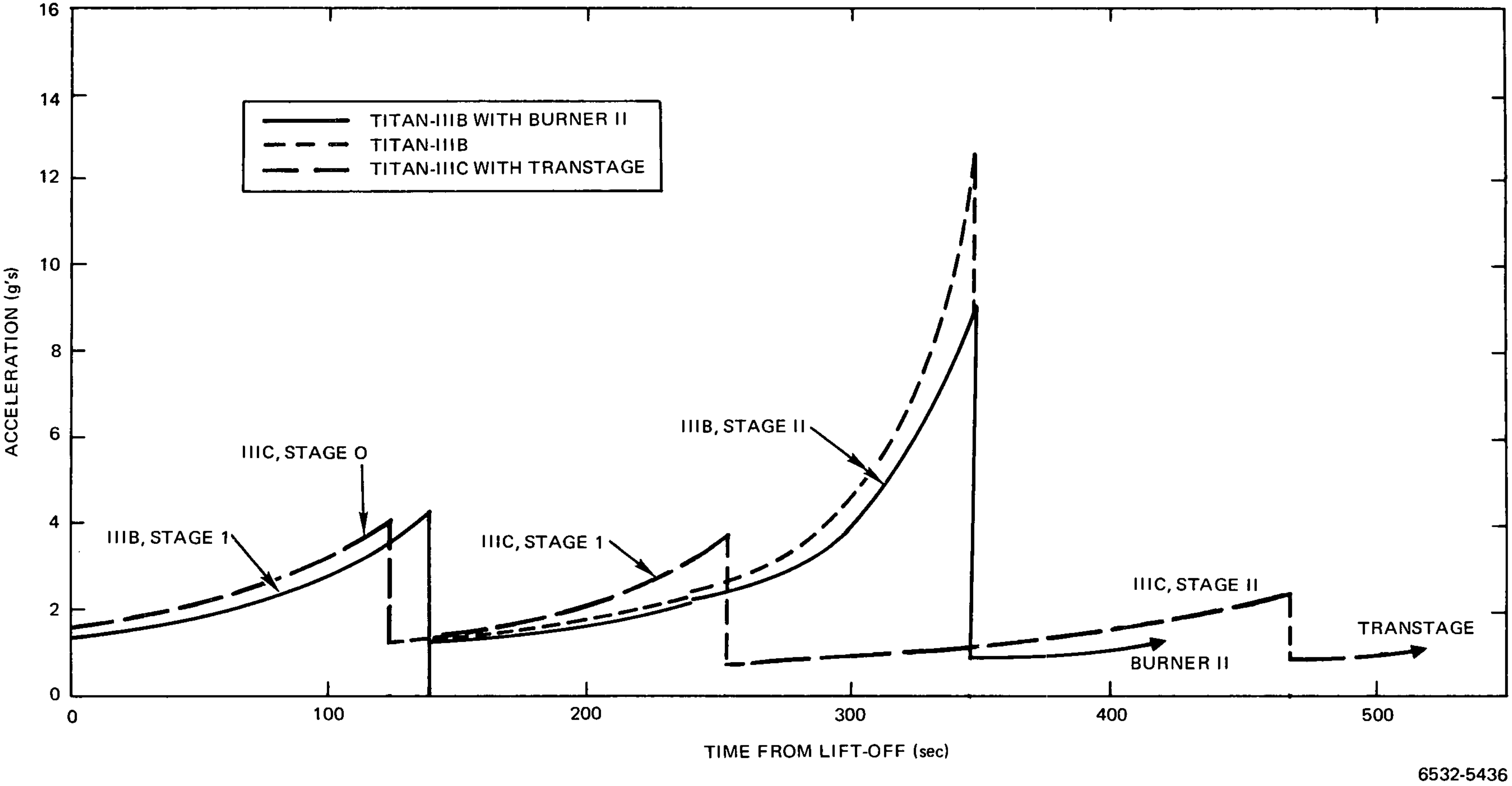

Figure 6. Titan Sustained Acceleration

TABLE 3
UNIT PANEL LOADS FOR LAUNCH ACCELERATIONS

Station	V 1 g Shear (lb)	M 1 g Moment (in.-lb)	R Radius (in.)	N_a Membrane (Thrust) (lb/in.)	N_b Membrane (Bending) (lb/in.)	q 1 g Shear (lb/in.)	Load (lb/in.)								
							Maximum qα			Stage I Burnout			Stage II Burnout		
							Maximum	Minimum	Shear Flow	Maximum	Minimum	Shear Flow	Maximum	Minimum	Shear Flow
0	1800	330000	36	-7.97	±81.05	15.9	102.3	-221.9	31.8	+21.6	-181.0	19.9	-78.9	-180.1	9.9
61.3	1660	225000	36	-7.34	±55.26	14.7	55.4	-165.6	29.4	-4.3	-142.5	18.4	-84.8	-153.8	9.2
80	1620	196000	33.2	-7.77	±56.64	15.5	55.0	-171.6	31.0	-6.9	-148.5	19.4	-90.9	-161.7	9.7
120	1530	130000	27.8	-8.76	±53.54	17.5	31.4	-172.8	35.0	-20.7	-154.5	21.9	-108.9	-175.9	10.9
150	1430	85000	22.0	-10.35	±55.90	20.7	34.2	-189.4	41.4	-33.6	-173.4	25.9	-133.3	-203.1	12.9
182	1030	52000	17.9	-9.16	±51.66	18.3	34.6	-172.0	36.6	-27.0	-156.2	22.9	-116.6	-181.1	11.4
212	880	25000	12.4	-11.31	±51.75	22.6	18.7	-188.3	45.2	-48.4	-177.8	28.3	-151.5	-216.1	14.2
236	620	11000	9.9	-10.02	±35.73	19.9	-3.7	-146.7	39.8	-55.5	-144.9	24.9	-140.5	-185.1	12.4

TABLE 3 UNIT PANEL LOADS FOR LAUNCH ACCELERATIONS AI-AEC-13093

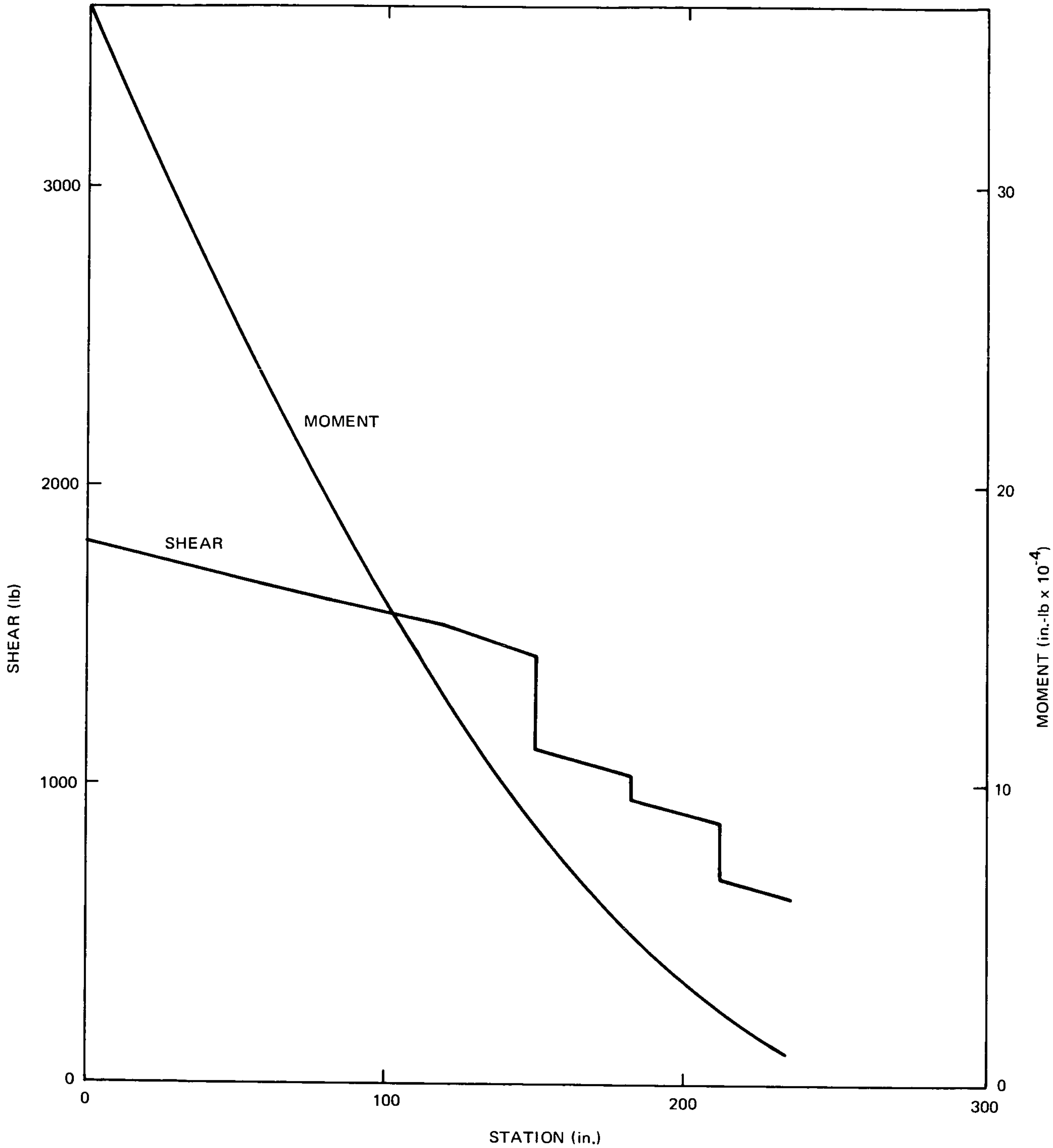

Figure 7. 1-g Shear and Moment

Figure 8 shows the unit panel loads for the three cases as listed in Table 2. Then for the full panel, defined as one tube and the fin and armor between tube centerlines, the radiator loads are shown in Figure 9. The maximum compression load is shown for both 36- and 48-tube arrays.

3. Acoustic Loads

There are essentially two sources of acoustic excitation during the Titan launch. At lift-off and for approximately 5 sec, engine noises reflect off the launch pads and couples with direct excitation of the nose shroud. At Mach 1 through maximum $q\alpha$, there is aerodynamic turbulence for approximately 55 sec. Titan nose shrouds are designed to attenuate acoustic field of this type to 145 db or less inside the fairing. The acoustic spectrum inside the shroud is shown in Figure 10. This is typical of all Titan configurations. The peak value is at 140 db. The overall value is 145 db.

Typically, a 145-db sound pressure level does not excite large payload masses. However, thin panels and components with large surfaces can be subjected to detrimental displacements. The nature of the 5-kwe radiator suggests that it will not be excited to the extent that it will sustain damage in this acoustic environment but that masses mounted on it will require evaluation.

The 5-kwe system configuration is unique and a method of adapting existing acoustic computer programs to suit it was developed. The modified method was checked on a simplified model. Mode shapes and component response to the acoustic energy can be achieved with the methods developed for the 5-kwe system.

4. Launch-Induced Shock

Shock loads generated in a Titan system have two primary sources. The first occurs when stages are separated. The shock stems from the pyrotechnic splitting of the seam at the stage fairings and also from the nose shroud split and separation. The second source occurs when the payload is ejected from the final stage.

All of these events occur at high altitude in a near vacuum that will not transmit shock pressure waves. Consequently, the shock can only be transmitted mechanically through the structure.

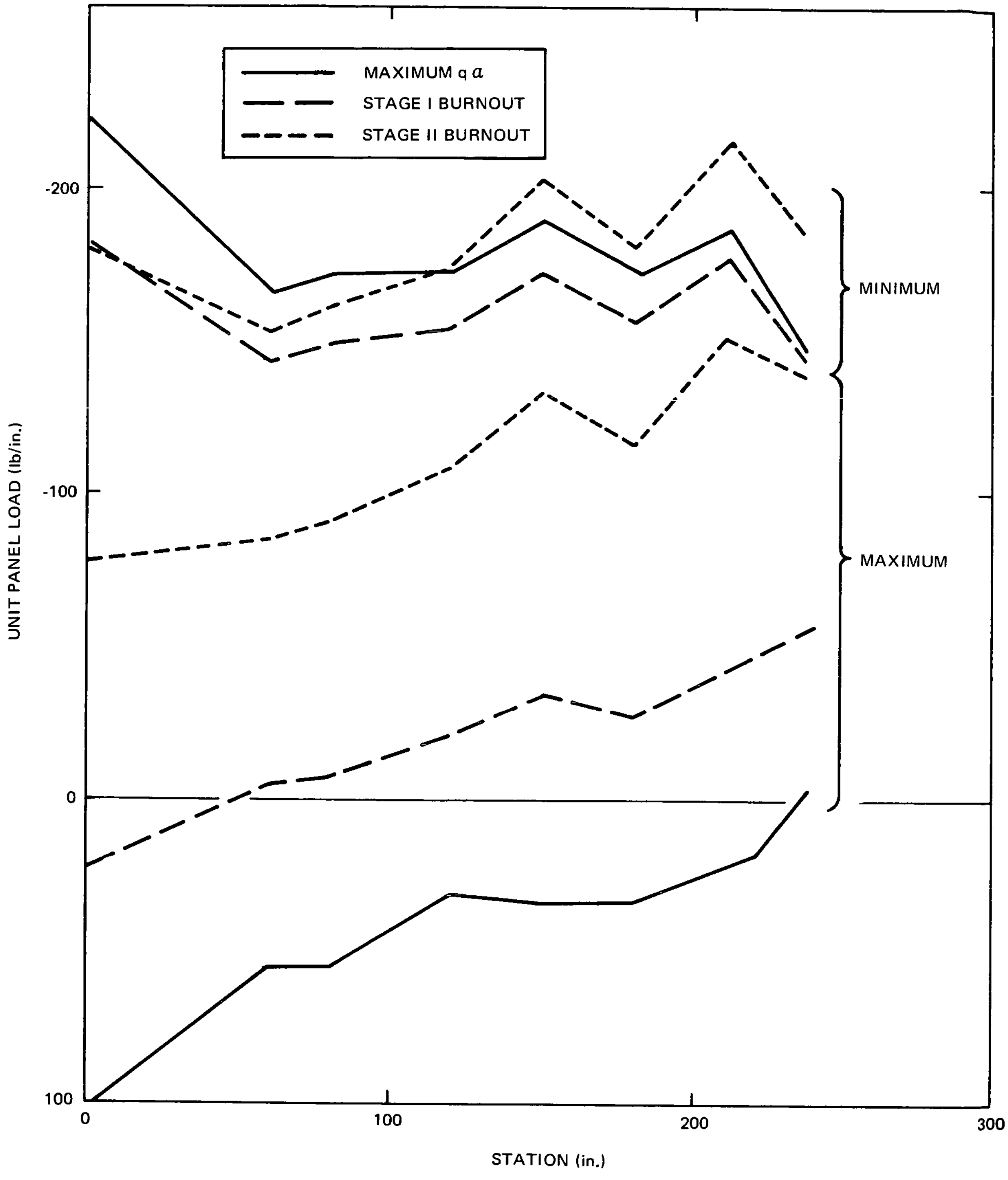

Figure 8. Acceleration-Induced Radiator Loads

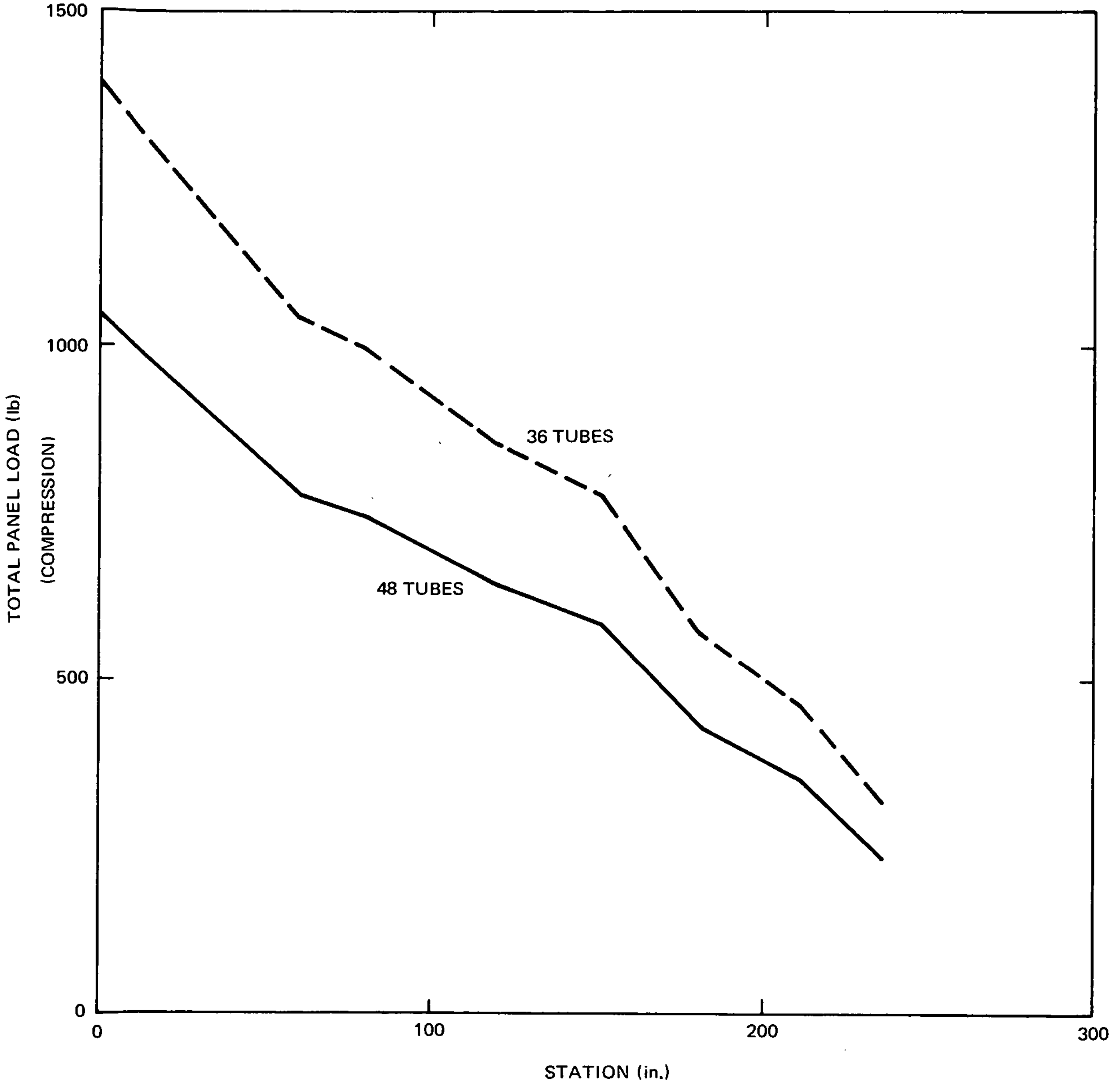

Figure 9. Radiator Panel Loads Due to Acceleration

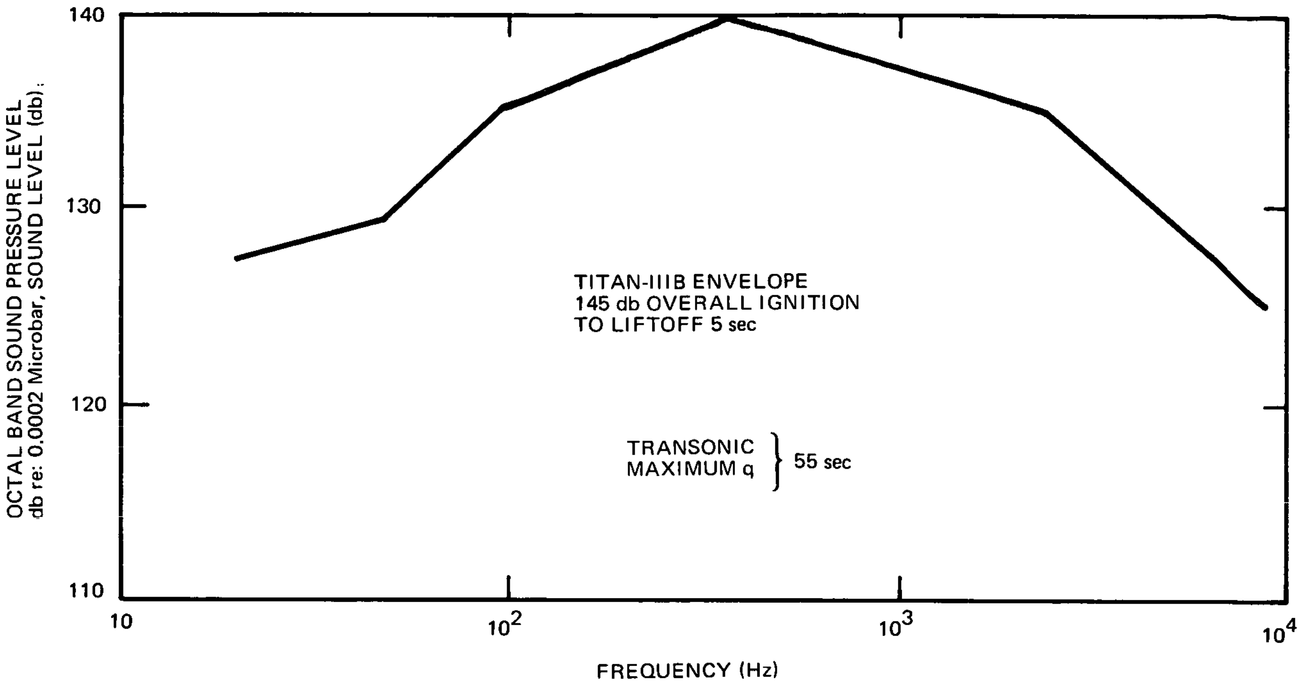

6532-5440

Figure 10. Internal Acoustic Spectrum

The 5-kwe system would be no closer than 12 ft to a shock source. Since these waves attenuate rapidly in a structure, there are no requirements for shock in the radiator design. It should be noted, however, that local components near the shock source would have shock requirement.

5. Orbital Mechanical Loads

During orbit, the system would be at an essentially zero gravity status. Small orientation engines on the payload may induce short time accelerations; however, there is no requirement for structural consideration in the radiator of these loads.

6. Ground Test Mechanical Loads

The 5-kwe system would be oriented with the reactor down during the 5-yr ground operation test. The support point would be at the base of the radiation shield with several "steady-rest" points at the base of the radiator. Thus, the radiator would be subjected to a sustained ≈1.0-g load.

B. THERMAL LOADING

1. Fabrication Temperature History

Fabrication of the radiator would involve various heating steps, depending on the materials used. In all cases, the tube-fin assemblies will be in the fully annealed condition after fabrication.

The Type 304L stainless-steel tubing, when used with the aluminum bearing fin materials, would require the deposition of a layer of titanium which would act as a diffusion barrier to prevent the formation of brittle intermetallics between the stainless steel and the braze (BAl-Si4). Deposition of the titanium is performed on the stainless-steel tubing at a temperature of approximately 1400°F. Vacuum brazing of the aluminum bearing fin materials would occur at a temperature of approximately 1120°F using BAl-Si4, the aluminum-silicon eutectic composition.

The alternate fin materials, Type 304ELC stainless steel and NARLOY-Z (copper alloy), would be vacuum brazed to the stainless-steel tubing at a temperature of approximately 1500°F using BAg-8a. No diffusion barrier coating of the Type 304L stainless-steel tubing would be required.

Heat treatment of the entire radiator assembly at 650°F for 15 min to oxidize the fin surfaces, prior to coating the AI-93, would be required for the aluminum bearing fin materials. Application of AI-93 requires three separate coatings, each of which must be baked at a temperature of 600°F for 15 min.

Techniques for the application of AI-93 coating to stainless steel and NARLOY-Z have not been developed and, therefore, the surface treatment, prior to coating, is unknown. It is assumed the coating application would require the same three applications at 600°F for 15 min.

2. Ground Test System Sequence

The thermal loading of the radiator was determined using a digital computer simulation of the reactor system. The simulation program used was written in the IBM - CSMP modeling language. The model consisted of a nodal lumped parameter simulation of the reactor, power conversion equipment, and remaining system components.

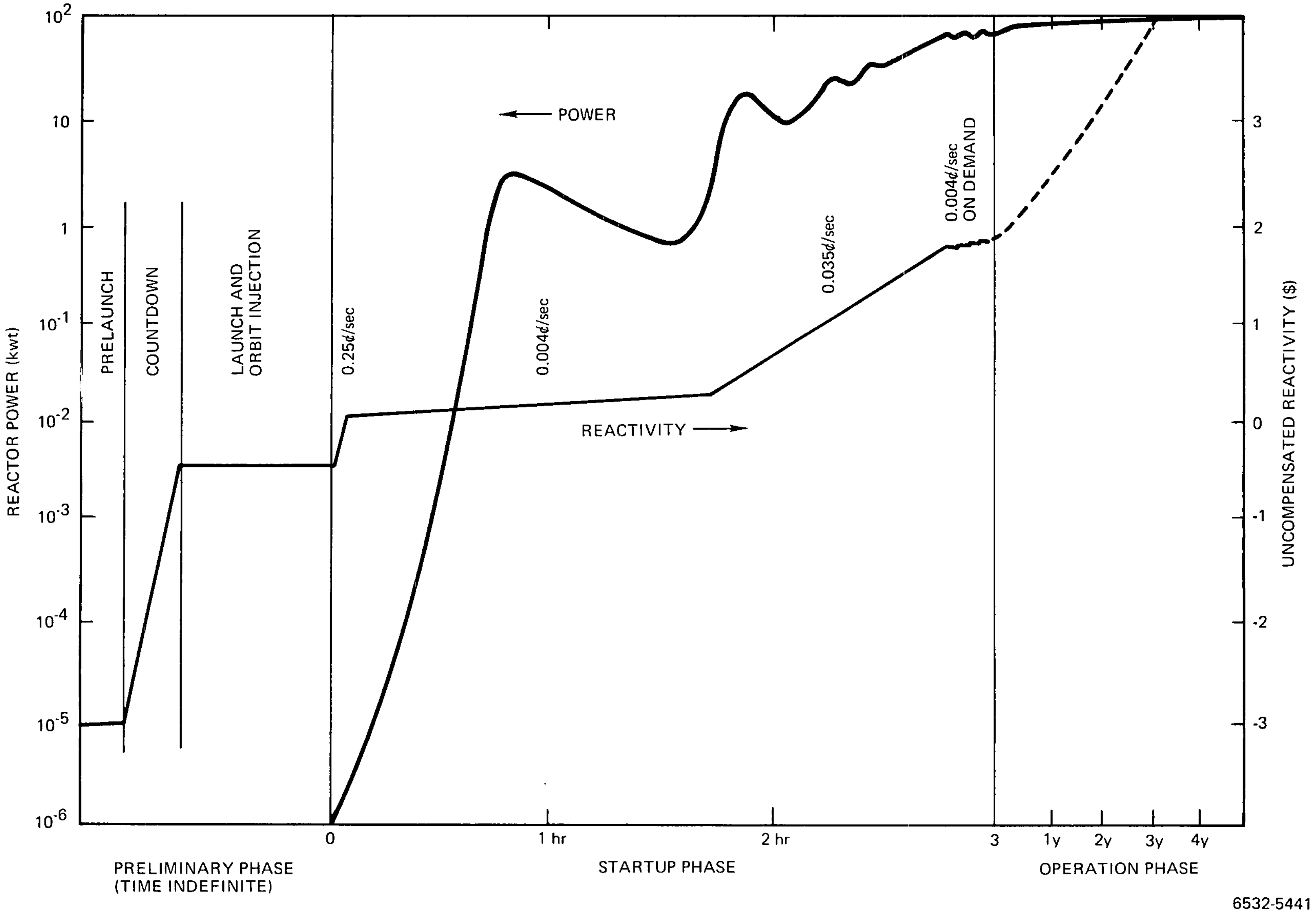

Figure 11. Reactor Power and Inserted Reactivity During Preliminary, Startup, and Operation Phases

The reactor kinetic behavior was calculated as the prompt subcritical multiplication of the delayed-neutron source. This approximation is accurate for reactivity up to a few cents less than prompt critical. The maximum reactivity encountered in these simulations was 60¢, so no appreciable error was introduced by this approximation. Reactivity was computed from the specified insertion and withdrawal rates with temperature-dependent reactivity feedback.

The NaK flows in the primary and secondary systems are calculated based upon the pump thermoelectric module performance as a function of temperature on the primary and secondary sides. The current generated by the thermoelectric power converter is calculated in a similar manner.

Heat rejection is by thermal radiation from the radiator to the environment at an assumed ambient temperature of 100°F. This represents the orbital condition with the thermal shroud in place during startup, and also nearly represents the ground test condition.

While reactivity additions and withdrawals by segment motion are actually in discrete steps of ±0.524¢, for simplicity the startup and control phases were converted to equivalent continuous rates. The fuel temperature coefficient was divided among the various fuel nodes in proportion to the square of the relative power.

a. Startup Transient

The reference system startup concept selected has a multiple reactivity insertion rate which brings the system to full power in less than 3 hours with a minimum of thermally induced stress transients on the reactor and thermoelectric system. The multiple rate system selected for the 5-kwe system is summarized in Table 4.

The startup time required by this scheme is 2.9 hours. Coolant temperature rise is kept below 150°F throughout startup and operation. The maximum rate of temperature increase is 75°F/min. The power overshoot can be maintained at less than 3%.

The inserted reactivity and reactor power as a function of time from prelaunch to final shutdown are shown in Figure 11. The resulting radiator temperatures, during the reference startup sequence, are shown in Figure 12 as

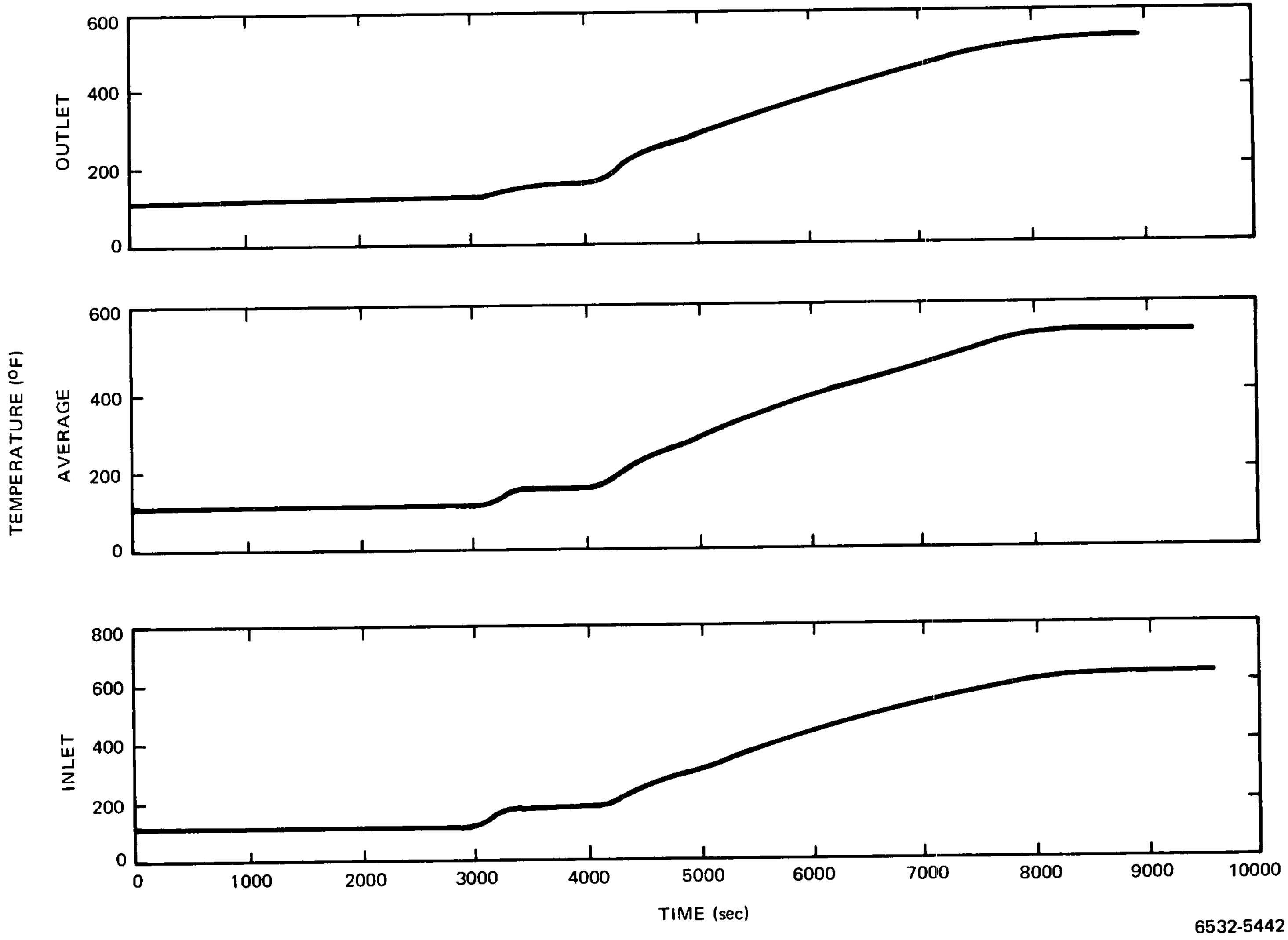

Figure 12. Radiator Temperatures During the Reference Startup

TABLE 4

REFERENCE STARTUP

	Switch at	Rate (¢/sec)	Time (sec)	Cumulative Insertion (¢)
Initial Rate	50¢ addition	0.25	200	50
Second Rate	74.4¢ addition	0.004	6100	74.4
Third Rate	5 kwe	0.035	4100*	182.9
Final Rate		0.004	(balance of life)	
Total Startup Time			10,000 sec or 2.89 hr	

*Switching to final rate at attainment of 5 kwe does not change this result for nominal values, but reduces either the actual startup time or the power overshoot for off-nominal cases compared to time-controlled switching.

functions of time. The radiator temperatures approach equilibrium values after approximately 9000 sec. At this time, the radiator inlet temperature is approximately 590°F. The average radiator temperature is about 520°F and the outlet temperature is approximately 480°F.

b. Shutdown

A reference shutdown sequence has not been determined for the 5-kwe reactor system. However, several postulated accidents were simulated at a normal scram rate. The normal scram simulation may be used to illustrate the radiator thermal response during a reactor shutdown.

During the normal reactor scram, reactivity is added (+0.5 ¢/sec) at a constant rate until the power trip level (125%) was exceeded. At this point, a constant negative reactivity insertion rate of -5.0 ¢/sec was added until a total of -$4 was added to the reactor.

The radiator inlet, average, and outlet temperatures occurring during the normal reactor scram are shown in Figure 13.

c. Steady-State Temperature Conditions

The steady-state thermal conditions during the ground test system sequence were calculated using the 5-kwe reactor thermoelectric system performance

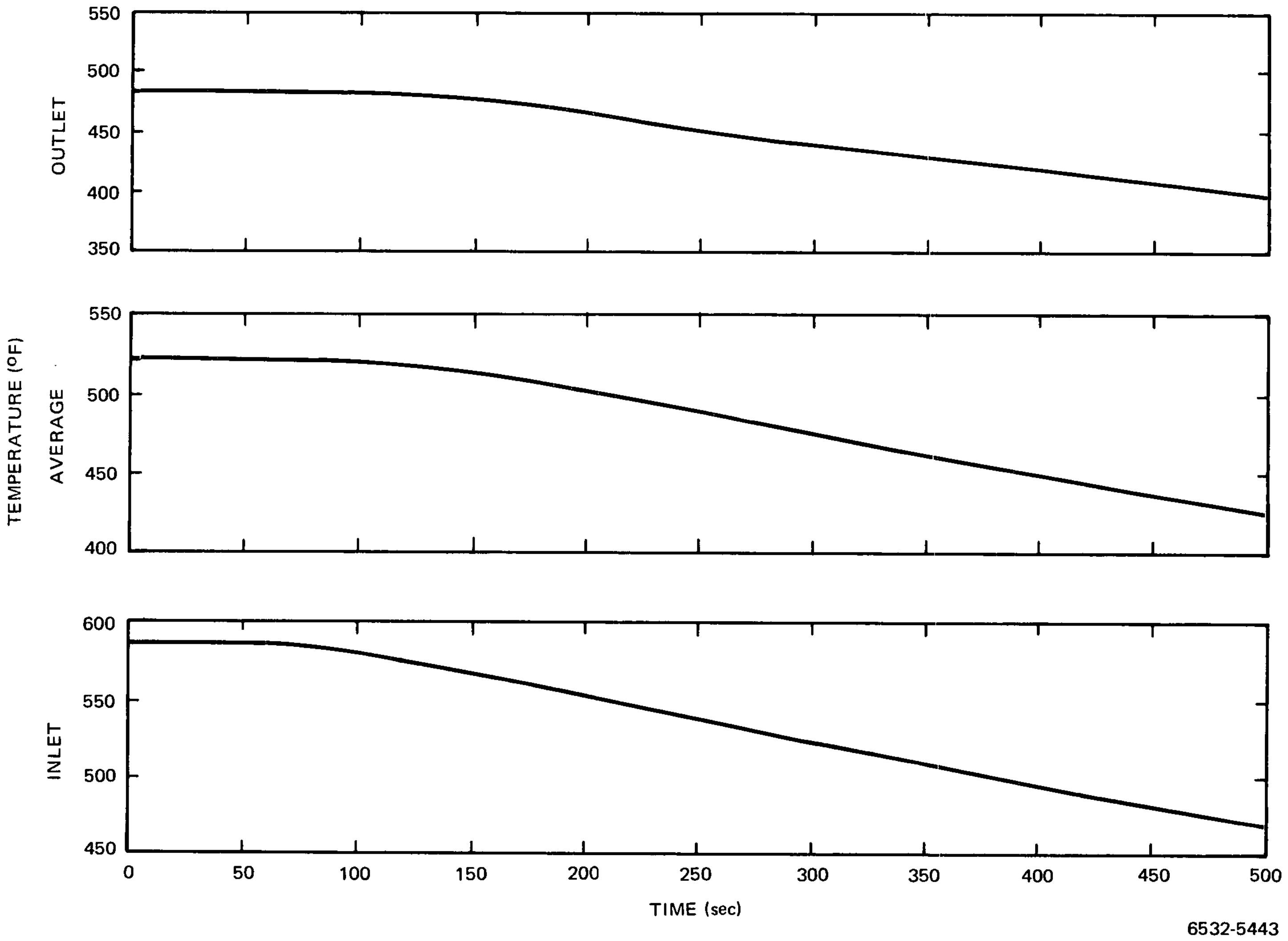

Figure 13. Radiator Temperatures During a Normal Reactor Scram

model. This model incorporates bulk simulation of the thermoelectric modules and pump and piping system, with nodal modeling of the radiator subsystem.

The radiator simulation is based on a five-node model which incorporates the fin effectiveness model of Mackay.(5) Fin effectiveness is a function of the specific radiating surface dimensions, temperature, emissivity, solar absorptivity, and environmental thermal input. The heat rejection is a function of area, fin effectiveness, and fourth-power absolute temperature. The equations are solved at each node, and the results integrated over the entire radiating surface.

Detailed analyses have been performed to determine the capability of the radiator heat sink during the ground test to duplicate the space environment. It was found that an average cold wall temperature of 100°F and an average emissivity of 0.85 will provide an environment very similar to space.

Since the ground and space environments are essentially equivalent, the detailed performance of the 5-kwe system remains identical in both situations (although minor second-order variations in the thermal rejection temperature dependence may occur).

Based upon a beginning-of-life (BOL) reactor power of 95.6 kwt, an outlet temperature of 1148°F, and a core temperature rise of 88.7°F, the BOL radiator thermal loading was found to be 89.3 kwt. The radiator inlet temperature at BOL was found to be 589°F.

Based upon an end-of-life (EOL) reactor power of 94.9 kwt, an outlet temperature of 1200°F, and a core temperature rise of 94.8°F, the EOL radiator thermal loading was found to be 94.9 kwt. The radiator inlet temperature at EOL was found to be 611°F.

d. Emergency Shutdown Transient

An emergency shutdown scram was simulated using the digital model described in Section IV-B-2-a. The emergency scram was accomplished by ejecting the reflectors at a power level of 125% normal power. Reactivity was added to the reactor at a constant rate of +0.5 ¢/sec until 125% of normal power was reached. At this power level the reflectors were dropped which had a reactivity of -$18. The total time required for this reactivity removal was approximately 200 msec.

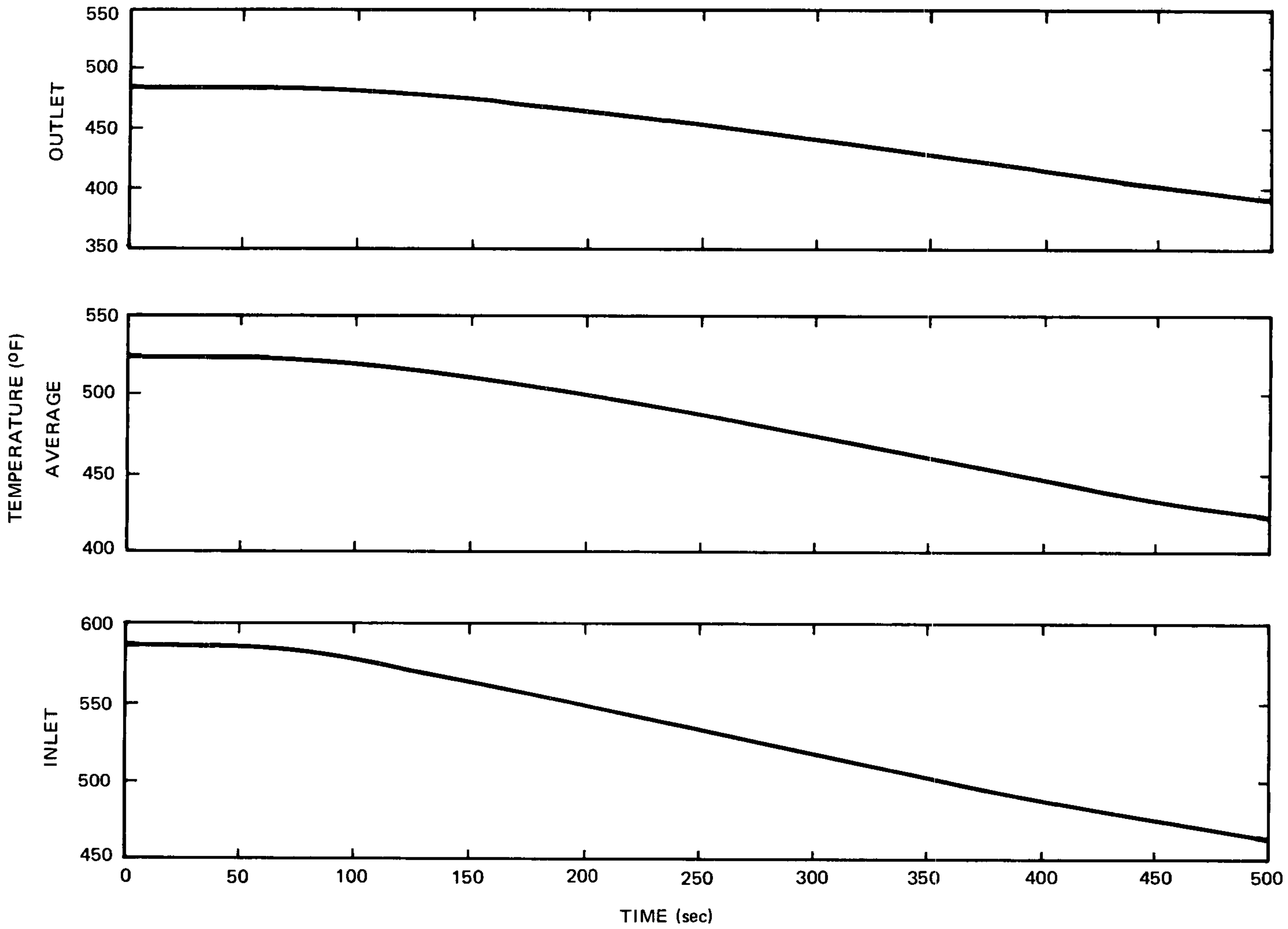

6532-5444

Figure 14. Radiator Temperatures During an Emergency Scram

The radiator inlet, average, and outlet temperatures during this emergency scram are given in Figure 14.

3. Flight System Sequence

a. Startup Transient

The flight system startup sequence thermal loading is the same as that given in Section IV-B-2-a for the ground test startup. The digital simulation of the 5-kwe reactor startup during the ground test rejected heat by thermal radiation from the radiator to an ambient temperature of 100°F. This represents the orbital condition with the thermal shroud in place during startup as well as the ground system test chamber wall.

The reference startup sequence is listed in Table 4. The reactor power and inserted reactivity during startup are illustrated as a function of time in Figure 11. The resulting radiator inlet, average and outlet temperatures during the reference startup sequence are shown in Figure 12. These temperature traces are applicable for both the ground test and flight system startup transients.

b. Steady-State Temperature Conditions

Since the ground test and space environments are essentially equivalent, as explained in Section IV-B-2-c, the flight system steady-state temperature conditions are the same as the ground test conditions given in Section IV-B-2-c. The BOL thermal loading and inlet temperatures are 89.3 kwt and 589°F, respectively, during space operation. The EOL thermal loading and inlet temperature during space operation are 94.9 kwt and 611°F, respectively.

4. Summary of Thermal Loading Requirements

The thermal design objectives for the reactor during startup have been established on the basis of operational requirements, engineering analyses on the system, and safety guides and standards. These objectives are:

1) Temperature rise through the core limited to less than 150°F
2) Rate of temperature change in the inlet plenum limited to less than 150°F/min.

Limiting the temperature rise through the core to less than 150°F prevents generation of excessive thermal stresses in the fuel, cladding, internal reflector, and core vessel. This temperature rise is affected mainly by the reactor power and its rate of increase, and by the primary NaK flow rate.

Limiting the rate of temperature change to 150°F/min avoids severe thermal shock.

The reference multiple rate startup provides a well-behaved power and temperature rise that meets the thermal design objectives for the reactor core. This startup results in a rate of temperature increase in the radiator of less than 50°F/min.

During the simulated normal and emergency reactor scrams discussed in this section, the maximum rate of radiator temperature drop is also less than 50°F/min.

The 50°F/min temperature rise during startup may result in critical stress levels in the cold regions between the individual radiator coolant tubes. A 30 to 50°F thermal lag may exist between the fin root and fin tip. This lag will produce a differential thermal expansion and consequently an increase in stress level between the fin root and tip. Additional analyses will be required to assess the degree of this thermally induced stress.

The BOL and EOL steady-state thermal characteristics of the reactor and radiator are summarized in Table 5.

TABLE 5

BOL AND EOL PERFORMANCE SUMMARY

	BOL	EOL
Reactor		
Power (kwt)	95.6	101.3
Outlet Temperature (°F)	1148	1200
Core Temperature Rise (°F)	88.7	94.8
Radiator		
Thermal Input (kwt)	89.3	94.9
Inlet Temperature (°F)	589	611
Temperature Drop (°F)	132	144
Average Temperature (°F)	522	538

These thermal characteristics are applicable to both the space system and the ground test system. The EOL steady-state thermal loadings will be used in the design analysis of the radiator for the 5-kwe reactor system.

V. ALUMINUM FIN RADIATOR

Much of the radiator effort was based on the assumption that it would have stainless-steel NaK tubes and aluminum fins with meteoroid armor of integral aluminum. It was assumed that each tube would be brazed to a fin and that the fin tips would be riveted to form the circular cross sections shown in Figure 2. This section presents the development of the aluminum radiator in a chronological order. The various sections deal with separate considerations. Milestones were reached and design modifications incorporated as a result of findings in several considerations simultaneously.

A. ALUMINUM FIN RADIATOR CONFIGURATION SELECTION

"Configuration" has several implications. The overall configuration of the radiator is basically that of the system. In the system, it refers to the shape, whether it be cone and cylinder or all cone, the angle of the cone, etc. This aspect of configuration selection is based on system considerations with performance, efficiency, and weight. The number of NaK tubes is also an aspect of configuration selection and is covered in Section V-C. The sense implied here, however, is that which is concerned with the tube size and shape, the fin size and shape, and the bonding method of joining the aluminum fin to the stainless-steel tube.

One of the first groundrules to be established on the radiator configuration was to make the fin and tube an integral part of the primary structure. Weight was a primary concern leading to the selection of aluminum for the fins with austenitic stainless-steel tubes. The alloy selection was based on requirements for high conductivity, maximum strength, compatibility with the environment, and durability. Material selection and fabrication methods are shown in Section V-B and thermal considerations are in Section V-C.

The structural requirements of launch were used as the primary basis for material strength in determining gross cross section requirements. The launch has a cold environment and is independent of operation or test structural requirements. Then as the various conditions were applied, the cross section evolved. It was found that thermal performance and armor requirements determined the aluminum fin dimensions and then that structural requirements for launch were

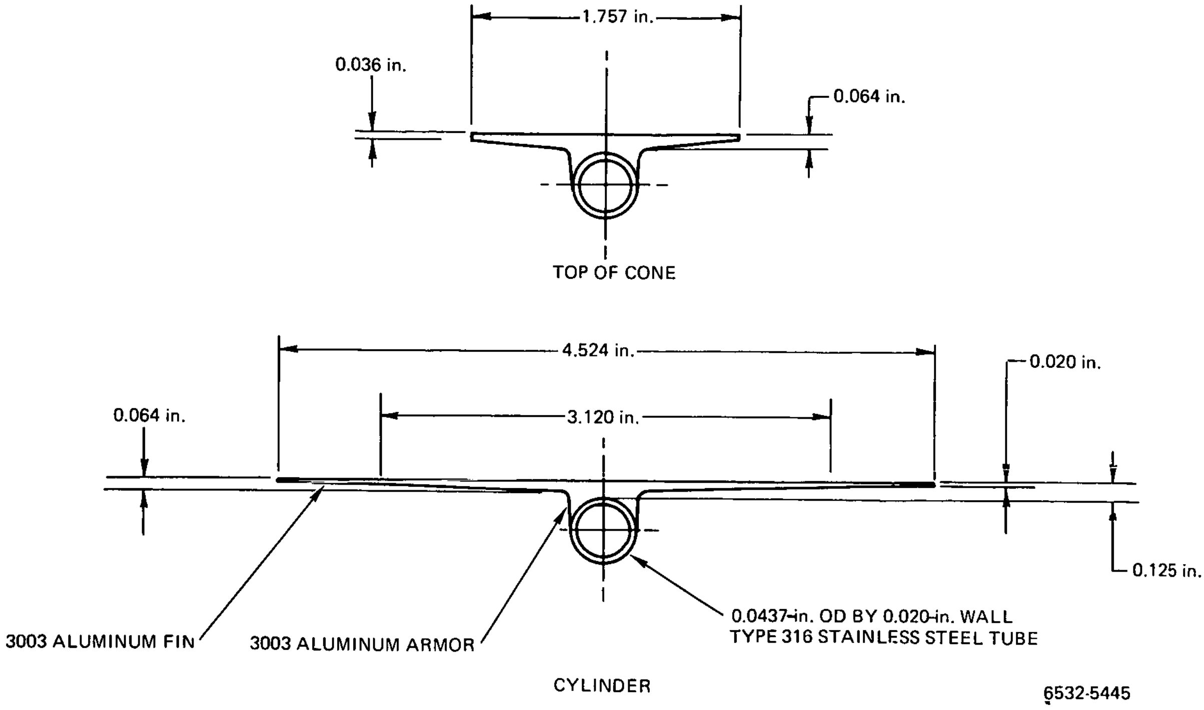

Figure 15. Asymmetric Tapered Aluminum Fin and Stainless-Steel Tube Cross Section

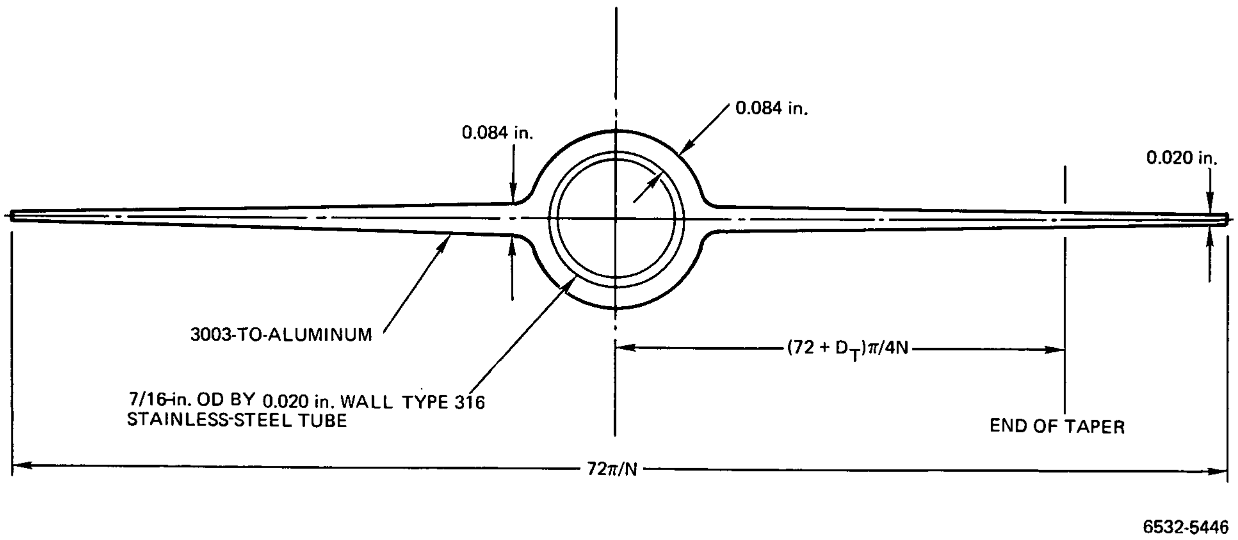

Figure 16. Symmetric Aluminum Fin and Stainless-Steel Tube Cross Section

exceeded. The initial cross section was asymmetric and tapered both axially and circumferentially (Figure 15). A number of asymmetric sections were considered but the basic differences were in the fabrication. The evaluation included the merits of tapered vs non-tapered. As the thermal stress analysis progressed, it became evident that bowing (see Section V-F-2) would occur if the asymmetric cross section were retained. The symmetric cross section of Figure 16 became the new reference design. Further optimization of material thicknesses, number of tubes (N in Figure 16) and taper relationships were made. The thermal stress analysis showed that thermal ratcheting would occur with the aluminum-austenitic stainless-steel configuration (Section V-F-6), and a study was made to alter the ratio of tube area to fin area. Simultaneously, there was an effort to use higher strength tube material such as hardened austenitic stainless steel, Inconel 718, etc. These studies showed that the problems associated with bonded aluminum fin-tubes exceeded the advantages, and a material change was made to Lockalloy.

B. MATERIAL CHARACTERISTICS AND SELECTION

The technical requirements for the aluminum radiator fin material were, in addition to the thermal requirements (Section IV-B-1),

1) The aluminum selected should optimize the properties of: (a) thermal conductivity, (b) strength, (c) brazeability, (d) availability with a minimum of process development, (e) low vaporization of any element in the space environment and at operating temperatures, and (g) weight.
2) The imposed loads on the radiator would be 1 g at pre-launch operating temperatures for up to 5 years, a higher g load during launch with the reactor at ambient temperature, and no g loading during operation at temperature in space for up to 5 years. However, for ground testing, a 1 g for 5 years would be required.

During the study, concern was expressed over the possibility of the evaporation of magnesium from the aluminum alloy which could then vapor deposit on components internal to the radiator shell. As this space contains electrical circuitry, metallic deposition could result in electrical malfunction. Therefore a calculation was performed to examine the possible evaporation rate from an Al-1% Mg alloy, as follows.

The evaporation rate of a material from a surface is affected by two factors. The first is the chemical activity of the evaporating species at the surface. The second is the degree of inhibition toward evaporation that is exhibited by the surface. One surface factor that may be present in an aluminum alloy is the presence of a thin, but not impermeable, oxide layer. Normally, this would present some kinetic inhibition to evaporation, but the extent of its effect cannot be estimated. In the present case, the conservative first approximation is to neglect the effect of the film.

The chemical activity of magnesium in the alloy can be estimated by assuming the $\Delta F(f)$ of the alloy is equal to the partial molal heat of formation of aluminum – magnesium alloys. This is equivalent to assuming that the $\Delta S(f)$ of the alloy is zero, a not unreasonable assumption for the reaction of condensed phases. The best evaluation of the partial molal heat of formation of the Al-Mg alloy is to set

$$\partial(\Delta H)/\partial n = \Delta H(f) \qquad \text{(cal/g atom Mg)}$$

The $\Delta H(f)$ of Al_3Mg_4 is reported to be -49,000 cal/mol, or about 12,000 cal/g atom Mg. Therefore, one can write the expression,

$$Mg(s) + Al(s) = \text{Mg in dilute Mg-Al alloy;}$$

$$\Delta F(f) = -12{,}000 \text{ cal/g atom Mg}$$

The vaporization reaction from the alloy is the sum of the two steps,

$$\text{Mg in dilute Mg-Al alloy} = Mg(s) + Al(s), \quad \Delta F = +12{,}000$$

$$Mg(s) = Mg(g) \qquad \Delta F = +19{,}430$$

$$\text{Mg in dilute Mg-Al alloy} = Mg(g); \ \Delta F = +31{,}430 \text{ cal/g atom Mg}$$

The effective vapor pressure of magnesium is given by the expression,

$$\Delta F = 31{,}430 = -RT \ln p(Mg)$$

$$= 31{,}430 = -(4.575)(589) \log_{10} p(Mg)$$

$$p(\mathrm{Mg}) = 3 \times 10^{-12} \text{ atm.}$$

The initial evaporation rate of Mg will be given by the Langmuir expression,

$$q = 44.4P(M/T)^{1/2} \text{ gm/sec-cm}^2$$

$$q = 2.7 \times 10^{-11} \text{ gm/sec-cm}^2 \text{ (Mg)}$$

In five years, there are $(3600)(24)(365)(5) = 1.58 \times 10^8$ sec and, if the above evaporation rate were to be sustained for the entire time, the total Mg loss would be

$$w = q\theta = (2.7 \times 10^{-11})(1.58 \times 10^8) = 4.26 \times 10^{-3} \text{ gm/cm}^2$$

$$= 4.3 \text{ mgm/cm}^2.$$

Thus, under the conditions, the loss of Mg is quite modest at 4.3 mgm/sq cm. Because the source material is a dilute alloy, the evaporation rate may be reduced if the diffusion rate of Mg in the alloy is too low to maintain the surface concentration of Mg at the nominal 1% value required to maintain the evaporation rate calculated above. The loss of Mg is thus controlled by a balance between the evaporation rate at the surface and the rate of approach to the surface as controlled by the unsteady state diffusion of Mg from the interior.

Jost(6) gives data from which the value of D can be estimated. The value of D at 589°K (600°F) is 3×10^{-12} cm^2/sec. Jost also gives an expression for the average concentration $\bar{c}$ of a diffusing species in a slab geometry as a function of time. The rate of transfer of the diffusing species can be obtained by differentiating the $\bar{c}$ expression with respect to time. The resulting expression is,

$$R = -\frac{4CoD}{h} \sum_{\nu=0}^{\infty} \exp\left[-(2\nu - 1)^2 \, (Dt\pi^2)/h^2\right]$$

where

Co = Original concentration, uniform through the slab
Co = 2.7×10^{-2} gm Mg/cm^3
D = Diffusion coefficient, $D = 3 \times 10^{-12}$ (cm^2/sec)
h = Thickness of the slab, h = 1 (cm)
t = Time (sec)
R = Transfer rate (gm/cm^2-sec).

At t = 0, R = ∞, as is required by the boundary conditions at t = 0. At t = 5 years, or 1.58×10^{8} sec, R = -2.09×10^{-12} gm/cm^2-sec.

Thus, the diffusion-controlled loss rate would begin at infinity at time zero, and decrease in 5 years to 2.09×10^{-12} gm Mg/cm^2-sec. However, at the outset, the Langmuir evaporation rate will limit the loss rate to 2.7×10^{-11} gm Mg/sec-cm^2. The 5-year diffusion-controlled rate is more than an order of magnitude less than the initial evaporation-controlled rate. This means that at the outset, the loss of magnesium will be controlled by the evaporation rate limitation. After about a year, the diffusion rate will be about the same as the evaporation rate, and thereafter, the diffusion rate will be the controlling factor. Under this sequence of loss-controlling mechanisms, the total loss of Mg will be less than the 4.3 mgm Mg/sq-cm computed for the idealized evaporation rate.

If the controlling mechanism changes from evaporation to diffusion after one year's operation, then the loss of magnesium will probably be less than 2 mgm Mg/sq-cm over the 5-year period.

Based on the calculated loss of magnesium from a radiator alloy with 1% Mg and the area of the inner surface of the radiator, the loss would be about 500 cc or a pint of material in the 5-year exposure. Accordingly, the use of magnesium-bearing alloys was considered unwise.

A number of aluminum alloys were considered. In general it was found that the higher strength alloys contained magnesium in unacceptable quantities. A discussion of each of the aluminum alloys follows:

1100	An alloy having high thermal conductivity, and high melting range, is brazeable and available but has low mechanical strength.
2011	A magnesium-free alloy but available only as bar stock and having lead, zinc, and bismuth as additions for free machining purposes and considered not suitable.
2024	A high strength alloy susceptible to stress corrosion and containing magnesium.
2219	A low magnesium alloy that maintains mechanical strength at temperatures up to 600°F better than 1100 or 3003 but due to low melting range would not be suitable for brazing.

3003	An alloy with thermal conductivity slightly inferior to 1100 but with higher mechanical strength.
3004	An alloy similar to 3003 but with higher mechanical strength and 1% nominal magnesium content.
5052	A high strength work hardening alloy that contains magnesium.
6061	A high strength heat treatable alloy that contains magnesium.
7075	An alloy that can be heat treated to high strengths but is susceptible to stress corrosion and contains magnesium.

The manufacturing, prelaunch, and space service conditions imposed requirements on the material selection that exceeded the conventional range of properties developed for engineering purposes. The specific selection of the materials was, of necessity, a compromise of a number of applicable factors. For these reasons, Alloy 3003, condition '0,' was selected for the radiator fin material. This alloy possessed the high thermal conductivity required for the component but had low mechanical strength. The selection was based on the assumption that the aluminum radiator panels would be brazed to the stainless-steel NaK tube and then the assembly of the panels and support structure would be accomplished by mechanical fasteners. The outer surface of the assembled radiator would then receive the emittance coating.

The mechanical and physical properties of the examined alloys are included in Table 6. The chemical analysis limits of the selected alloys are in Table 7.

C. PERFORMANCE TRADES

1. Performance Requirements

Two sets of system performance requirements were used during the trade studies involving the aluminum fin radiator design. The performance requirements used in the optimization of the tapered asymmetric radiator fin-tube cross section for power rejection of 86.8 kwt are given in Table 8.

As the optimization analysis continued, the power rejection requirements for the thermal radiator increased to 92.9 kwt. The corresponding radiator design requirements were then changed as shown in Table 8.

TABLE 6

MECHANICAL AND PHYSICAL PROPERTIES OF ALUMINUM ALLOYS

Property	Temperature (°F)	Alloy						
		1100	2219	T 62	3003	3004	5052	6061
		0	0		0	0	0	0
Ultimate Tensile Strength (ksi)	75	13	25	58	16	26	28	18
	600	2.9	§	10	4	7.5	7.5	8
Yield Strength (ksi)	75	3.5-5	11	40	5-6	10	13	8
	600	2	§	8	2.4	5	5.5	4
Elongation % in 2 in.	75	40	18	12	30	25	30	30
	600	80	§	40	70	80	110	100
Shear Ultimate (ksi)	RT	9	§	§	11	16	18	12
	600	§	§	§	§	4.6	4.6	4.9
Endurance Limit RR Moore,* 5 x 10^8 cycles	RT	5	§	15	§	14	16	9
Tensile Modulus 10^6 (psi)	75	10.0	10.6	10.6	10.0	10.0	10.2	10.0
	600	6.9†	§	7.5	§	6.4†	7	9
Density (lb/in.^{3})	RT	0.098	0.103	0.103	0.099	0.098	0.097	0.098
Coefficient of Expansion (in./in. x 10^{-6})	75-212	13.1	12.4	12.4	12.9	13.3	13.2	13.1
	75-600	§	13.7	13.7	§	§	§	§
Thermal Conductivity (Btu/in./ft^2/°F-hr)	75	1540	1190	980	1340	1130	980	1250
	†600	1455	1270	1040	1270	§	1108	1310
Annealing Temperature (°F)		650**	775†		775**	650**	650**	775††
Melting Range (°F)		1190	1010	1010	1190	1165	1100	1080
		1215	1190	1190	1210	1205	1200	1200

Note: The tensile, yield, and elongation values above represent exposure to temperature for 10,000 hours, the properties are at temperature.

*Rotating beam †Calculated §No data **No dwell time required ††2 to 3 hours

TABLE 7
CHEMICAL COMPOSITION LIMITS FOR ALUMINUM ALLOYS*

Element	Alloy								
	1100	2011	2024	2219	3003	3004	5052	6061	7075
Silicon	1.0	0.4	0.5	0.2	0.6	0.3	0.45	0.4	0.4
Iron		0.7	0.5	0.3	0.7	0.7		0.7	0.5
Copper	0.05 0.20	5.0 6.0	3.8 4.9	5.8 6.8	0.05 0.2	0.25	0.1	0.15 0.4	1.2 2.0
Manganese	0.05	-	0.3 0.9	0.2 1.5	1.0 1.5	1.0	0.1	0.15	0.3
Magnesium	-	-	1.2 1.8	0.02†	-	0.8 1.3	2.2 2.8	0.8 1.2	2.1 2.9
Zinc	0.10	0.30	0.25	0.10§	0.10**	0.25	0.10	0.25	5.1 6.1
Lead	-	0.2 0.6	-	-	-	-	-	-	-
Bismuth	-	0.2 0.6	-	-	-	-	-	-	-
Vanadium	-	-	-	0.05 0.15	-	-	-	-	-
Zirconium	-	-	-	0.1 0.25	-	-	-	-	-
Titanium	-	-	-	0.02 0.1	-	-	-	0.15	0.2
Chromium	-	-	0.1	-	-	-	0.15 0.35	0.04 0.35	0.18 0.35

*Composition in percent maximum unless range is shown
†Typical 0.005
§Typical 0.010
**Typical 0.025

TABLE 8
PERFORMANCE REQUIREMENTS

Power Rejected (kwt)	86.8	92.9
Area (ft^2)	246.3	273.2
Inlet Temperature (°F)	590	590
Coolant Temperature Drop (°F)	136	144
Emissivity	0.9	0.9
Solar Absorptivity	0.4	0.5
Environmental Heat Input (Btu/ft^2-hr)	102	102 (8.16 kwt)
Coolant Flow Rate (lb/sec)	2.84	2.88

These revised performance requirements were used during the optimization analysis of the symmetric aluminum fin-tube cross section.

2. Meteoroid Armor Requirements

Using the various equations and parameter values given in the Appendix to this report, the armor thickness required to protect the coolant tubes of the aluminum fin radiator was determined for various noncritical damage probabilities. The coolant tube configuration considered was that of an aluminum radiator fin attached to a stainless-steel coolant tube which served as an inner liner.

The assumed mission dependent input values were as follows:

Vulnerable area = 30 ft^2
Mission time = 5 yr
Orbital altitude = 600 n. mi

The 600 n. mi orbital altitude yielded an earth shielding factor, E, value of 0.7631. The 30 ft^2 vulnerable area corresponds to the projected surface area of the 50, 0.4375-in. OD coolant tubes used in the 246.3 ft^2 radiator.

The initial damage thickness parameter, a, for stainless-steel tubes inside aluminum armor was set to 1.5. This corresponds to the stainless-steel liner being dimpled upon impact with the dimple height between 10 and 20% of the tube diameter. Using this with the asymmetric fin-tube cross section design, a value of an aluminum armor thickness of 0.125 in. must be placed on the outer surface of the coolant tubes to provide a 0.99 noncritical damage probability. This thickness includes the radiator fin thickness

The damage thickness factor was later changed to 0.90 which corresponds to a 0.75 dimple upon impact. Using this value, an aluminum armor thickness of 0.082 in. is required to provide a 0.99 noncritical damage probability during the 5-year mission lifetime. This armor thickness was used for the design optimization of the symmetric aluminum fin-tube cross section radiator.

3. Design Optimization

The optimization study of the asymmetric tapered aluminum fin and tube cross section involved three series of calculations to determine the coolant tube diameter, the number of coolant tubes, and the dimensional characteristics of the radiator fin. The performance requirements corresponding to a rejected power of 86.8 kwt given in Section V-C-1 were used as the design parameters for all optimization analyses performed on the asymmetric aluminum radiator.

A series of calculations was made to determine the pressure drop through the radiator and system weight for various number of coolant tubes. Two tube sizes were considered in these calculations, 0.4375- and 0.375-in. OD both with a 0.020-in. wall thickness. The number of coolant tubes was varied from 44 to 58. In each case the coolant tubes were assumed to be equally spaced around the circumference of the radiator structure.

The results are shown in Figures 17 and 18. As can be seen in Figure 17, the larger coolant tube size yielded a pressure drop approximately 0.12 to 0.20 psi lower than the 0.375-in. OD coolant tubes, depending upon the number of tubes. The radiator weight using the 0.4375-in. OD coolant tubes was approximately 20 lb heavier than the corresponding radiator employing the smaller coolant tubes. This weight increase is partially offset by a 5-lb decrease in secondary loop piping system weight. The use of larger coolant tubes through the heat rejection portion of the radiator permits the use of smaller pipes in the remaining portions of the secondary coolant system.

The U-shaped radiator weight curves in Figure 18 show the influence of fin root thickness as the number of coolant tubes increase. As the coolant tube spacing decreases, the required fin root thickness also decreases. More weight

F

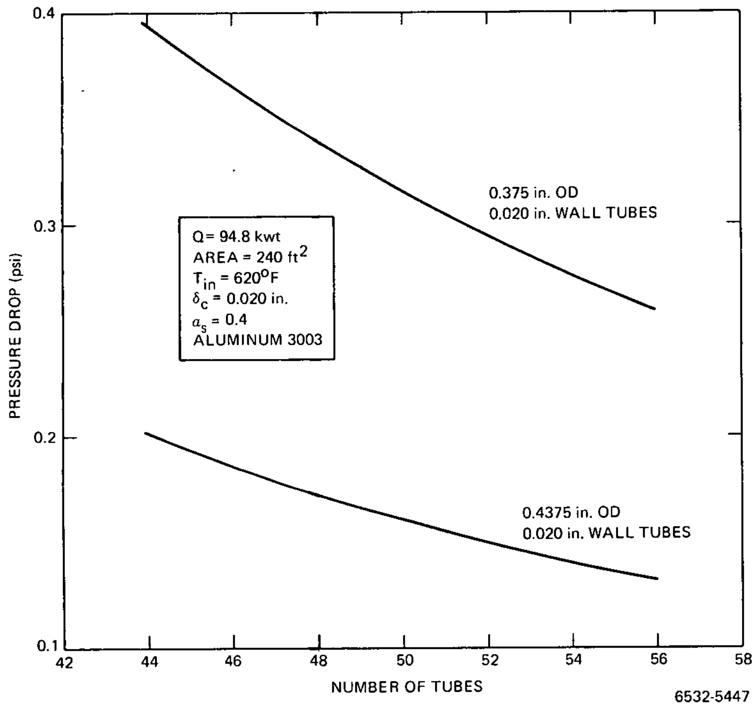

Figure 17. 5-kwe Radiator Characteristics, Pressure Drop vs Number of Tubes

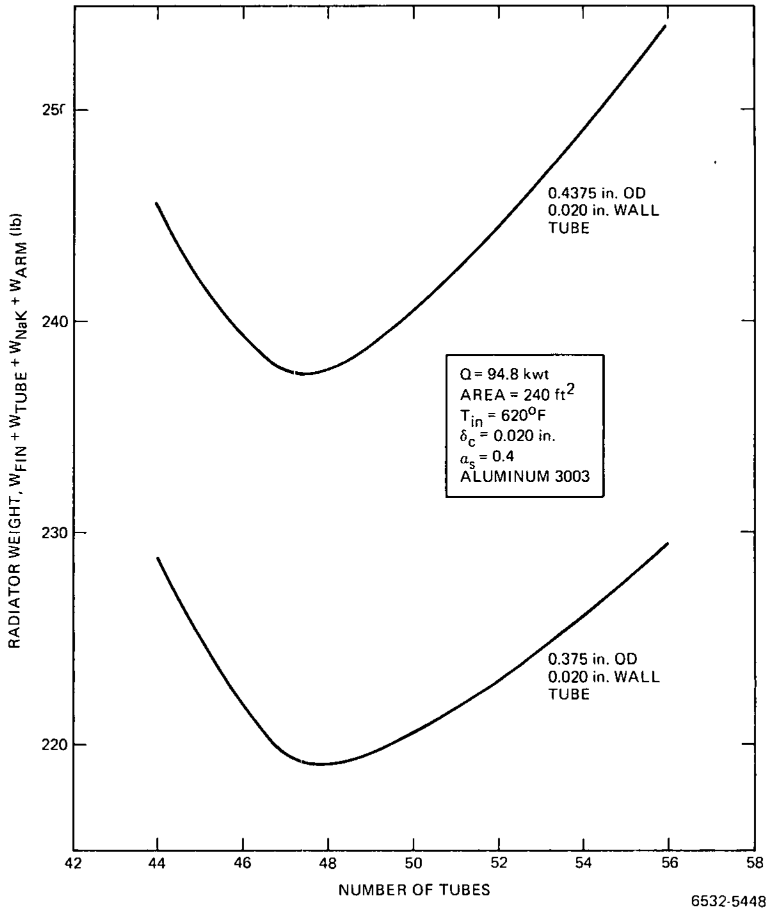

Figure 18. 5-kwe Radiator Characteristics, Radiator Weight vs Number of Tubes and Tube Size

is saved initially by the decrease in fin root thickness than is added by increasing the number of coolant tubes. At approximately 48 to 50 tubes, the decreased fin root thickness weight savings does not compensate for the additional coolant tube weight, and radiator system weight tends to increase.

From the results of this analysis, it was decided that the larger coolant tube should be used in the system design. The decreased pressure drop through the radiator with the larger tubes warrants the increased radiator weight. The larger coolant tubes will also minimize the chance of system plugging by NaK coolant at lower radiator temperatures.

Figure 19 shows the results of a series of calculations that were made to determine the radiator weight as a function of coolant tube number. These calculations were made using the three types of aluminum that were considered for the radiator fin material; Al-1100, Al-3003, and Al-2219.

The coolant tube size used in this analysis for all three types of aluminum was 0.4375-in. OD with a 0.020-in. wall thickness. As determined in Section V-C-2, a meteoroid armor plus fin root thickness of 0.125 in. was used in all cases considered. This thickness will provide a noncritical meteoroid damage probability of 0.99 for a 5-year mission life for the stainless-steel-lined radiator fin configuration.

As described earlier, the weight curves in Figure 19 exhibit a characteristic U shape. Each of the three types of aluminum has a different thermal conductivity at the 600°F operating temperature. Al-1100 has the highest thermal conductivity and Al-2219 has the lowest. As the thermal conductivity decreases, the point of minimum weight shifts toward increased number of coolant tubes.

Using Al-3003 as the reference fin material, the radiator weight reaches a minimum value at approximately 48 coolant tubes. A lower pressure drop can be obtained by increasing the number of coolant tubes to 50, with a slight increase in radiator weight. The reference number of coolant tubes was therefore set at 50.

Figure 20 shows the corresponding radiator fin root thicknesses for each type of aluminum as a function of number of coolant tubes. Using the reference

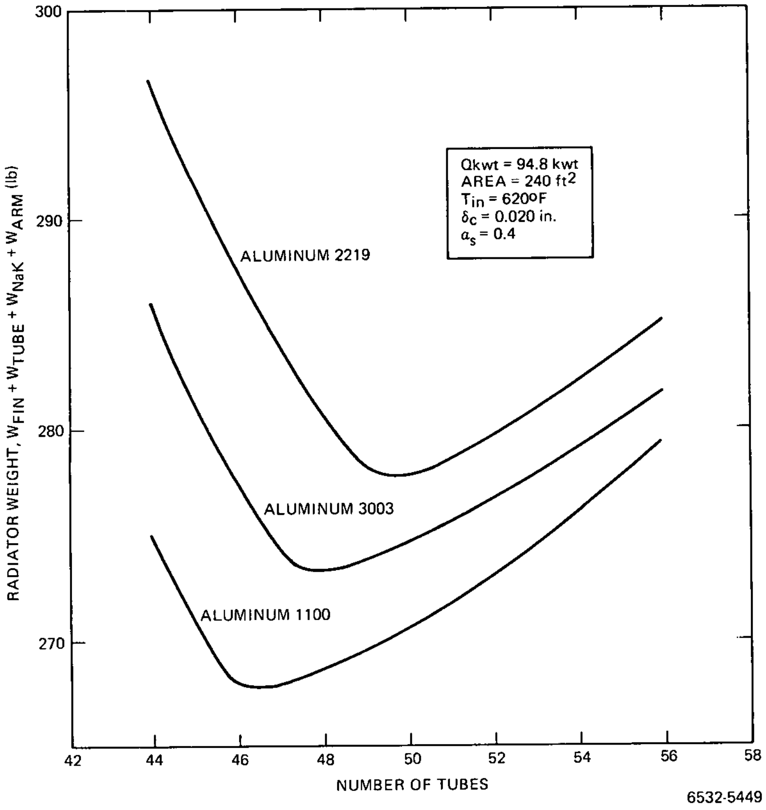

Figure 19. 5-kwe Radiator Characteristics, Radiator Weight vs Number of Tubes and Radiator Material

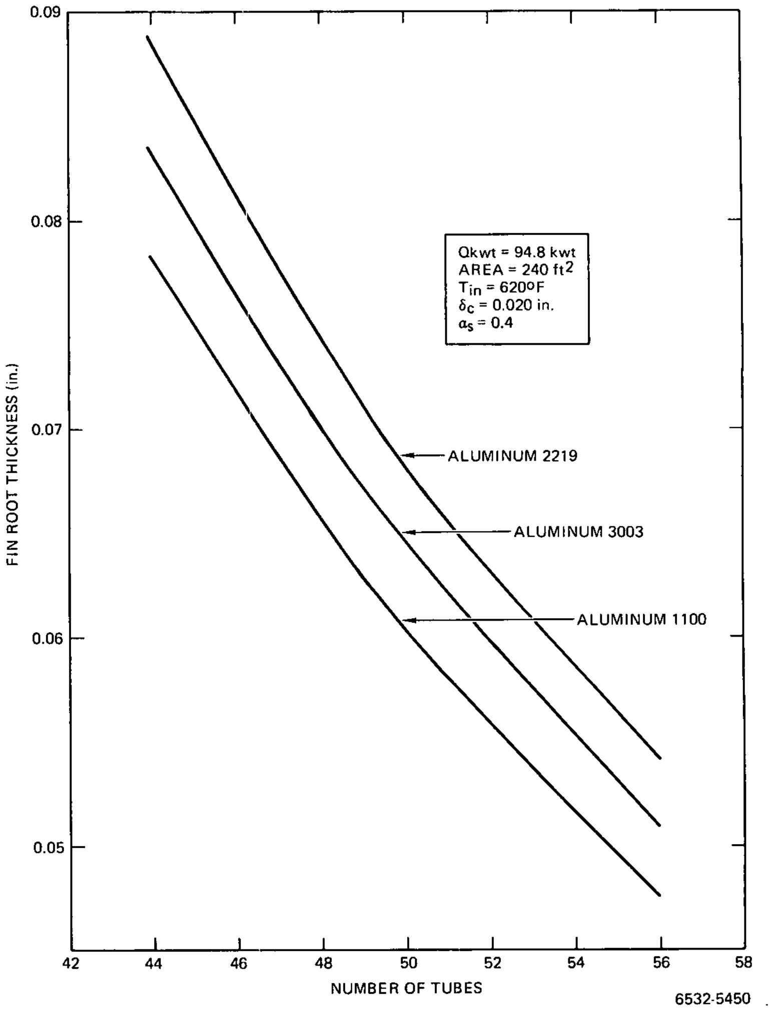

Figure 20. 5-kwe Radiator Characteristics, Fin Root Thickness vs Number of Tubes

material and 50 coolant tubes, the required fin root thickness is 0.0646 in. The shaved armor thickness required is then 0.0604 in. Figure 15 shows the dimensions of the asymmetric tapered aluminum fin-tube cross section required to meet the performance requirements given in Section V-C-1.

The optimization study of the symmetric aluminum fin-tube cross section considered both tapered and constant fin geometries. The performance requirements corresponding to a rejected power of 92.9 kwt given in Section V-C-1 were used as the design parameters for all analyses performed on the symmetric aluminum radiator configurations. Al-3003 was used as the fin material for both symmetric fin-tube radiator cross sections.

Two coolant tube outside diameters were considered in these studies; 0.4375 and 0.500 in. The coolant tube wall thickness was varied from 0.020 to 0.055 in. for the 0.4375-in. OD coolant tubes and from 0.040 to 0.055 in. for the 0.500-in. OD coolant tubes.

Figures 7, 21, and 22 present the results of the calculations using a 0.4375-in.-OD coolant tube. Figure 21 shows the total radiator system weight as a function of the number of coolant tubes for various values of coolant tube wall thickness. These curves all show a minimum weight in the region of 34 to 40 coolant tubes.

Figure 22 illustrates the coolant pressure drop through the radiator for the cases considered in Figure 21. The maximum allowable pressure drop through the radiator is felt to be approximately 0.40 psi. From Figure 22, it can be concluded that a larger coolant tube OD will be required if a wall thickness greater than 0.035 in. is required from a stress standpoint.

On the basis of the results shown in Figures 21 and 22, 36 coolant tubes were chosen as the optimum value for radiator cross sections with a 0.4375-in. OD and wall thickness of 0.035 in. or less.

Figure 7 shows the typical symmetrical fin-tube cross section dimensions using 36 coolant tubes with an OD of 0.4375 in. The fin spacings, fin root thickness, and armor thickness shown in Figure 7 should be used for all wall thicknesses less than or equal to 0.035 in. The required wall thickness will be determined from the stress analysis.

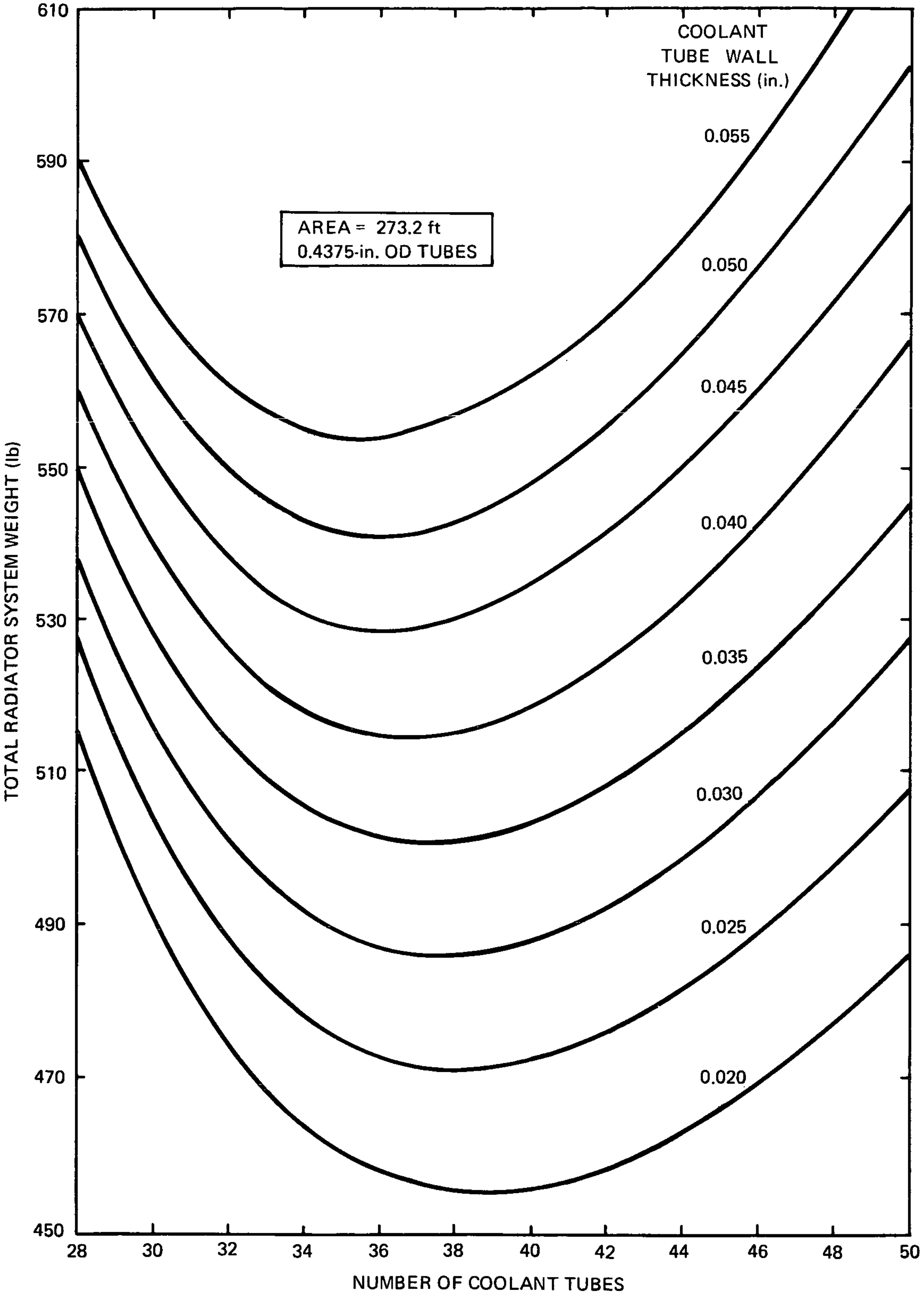

Figure 21. Symmetric Aluminum Fin and Stainless-Steel Tube, System Weight vs Number of Coolant Tubes, 0.4375-in. OD Tubes

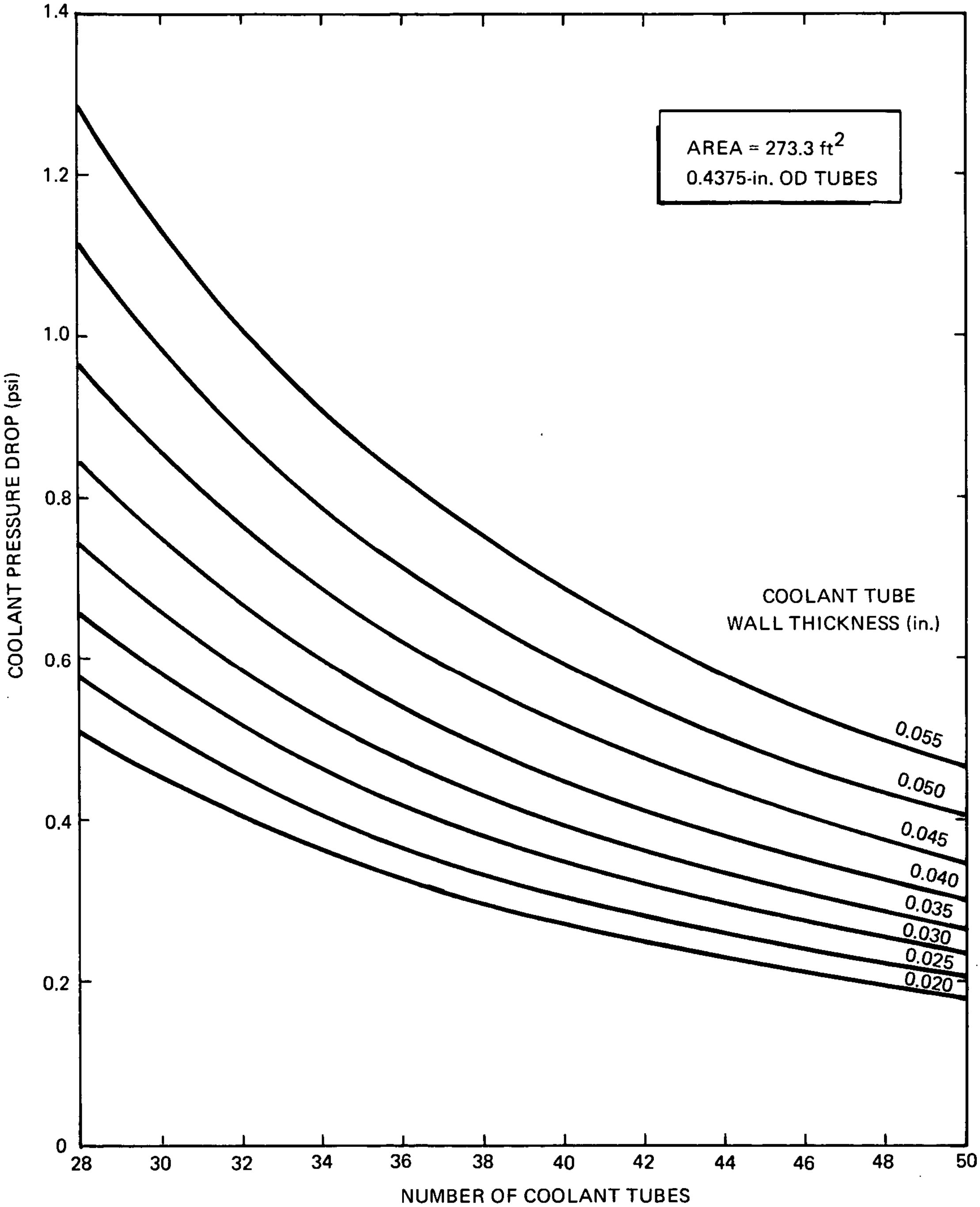

Figure 22. Symmetric Aluminum Fin and Stainless-Steel Tube, Coolant Pressure Drop vs Number of Coolant Tubes, 0.4375-in. OD Tubes

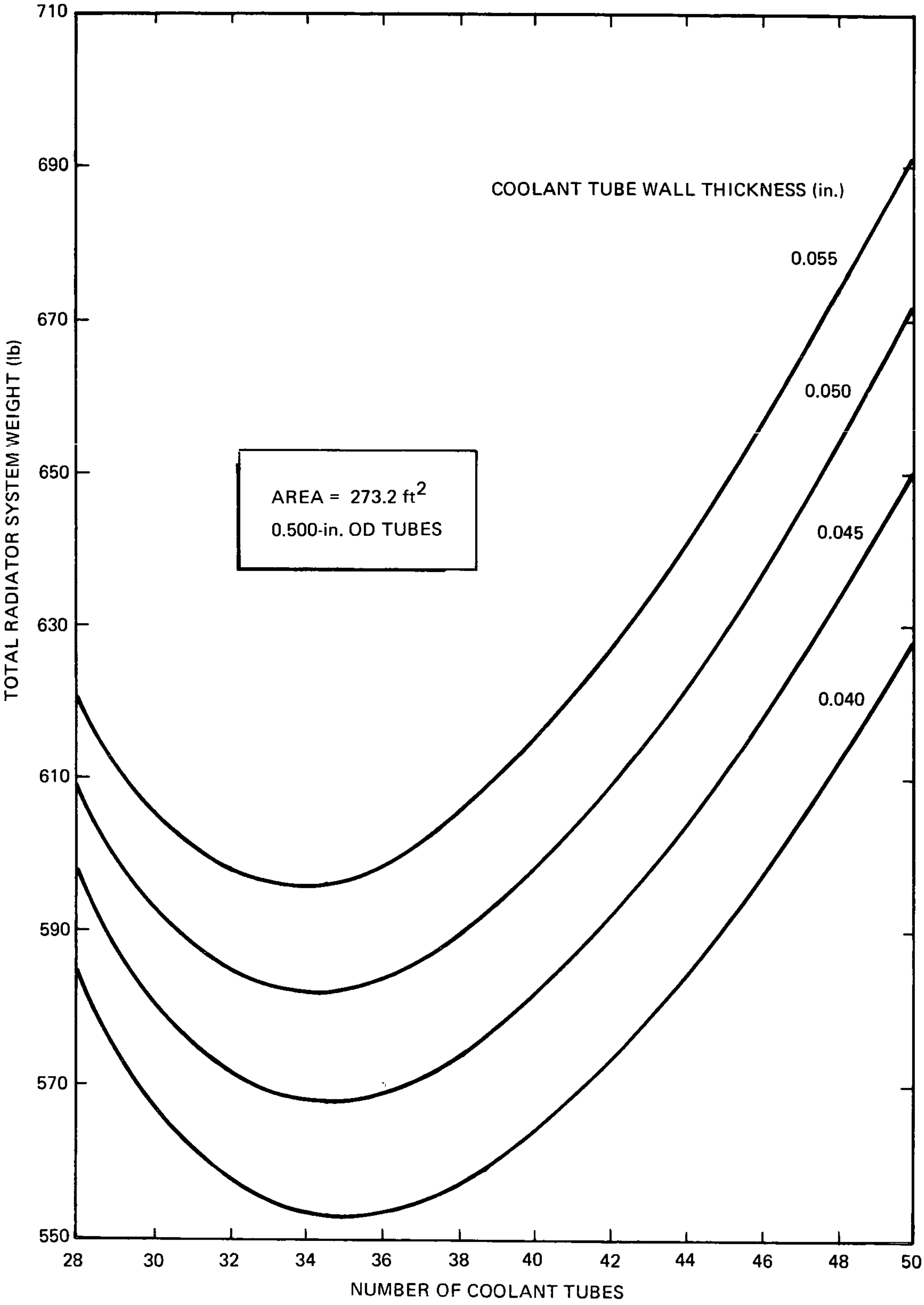

6532-5453

Figure 23. Symmetric Aluminum Fin and Stainless-Steel Tube, System Weight vs Number of Coolant Tubes, 0.500-in. OD Tubes

Figures 23 and 24 present the results of the calculations using a 0.500-in.-OD coolant tube. As in the cases using the 0.4375-in. -OD coolant tube, Figure 23 shows that a minimum weight system may be designed using 36 coolant tubes. Figure 24 shows that the coolant pressure drop using a 0.500-in. OD coolant tube will be lower than 0.400 psi for all wall thicknesses considered.

An additional design study was made to determine the characteristics of the symmetric aluminum fin-tube cross section with a constant fin thickness. The same performance requirements were used in this analysis as was used for the tapered symmetric radiator. The coolant tubes had an outside diameter of 0.4375 in. and a 0.020-in. wall thickness.

Figures 25 and 26 present the results of the calculations for the Al-3003 symmetric constant fin radiator fin-tube cross section. Figure 25 illustrates the Al-3003 constant fin radiator system weight and rejected power as functions of constant fin thickness. Thirty-six coolant tubes were used in the constant fin cross section calculations. Figure 25 shows that a constant fin thickness of 0.068 in. is required to reject 92.9 kwt net power. This radiator configuration weighs approximately 534 lb.

Figure 26 shows the typical symmetric Al-3003 fin-tube cross section dimensions using 36 coolant tubes with an OD of 0.4375 in. and a wall thickness of 0.020 in.

D. ALUMINUM FIN RADIATOR REFERENCE DESIGN

Figure 2 represents the system for the aluminum and stainless-steel radiator structure but with a slight difference in the axial dimensions. The radiator structure extended from Stations 5.5 to 219.9 with the cone-cylinder transition at Station 78.4. It was composed of 48 fin-tube panels joined at the thin, cold edge to form the radiator shell. Although this joint had not been established, it would be a riveted joint. At approximately 18-in. axial spacing, internal "Z" shaped frames (rings) were riveted to form the circular cross section. The rings were to be 0.020-in. -thick 2219-T0 aluminum as shown in Figure 27. The splice at the cone and cylinder interface was also to be of 2219-T0 and is shown in detail on Figure 28. The removable access panels, the pump support brackets, and the spacecraft interface are also shown on Figure 27.

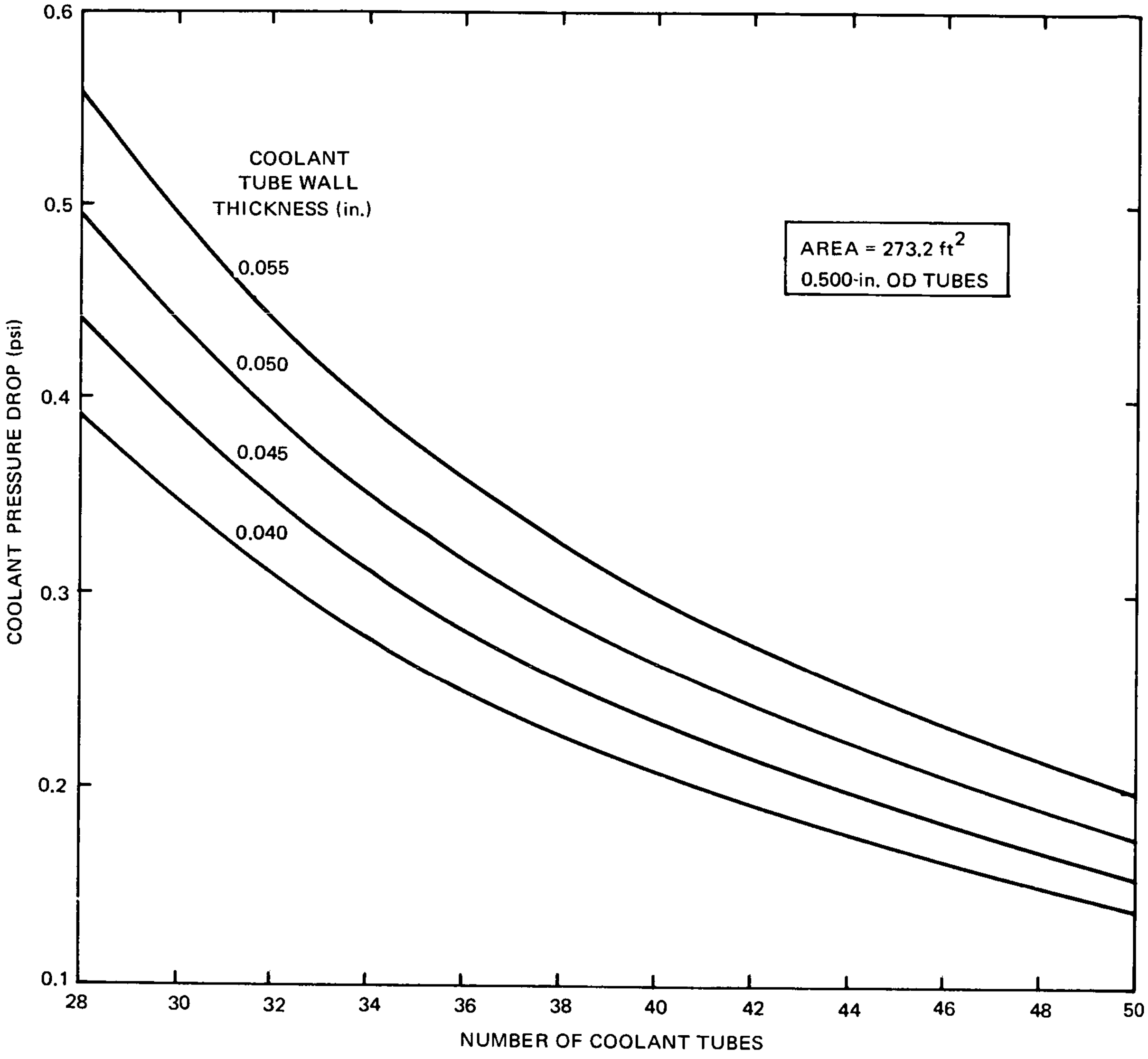

Figure 24. Symmetric Aluminum Fin and Stainless-Steel Tube, Coolant Pressure Drop vs Number of Coolant Tubes, 0.500-in. OD Tubes

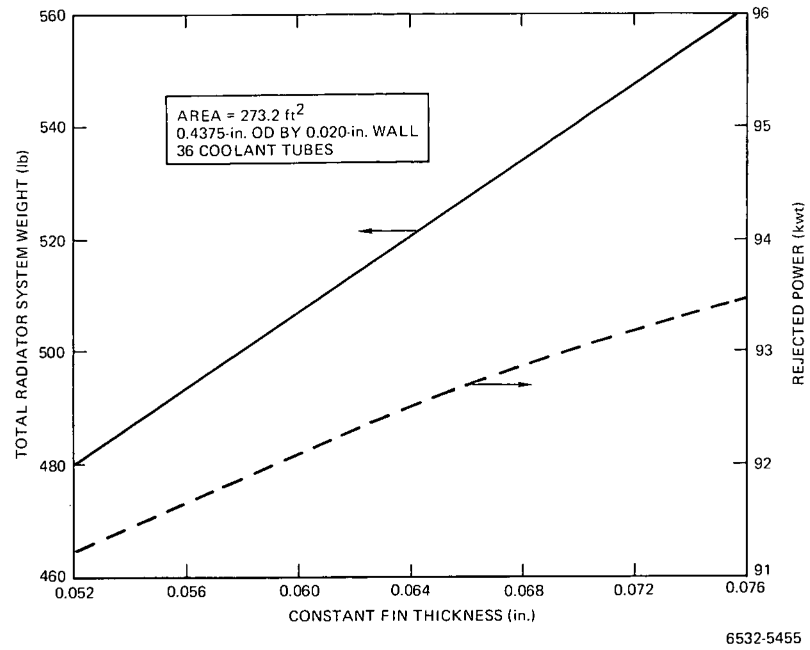

Figure 25. Symmetric Constant Thickness Aluminum Fin, Radiator Weight and Rejected Power vs Constant Fin Thickness

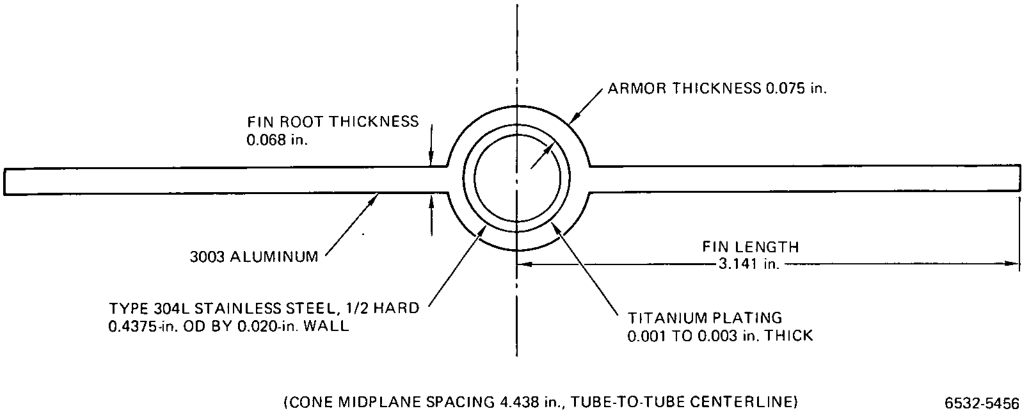

Figure 26. Symmetric Constant Thickness Aluminum Fin and Stainless-Steel Tube Radiator Cross Section, 36 Coolant Tubes

Page intentionally left blank

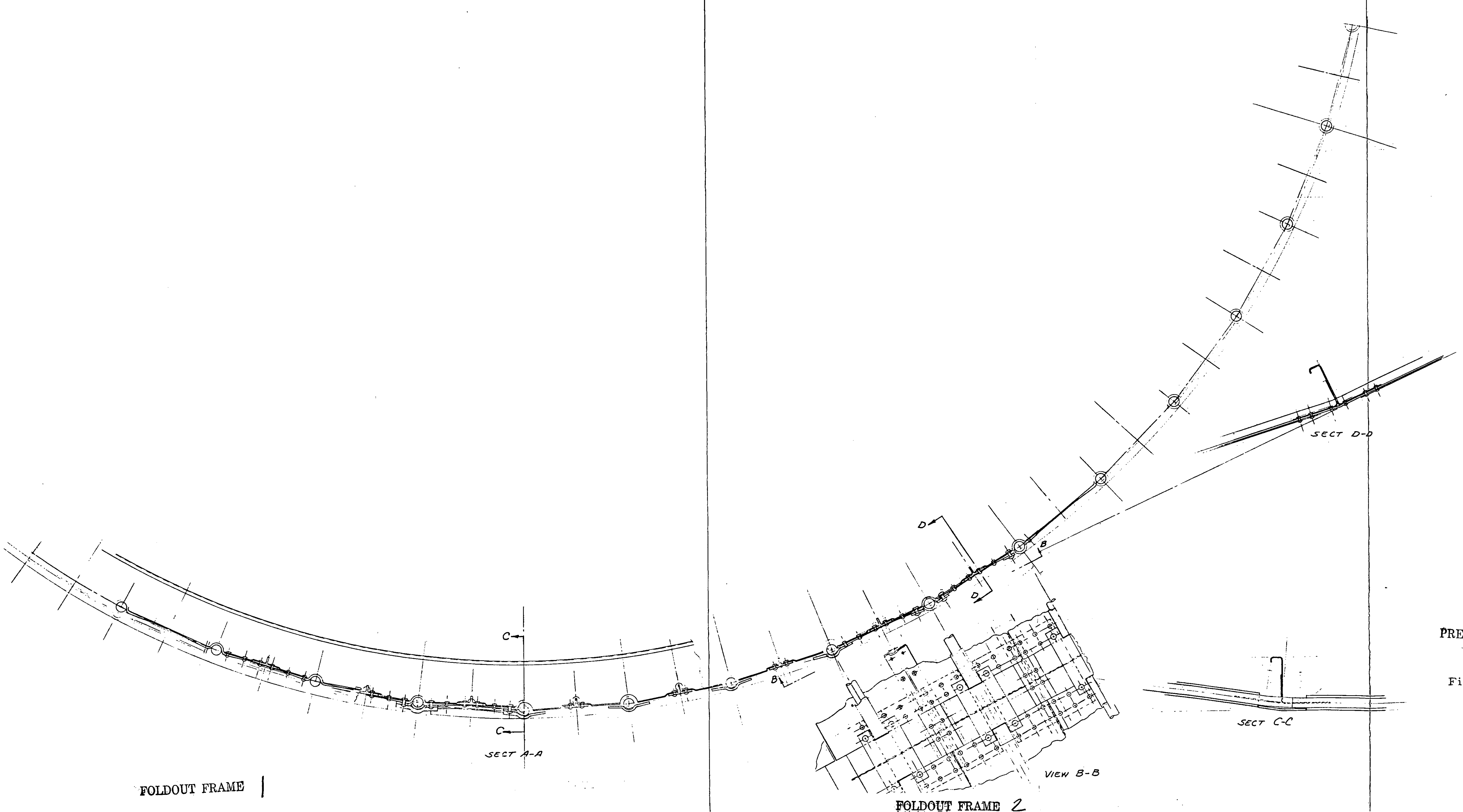

FOLDOUT FRAME 1

FOLDOUT FRAME 2

PRECEDING PAGE BLANK NOT FILMED

Figure 28. Radiator Assembly Layout, Cone and Cylinder Interface

FOLDOUT FRAME 3

E. RADIATOR THERMAL CHARACTERISTICS

The symmetric tapered aluminum fin-tube cross section shown in Figure 16 was selected as the reference aluminum radiator configuration.

A 600-n. mi constant sun shade polar orbit was used to determine the radiator thermal performance in space. This orbital attitude was considered to provide the maximum environmental thermal flux to the radiator surface as follows:

Direct solar = 146 Btu/ft^2-hr
Direct earth = 13.8 Btu/ft^2-hr
Earth reflected = 9.5 Btu/ft^2-hr

In this analysis, the radiator surface was assumed to be revolving around its axis at 3 revolutions per minute.

The performance requirements corresponding to a rejected power of 92.9 kwt given in Section V-C-1 were used as the design parameters in this series of calculations. The power rejection capability of the reference aluminum radiator was calculated as a function of solar absorptivity for emissivity values of 0.8, 0.85, 0.9, and 0.95. The results of these calculations are shown in Figure 29.

In Section III-F, the radiator coating solar absorptivity was shown to increase by approximately 30%. It was also shown that the coating thermal emissivity will increase to approximately 0.91 during the 5-year mission lifetime. From Figure 29 it can be seen that with the reference emissivity and solar absorptivity values of 0.90 and 0.50, respectively, the radiator will reject 92.9 kwt. With a solar absorptivity of 0.65 and an emissivity of 0.91, the radiator will reject approximately 90.5 kwt. Figure 5 shows the initial $\alpha_s = 0.3$ and the initial $\epsilon = 0.9$. The values of $\alpha_s = 0.5$ and $\epsilon = 0.9$ were used as the initial values in this analysis to be conservative.

The results of these calculations show that the thermal performance of the reference aluminum radiator will not degrade significantly due to surface coating changes.

In addition, the environmental heat inputs used in this series of calculations are considered to represent maximum values. Other orbital attitudes will provide

PRECEDING PAGE BLANK NOT FILMED

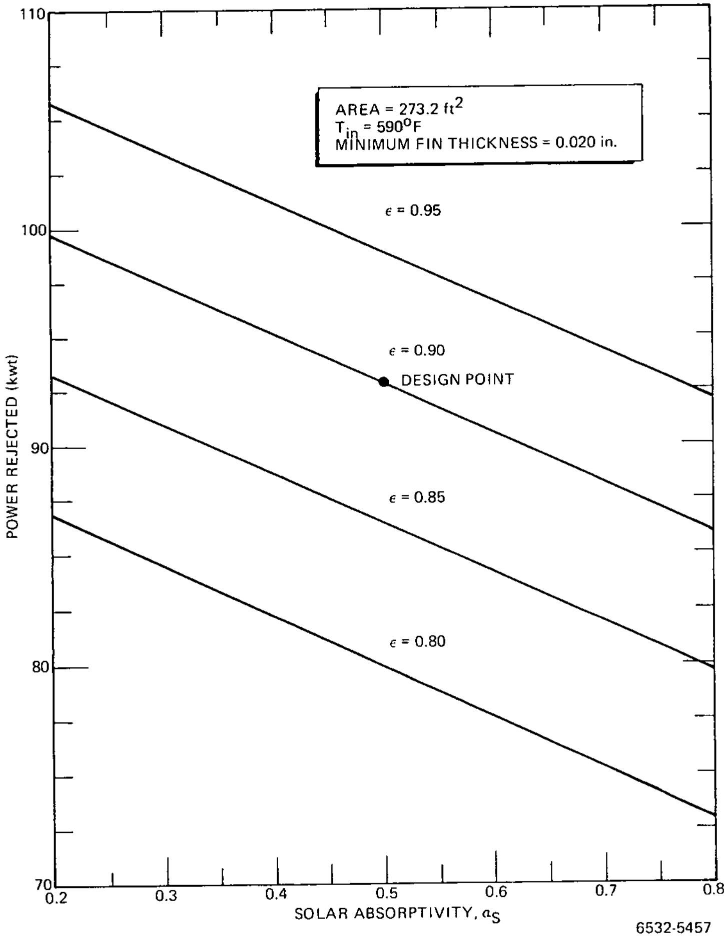

Figure 29. 5-kwe Radiator Operating Characteristics in Space for Maximum Orbital Environmental Heat Input

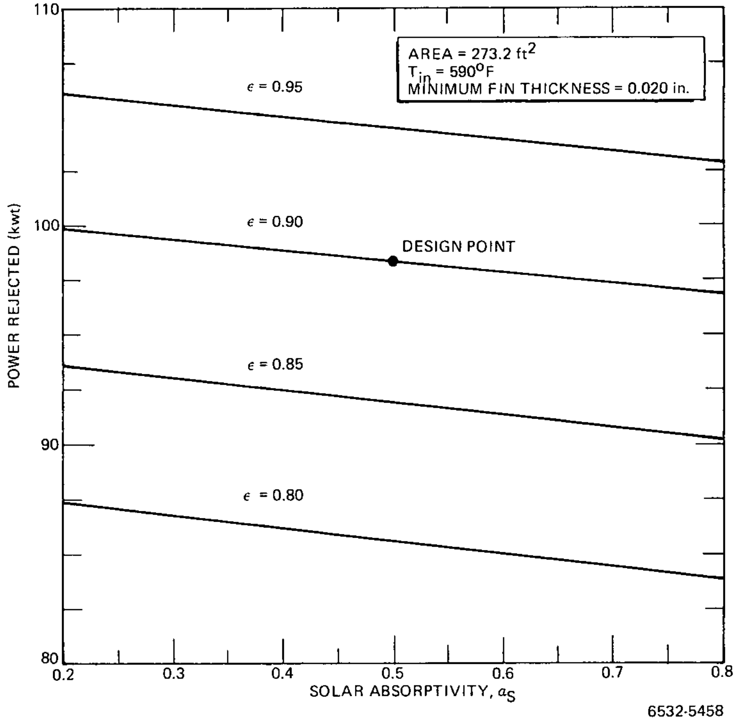

Figure 30. 5-kwe Radiator Operating Characteristics in Space for Minimum Orbital Environmental Heat Input

a less severe thermal input and thereby provide improved radiator thermal performance.

To determine the radiator performance during less severe attitudes, a series of calculations was made using the minimum environmental thermal flux to the radiator surface as follows:

Direct solar = 68.5 Btu/ft^2-hr
Direct earth = 13.8 Btu/ft^2-hr
Earth reflected = 9.5 Btu/ft^2-hr

The radiator surface was assumed to be revolving around its axis at 3 revolutions per minute.

The results of this series of calculations are shown in Figure 30. Using the same input values as were used for the maximum orbit, the radiator will reject 98.3 kwt; with $\epsilon = 0.91$ and $\alpha_s = 0.65$, the radiator will reject approximately 99 kwt. As in the maximum orbit cases, the thermal performance of the radiator will not degrade significantly due to surface coating changes.

F. STRUCTURAL ANALYSIS

Requirements for armor protection and thermal performance were such that the aluminum and stainless-steel radiator had a high margin of safety for mechanical loads. There is a significant difference in the coefficients of thermal expansion of the aluminum fin and the stainless-steel tubes. When subjected to thermal cycling, large differential strains are induced in the assembly. Much of the following analysis deals with the thermal stresses or strains due to the thermal gradients.

It should be noted that most of the evaluation of the aluminum and stainless-steel radiator was done while Type 316 stainless steel was considered as the tube material. Just prior to the change from aluminum to Lockalloy for fins, there was a change from Type 316 to Type 304 stainless steel for the tubes. The difference in the expansion coefficient between Types 304 and 316 stainless steel is small when compared to aluminum since they are similar to each other but much different from aluminum. When compared to Lockalloy whose expansion is similar to that of stainless steel, the relative difference between the two

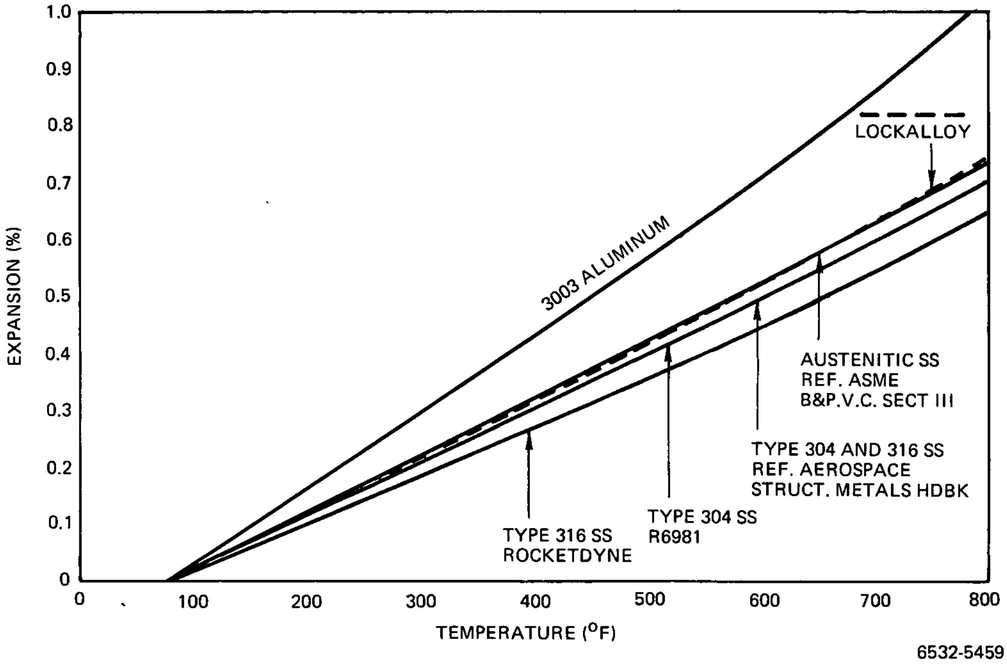

Figure 31. Thermal Expansion of Radiator Materials Expressed as Expansion from Room Temperature vs Temperature

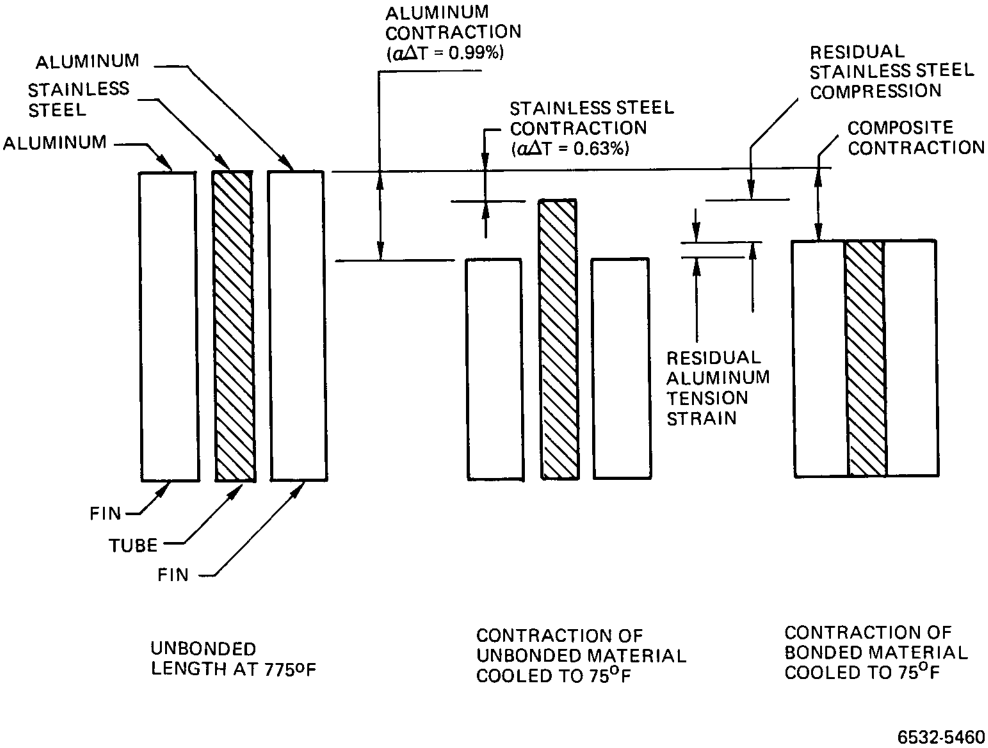

Figure 32. Aluminum Fin and Stainless-Steel Tube Thermal Strain Schematic

stainless steels is more significant. To facilitate this report, the analysis for aluminum and stainless steel will refer to Type 316 stainless steel as the tube material. A slight reduction in strains and stresses would have been shown with the Type 304 stainless steel properties, but not sufficient to warrant reanalysis on an abandoned configuration.

1. Braze Cycle

The basic fabrication of the aluminum-fin and stainless-steel-tube panel assembly is by a braze process. Although the process had not been fully developed, it was recognized that temperatures near 1100°F would be encountered. At the instant of the braze solidification, the tube and fin would be essentially stress free. The contraction of the aluminum is greater than that of the steel while cooling to room temperature. Figure 31 shows the thermal expansion coefficients for the 3003-T0 aluminum.

There is a tendency for forces to be generated between the two materials by the relative growth or contraction rates. It is assumed that since 3003-T0 has the characteristic of annealing at 775° without a time requirement, no forces will be generated above 775°F. Rapid cooling to room temperature was assumed as a worst case possibility. Figure 32 shows the relative interference strains associated with the cooling from 775°F to room temperature. If the fin were unbonded and free to contract its full amount, it would shorten by 0.99%. Similarly, the tube would contract by 0.63% (Figure 31). The fin and tube are bonded, however, and the combination will contract an intermediate amount based on the relative areas, modulus of elasticity, and expansion rates:

$$\epsilon_r = \Delta T \left[\alpha_f - \frac{(\alpha_f - \alpha_t)(A_t E_t)}{(A_t E_t + A_f E_f)} \right]$$

where

ϵ_r = Net contraction of fin-tube composite

α_f = Coefficient of expansion of fin

α_t = Coefficient of expansion of tube

A_f = Cross section area of fin

A_t = Cross section area of tube

C2

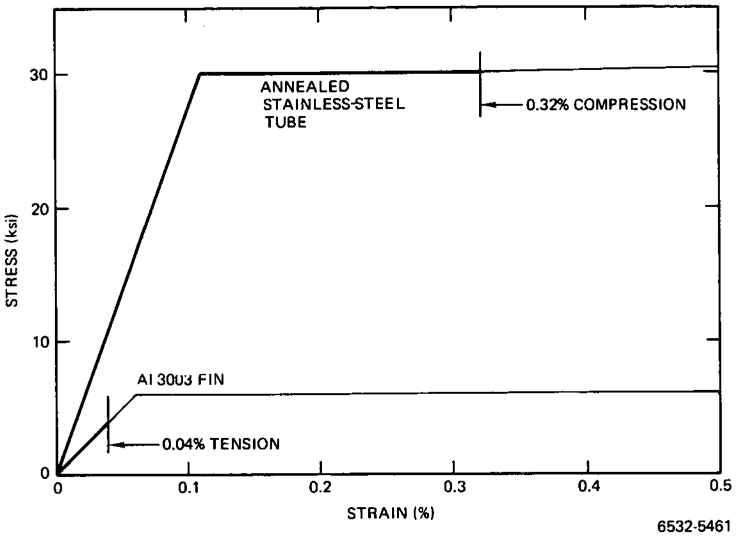

Figure 33. Aluminum Fin and Stainless-Steel Tube Residual Strain, 750°F to Room Temperature

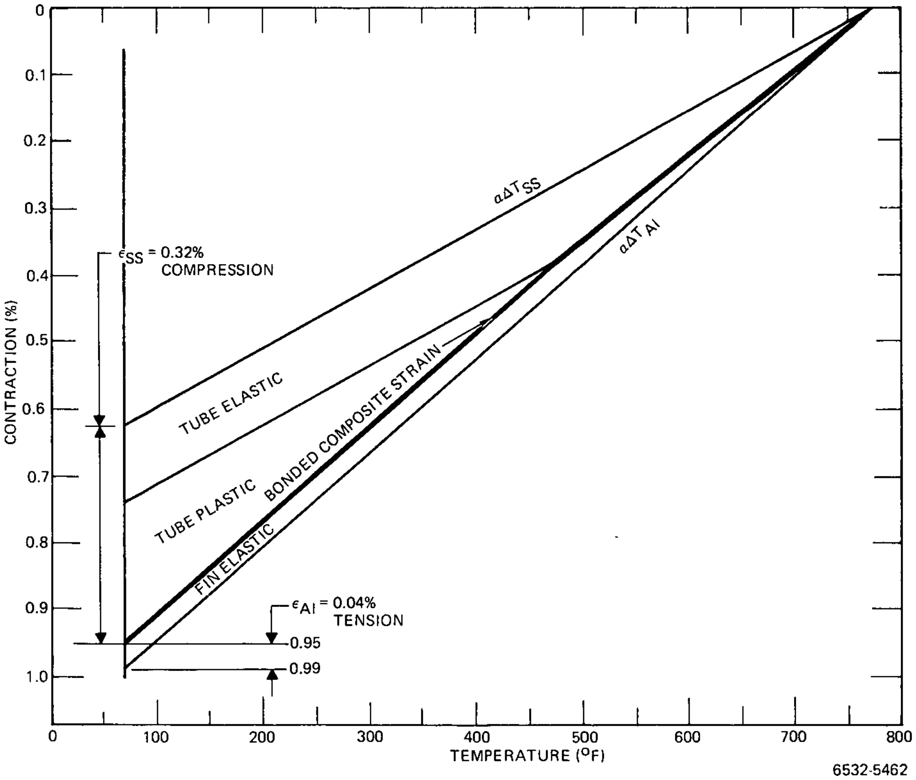

Figure 34. Unsymmetric Aluminum Fin and Stainless-Steel Tube Contraction, 775°F to Room Temperature

E_f = Modulus of elasticity of fin

E_t = Modulus of elasticity of tube

ΔT = Temperature change.

There will be a residual tensile strain in the fin and a residual compression strain in the tube. The total strain is dependent on the differential thermal expansion rates and the temperature change.

$$\epsilon_f + \epsilon_t = \Delta T(\alpha_f - \alpha_t)$$

The relative magnitude of the residual strains are directly dependent on the relative areas as shown in the preceding relationship.

The stress strain relationship of the tube and fin is based on a plane strain analysis. It was shown with a finite element program (APSA) that the stresses in the tube are nearly constant over the cross section. The stress level in the fin tips is lower than that near the tube bond, however, the variation across the section is not great. Further analysis was made with the assumption that stresses were uniform within each material. Two axial relationships were used: (1) the sum of the axial mechanical strains, tension in the aluminum and compression in the steel, equals the differential axial thermal contraction; and (2) the sum of axial forces, tension, and compression, equals zero.

The total axial strain difference from Figure 32 is 0.36% (0.99% in the aluminum, -0.63% in the steel). Then with a force balance, the strain in the steel is 0.32% and that in the aluminum is 0.04%. Figure 33 shows the stress-strain relationship of the aluminum and stainless steel with the strains superimposed. It is evident that the tube is far into the plastic range and not acceptable. Figure 34 shows the sequence of the strain relationship as the panel cools from 775°F to room temperature. The heavy line represents the contraction of the composite. The two outer lines represent the unbanded contraction of the tube and fin. Then, the differential between the outer lines and the composite line represents the mechanical strain in the respective materials.

It was recognized that alternate procedures were necessary. Using the relationship of time at temperature to anneal for the aluminum, there appeared

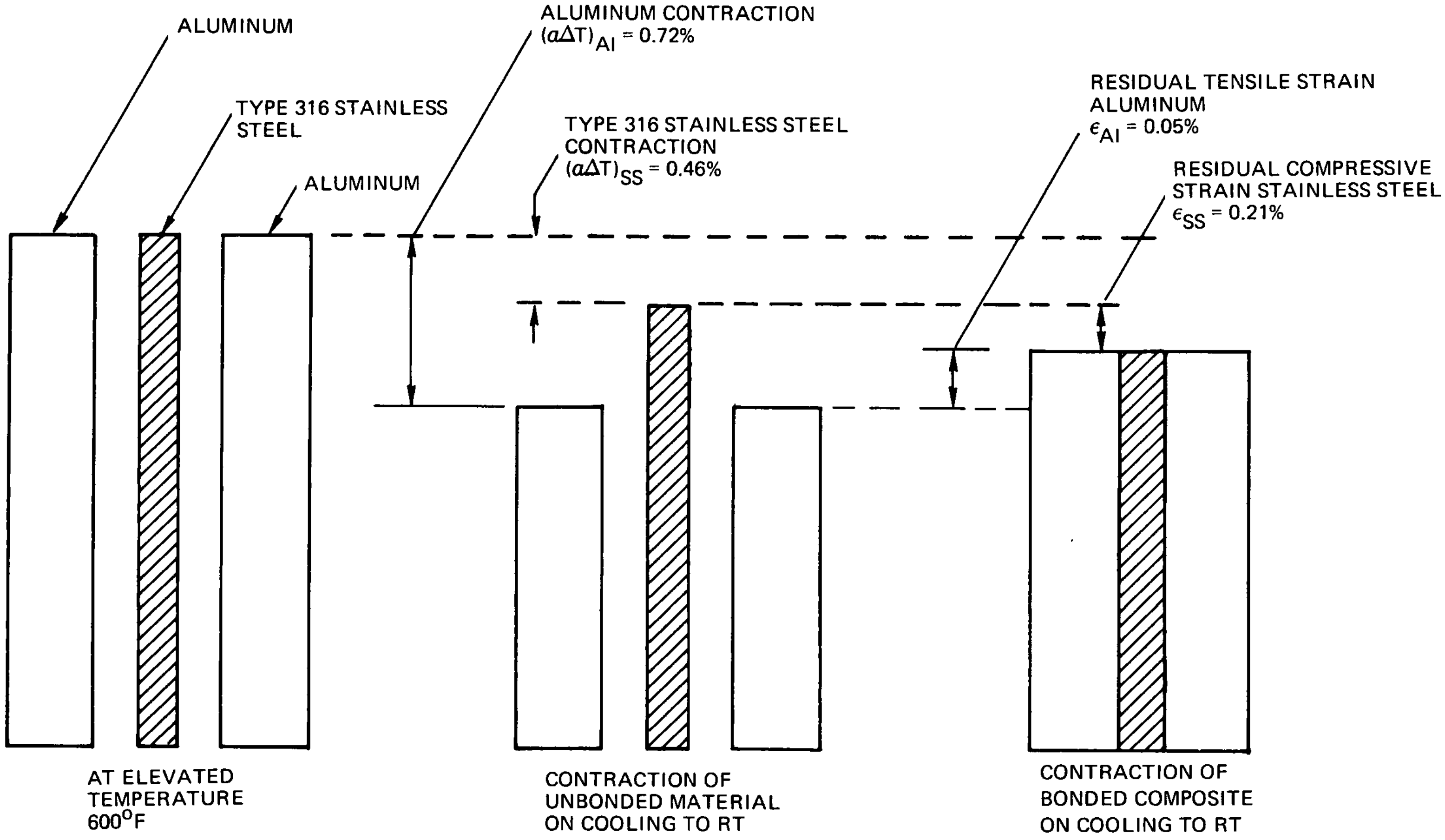

6532-5463

Figure 35. Aluminum Fin and Stainless-Steel Tube Thermal Strain Schematic, 600°F to Room Temperature

to be a potential for the configuration. If soaking at 600°F could be accomplished to provide an essentially stress free panel at 600°F, the strains would be lower at room temperature.

Complete relaxation data were unavailable on the 3003 aluminum but that data on hand indicated that several hours of soaking at 600°F would provide an essentially stress free assembly. It was assumed that this would be an optimum condition, if workable, since subsequent thermal cycles to 600°F during operation would re-anneal. A stress-free temperature below 600°F would serve no purpose other than provide lower strains at the end of the braze cycle since subsequent rises to 600°F would raise the stress-free temperature. For reasons explained in Section V-F-2, the cross section was modified to provide structural symmetry. The area ratio was effected giving a different strain relationship. Figure 16 shows the modified cross section. The results of the study for 600°F stress free to room temperature cycle showed that the residual strains were 0.21 and 0.05% in the tube and fin, respectively, a total of 0.26%. There was 0.10% plastic strain in the tube compared to the 0.21% plastic strain in the tube with the nonsymmetric cross section and cooling from 775°F. Figures 35, 36, and 37 show the relative strain at room temperature, the strains superimposed on the stress strain curves, and the strain history in cooling from 600°F to room temperature. This is a significant improvement; however, the effect of the operational cycles needs consideration prior to the final evaluation of the cross section and the temperature cycle. Further evaluation is presented in Section V-F-6.

2. Aluminum and Stainless-Steel Radiator Panel Bowing

As shown in Section V-F-1, there are stresses induced in the fin-tube during a thermal cycle. Cooling from a stress-free temperature to room temperature will generate tension in the aluminum and compression in the steel. The stresses over the cross section produce forces of equal and opposite magnitude. It can be seen, then, that if the forces are not concentric, there will be a couple whose magnitude depends on the degree of eccentricity of the forces, the relative coefficients of thermal expansion, the material areas, and the change in temperature. If these parameters are constant over the length of the panel, it will bow in a circular arc based on the relationship

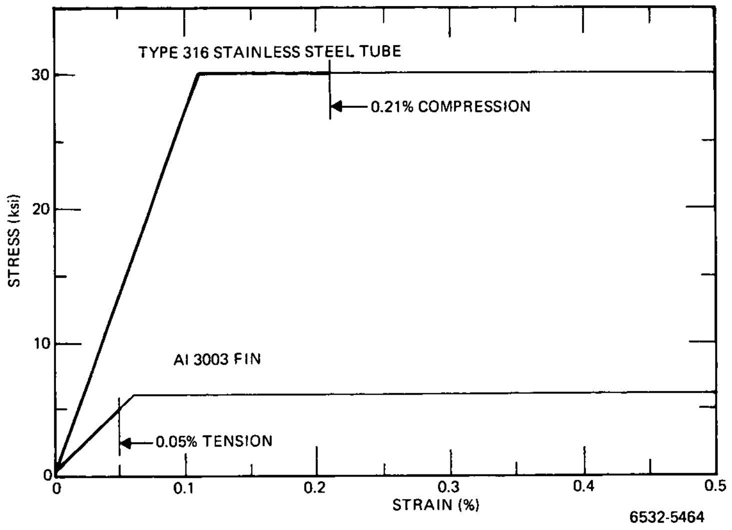

Figure 36. Symmetric Aluminum Fin and Stainless-Steel Tube Elongation and Contraction, 600°F to Room Temperature

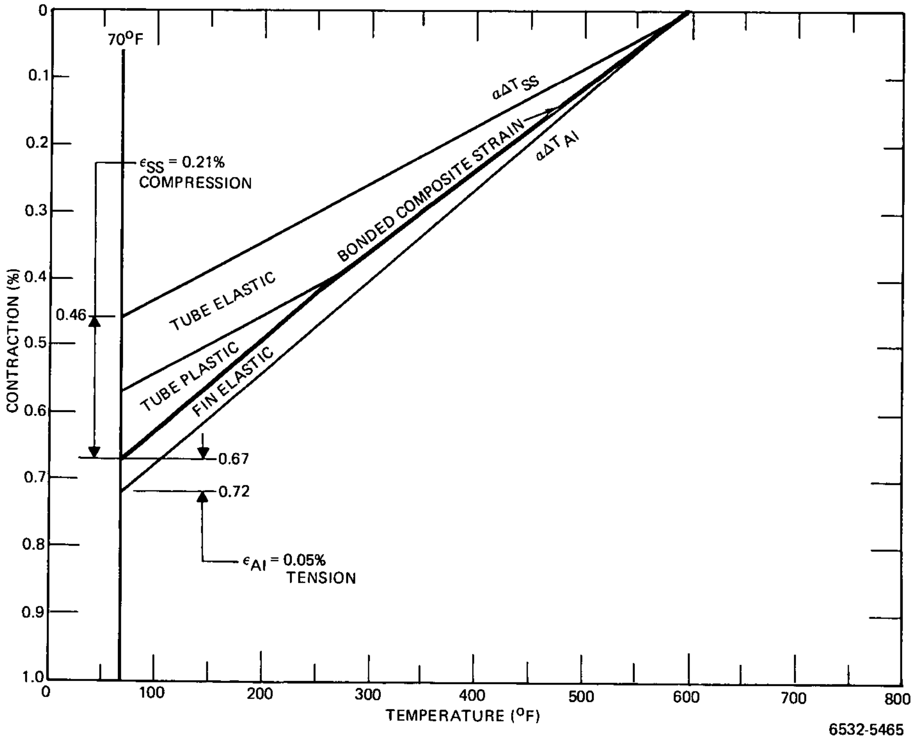

Figure 37. Symmetric Aluminum Fin and Stainless-Steel Tube Contraction, 600°F to Room Temperature

$$\frac{M}{EI} = \frac{1}{R}$$

where

M = Moment in cross section
E = Equivalent modulus of elasticity
I = Moment of inertia
R = Radius of curvature.

The asymmetric configuration (Figure 15) was evaluated and found that it would bow to a 325-in. radius (Figure 38). Three experimental values were measured at 81-, 79-, and 119-in. radii. These values were measured on "similar" cross sections but with various means of clamping and support. Thicknesses and panel widths were not the same as the reference design, however, the effect was clearly indicative of the potential problem.

Incorporating the asymmetric panels into the radiator structure would have introduced potential damaging forces on the panel splices and rings. These forces are those needed to hold the panels straight or flat where the tendency is to bow.

Several alternate designs were proposed to limit the bowing, all of which entailed a means of making the forces concentric and eliminating the moment. One such design is shown in Figure 39 which was applicable to the cylindrical section. It would not be acceptable for the cone, however, due to the variable panel width. Thus, the eccentricity of the fin could not be a constant and the panel would be difficult to fabricate. Although this provided the potential of reducing the bow with minimum weight, the configuration selected was the symmetric cross section of Figure 16. Symmetry was an absolute means of avoiding bow regardless of fin length (Figure 40).

3. Launch Capability

The ability of the radiator to sustain the launch acceleration is based on the strength compared to the panel loads of Table 2 and Figures 8 and 9.

The panel is composed of the tube-armor, the splice, and the fin. The strength of the panel is the sum of the strengths of these three components.

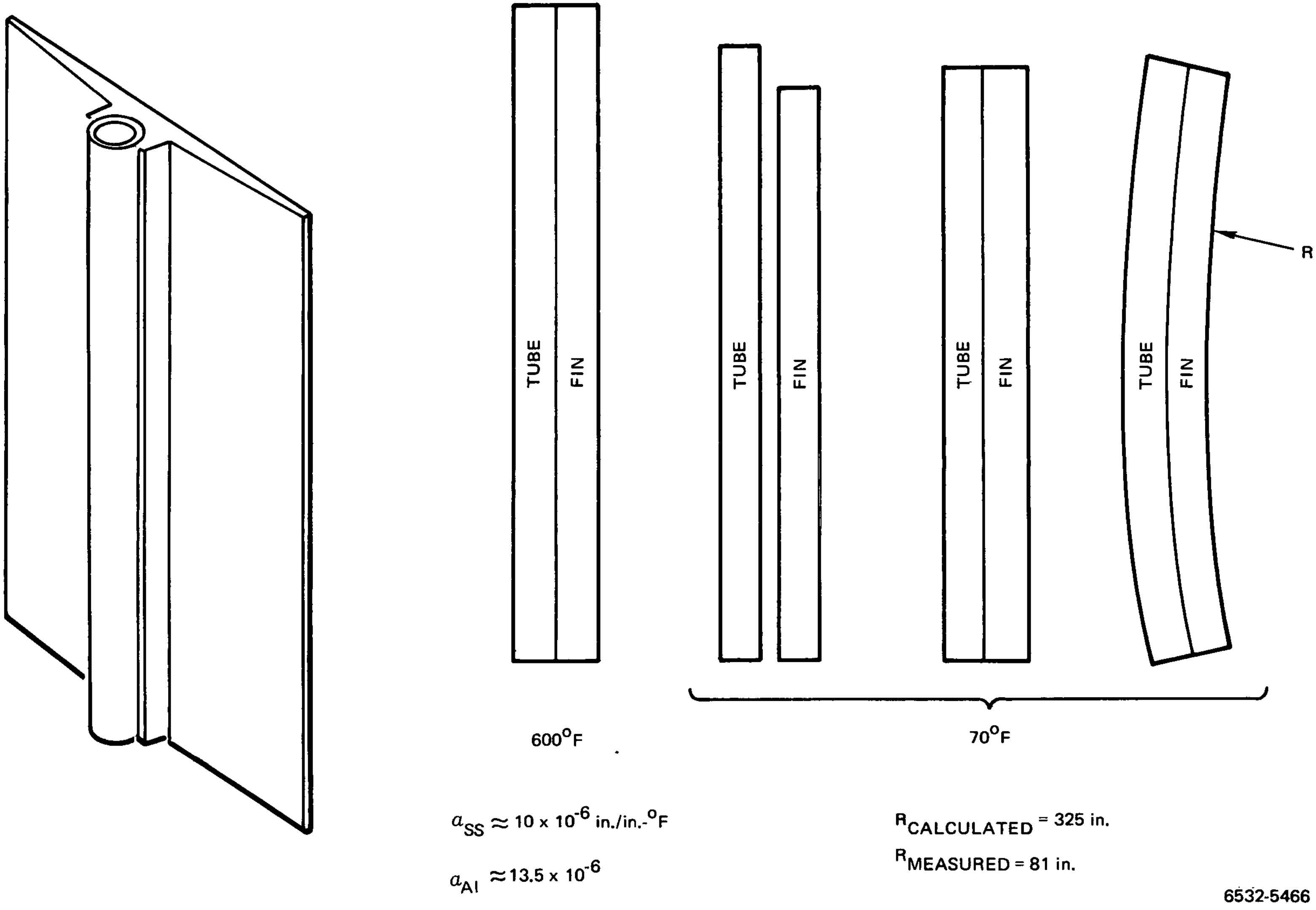

Figure 38. Thermal Bowing, Asymmetric Section

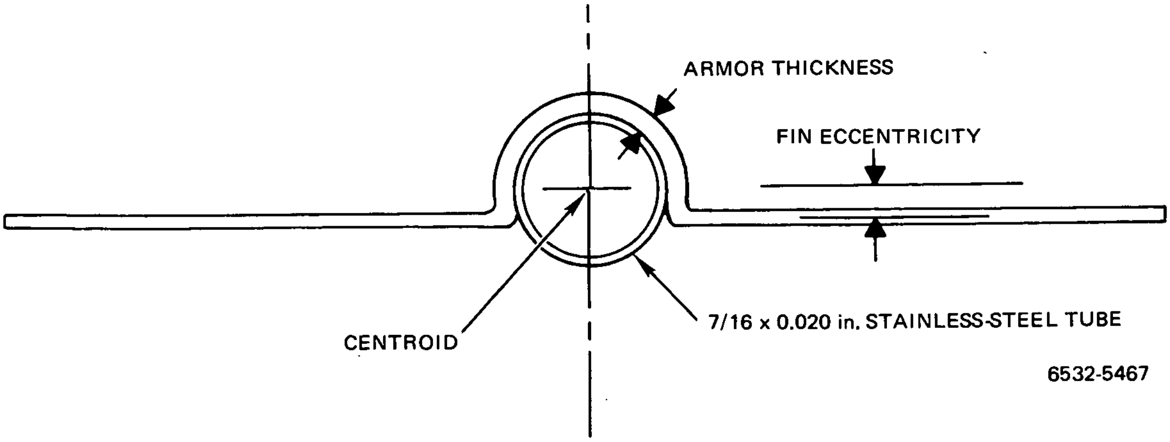

Figure 39. Potential Configuration to Limit Bowing

The column strength is from the relationship:

$$P_{cr_c} = \frac{\pi^2 EI}{L^2}$$

where

E = Effective modulus of elasticity

I = Moment of inertia

L = Column length between rings

P_{cr_c} = Load capacity of column.

This relationship applies to the tube-armor and the splice. The fin strength is from the following:

$$P_{cr_f} = \frac{K_c \pi^2 EA_f}{12(1 - \mu^2)} \left(\frac{t}{b}\right)^2$$

where

K_c = Buckling constant

μ = Poisson's ratio

t = Fin thickness

b = Fin effective width

A_f = Fin effective area

a. Stress Analysis, Asymmetric Configuration

As noted, the asymmetric configuration went through an evolution from Figure 15. A final configuration (Figure 41) is used to demonstrate the launch capacity of aluminum and stainless-steel radiator.

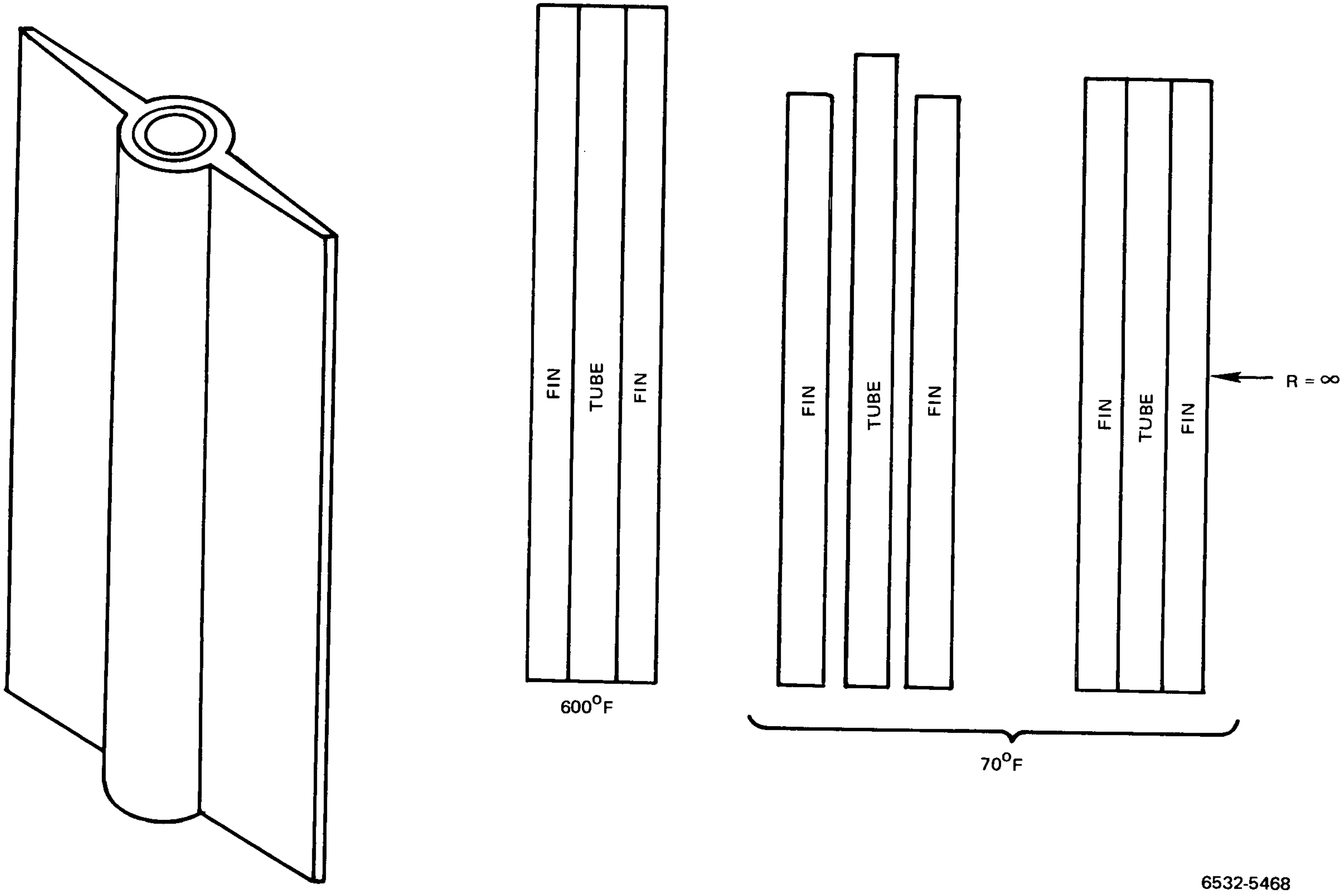

Figure 40. Thermal Bowing, Symmetric Section

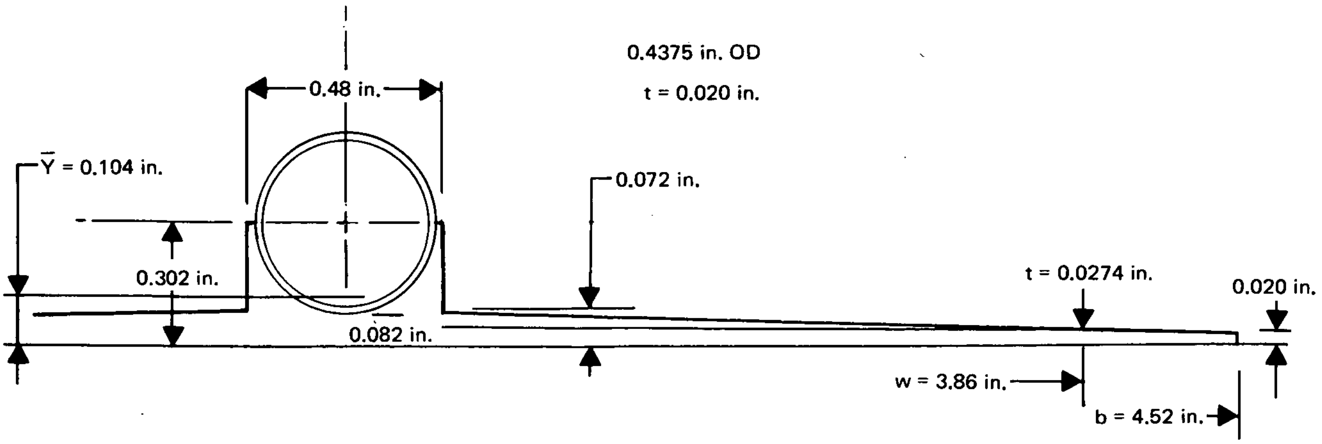

Figure 41. Asymmetric Aluminum and Stainless-Steel Panel

(1) Allowable Unit Load

$$w = \text{Effective width of sheet} = 1.7 \times t_s \sqrt{E/\sigma}$$

For S_1, S_2, S_3, and S_4 (panels on Figure 42),

$L = 18.50$ in.

$b = \pi D/50 = 4.52$ in. (center to center of tube spacing)

Width of panel = b - w = 4.52 - 3.88 = 0.64 in.

The tube strength is expressed as an equivalent area of aluminum.

Equivalent Area of the Tube

$$t_{eq} = \frac{E_{steel}}{E_{Al}} t = 0.059 \text{ in.}$$

$$\text{Area} = \pi Dt = \pi \times 0.4175 \times 0.059 = 0.0775 \text{ in.}^2$$

$$\text{Area of Al 3003 (fin and armor)} = 0.1715 \text{ in.}^2$$

$$\text{Total aluminum area} = 0.249 \text{ in.}^2$$

Centroid

$$\bar{y} = \frac{\Sigma Ay}{\Sigma A} = \frac{0.0340}{0.3265} = 0.104$$

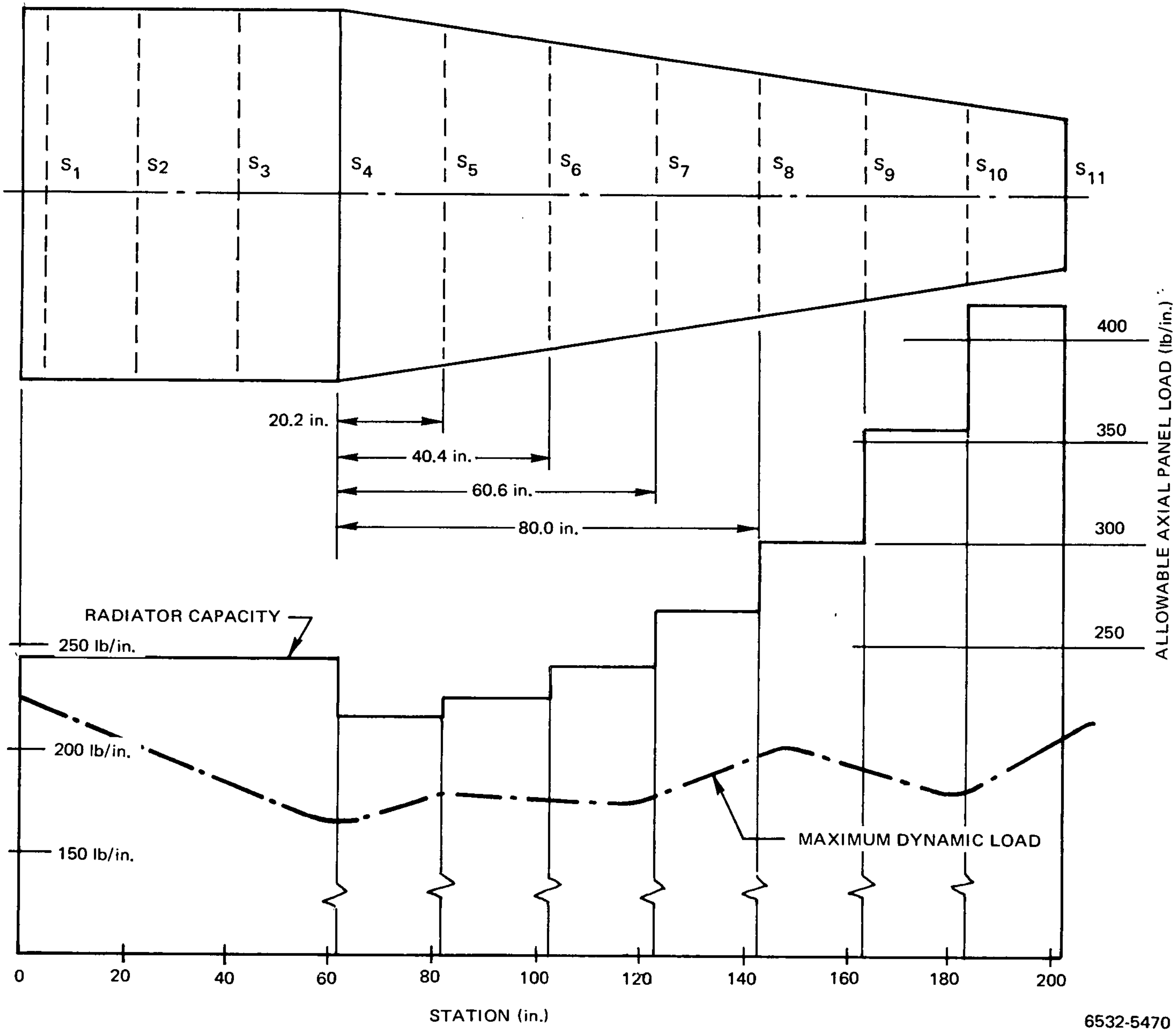

Figure 42. Radiator Load vs Capacity

Moment of Inertia

$$I = \Sigma y^2 \, dA$$

$$\text{Total } I = 0.00677 \text{ in.}^4$$

Radius of Gyration

$$\rho = \sqrt{\frac{I_{xx}}{A}} = \sqrt{\frac{0.00677}{0.3265}} = 0.144$$

Column Strength

$$\sigma_{cr} = \frac{\pi^2 E}{\left(\frac{L}{\rho}\right)^2} = \frac{\pi^2 \times 10 \times 10^6}{\left(\frac{18.5}{0.144}\right)^2} = 6000 \text{ psi}$$

Since the calculated stress exceeds the yield strength, the yield strength is used as σ_{cr}. Then:

$$\text{Critical load} = A \times 5000$$
$$= 0.3265 \times 5000 = 1630 \text{ lb}$$

Fin Strength

$$t = 1/2(0.0275 + 0.020) = 0.0237$$

$$b = 0.64 \text{ (panel width)}$$

$$a = 18.5 \text{ (panel length)}$$

$$\text{Area} = 0.64 \times 0.0237 = 0.152 \text{ in.}^2$$

$$z = b^2/Rt(1 - \mu^2)^{1/2} = 0.46$$

Then

$$K_c = 4$$

$$F_{cr} = \frac{K_c \pi^2 E}{12(1 - \mu^2)} \left(\frac{t}{b}\right)^2 = \frac{4 \times \pi^2 \times 10 \times 10^6}{11} \times \left(\frac{0.0273}{0.64}\right)^2$$

Use σ_y as limit

$$\text{Critical load} = 5{,}000 \times 0.0152 = 76 \text{ lb}$$

Panel Strength

$$\text{Total load} = 1630 + 76 = 1706 \text{ lb}$$

Unit load

$$\frac{F}{b} = \frac{1706}{4.52} = 378 \text{ lb/in.}$$

In a similar manner, the radiator capacity at the various ring spacing and circumferential distances is determined. Figure 42 shows the strength and maximum applied loads. There was a positive margin of safety at all stations.

b. Stress Analyses, Symmetric Configuration

At the stage of radiator evolution that the symmetric cross section was adapted the ring spacing had not been established (Figure 43). The strength is left as a function of ring spacing (column length).

Equivalent Area and Moment of Inertia of Tube

$$A_{eq} = \pi \times 0.4275 \times 0.020 \times \frac{29.2}{10.0} = 0.07826 \text{ in.}^2$$

$$I_{eq} = \pi R^3 t \frac{E_s}{E_{4L}} = \pi \times 0.20825^3 \times 0.02 \times \frac{29.2}{10.0} = 0.001657 \text{ in.}^4$$

Area and Moment of Inertia of Fin and Armor

$$\begin{aligned} A &= \pi(0.084)(0.4375 + 0.084) + 2(0.084 + 0.020)(0.5)(1.96) \\ &= 0.3392 \text{ in.}^2 \end{aligned}$$

$$\begin{aligned} I &= \pi \times (0.21875 + 0.042)^3 \times 0.084 \\ &\quad + 2\{1/12[0.042^3 \times (1.96 + 0.6056) + 0.01^3(0.6056)]\} \\ &= 0.00471 \text{ in.}^4 \end{aligned}$$

Cross Section Area and Moment

$$A_t = 0.4175 \text{ in.}^2$$
$$I_t = 0.006367 \text{ in.}^4$$

Radius of Gyration

$$\rho = \sqrt{I/A} = \sqrt{0.006367/0.4175} = 0.12344 \text{ in.}$$

3

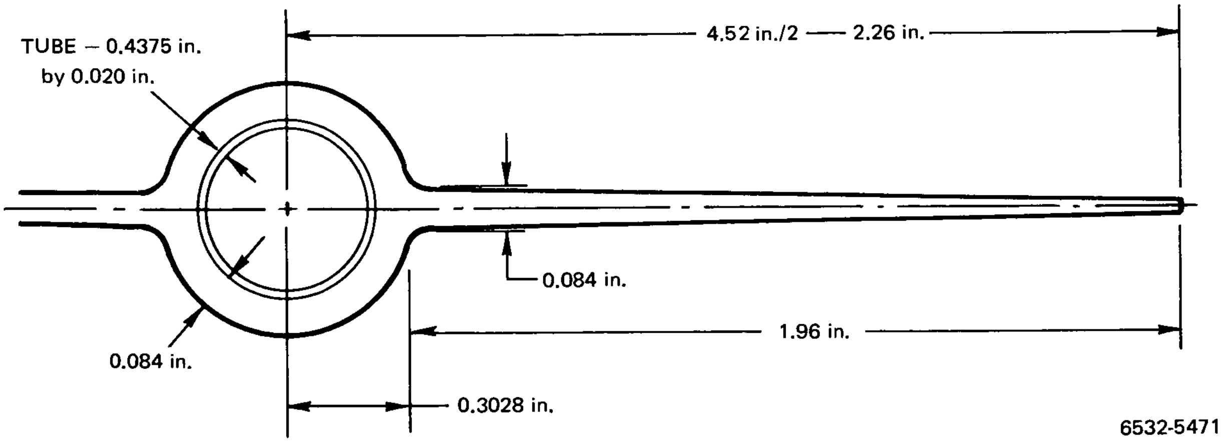

Figure 43. Symmetric Aluminum and Stainless-Steel Panel

Column Strength with Yield Strength Cut-off (Figure 44)

$$\sigma = A \times \pi^2 \epsilon \rho^2 / L^2$$

L (in.)	σ (psi)	P (lb)	P/in. (lb/in.)
5	6000	2506	554
10	6000	2506	554
15	6000	2506	554
20	3778	1578	349
25	2418	1010	223
30	1679	701	155

This shows adequate capacity at all stations for ring spacings up to 24 in.

c. Ring Requirements (Moment of Inertia)

The flexural rigidity requirements for the ring are given by the following relationship from Shanley:(7)

$$EI_{(FRAME)} = \frac{1}{16{,}000} \frac{MD^2}{L}$$

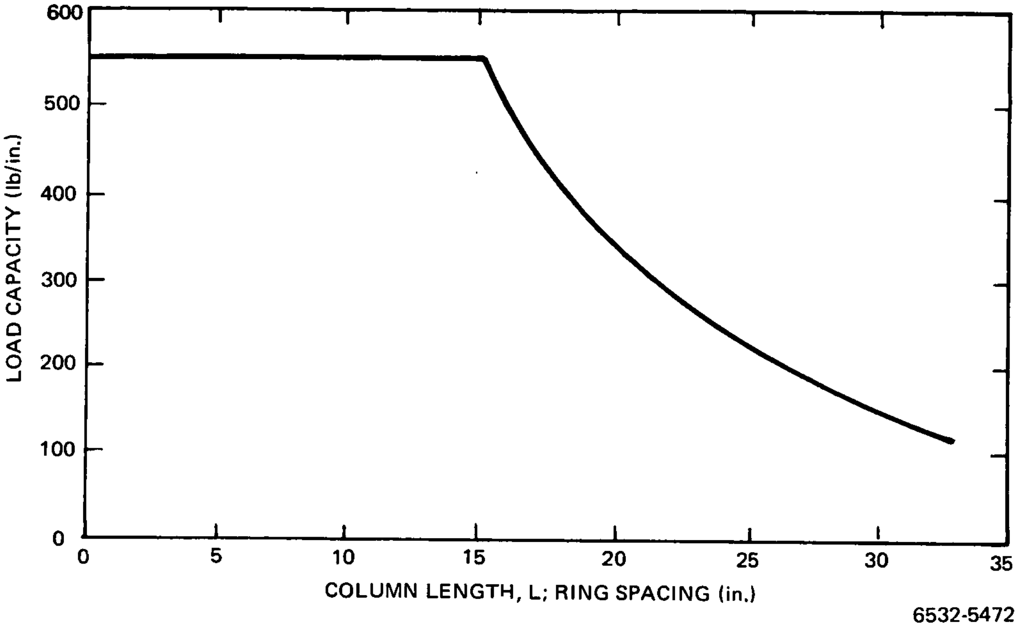

Figure 44. Load Capacity vs Column Length

where

E = Modulus of elasticity

I = Moment of inertia of frame

M = Bending moment on shell

D = Shell diameter

L = Frame spacing

From the compression and bending loads of Table 3, an equivalent bending moment is determined and used above.

$$M_{eq} = N\pi R^2$$

where

N_{max} = Maximum panel unit load.

Station	N_{max} (lb/in.)	R (in.)	M_{eq} (in.-lb)
0	221.9	36	903500
61.3	165.6	36	674200
80	171.6	33.2	594200
120	175.9	27.8	427100
150	203.1	22.0	308800
182	181.1	17.9	182300
212	216.1	12.4	104400
236	185.1	9.9	57000

The rings will be fabricated of 2219-T0 with $E = 10 \times 10^6$. Then,

$$I_F = MD^2/L(1/16 \times 10^{10})$$

Station	M (in.-lb)	D (in.)	L (in.)	I (in.^{4})
0	903,500	72	24	0.00122
61.3	674,200	72	24	0.00091
80	594,200	66.4	24	0.00068
120	427,100	55.6	24	0.00034
150	308,800	44	24	0.00016
182	182,300	35.8	24	0.000061
212	104,400	24.8	24	0.000016
236	57,000	19.8	24	0.000005

Ring spacing will not exceed 24 in. The probable configuration will be "Z" as shown in Figure 45. The moment of inertia of this configuration is 0.0288 in.^{4} which is 20 times greater than that required. Rings at component attachments will have greater stiffness as needed.

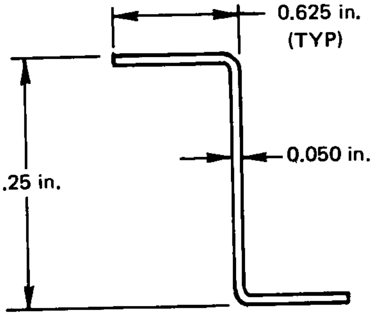

6532-5473

Figure 45. Ring Configuration

4. Acoustic Fatigue

The acoustic loads exist from the time of engine ignition until the launch vehicle has reached an altitude of negligible transmissibility. The sound pressure levels shown on Figure 10 are inside the vehicle nose shroud and represent peak values lasting for approximately 5 sec at ignition and 55 sec at transonic, maximum $q\alpha$. The Titan user's manual(4) states that the levels inside the shroud at 145 db peak (140 db overall) rarely cause severe structural excitation. There is not sufficient energy to cause damaging displacements to massive components. However, large thin panels and components mounted directly to them may show adverse responses.

The effort to evaluate the radiator response to acoustic excitation was not completed. Since the radiator was to be composed of axial members, rings, and panels, its response characteristics were conceivably in the range where damages could have been induced. It was considered a remote chance, however, because the panels were relatively thick with respect to their area.

5. Thermal Stress Due to Startup and Shutdown

The stresses associated with the brazing were covered in Section V-F-1. The residual stresses were such that the tube had 0.10% plastic strain at room temperature and the fin was elastic. The effect of subsequent thermal cycling was needed to determine the possibility of ratcheting. If the radiator would reach a shakedown relationship such that subsequent thermal cycles would not create additional plastic strain, aluminum could be acceptable radiator material.

The maximum radiator temperature during operation would be slightly over 600°F. This was to be at the inlet end at EOL. For convenience, it was assumed that the operational cycling would be from 75 to 600°F both in ground testing and in space. It was further assumed that a stress-free condition could be achieved at 600°F during the braze phase by soaking (annealing) during the cooldown. Then, the stresses shown in Section V-F-1 represented the starting point and most favorable condition that could be expected for austenitic stainless steel and 3003-T0 aluminum.

As the temperature increases from 75°F, the material tends to return to the original stress free state at 600°, however, there has been 0.10% permanent strain in the tube. Figure 46 shows the complete cycle of strain vs temperature starting with equal length, stress-free material at 600°F. Both fin and tube are essentially stress-free and equal length at point 0.

The stress-strain curves are idealized for simplicity but are within engineering tolerances of the actual conditions. As cooling commences, the strain is elastic. At about 270°F, the steel tube is at its elastic limit and yields approaching room temperature, Point 1. At this point, the tube is in compression about 30,000 psi and the fin is in tension about 5000 psi. These are axial stresses not combined or effective stresses. The tube has undergone 0.10% plastic deformation.

On reheat from room temperature to the 600°F operating temperature, Point 1 to Point 2, the stresses are relieved elastically and a new position is reached about 0.03% shorter than the original position. This is due to totally elastic behavior and 600°F end-point properties for the materials. Note that the aluminum and stainless steel have opposing forces at 600°F and that the strains have not followed a line of plasticity. With sustained 600°F conditions, the aluminum tends to relax or anneal. Although complete relaxation properties of the alloy are not available at 600°, the creep properties on Figure 47 are indicative of the effect. It can be presumed that the relaxation is effective and that the aluminum conforms to the stainless steel by virtue of 0.10% strain of relaxation. Since the stainless steel does not relax appreciably at 600°F and has not entered the plastic range of positive strain, it unloads elastically to the -0.1% strain, Point 3 on Figure 46. Now, both materials have undergone 0.1% permanent strain in the cycle, the tube during the cooling and the fin in reheating. Both materials are equal length, and if the bond were broken, would not assume a new length. This represents a new starting point for subsequent thermal cycles but is 0.10% shorter than the previous starting point. Each repeat of this cycle would produce an additional 0.10% strain, and with sufficient cycles, rupture would occur. The assembly is shown to encounter thermal ratcheting and is not satisfactory.

Figure 48 shows the effect of freezing at 775°F and two full cycles between 600°F to room temperature and back to 600°F. With both materials starting at 0.0 strain at 775°F, then dropping to 600°F and soaking there, the aluminum

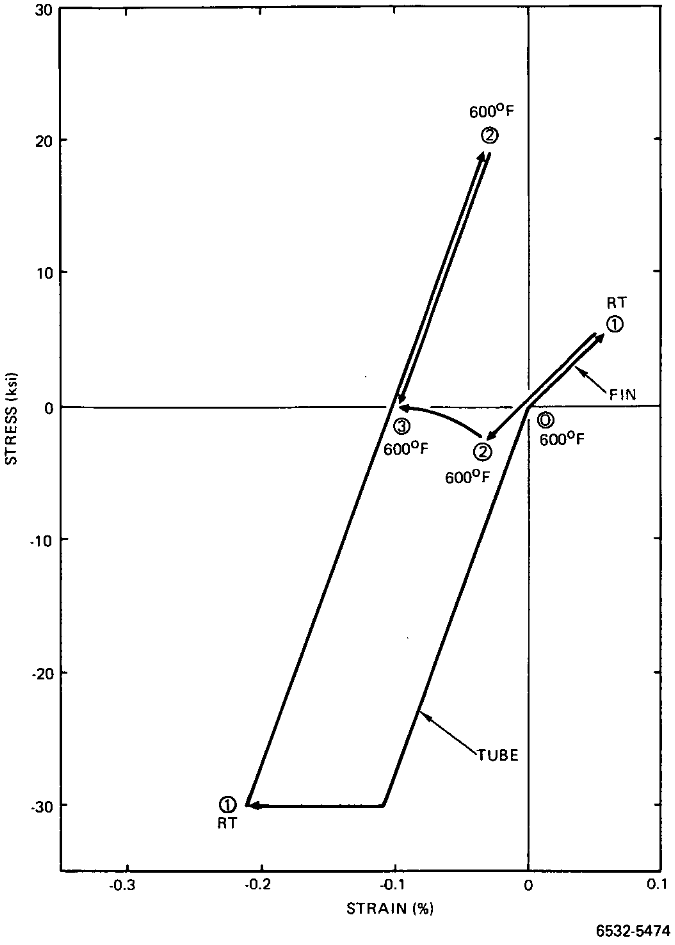

Figure 46.
Symmetric Aluminum and Stainless-Steel Tube Thermal Cycle

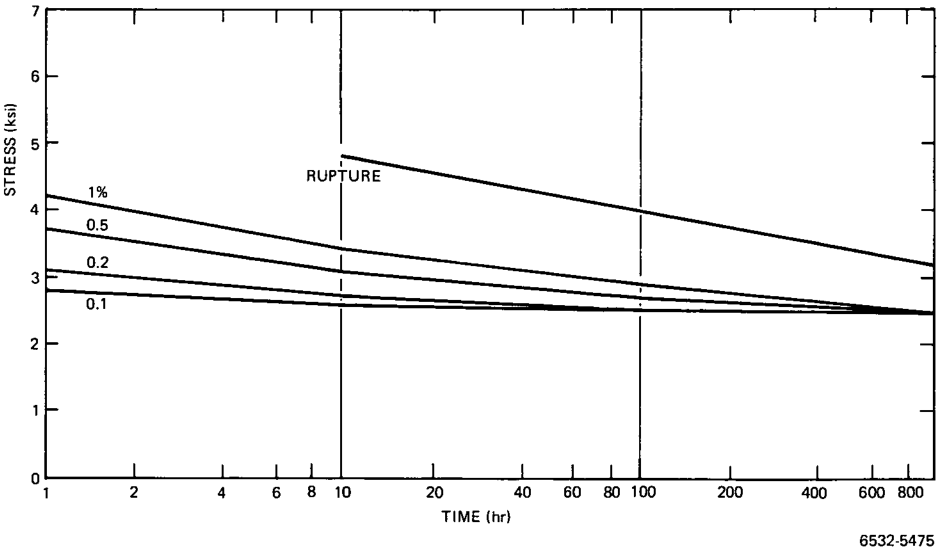

Figure 47. Aluminum 3003 Creep and Rupture at 400°F

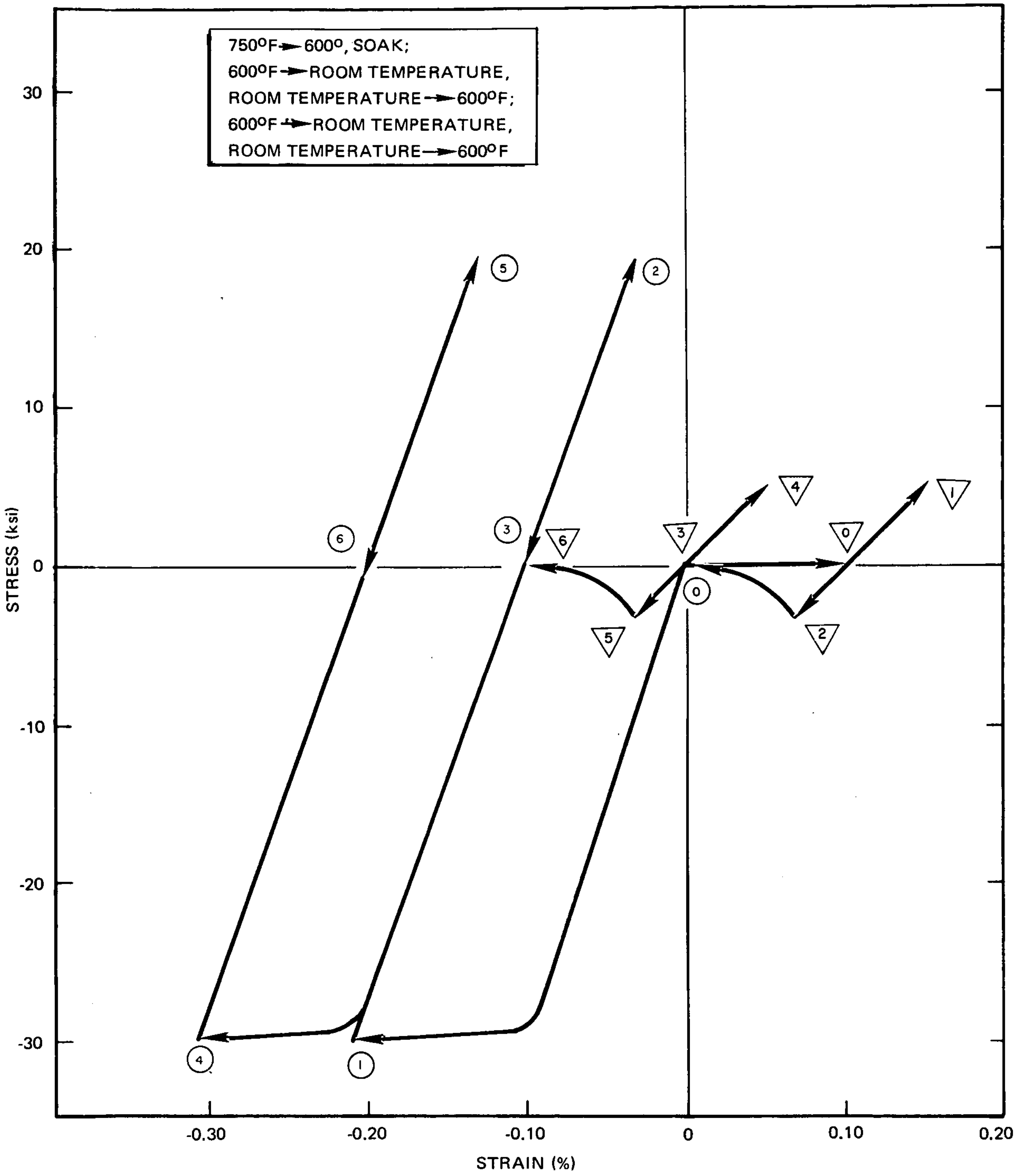

6532-5476

Figure 48. Aluminum 3003 — Stainless-Steel Thermal Cycle

creeps or relaxes 0.10%. Both materials are now at a Point 0 on the curve. Cooling to room temperature without the benefit of creep or relaxation, the stainless-steel tube endures 0.10% plastic and 0.11% elastic strain and the aluminum has 0.05% elastic strain; ① and ▽1 on the curve. Reheating to 600°F, both materials go to Points ② and ▽2. Sustained 600°F operation allows the aluminum to relax to Point ▽3 and the stainless steel to Point ③. This shows 0.10% contraction of both materials. Subsequent cycles, 4, 5, and 6 show repeated 0.10% contraction and the ratcheting effect.

It was evident that the radiator could not be fabricated of annealed austenitic tubes and 3003-T0 aluminum in the proportions shown. Several concurrent studies were made to find an acceptable radiator. They included: (1) variation of the area ratios with the same materials; (2) alternate tube materials; (3) alternate fin materials, and (4) alternate materials for both the tube and the fins.

The approach for changing the area ratio was based on the assumption that the radiator would perform properly if the tube remained elastic during the thermal cycling. Then, since the total differential contraction would not change, the aluminum would absorb most of the strain and go plastic on cooling. On reheating, the elastic strain of the tube would allow it to return to its original length. The permanent strain of the aluminum would relax out and it also would return to its original length. Thus, ratcheting would be avoided.

A parametric relationship between area ratios, yield strengths, and expansion rate differences was made. This covered all of the material combinations with modulus of elasticity of 29×10^6 psi for the tubes and 10×10^6 psi for the fins (iron or nickel base alloy tubes and aluminum fins). Then, with the established relationships for the thermal growth or contraction of the panel and adding the stipulation that the materials remain elastic, the following equations were derived

$$\left[\frac{1}{E_t} + \frac{1}{(A_f/A_t)E_f}\right]\sigma_t = \Delta\alpha\,\Delta T \qquad \ldots(1)$$

$$\left[\frac{(A_f/A_t)}{E_t} + \frac{1}{E_f}\right]\sigma_f = \Delta\alpha\,\Delta T \qquad \ldots(2)$$

These equations were solved parametrically for the area ratio (A_f/A_t) and differential expansion coefficient ($\Delta\alpha$). Figure 49 shows this relationship. The radiating lines are stress levels for the fin and the curved lines are the tube stresses. It can be seen that for the differential of expansion rates between aluminum and stainless steel or aluminum and a nickel alloy ($\Delta\alpha \approx 5.4 \times 10^{-6}$), and from the area ratio for the design current at the study time ($A_f/A_t \approx 13.5$), that tube strength in excess of 50,000 psi is required. To continue with annealed austenitic tube would require an area ratio of less than 2.0 imposing a very large weight penalty. Since the fin thicknesses were determined by thermal performance, the area ratio could only be achieved by increasing tube size. For the design of Figure 16, the tube wall would be 0.045 in. and the increase in tube weight would be 129.0 lb. It would be impossible to use annealed austenitic stainless steel and aluminum and maintain elasticity in both materials.

The curves suggested that either high strength tubes ($\sigma_y \geq 60{,}000$) or a close match of the expansion coefficients were needed to maintain elasticity.

Several high strength materials were evaluated including hardened austenitic stainless-steel tubes. There appeared to be an acceptable solution to the problem for an ideal environment and operation. When the conditions of thermal variations were considered, however, an aluminum radiator lost status. Considering the circumferential and axial thermal gradients, and the ground test conditions described in the following sections, aluminum fin design was abandoned.

Several aspects of the analysis were incomplete due to the sequence leading to the abandonment of aluminum for fins. The following items were more in the nature of philosophic rather than analytical since they were pre-preliminary. They showed more evidence on the complexity of the analysis of the aluminum and steel assembly and would have led to more intricate analysis had the configuration been maintained.

Although not entirely thermal, the combination of residual stresses at room temperature with launch-induced stresses would influence material and configuration selection. Figure 50 shows the influence of the axial and transverse accelerations on the loads in the structure. On the critical side (left in the Figure), both components are added and lead to the maximum compressive loads. On the opposite side, the axial acceleration induces compression and the transverse

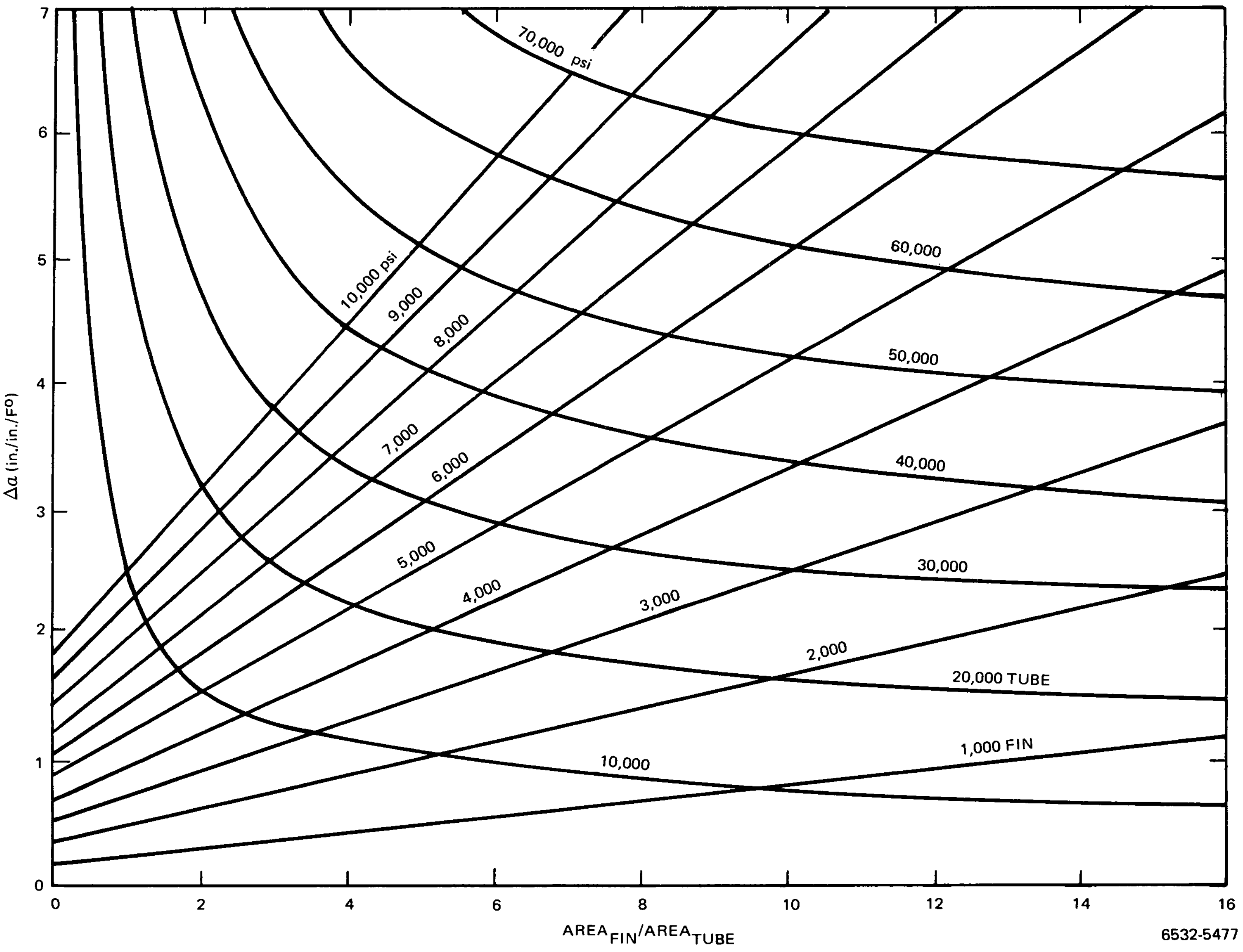

Figure 49. Fin and Tube Elastic Stresses vs Area Ratio and Expansion Rate Difference, 600°F to Room Temperature

acceleration induces tension. Under some conditions, the tension prevails with a resulting net tension load. Other conditions combine as net compressive load but not as severe as on the opposite side. In either case, the combination of launch-induced loads with the residual stresses creates a complex loading as noted in Figure 51.

The total strain is the sum of the braze-induced and launch-induced strains. It can be seen that the elastic limits will be exceeded if the braze residuals are at the elastic limit. It is necessary, therefore, to be certain that the residuals are sufficiently low so that the superposition of the launch loads does not cause allowable strains to be exceeded.

A second problem related to temperature stresses deals with the edge joining of the fin tips. Note that the minimum stresses in the fin and tube assembly were at 600°F after a long soaking (time dependent annealing).

$$\sigma_{Al} = \sigma_{SS} = 0 \text{ at } 600°\text{F}$$

On cooling to room temperature, there are residual compressive stresses in the tube and tension in the fin. The total forces in each are equal and opposite. The forces are based on the relative areas and modulus of elasticity.

Of the several methods of splicing the fin tips, an extruded "T" was the most obvious. The outstanding leg would also provide added strength. A stress-free stringer added to the thermally contracted composite fin-tube assembly would upset the potential for returning to a stress-free condition at operating temperatures. The stringer would expand thermally but at a different rate than the fin-tube composite and consequently have a residual strain at elevated temperature.

Similarly, if the stringer were pre-stressed, it would induce a load in the fin-tube composite after attaching and removing the preload. This would also alter the area ratio and effect the ability to attain a stress-free condition at operating temperature.

If the stringer were added during the brazing operation, the assembly would be stress-free at 600°F but the area ratio would have been modified. It would be necessary to trim the fins before brazing or make the braze a two-step process.

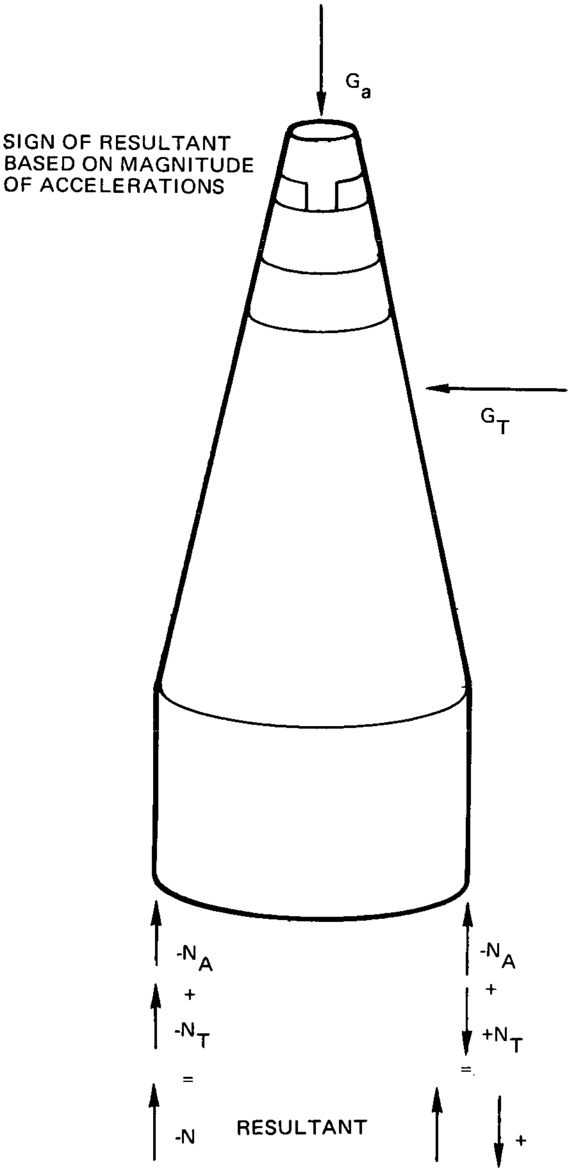

6532-5478

Figure 50. Launch Loads

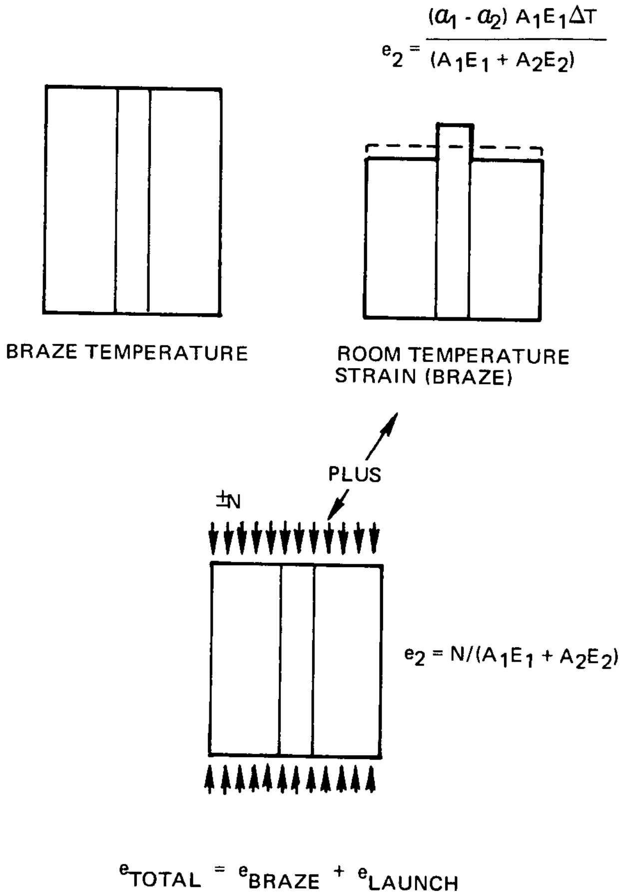

6532-5479

Figure 51. Braze and Launch Strains

The procedure that appeared to have the best potential was to increase the fin length in the circumferential direction. Then, turning the edge in, the splice could be made by riveting along the flange as shown in Figure 52.

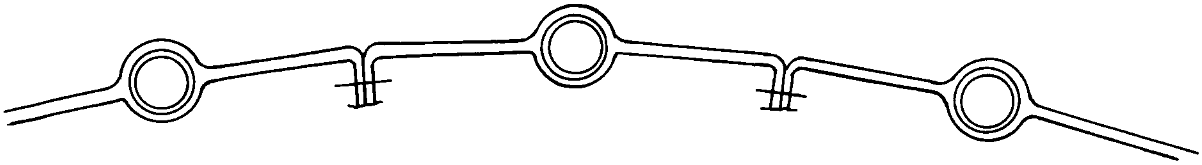

Figure 52. Radiator Panel Joint Option

Whatever method of joining fin tips was selected, the fabrication would be intricate. The large variation in the expansion coefficients was the basis for the problem.

Although it was conceded that repeated plastic strain and relaxation of the aluminum may be acceptable, it was recognized that this effect could offer other problems. An analysis for low cycle fatigue would have been necessary. This analysis would be difficult owing to the limited data available. These effects along with the other known problems related to aluminum fins contributed to its abandonment.

6. Thermal Stresses — Operational

The stresses related to the operational-induced temperatures were evaluated as 48 θ values. Using temperatures that were preliminary but indicative, potentially damaging conditions were shown.

The circumferential temperature distribution for several axial stations are shown in Figure 81. At any cross sections, stresses are expressed by:

$$\sigma = (T_{avg} - T)\alpha E$$

where

σ = Axial stress (normal to cross section)

T_{avg} = Average temperature on cross section

T = Temperature at point in question

α = Coefficient of thermal expansion

E = Modulus of elasticity.

Since the gradients were preliminary, the average temperatures must be considered approximate. The stresses on the aluminum fins are shown in Table 9 with the yield strength, F_{ty} at the temperature in question.

TABLE 9

48 θ STRESSES, ALUMINUM FIN

Location	T_{hot} (°F)	T_{cold} (°F)	T_{avg} (°F)	α (in./in./°F)	E (psi x 10^{-6})	σ_{max} (psi)	σ_{min} (psi)	F_{ty} (psi)
Top of Cone	588	578	585	13.4	6	570	-285	1600
Mid Cone	540	520	533	13.4	6	1050	-525	1700
Mid Cylinder	465	435	455	13.2	7	1850	-925	2200

Not only would the radiator not return to a stress-free 600°F condition during operation, or to a condition where relaxation would produce a stress-free condition, but the temperature distribution would be sufficiently complex to create both tension and compression on the same cross section. Relaxation would be at a variable rate circumferentially and axially (axial gradient is $\approx$135°F, circumferential gradient is 10 to 30°F). The stress state of the radiator would be impossible to predict, evaluate, or duplicate in test. It was concluded that the fin material would be distorted ("oil canned") out of its plane resulting in loss of structural capability for launch loads. There would be no way to predict the nonuniform axial strains and consequently no way to predict the out-of-plane deformations. It would have been difficult or impossible to test for these relationships. This added further to the desirability of using some other material for the fins.

7. Ground Test Creep

As noted, the system would be oriented vertically with the reactor down during ground test. It would be a 5-year test with operational temperatures between 455 and 610°F at various locations on the radiator.

The effect of sustaining these temperatures on the radiator structure added to the rejection of aluminum.

From the limited creep data available and shown on Figure 47, it is evident that the aluminum cannot be used as the primary load bearing member at the operating temperature. The total weight above the radiation shield during test would be approximately 1000 lb or 21 lb per fin-tube. It would be 600 lb total or 12.5 lb per fin-tube above the pump ring as installed in the test chamber.

The pump, thermoelectric conversion system, and associated tubing would be approximately 400 lb suspended on eight brackets. It would be necessary to fabricate these brackets of stainless steel and provide direct load transfer to the tubes which would be required to support the entire radiator.

Similarly, with the loads in the tubes, it would be necessary to provide a load path from the upper end of the tubes (lower end in test chamber) to the access panel ring. This was also a structural detail that was not designed but recognized as a necessity.

G. FABRICATION STATUS

An experimental fabrication effort was carried out at Atomics International and at the Solar Division of International Harvester Co. In addition, samples of brazed radiator segments produced by Lockheed-Sunnyvale in 1963-64 for a NASA SNAP 8 heat rejection system, were thermally cycled to determine the acceptability of the fabrication technique for the 5-kwe system.

1. Solar Fabricated Radiation Specimens

Solar utilized two techniques for the brazing of Type 304 stainless-steel tubing to 3003 aluminum fin material in two configurations (Figures 53 and 54). The first technique was an inert atmosphere furnace braze in which a flux was used in conjunction with BAl-Si4. The process is shown graphically in Figure 55. The second technique was a fluxless, resistance heating method, using pre-placed, BAl-Si4 foil between the stainless-steel tube and the aluminum fin. Heat was generated at the braze interface by passing electric current through the joint interface with a moving roller, which also applied pressure to the joint (see Figure 56). The operation was carried out in air with an inert atmosphere cover gas.

The stainless-steel tubing, used with both techniques, was plated with titanium by the use of a proprietary fused salt bath. The purpose of the titanium

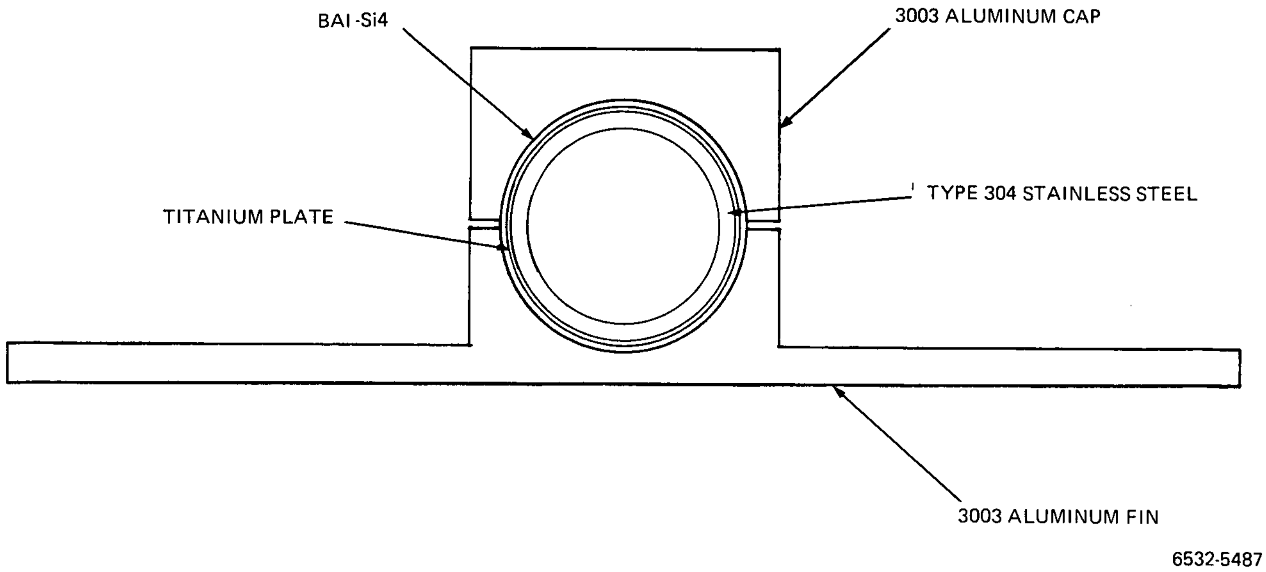

Figure 53. Solar Radiator Fin Configuration 1 Cross Section

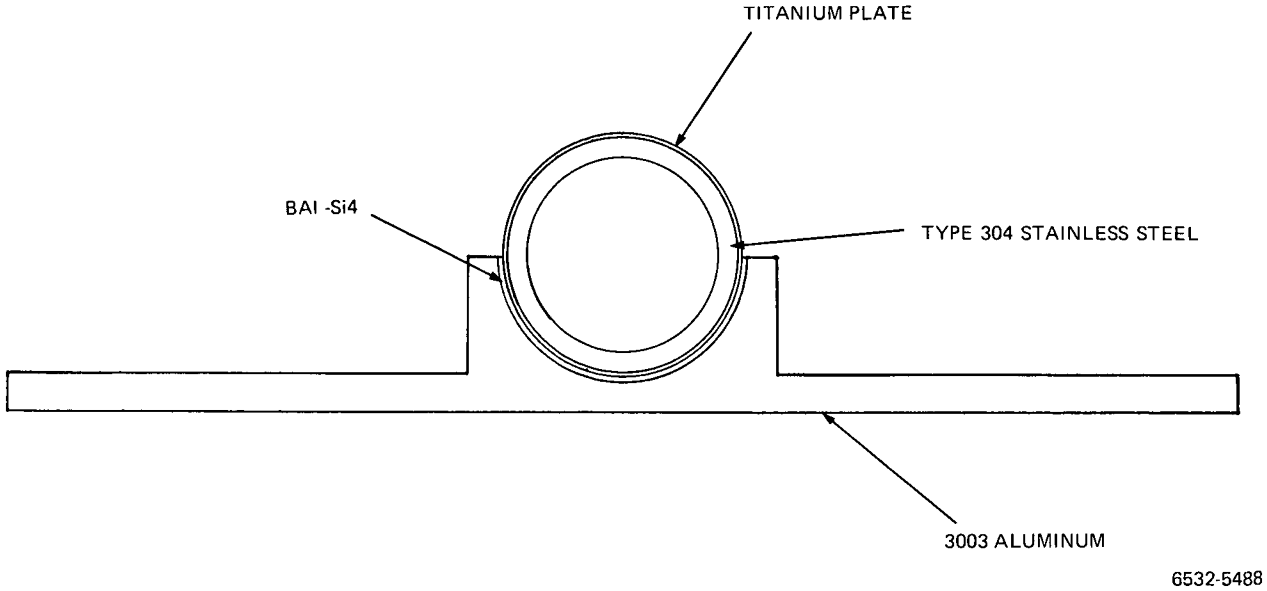

Figure 54. Solar Radiator Fin Configuration 2 Cross Section

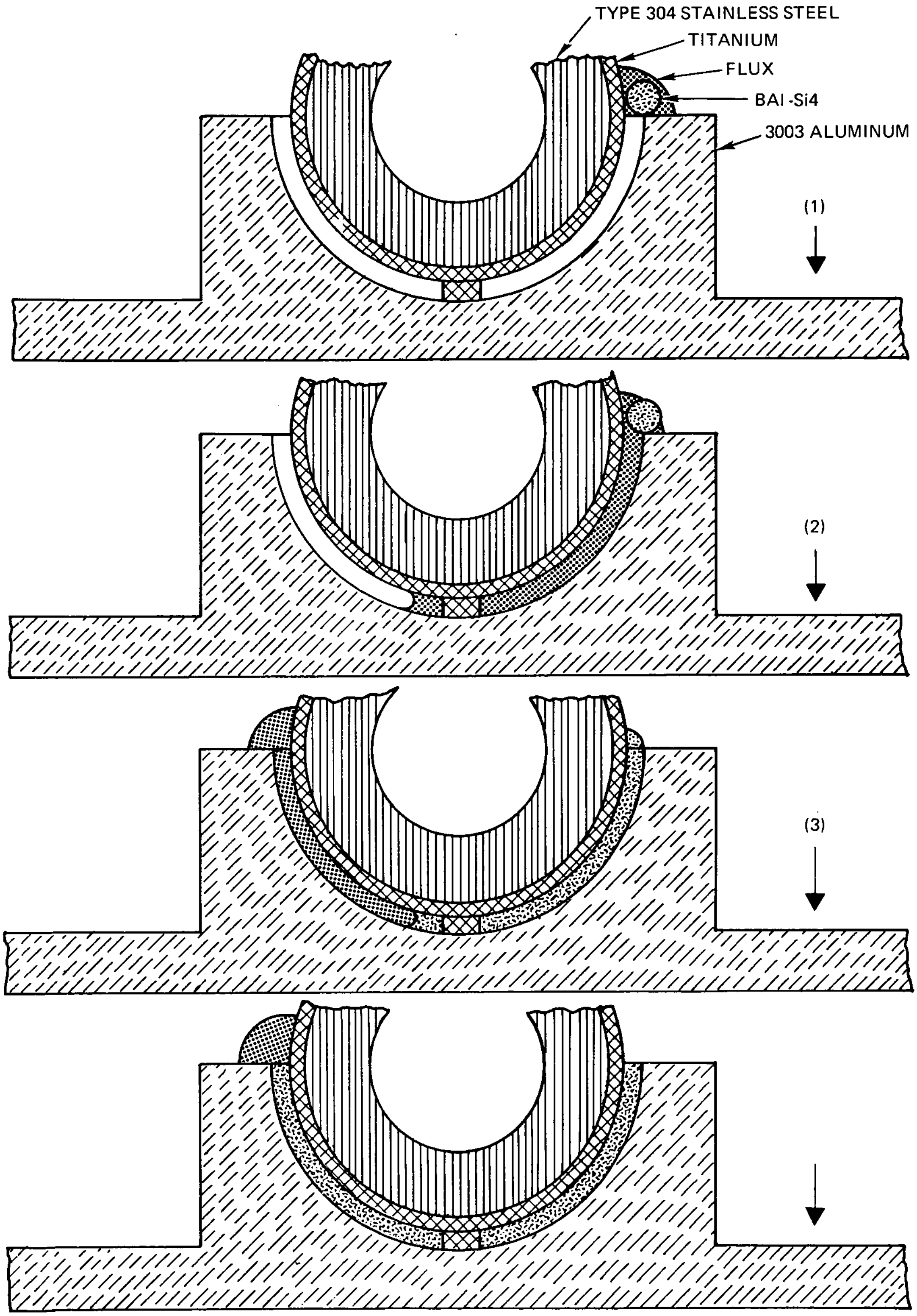

Figure 55. Solar Braze Technique

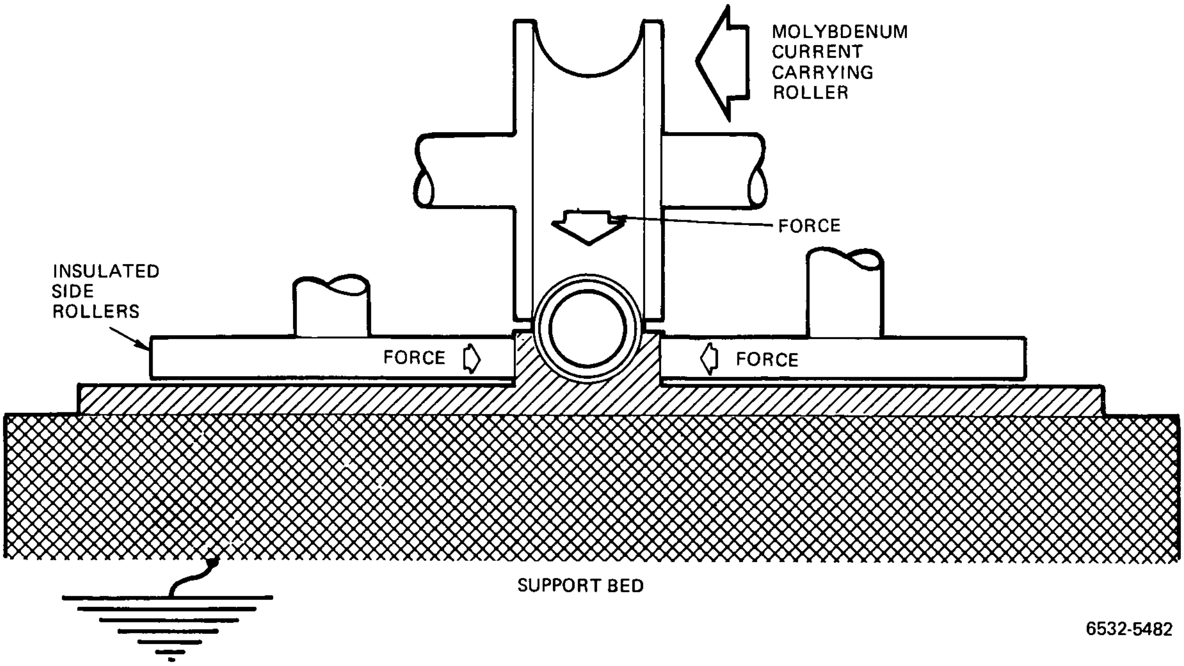

Figure 56. Solar Fluxless Brazing

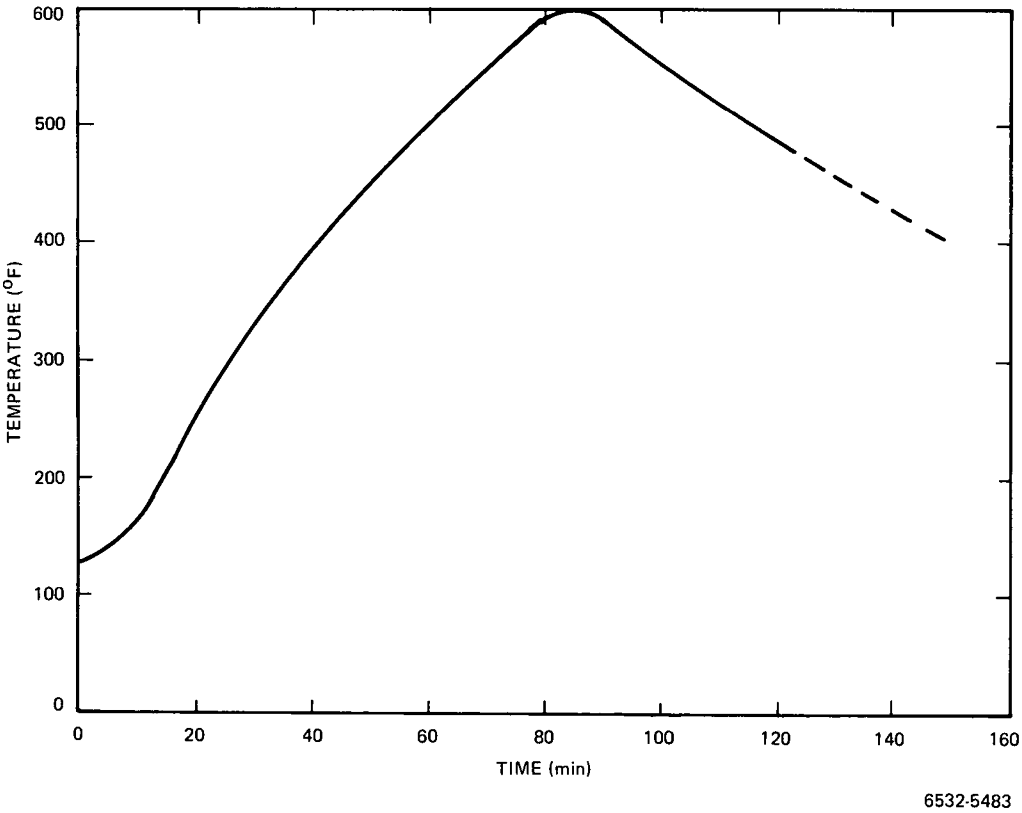

Figure 57. Solar Fluxless Brazed Fin, 9.5° F/min Heating Rate

plating was to provide a surface more readily wet by the braze material and to provide a diffusion barrier to the transfer of aluminum into the stainless steel which could produce brittle intermetallics at the braze and stainless-steel interface. The formation of the intermetallics could be a bond failure site during thermal cycling of the radiator.

Two types of tests were conducted on the Solar samples: (1) thermal cycling between room temperature and 600°F to determine the soundness of the brazed joint under differential thermal expansion stress, and (2) thermal aging to determine the effectiveness of the titanium plating as a diffusion barrier.

Fin and stainless-steel tube radiator segments, 6 in. in length, produced by furnace brazing and resistance brazing were thermally cycled. A fluxless-brazed fin was thermally cycled once by the schedule shown in Figure 57. The bond failed between the titanium plating and the BAl-Si4 braze as shown in Figure 58. A flux-brazed fin sample was thermally cycled ten times as per the heating schedule shown in Figure 59. The bond failed between the titanium plating and the stainless steel, as shown in Figure 60. Neither condition was satisfactory for long term use in the radiator structure, since the structural integrity of the radiator must be maintained and adequate thermal conduction through the braze interface was required.

Solar felt the titanium plating was faulty and that an adequate bond could be produced for the radiator.

Samples of each type of tube and fin assembly were thermally aged to determine the effectiveness of the titanium plating, as a diffusion barrier. The samples were aged at 550°C for 72 hours, the thermal equivalent of 40,000 hours at 28 kcal/mole, in a vacuum of 10^{-5} torr. Photomicrographs of the flux-braze Solar sample before and after aging are shown in Figure 61. Photomicrographs of the fluxless-brazed Solar sample before and after aging are shown in Figure 62. In the base of the flux-braze sample, there was a diffusion zone to a depth of about 20% of the titanium thickness adjacent to the BAl-Si4. In the case of the fluxless-brazed sample, there was a diffusion zone of about 20% of the titanium thickness adjacent to the BAl-Si4 and about 5% of the titanium thickness adjacent to the stainless steel. In neither case did diffusion of materials appear to be a problem.

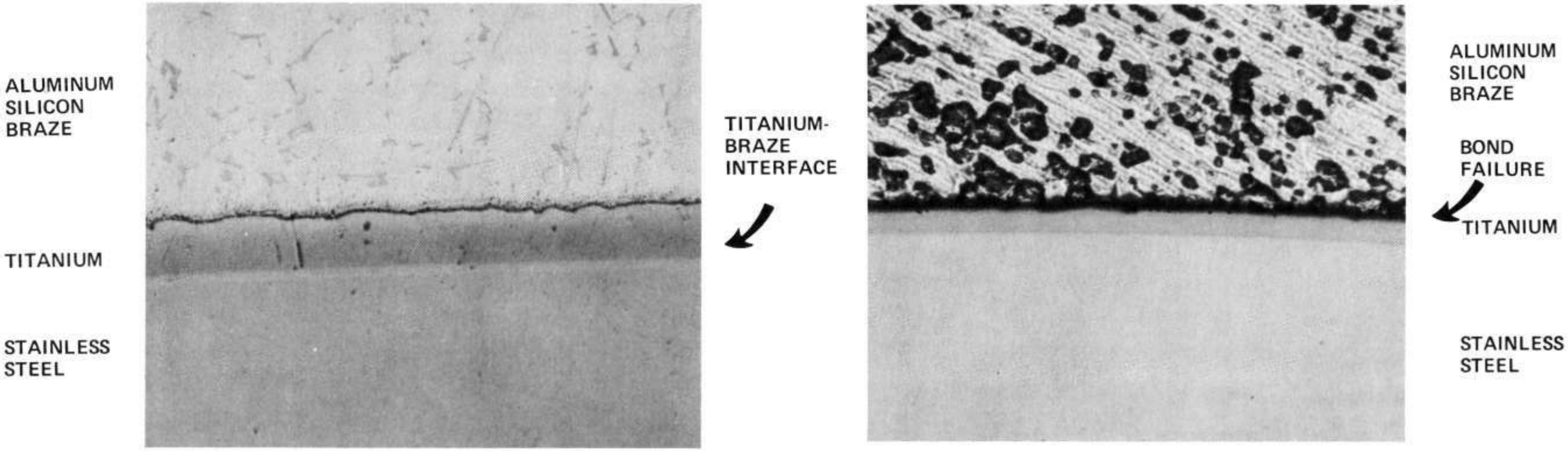

500X
AS-RECEIVED MET. LAB NO. 9732-1

250X
AFTER ONE THERMAL CYCLE MET. LAB NO. 9742-2

72-017-48-269A

Figure 58. Fluxless Brazed Solar Sample, As-Received and After One Thermal Cycle

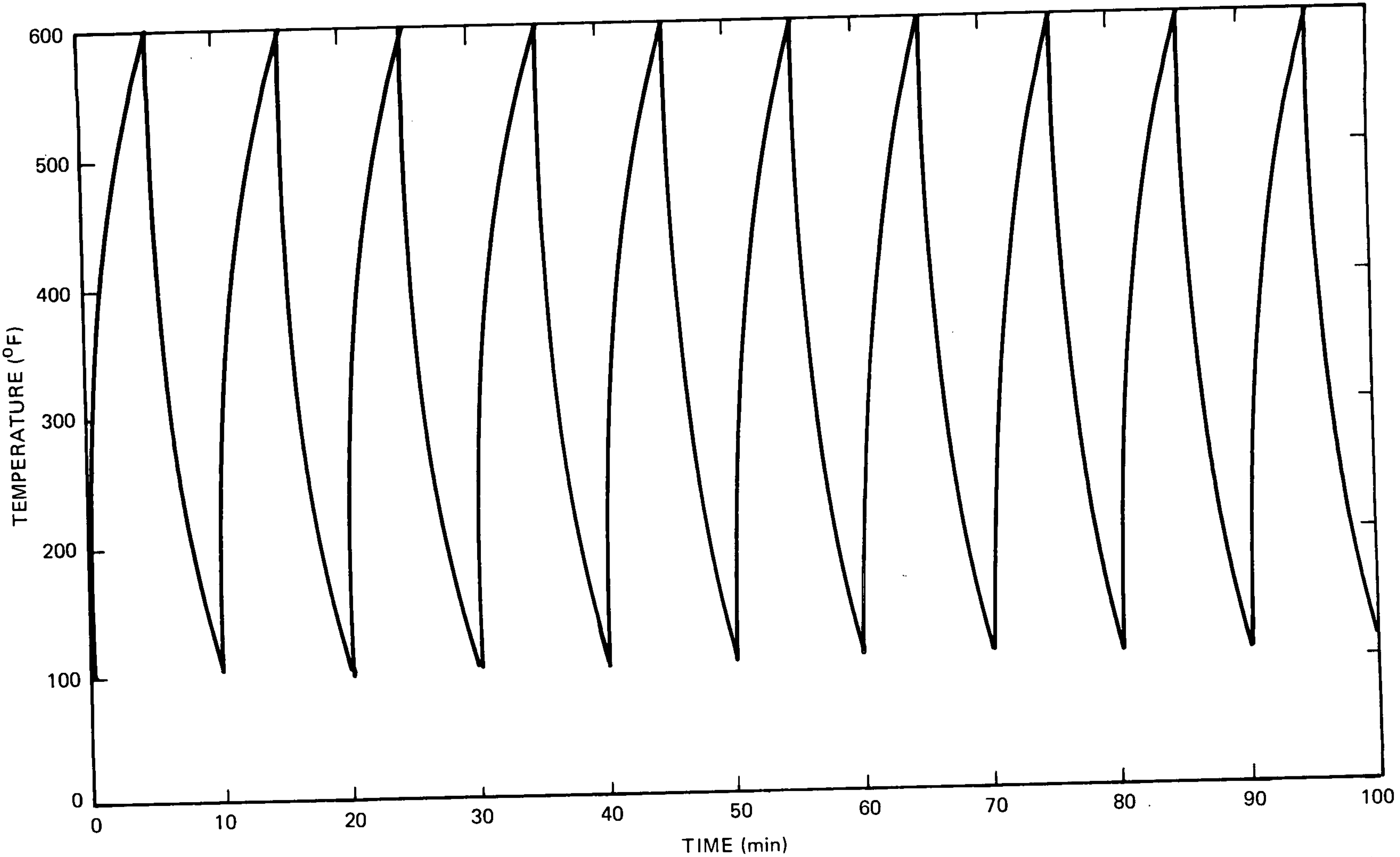

6532-5484

Figure 59. Solar Flux Brazed Fin, 83°F/min Heating Rate

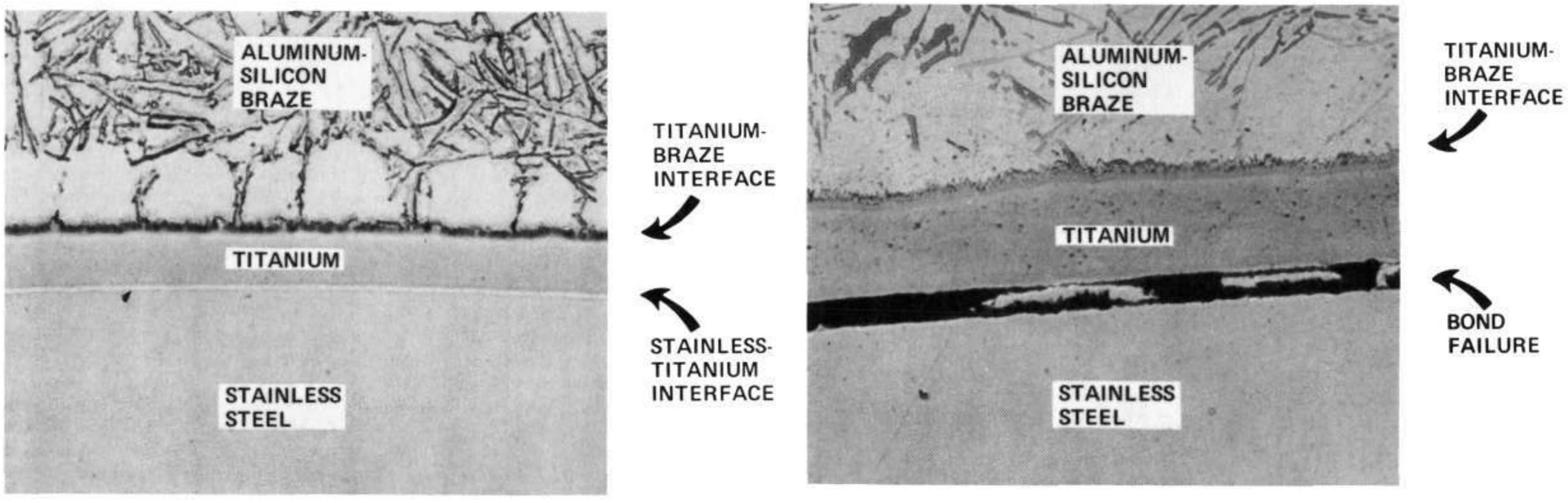

250X
AS-RECEIVED

MET. LAB NO. 9724-3

500X
AFTER TEN THERMAL CYCLES

MET. LAB NO. 9742-1

72-017-48-268A

Figure 60. Flux Brazed Solar Sample, As-Received and After Ten Thermal Cycles

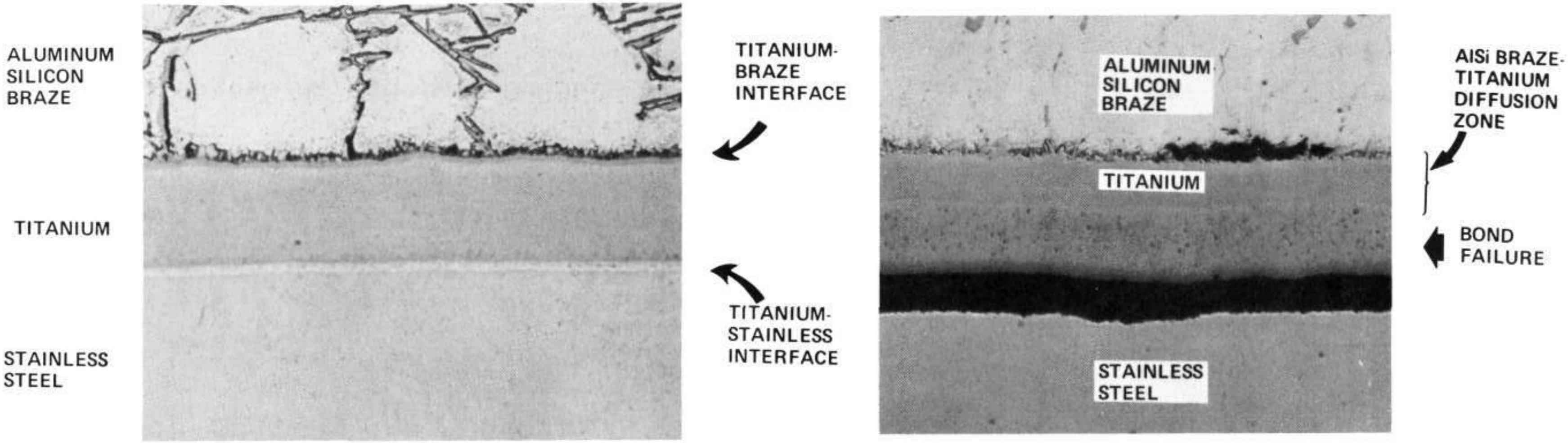

500X AS-RECEIVED

MET. LAB NO. 9724-3

500X AFTER 72 hr AT 550°C

MET. LAB NO. 9739-1

72-017-48-270A

Figure 61. Diffusion Couple — Flux Brazed Solar Sample, As-Received and After 72 hr at 550° C

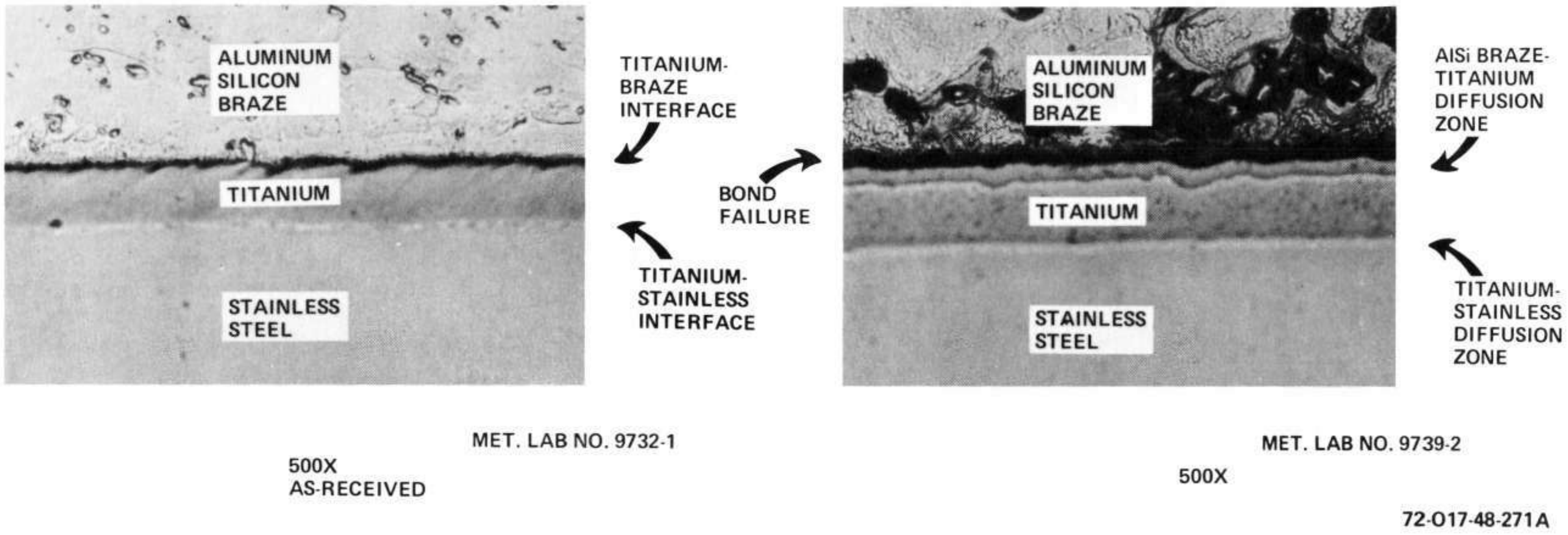

Figure 62. Diffusion Couple — Fluxless Brazed Solar Sample, As-Received and After 72 hr at 550°C

2. Lockheed-Fabricated Radiator Specimen

The fabrication technique for the Lockheed specimen is described in LMSC-A662481, titled, "Fabrication and Testing of Component Assemblies for a SNAP 8 Heat Rejection Radiator," dated June 17, 1964. In brief, the radiator sections were fabricated by a hand brazing technique. The Type 316 stainless-steel tubing was tinned with BAl-Si4 by a scratch brushing technique immediately followed by the application of braze material with a torch. The tinning operation was automated to produce consistent results. Following the tinning operation, pre-formed and cleaned sheets of 3003 aluminum, with a semi-circular formed groove down the center, were placed on a heated plate. The stainless-steel tube was placed in the groove and the assembly was heated to 800°F. BAl-Si4 was then used to fill the space between the tube and groove by capillary action, using a hand operated brazing torch. After filling, a puddle of BAl-Si4 was placed over the entire exposed tube surface. Subsequent milling removed undesired BAl-Si4 from the tube side of the tube-fin assembly (Figure 63).

A thermal cycle test was run on a sample of the Lockheed produced fin-tube material. The sample was cycled once from room temperature to 600°F as per the schedule shown in Figure 64. Failure of the braze occurred at the base of the groove in the 3003 aluminum fin (Figure 65). Further thermal cycling increased the extent of the separation. This fin-tube processing technique was eliminated from further consideration.

H. ALUMINUM RADIATOR EVALUATION

The initial selection of aluminum as the radiator fin material was based on its high thermal conductivity and low density. There had been considerable evidence to suggest that it would be bonded successfully to the stainless-steel tubes, and it appeared to have adequate strength to support the launch loads. Aluminum is a relatively low cost material and the machining and assembly would be straightforward at moderate cost.

Aluminum showed excellent thermal performance characteristics and the configuration shown (Figure 3) represented a low weight system. Previous experience with aluminum fins bonded to stainless-steel tubes indicated a viable approach to the integrated space radiator for the 5-kwe system. Although the

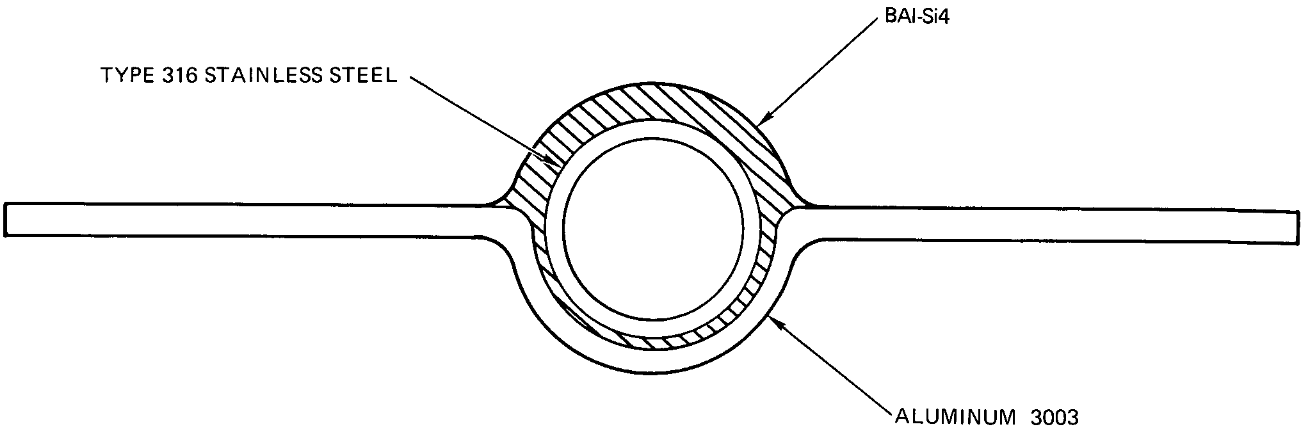

6532-5485

Figure 63. Lockheed Radiator Fin Cross Section

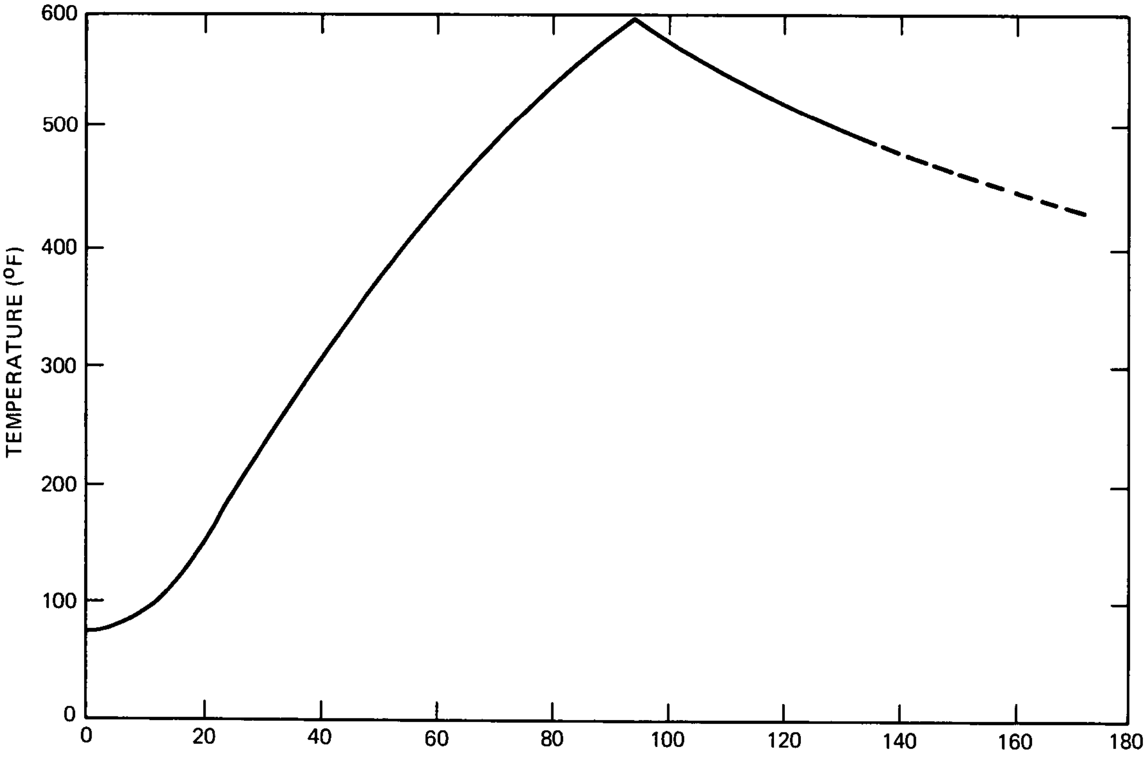

6532-5486

Figure 64. Lockheed Fin, 6.4°F/min Heating Rate

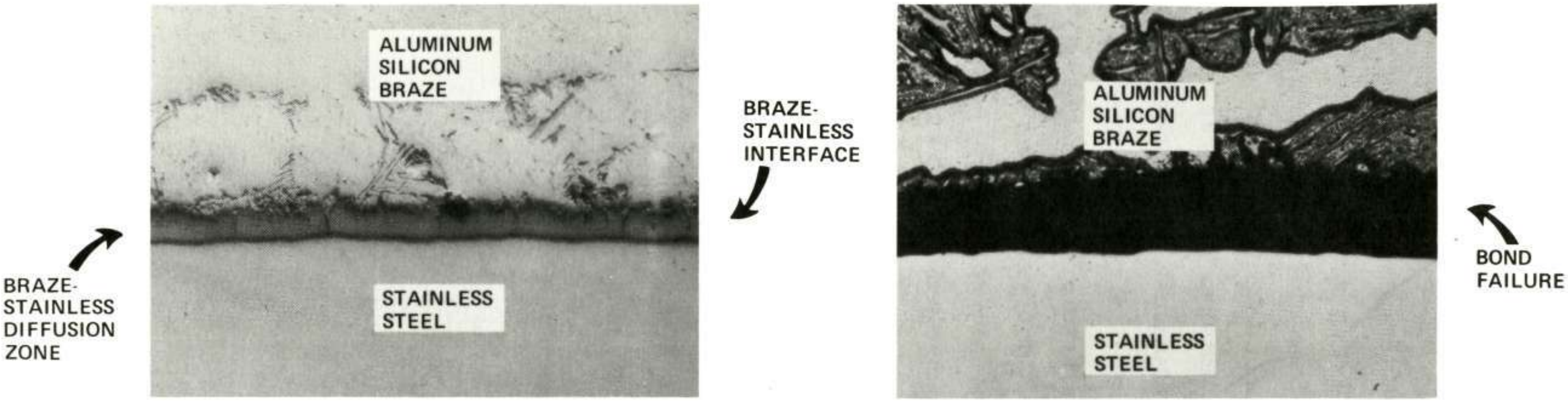

MET. LAB NO. 9739-3

250X
AS-RECEIVED

MET. LAB NO. 9742-3

250X
AFTER ONE THERMAL CYCLE

72-017-48-267A

Figure 65. Lockheed Sample, As-Received and After One Thermal Cycle

problem potential had been previously recognized, the differential expansion between the aluminum and stainless steels caused greater problems than could be tolerated. When large ratios of aluminum to stainless steel in the cross section existed, the force of the aluminum overwhelmed the stainless steel in thermal applications, particularly at lower temperatures. The ratio of areas in the 5-kwe radiator and the requirement for repeated cycles between room temperature and the 600°F operation would induce thermal distortion and stresses that would preclude successful performance. Increasing the ratio of aluminum to stainless steel or stainless steel to aluminum to suppress visual distortion but permit plastic distortion would cause a significant increase in system weight as well as introduce technical uncertainties. A reasonably good prediction could be made of strains and stresses for an isothermal operational condition; however, there would be thermal gradients both axially and circumferentially. The stress levels would range from compression to tension at all axial locations, and with the aluminum creep rate unknown but high creep rates a certainty at temperatures over 400°F, the use of aluminum for the fins became suspect. Further evaluation of the long-term (5-year) effect of creep on the ground test unit, the ratcheting of the stainless-steel tube during cycling, and the forces required to restrain distortions indicated that aluminum could not be used in conjunction with austenitic stainless-steel tubes for the 5-kwe radiator structure.

D

VI. LOCKALLOY FIN RADIATOR

When the evaluation of the aluminum fin and stainless-steel tube indicated that an alternate design was needed, a number of materials were investigated. It was necessary to obtain a close match in the expansion coefficients of the tubes and fins or use materials with sufficient strength to resist permanent strain. Lockalloy 38 with Type 304 stainless-steel tubes was selected. Section VI covers the evaluation of Lockalloy. Other material combinations given consideration are covered in Section VII.

The basis for the selection of Lockalloy for the fins was its thermal expansion characteristic along with its high thermal conductivity, modulus of elasticity, and strength. Most of the problems with aluminum were related to the large difference between its expansion compared to that of the tubes. With Lockalloy, this difference is very small and strains generated in thermal cycling are correspondingly small.

A. CONFIGURATION SELECTION

The configuration selection was based on both physical and mechanical characteristics, cost, availability, and joining procedure. Since the thermal coefficient of Lockalloy was a close match to that of the stainless steel it was not necessary to retain the symmetric cross section configuration. Stresses induced during a braze cycle would be low so that assembly could be accommodated by edge splicing.

Figure 66 shows the evolution of the Lockalloy fin. The initial design called for a machined tapered fin with a formed saddle to hold the 7/16-in. circular tube. The large loss in machining would increase raw material cost considerably. This led to the brazed flat fin configuration also employing the circular tube. Then to avoid the potential mismatch between the saddle and the tube and its related problems in making the braze, the D tube was adapted. The armor was to be brazed on the outside. This configuration did not provide sufficient stiffness to meet the launch strength requirements. The final configuration has an increase in height of the D tube, and decreased width. This provides sufficient stiffness to allow the elimination of the outstanding leg of the splice T.

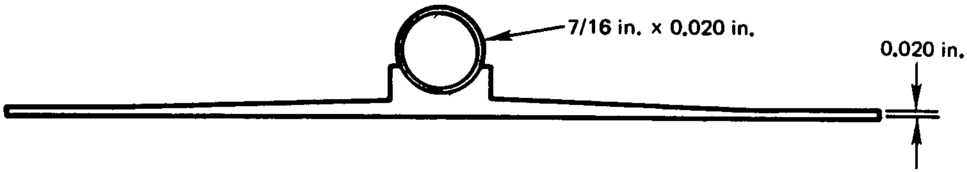

(1) MACHINED TAPERED FIN

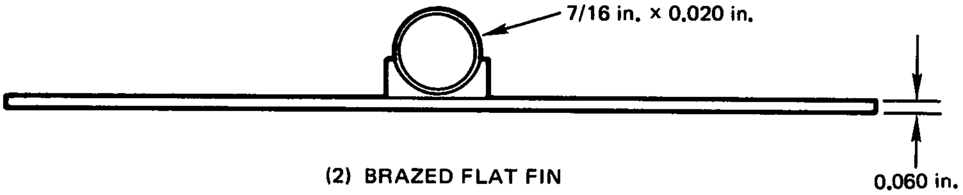

(2) BRAZED FLAT FIN

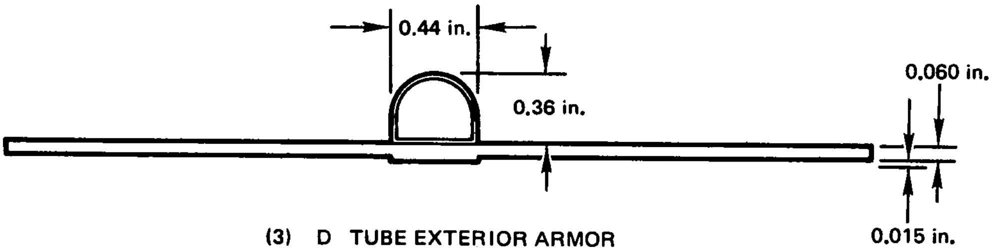

(3) D TUBE EXTERIOR ARMOR

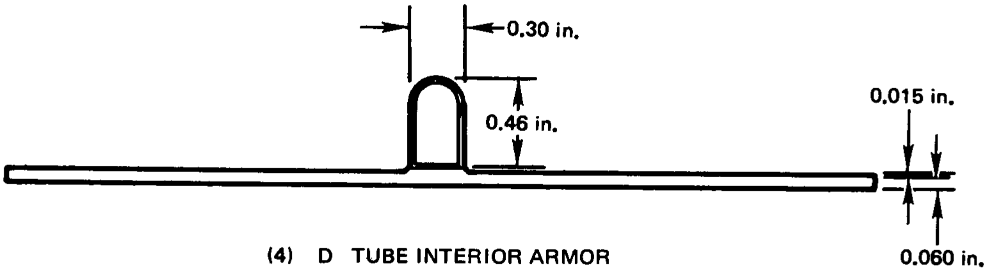

(4) D TUBE INTERIOR ARMOR

6532-5489

Figure 66. Lockalloy Radiator Panel Development

This would provide a 28-lb weight reduction. A further advantage is the reduction in the armor width, from 0.46 to 0.30 in. The tube would have the same midcircumference as a 7/16-in.-diameter tube with a cross sectional area of 0.100 in.^{2} compared to 0.1241 in.^{2}.

B. MATERIAL CHARACTERISTICS AND SELECTION

Lockalloy is the trade name of a powder metallurgy product of aluminum and beryllium (Be-38Al). As will be noted in the Be-Al phase diagram (Figure 67) the two materials are essentially insoluble in each other below 645°C (1193°F). The material is prepared by blending the powders, hot pressing into a billet, and extruding into a finished shape or stock for hot rolling. The end product possesses less brittle characteristics than pure beryllium, but, due to the beryllium crystallites, is anisotropic, particularly in transverse ductility (at right angles to the direction of extrusion). Since all fabrication is done below the solidus temperature of the Al-Be phase diagram, the product is composed of two distinct phases, one beryllium, the other aluminum. Some reduction in anisotropy of properties is possible by cross rolling, at right angles to that of the original

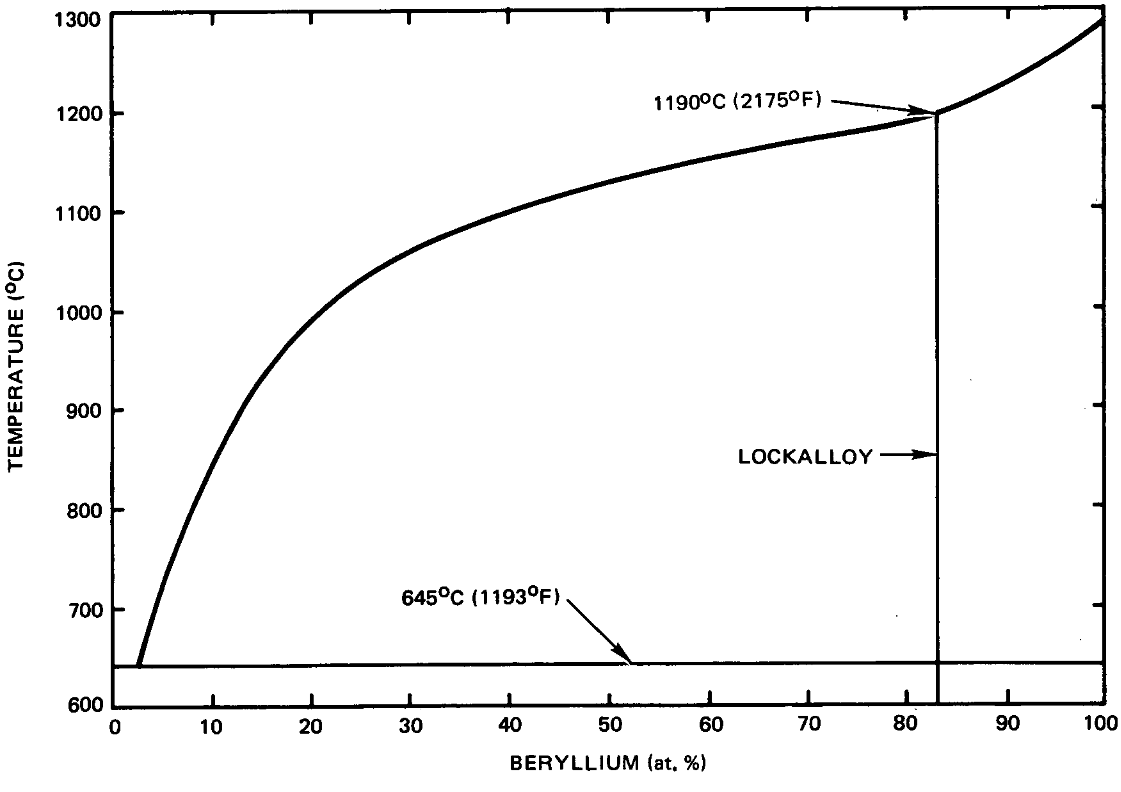

6532-5490

Figure 67. Aluminum-Beryllium Phase Diagram

extrusion direction. However, as will be noted in Table 10, the anisotropy primarily affects the transverse ducitility. It should be pointed out, that all beryllium products, when fabricated in a manner which tends to align the crystallites in the same crystallographic direction, are anisotropic in ductility.

TABLE 10

PROPERTIES OF EXTRUDED LOCKALLOY

Property	Temperature (°F)	Longitudinal	Transverse
Ultimate Tensile (ksi)	75	56	56
	600	37	No Data
Yield Strength (ksi)	75	44	44
	600	34	34
Elongation (% in 2 in.)	75	7 to 10	1-1/2 to 2
	600	7 to 10	No Data
Shear Ultimate (ksi)	75	29	No Data
	600	20	No Data
Tensile Modulus (x 10^6 psi)	75	27	No Data
	600	26	No Data
Density (lb/in.^{3})	75	0.075	0.075
Mean Coefficient of Expansion (in./in./F° x 10^6)	75 to 212	9.1	No Data
	75 to 600	9.8	No Data
Thermal Conductivity (Btu/in./ft^2/F°-hr)	75	1476	No Data
	600	1110	No Data

Annealing Temperature (°F) 950 to 1100°F in vacuum for 24 hours
Melting Range (°F) 1193 to 2175°F

Fabrication properties of Lockalloy are shown in Table 11.

Lockalloy was chosen as an alternate fin material due to the thermal expansion match with Type 304 stainless steel, 9.8 in./in.-F° for Lockalloy and 9.9 in./in.-F° x 10^{-6} for Type 304 stainless steel and because of its high thermal conductivity. In addition, the material possesses a low density, 76% of

TABLE 11

SUMMARY OF FABRICATION PROPERTIES OF LOCKALLOY

Process	Comment
Milling	Similar to aluminum
Drilling	Easy
	Carbide-tipped drills for 125 rms finish
Shearing and Punching	Easy
	No adverse edge effects
Welding	Readily done
TIG	60 to 80% joint efficiency
Electron Beam	80 to 90% joint efficiency
Brazing	Lockalloy to Lockalloy and Lockalloy to beryllium with BAl-Si4
Riveting	Readily done
Single Lap Joints	Slightly more efficient than aluminum
Double Lap Joints	Slightly less efficient than aluminum
Formability	Difficult
	Minimum bend radii, 10 to 12T, formed at 550°F

the density of 3003 aluminum, and has the same solidus temperature as 3003 aluminum.

C. PERFORMANCE TRADES

1. Performance Requirements

The following end-of-life (EOL) criteria were used for the initial 5-kwe system Lockalloy radiator design analyses. The initial radiator design was based on these criteria. As the program progressed, performance requirement changes led to a final reference design which is described in Section VI-E.

a. Configuration

The configuration is a combination right cylinder topped by a frustum right circular cone.

b. Size

The surface available for radiating heat to space is 273.2 ft^2. The outside diameter at the large end of the conical section and the diameter of the cylindrical section is 72 in. The diameter of the small end of the cone is 29.71 in. The axial length of the cone is 141.5 in., while the length of the cylinder is 72.9 in.

c. Power Rejected

The power rejection capability of the radiator system is to be 92.9 kwt at end of life. This amount of power rejection capability is the aggregate waste heat from all of the thermoelectric converter modules.

d. Radiator Inlet Temperature

The radiator inlet temperature is 590°F. This temperature was established by the thermoelectric module and electromagnetic pump operating temperatures.

e. Coolant Temperature Difference Through Radiator

The temperature difference between the radiator inlet and outlet coolant is to be 144°F. This delta T is dependent upon the required temperature difference through the reactor and the secondary coolant loop electromagnetic pump operating characteristics.

f. Radiator Surface Solar Absorptivity and Emissivity

In Section III-F, the radiator coating solar absorptivity was shown to increase by approximately 50% during simulated solar exposure. The initial solar absorptivity was 0.3 and the final value was approximately 0.45. It was also shown that the coating thermal emissivity will increase to approximately 0.91.

The values of solar absorptivity, $\alpha_s = 0.5$, and emissivity, $\epsilon = 0.9$, were used as the initial values in this analysis to be conservative.

g. Environmental Heat Input

A 600 n. mi constant sunshade polar orbit was used to determine the environmental heat input to the radiator surface in space. This orbital attitude is considered to provide the maximum environmental thermal flux to the radiator surface from direct solar, direct earth, and earth-reflected sources totalling 146, 13.8, and 9.5 Btu/ft^2-hr, respectively. In this analysis, the radiator surface was assumed to be revolving around its axis at 3 revolutions/min.

Using these input parameters with $\alpha_s = 0.5$ and $\epsilon = 0.90$, the environmental heat flux absorbed by the radiator fin is 102 Btu/ft^2-hr. This absorbed heat flux represents a total average environmental heat input to the 273.2ft^2 radiator of 8.16 kwt.

The 5-kwe reactor system radiator performance requirements used in the optimization of the Lockalloy-38 radiator for 92.9-kwt power rejection were summarized in Table 8.

2. Meteoroid Armor Requirements

The method used for calculating the meteoroid armor requirements is described in detail in the Appendix of this report.

The cratering coefficients, γ_R, and the rear surface damage factors, a, in the meteoroid armor equation vary for different armor materials and as a function of temperature. The method used to calculate the cratering coefficient of Lockalloy 38 is shown below:

The cratering coefficient of Lockalloy 38 was obtained by composition weighting the coefficients of Be and Al.

$$\gamma_R \text{ for Be} = 2.28^{(8)}$$

$$\gamma_R \text{ for Al} = 1.70^{(9)} \quad ;$$

therefore, for Lockalloy,

$$\gamma_R = 0.62(2.28) + 0.38(1.70) = 2.06$$

The value of a, used for the asymmetric fin-tube radiator cross section, was 0.9.

The armor equation was used to determine the required thickness of Lockalloy armor that must be provided to protect the front side of the thermal radiator coolant tubes. Figure 68 shows Lockalloy armor thickness as a function of

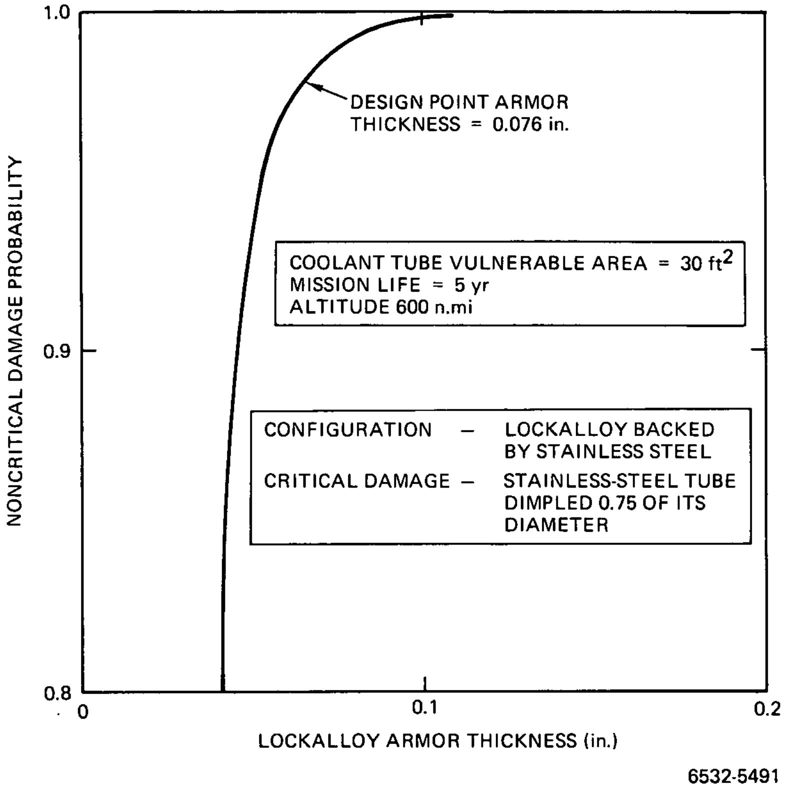

Figure 68. Lockalloy Armor Thickness vs Noncritical Damage Probability

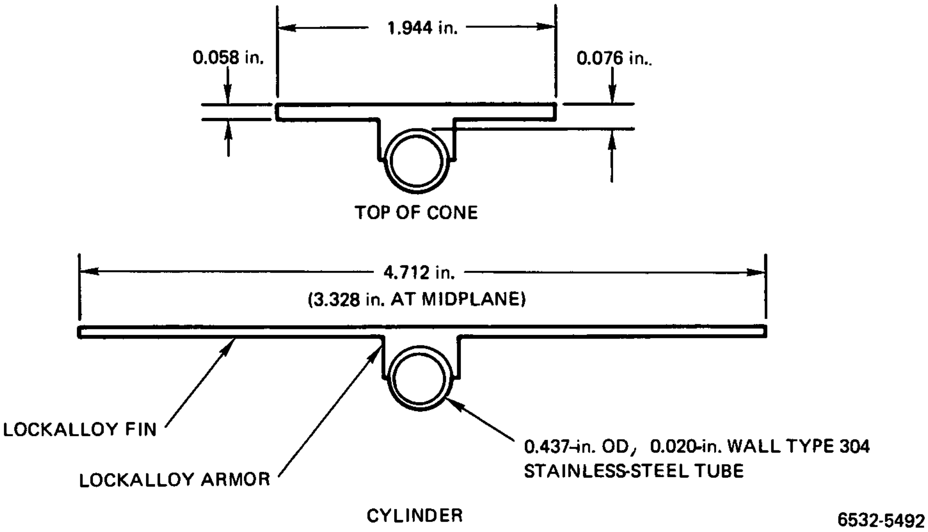

Figure 69. Constant Lockalloy Fin and Tube Cross Section

the noncritical damage probability. The critical event for these calculations was a 0.99 probability of not receiving a 0.75 dimple of the coolant tube during the 5-year mission lifetime. As shown in Figure 68, a 0.076-in. thickness of Lockalloy will be required. This must be the total material thickness between the outer edge of the coolant tubes and the outer surface of the radiator fin.

Figure 69 illustrates the typical location and dimensions of the meteoroid armor relative to the initial Lockalloy radiator fin and tube cross section.

Secondary armor must be provided to protect the interior surfaces of the radiator piping from fragments of primary meteoroid impacts. The mechanisms of secondary impact and the method used to calculate the amount of armor required to protect the system from this type of damage are also discussed in the Appendix.

Figure 70 gives the single plate stainless-steel thickness and the secondary armor thickness requirements for a 30 ft^2 vulnerable area as functions of the noncritical damage probability. The critical event for these calculations was also a 0.99 probability of not receiving a 0.75 dimple. This critical event was used since most of the internal system components are composed of piping. These components have a stainless-steel wall thickness of at least 0.020 in. A secondary armor thickness of 0.020 in. provides a noncritical damage probability of 0.998 when the 0.25 t_p relation is used as discussed in the Appendix.

It was therefore concluded that the coolant tube wall thickness and the internal component material thickness will provide sufficient protection from secondary meteoroid impacts.

3. Design Optimization

Based upon a reference armor thickness of 0.076 in., a study was made to determine the characteristics of the Lockalloy radiator fin cross section. The 5-kwe reactor system radiator performance requirements used in this optimization were given in Section IV-C-1.

This analysis was made for the asymmetric tapered and constant fin-tube cross sections. A D-shaped coolant tube made of Type 304L stainless-steel seamless tubing was used as the reference coolant tube design for the Lockalloy

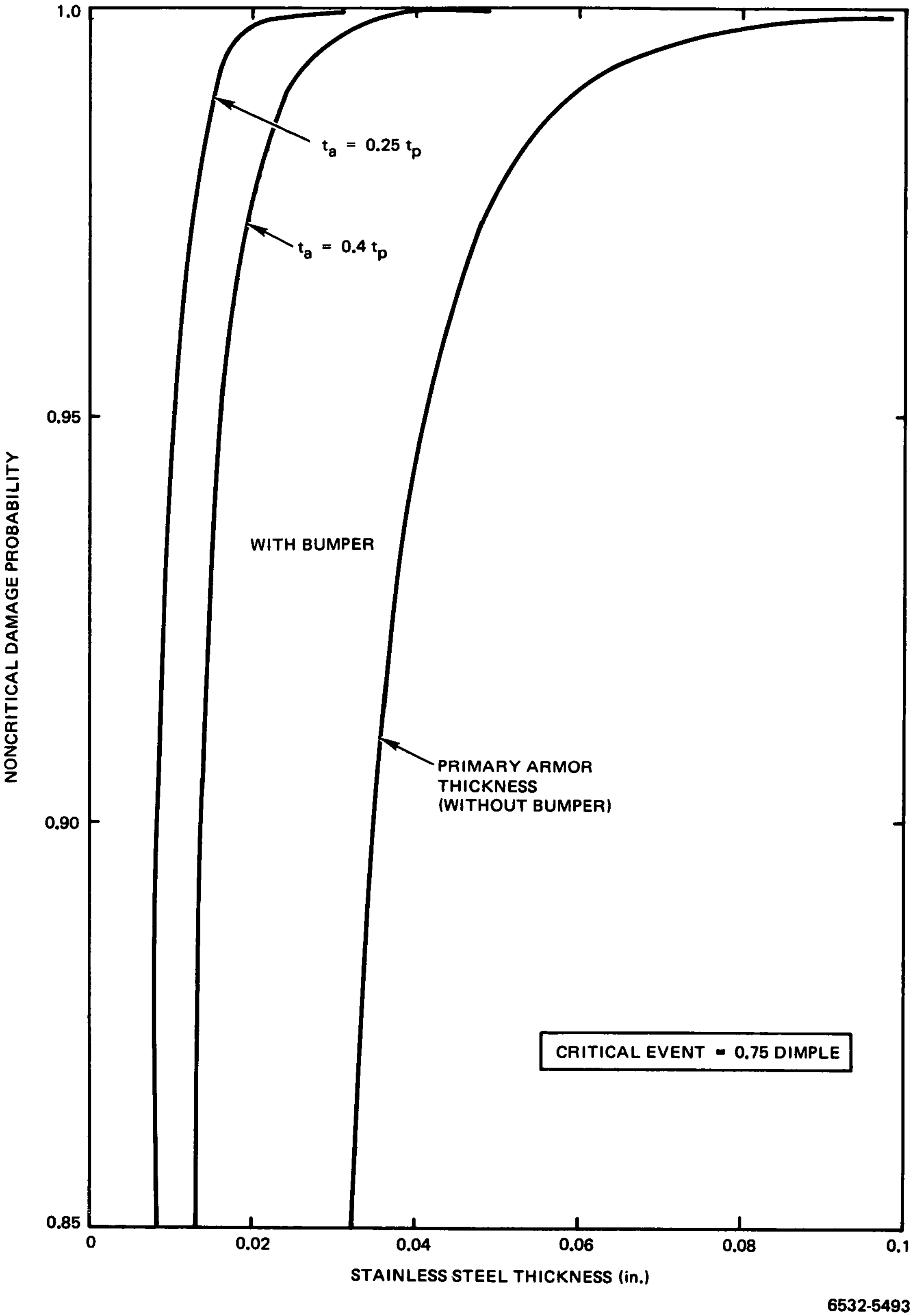

Figure 70. Coolant Tube Backside Armor Requirements

radiator. The coolant tube has a D-shaped cross section. This tube has the same midcircumference as the 0.4375-in. OD, 0.020-in.-wall, stainless-steel tubing that was used in the analysis of other radiator designs. The D-shaped coolant tube shown in Figure 66(4) is bonded directly to the lower flat surface of the Lockalloy fin. This method of attachment eliminates the need for the saddle-shaped groove that was used in other asymmetric radiator designs and lowers the radiator system weight approximately 23 lb.

The thermal conductivity for the Lockalloy 38 fin material varies as a function of temperature as shown in Figure 71. The dashed trace in Figure 71 illustrates the linear fit used in the radiator computer code.

The general radiator structure configuration is shown in Figure 1. This configuration consists of a conical radiator section and a cylindrical radiator section with a combined area of 273.2 ft^2.

Figures 72 and 73 present the results of the calculations using the tapered fin-tube cross section. Figure 72 shows the total radiator system weight and fin root thickness as functions of the number of coolant tubes. The minimum fin thickness for these cases was 0.020 in. From the results shown in Figure 72, 48 coolant tubes were chosen as the design value for the tapered radiator fin. The tapered asymmetric radiator fin using 48 coolant tubes has a maximum fin thickness of 0.094 in. and a total radiator system weight of approximately 468 lb.

Figure 73 shows the typical asymmetric tapered fin cross section using 48 coolant tubes.

Due to the high cost of fabricating the tapered fin cross section, as will be discussed in Section VI-I, the constant fin configuration was used as the initial Lockalloy radiator design.

The optimization study of the constant fin Lockalloy radiator was based upon a range of the number of coolant tubes from 44 to 50. This range of the number of coolant tubes was used for the following reasons:

1) Total radiator system weight increase if fewer than 44 coolant tubes are used.

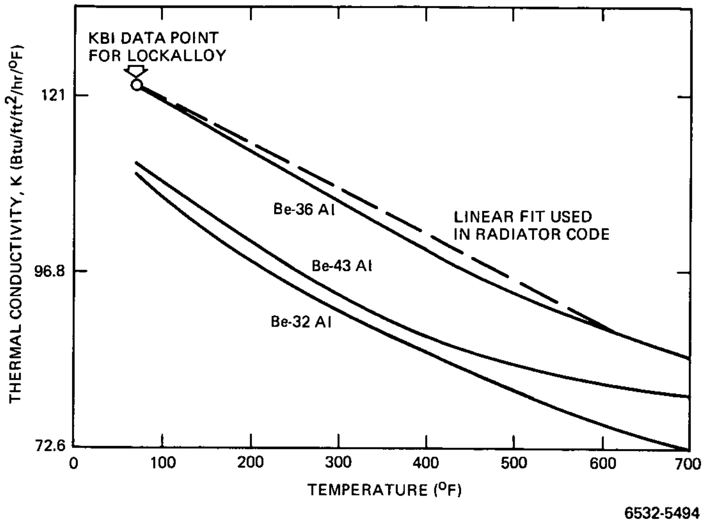

Figure 71.
Thermal Conductivity of Beryllium-Aluminum Composite vs Temperature

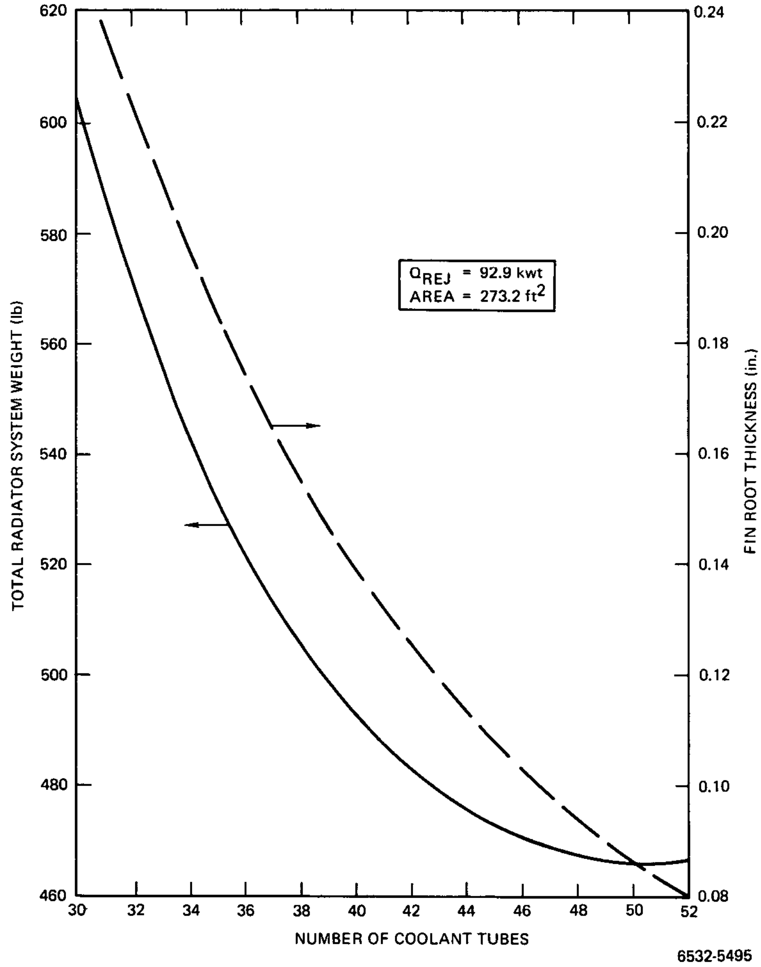

Figure 72. Tapered Lockalloy 38 Fin, Radiator System Weight and Fin Root Thickness vs Number of Coolant Tubes

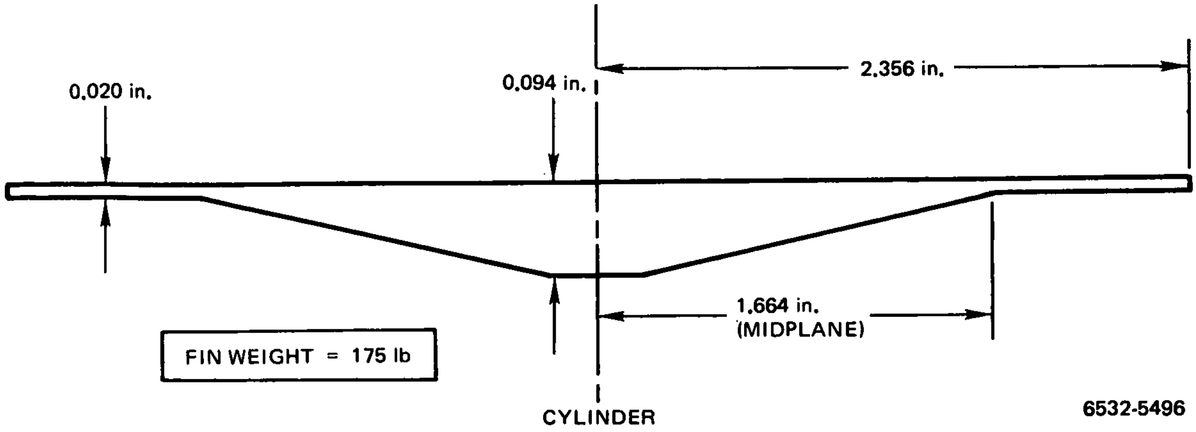

Figure 73. Asymmetric Tapered Lockalloy Fin Cross Section

2) If more than 50 coolant tubes are used, the tube spacing at the top of the conical radiator section is less than the 1.86 in. required for machine welding.

Figure 74 shows the total power rejected from the radiator as a function of constant fin thickness for 44, 46, 48, and 50 coolant tubes. The total power rejected for a given number of coolant tubes increases with increasing fin thickness. The dashed line in Figure 74 designates the required power rejection of 92.9 kwt. The required constant fin thickness, as determined by thermal performance, and the required meteoroid armor thickness for the various numbers of coolant tubes are shown in Table 12.

TABLE 12

CONSTANT FIN THICKNESS AND METEOROID ARMOR THICKNESS REQUIREMENTS

Number of Coolant Tubes	Constant Fin Thickness (in.)	Meteoroid Armor Thickness (in.)
44	0.069	0.074
46	0.063	0.075
48	0.058	0.076
50	0.053	0.077

Figure 75 illustrates the total radiator system weight as a function of constant fin thickness for the number of coolant tubes considered. The dashed line in Figure 75 shows the configuration for each number of coolant tubes that will reject the required 92.9 kwt.

Figure 76 shows the constant fin thickness and total radiator system weight as functions of the number of coolant tubes for those radiator designs that will reject 92.9 kwt. From Figure 76 it can be seen that any of the number of coolant tubes considered may be used with a large weight penalty. Forty-eight coolant tubes were chosen as the reference value to obtain four-quadrant symmetry in the reactor design.

As shown in Figure 76 the radiator using 48 coolant tubes has a constant fin thickness of 0.058 in. An additional thickness of Lockalloy of 0.018 in.

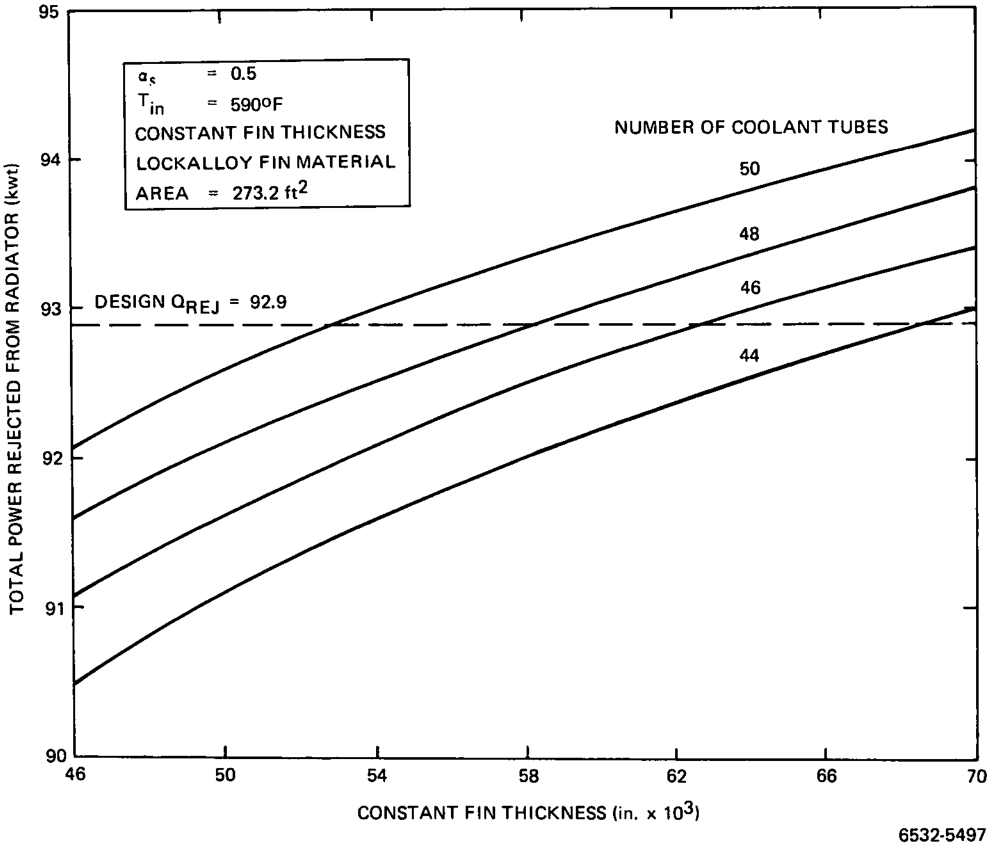

Figure 74. Radiator Power Rejected vs Constant Radiator Fin Thickness

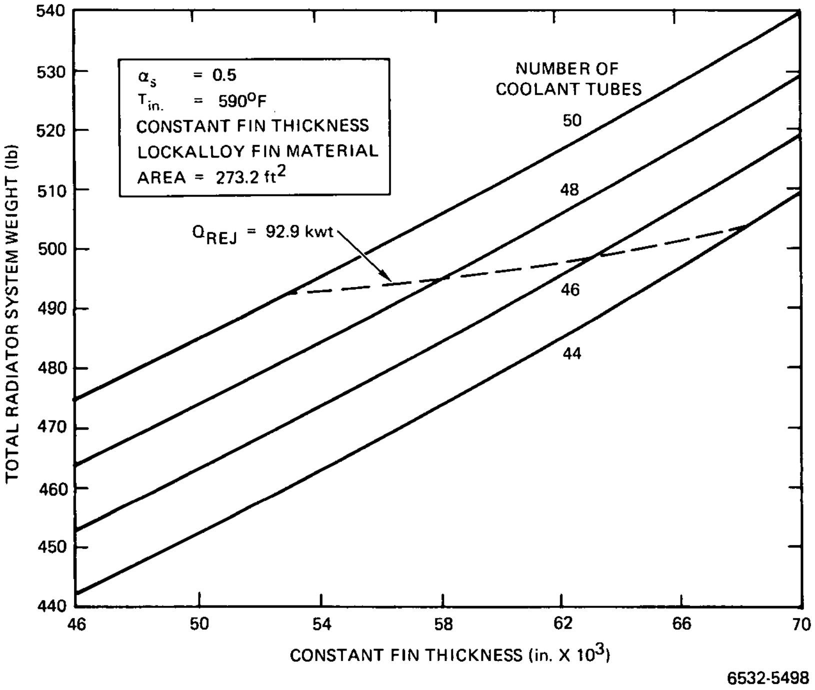

Figure 75. Total Radiator System Weight vs Constant Radiator Fin Thickness

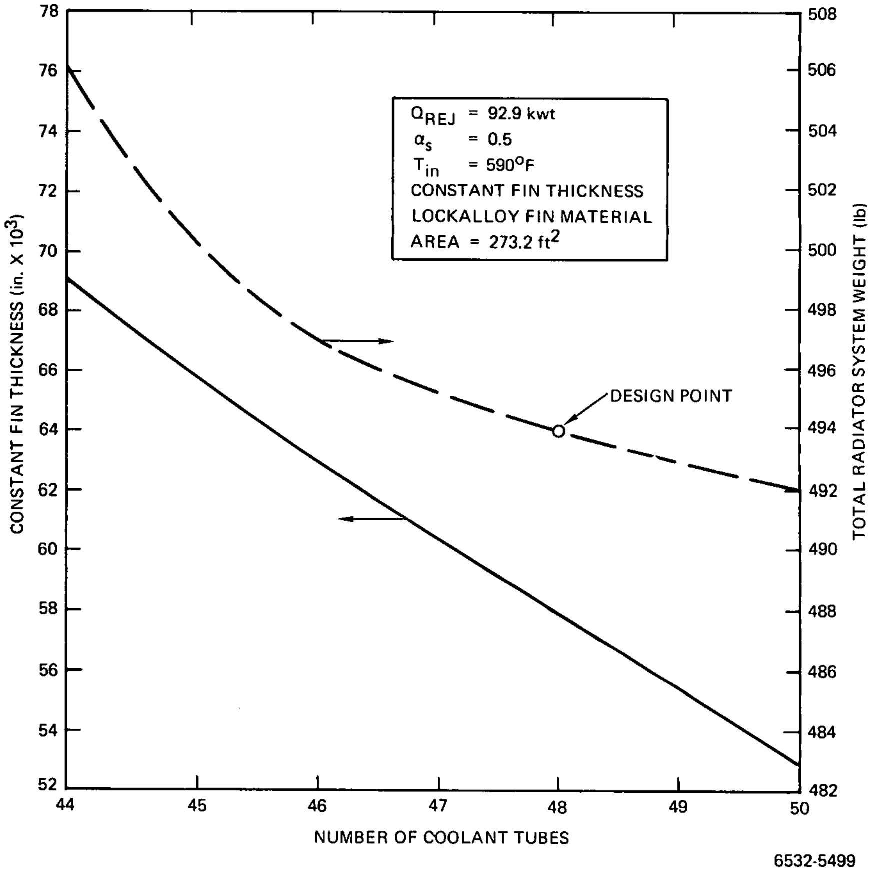

Figure 76. Constant Fin Thickness and Radiator System Weight vs Number of Coolant Tubes

would be required between the coolant tube and the inner surface of the radiator fin to provide sufficient meteoroid armor.

The overall dimensions of the 273.2 ft^2 radiator are given in Table 13.

TABLE 13

OVERALL RADIATOR DIMENSIONS

Minor Diameter (in.)	29.71
Major Diameter (in.)	72
Cone Height (in.)	141.5
Cylinder Height (in.)	72.9
Area (ft^2)	273.2
Coolant Tube OD (in.)	0.4375
Coolant Tube Wall Thickness (in.)	0.020
Coolant Tube Spacing (in.)	
At top of cone	1.944
At cone midplane	3.328
In cylindrical segment	4.712

The detailed fin-tube cross sections in the cylindrical section and at the top of the conical section are shown in Figure 69.

The performance characteristics of the intermediate reference radiator are given in Table 14.

TABLE 14

RADIATOR PERFORMANCE CHARACTERISTICS

Power Rejected (kwt)	92.9
Coolant Temperature Drop (°F)	143.6
Coolant Pressure Drop (psi)	0.199
Coolant Flow Rate (lb/hr)	10368
Average Fin Effectiveness	0.847

The detailed weight breakdown of the intermediate reference radiator system, using Lockalloy 38 as the fin material and Type 316 stainless steel as the support structure material, is given in Table 15.

TABLE 15
RADIATOR WEIGHT BREAKDOWN

Component	Material	Weight
Fin	Lockalloy	172.5
Armor	Lockalloy	24.1
Tube	Type 316 stainless steel	89.8
AI-93	-	15.8
Rings	Type 316 stainless steel	30.4
Saddles	Type 316 stainless steel	4.6
Stringers	Type 316 stainless steel	60.0
Struts	Type 316 stainless steel	1.9
Rivets	Type 316 stainless steel	25.1
Access Panels	Type 316 stainless steel	7.8
Thermal Barrier	-	6.0
Thermal Baffles	Super Insulation	7.1
Pump Support Flange	Type 316 stainless steel	6.0
Coolant	NaK	43.4
Total Radiator System		494.6

D. INITIAL DESIGN LOCKALLOY RADIATOR

There was much similarity in the system appearance when comparing the Lockalloy to the aluminum radiator. Figure 1 is used to illustrate both systems. The basic differences are in the fin and tube panel cross section. Other radiator components, stringers, rings, cone-to-cylinder transition splice, are similar in geometry, but are to be fabricated of stainless steel rather than aluminum.

Figure 77 shows the Lockalloy fin radiator incorporating D tubes (Figure 84). The drawing also shows the fin panel edges spliced to "T" shaped stringers but the final design had the outstanding leg removed. The cold edge joint will be riveted with particular care given to hole sizes, rivet bucking practices and rivet length as defined in Reference 10.

The transition between the cone and cylinder is the most intricate segment of the assembly and is shown on Figure 78. It also is shown with

T stringers; however, "chevron" stringers would have been shown on the latest revision.

Once the brazed fin tube panels have been tapered and pilot drilled, the assembly is relatively straightforward and follows usual aerospace practice.

E. REFERENCE LOCKALLOY RADIATOR THERMAL CHARACTERISTICS

Based upon the meteoroid armor requirements and design optimization study given in Section VI-C, further analysis was undertaken to determine the reference configuration of the Lockalloy 38 radiator. The reference radiator uses 48 D-shaped coolant tubes, and has a constant asymmetric fin and tube cross section.

The performance requirements and dimensions for the reference design radiator are listed in Table 16.

TABLE 16

REFERENCE RADIATOR PERFORMANCE REQUIREMENTS AND DIMENSIONS

Parameter	Reference Radiator Requirements
Performance	
Power Rejected (kwt)	94.9
Inlet Temperature (°F)	611
Coolant Temperature Drop, ΔT (°F)	144.3
Emissivity	0.9
Solar Absorptivity	0.5
Environmental Heat Input (Btu/ft^2-°F)	102
Dimensions	
Area (ft^2)	266.8
Minor Diameter (in.)	30
Major Diameter (in.)	72
Cone Height (in.)	140.6
Cylinder Height (in.)	69.2
Coolant Tube Spacing (in.)	
At top of cone	1.963
At cone midplane	3.338
In cylindrical segment	4.712

Page intentionally left blank

Page intentionally left blank

A constant fin thickness of 0.060 in. would be required to reject the 94.9 kwt. An additional thickness of Lockalloy 38 of 0.015 in. would be needed between the coolant tube and the radiator fin to provide sufficient meteoroid armor. A schematic of the reference asymmetric constant fin and tube cross section is shown in Figure 79.

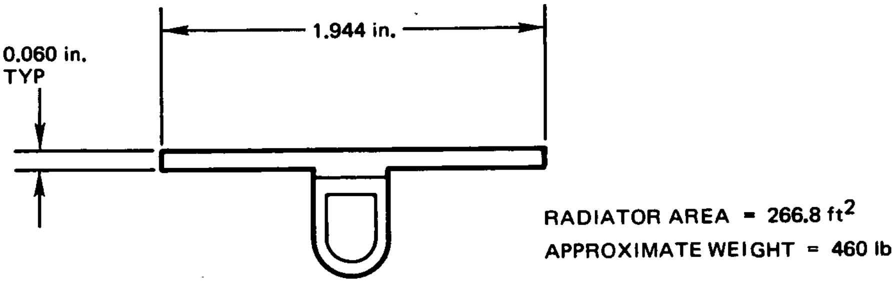

RADIATOR AREA = 266.8 ft^2
APPROXIMATE WEIGHT = 460 lb

TOP OF CONE

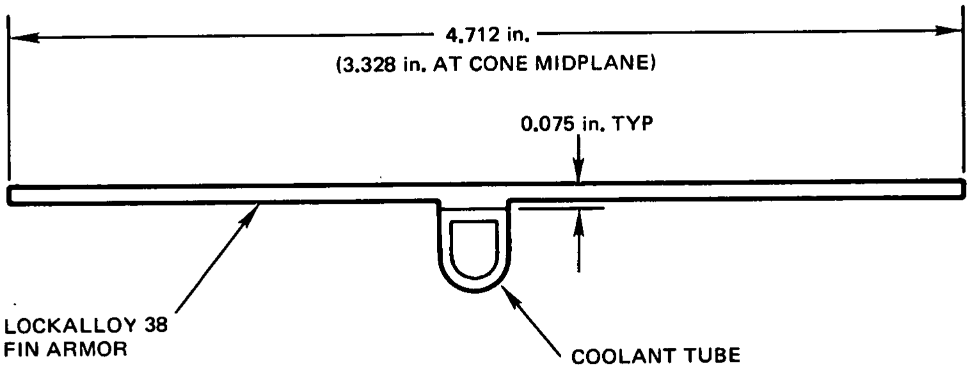

CYLINDER

6532-54100

Figure 79. Reference Constant Thickness Lockalloy 38 Fin and Stainless-Steel Tube Cross Section with D-Shaped Coolant Tubes

The performance characteristics of the reference Lockalloy 38 radiator are 0.20 psi coolant pressure drop, 10,584 lb/hr coolant flow rate, and 0.835 average fin effectiveness.

The detailed weight breakdown of the radiator system using Lockalloy as the fin material and stainless steel as the structural support material is given in Table 17.

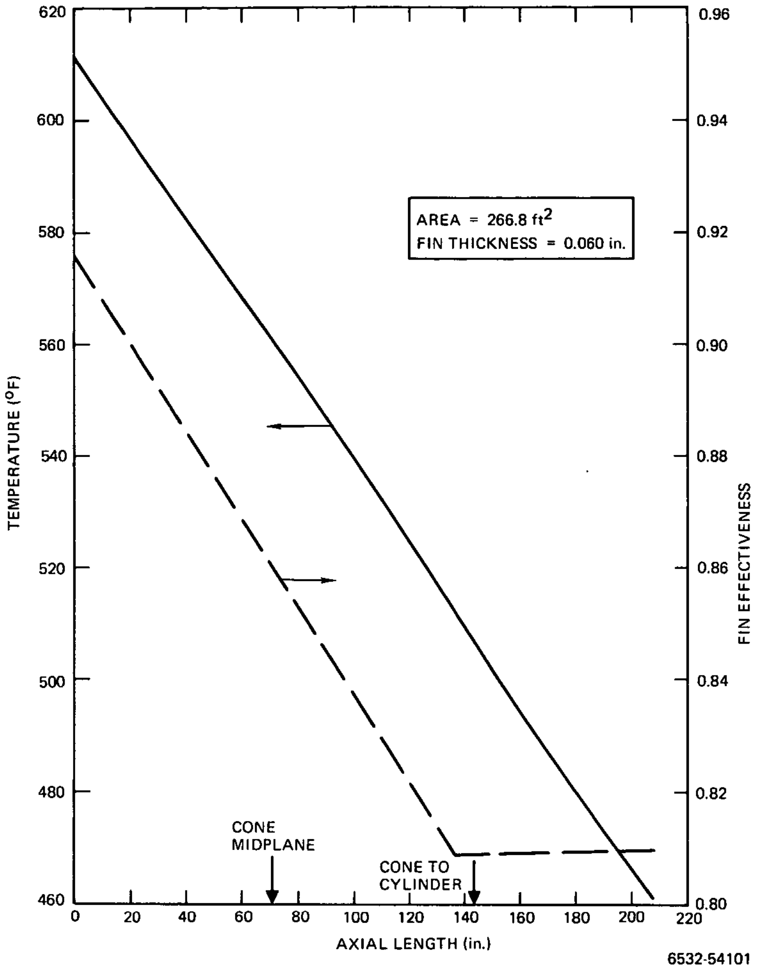

Figure 80.

Temperature and Fin Effectiveness vs Axial Length

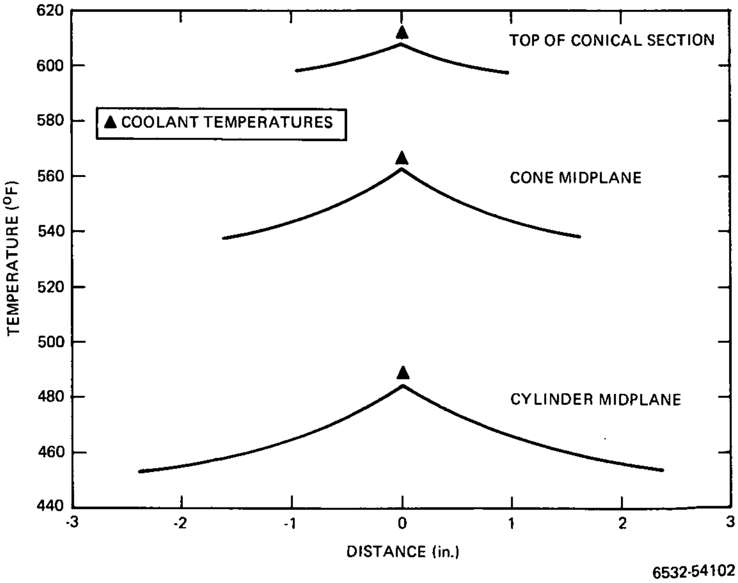

Figure 81.

Lockalloy Radiator Fin Thermal Profiles

TABLE 17

REFERENCE RADIATOR WEIGHT BREAKDOWN

Component	Material	Weight (lb)
Fin-Armor	Lockalloy	179
Tubes and NaK	Type 304 stainless steel	124
AI-93	-	16
Rings and Stringers	Type 316 stainless steel	57
Support Skirt	Type 316 stainless steel	6
Rivets	Type 316 stainless steel	37
Access Panels	Type 316 stainless steel	15
Thermal Baffles	Type 316 stainless steel	7
Pump Support Flange	Type 316 stainless steel	9
Miscellaneous Bracketry	Type 316 stainless steel	10
Total Radiator System		460

The thermal performance characteristics of the reference radiator are shown in Figures 80 and 81. Figure 80 shows the radiator fin root temperature and fin effectiveness as functions of the axial radiator length. The solid trace in Figure 80 illustrates the radiator temperature as a function of axial length. The dashed trace in Figure 80 shows the corresponding fin effectiveness as a function of the axial radiator length.

Figure 81 presents the radiator peripheral thermal profiles at the top of the conical section, at the cone midplane, and at the midplane of the cylindrical portion of the radiator.

F. STRUCTURAL ANALYSIS

The Lockalloy fin with the Type 304 stainless-steel tube has essentially the same loading requirements for launch as did the aluminum. Although there is variation in system dimensions and weights, the load requirements of Section IV-A are applicable to both systems.

While the Lockalloy and stainless steel have nearly equal coefficients of expansion, the system is subjected to both braze cycle and operational thermal stresses. Figure 82 shows the residual stresses after cooling from the braze

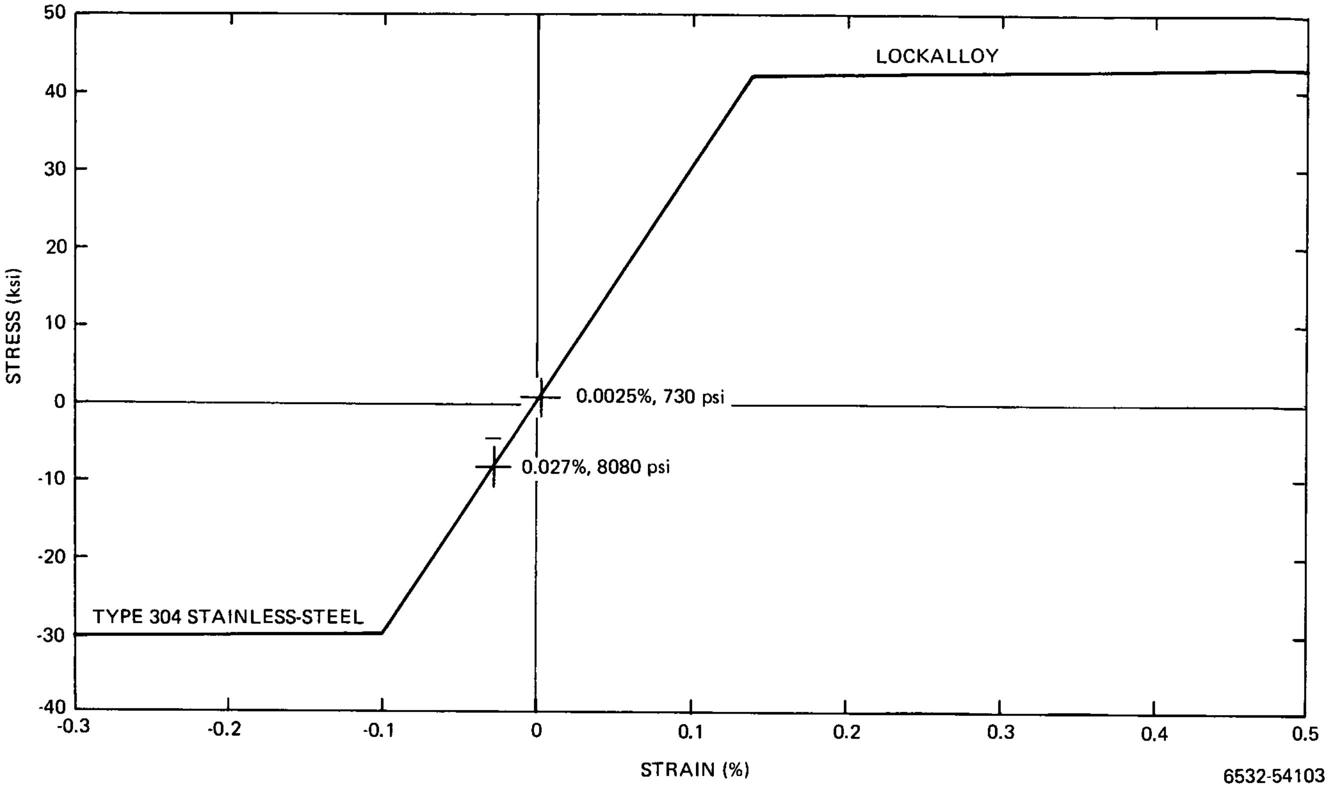

Figure 82. Stress-Strain in Lockalloy — Type 304 Stainless-Steel Composite Cooling from 775°F to Room Temperature

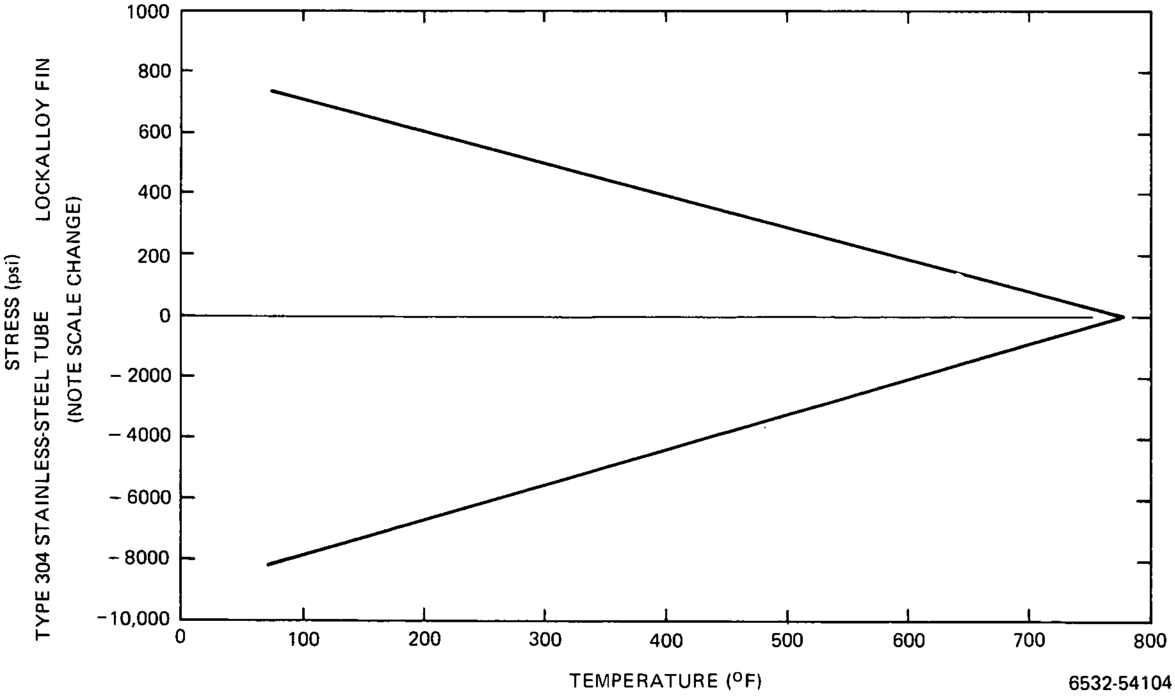

Figure 83. Stress in Lockalloy — Type 304 Stainless-Steel Composite at Temperatures Below Braze "Lockup" (775°F)

lockup temperature assumed to be 775°F. The method of analysis is described in Section V-F-1. From Figure 31, the expansion coefficients are:

$$\alpha_L = 10.15 \times 10^{-6} \text{ in./in./F° (RT to 775°)}$$
$$\alpha_{304} = 9.73 \times 10^{-6} \text{ in./in./F° (RT to 775°).}$$

The differential strain in cooling is 0.029% between the Lockalloy and Type 304 stainless steel. Then with the equations of Section V-F-1, the Lockalloy strains 0.005% or 735 psi, and the tube strains 0.0269% or 8080 psi. These stresses are well below the yield strengths. Note that the analysis is conservative and has not considered any relaxation potential. Figure 82 shows the superposition of these values on the stress-strain curves.

Reheating to temperatures of 450 to 610°F will reduce the stresses. Figure 83 shows the residual stresses for all temperatures below 775°F. At 522°F, which is the average radiator temperature at BOL, the residual stresses are -3400 psi and 310 psi in the tube and fin respectively. These values are typical of the levels on which the 48 θ stresses are superimposed. The 48 θ stresses are based on the temperature gradient between the tube and fin tip as shown in Section IV. Then from Figure 82, given the residual temperature stresses and the method of Section V-F-6, the stresses in the radiator at operational temperature are shown in Table 18.

It is evident that a better understanding of the Lockalloy relaxation characteristics is needed to evaluate these stresses. The most severe stresses are at the colder end of the radiator where relaxation would be at the lowest rate. The combination of the residual stresses (maximum in cold radiator) with the 48 θ stresses (maximum with widest fin) does not appear critical.

The mechanical capacity of the Lockalloy system was more than adequate for the saddle configurations of Figure 66. The critical load for the cross section exceeded launch loads by more than 2.0 at all stations. Since the critical load of the cross section is based on the moment of inertia:

$$P_{cr} = \frac{\pi^2 EI}{L^2} \quad ,$$

TABLE 18
OPERATIONAL STRESSES – LOCKALLOY RADIATOR

Location	Operating Temperature (°F)			Residual Stress (psi)		α (in./in.-°F)	E (psi)	Operation Stress (psi)			Total Stress (psi)		
	Average	Hot End	Cold End	Fin	Tube			Fin Hot	Fin Cold	Tube	Fin Hot	Fin Cold	Tube
Top of Cone	585	588	578	200	-2200	9.8×10^{-6}	27×10^{6}	-795	1850	-795	-595	2050	-2995
Mid-Cone	533	540	520	260	-2800	9.65	28.5	-2026	3763	-2030	-1770	4020	-4830
Mid-Cylinder	455	465	435	340	-3750	9.5	30	-2850	5700	-2850	-2510	6040	-6400

the capacity became much less than the applied loads when the D tube configuration was adapted. The moment of inertia reduced with the removal of the saddle and when the out-of-plane dimensions decreased.

The deficiency could be corrected by increasing the moment of inertia and/or decreasing the ring spacing. The latter has the undesirable effect of increasing the system weight due to the need for additional rings (frames). It is desirable to maintain a ring spacing as great as practical but not exceeding 24 in. Although cross-rolled Lockalloy was not established as the radiator fin material, it was a strong candidate with extruded Lockalloy and plain-rolled Lockalloy as cost-conscious alternates.

The moment of inertia is increased by increasing the y dimension in the relationship.

$$I = \int y^2 \, dA \quad .$$

For the D tube configuration, this is given schematically in Figure 84, and is accomplished by increasing the ratio H/W of the D tube. The tube mid-perimeter

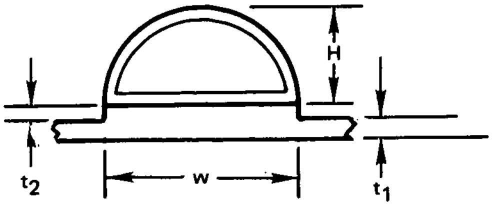

Figure 84. D Tube Dimension Parametrics

was established as being equal to that of a 7/16-in. OD by 0.020-in.-round tube. The fin thickness (t_1) was established at 0.060 in. (Ref. Section VI-E), and the armor thickness (t_2) at 0.015 in.

The applied loads are shown on Figures 9 (lb/in.) and 10 (lb) and in Table 3. The column relationship:

$$P_{cr} = \frac{\pi^2 EI}{L^2}$$

can be rearranged to show the required moment of inertia for a given frame spacing and load.

$$I_{rqd} = PL^2/\pi^2 E$$

Figure 85 shows the moment of inertia requirements for the loads of Figure 8 as a function of frame spacings. The I required at the base with 24-in. frame spacing is 0.00226 in.^{4} From Figure 86, it can be seen that the cross section with a tube width of 0.30 in. and height of 0.46 in. provides 0.000227 in.^{4} moment of inertia. This cross section is recommended. At Stations 0.0 to 62.0, frame spacing will not exceed 23 in. Thus the requirement is closer to 0.0021 in.^{4} There will also be some additional stiffness provided by the panel splice which will have a chevron configuration. Then the margin of safety will be adequate to meet the launch requirements.

G. LOCKALLOY FRACTURE TOUGHNESS

With beryllium as one of Lockalloy's constituent materials, it is natural to be concerned about the crack propagation of Lockalloy. Beryllium was notorious for its characteristic cracking at riveted joints and for its high notch sensitivity. These were primarily the reasons for the development of Lockalloy.

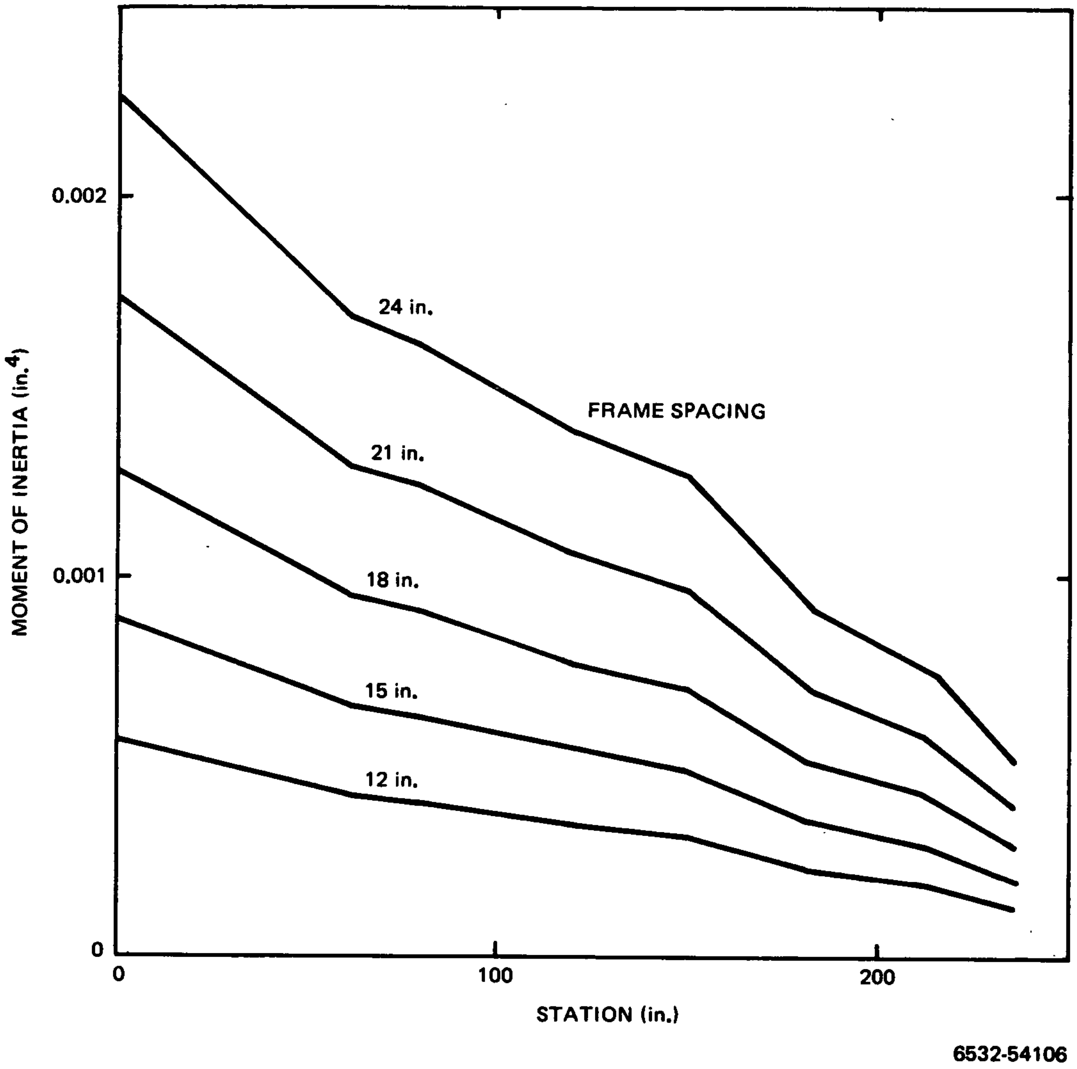

Figure 85. Moment of Inertia Required for Loads Shown in Figure 8

The combination of ductile aluminum with beryllium was to provide a material having properties intermediate between the two. The notch sensitivity and resistance to crack propagation is significantly improved over that of beryllium but not as good as that of aluminum. With the limited data available on Lockalloy, the following will show its ability to sustain the imposed mechanical loading without crack propagation.

G

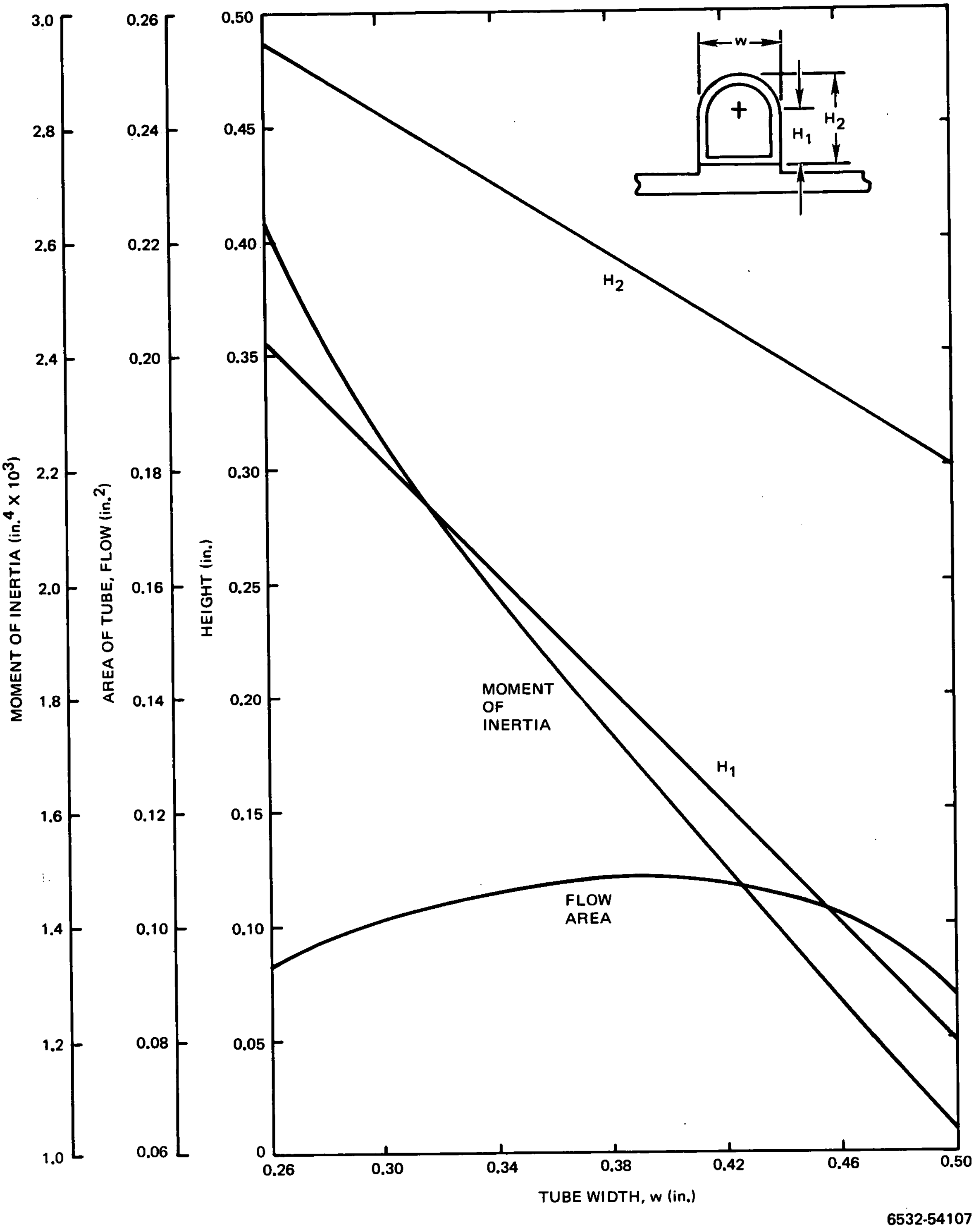

Figure 86. Tube and Fin Geometric Properties

The tensile failure crack propagation is characterized by the K_{Ic} value and the in plane shear by K_{II_c}. Out of plane shear is represented by K_{III_c}. K_{I_c} is always the lowest of the three and consequently the most frequently available. K_{I_c} for the transverse direction of extruded Lockalloy is 18,000 psi-in.^{2} and is the lowest value of K_c for any direction and any form of Lockalloy. This value will be used for the tensile crack evaluation. It is assumed that the K_{II_c} value is 25,000 psi-in.^{2}

The relationship between crack size, stress field, and the material resistance to crack propagation is expressed by:

$$K_{I_c} = \sigma_c \sqrt{\pi a_c}$$

where

σ_c = Critical stress

K_{I_c} - Material characteristic

a_c = 1/2 crack or inclusion diameter.

Stresses greater than σ_c will induce propagation of the crack. Conversely, stresses less than σ_c are safely handled by the material without propagation. Figure 87 shows the relationship between crack, hole, or inclusion diameter (2 a_c) and the allowable stress field below which there will not be propagation. The yield strength (42,000 psi) is the cutoff value. Note that at the yield stress, the hole size can be 0.11 in. diameter; at 20,000 psi, 0.5 in. diameter; 10,000 psi, 1.95 in. diameter, etc. Thus, it appears that Lockalloy is relatively resistant to crack propagation in a tension field.

There has been concern with respect to the possbility of "zippering" failure along a line of rivets. The following relationship is used in this evaluation.

$$K_{II_c} = \tau(\pi a)^{1/2}\left(\frac{2b}{\pi a} \tan \frac{\pi a}{2b}\right)^{1/2}$$

where

τ = Shear stress field

2b = Rivet spacing

2a = Rivet diameter

K_{II_c} = Material characteristic.

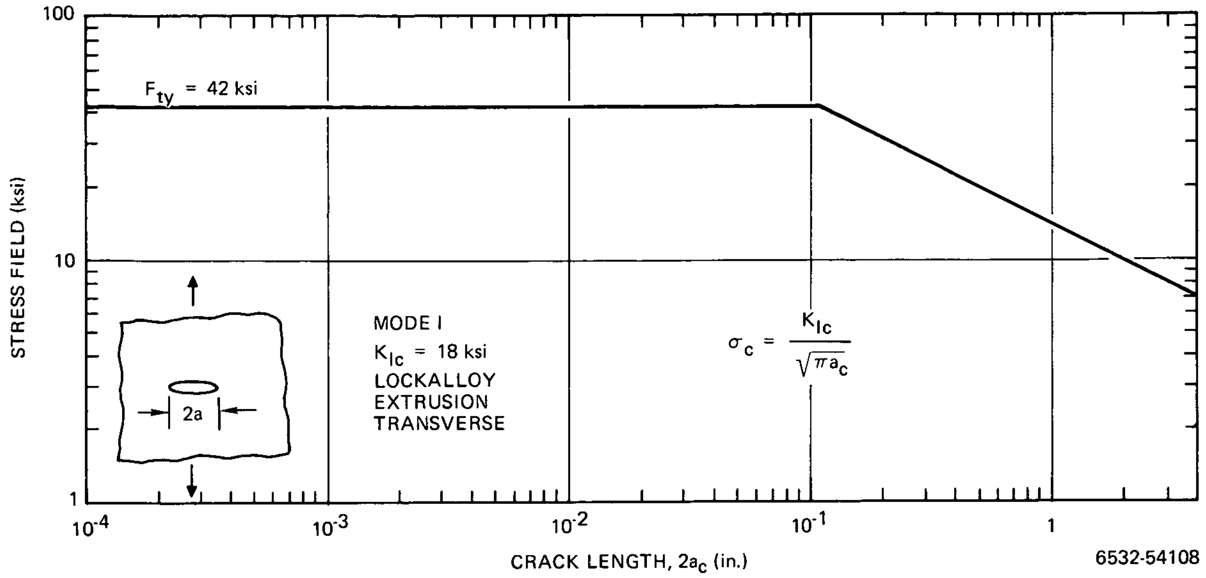

Figure 87. Crack Propagation in Lockalloy in Tension

The rivet spacing and rivet diameter have not been established. From the table of panel loads (Table 3), maximum shear flow is 45.2 lb/in., the maximum panel tensile load is 102.3 lb/in. and the maximum panel compressive load is 221.9 lb/in. It is evident, then, that the rivet diameter will be between 3/32 and 3/16 in., and that the spacing will be between 0.625 and 1.000 in. center to center. Figure 88 shows the allowable shear stress field for these rivet sizes and spacings based on the above relationship. It is clear that shear stress fields below 44,000 psi can be tolerated. The actual shear stress will be:

$$\tau = \frac{q}{t} ,$$

where

τ = Shear stress

q = Shear flow

t = Material thickness.

The maximum shear flow is 45.2 lb/in., and the thickness range will be 0.040 to 0.070 in. at the rivets. Then, the maximum shear stress will be 646.0 to 1130.0 psi, very much below the critical level for propagation.

It is evident that operational stresses will not offer problems associated with rivet holes, potential cracks, or inclusions.

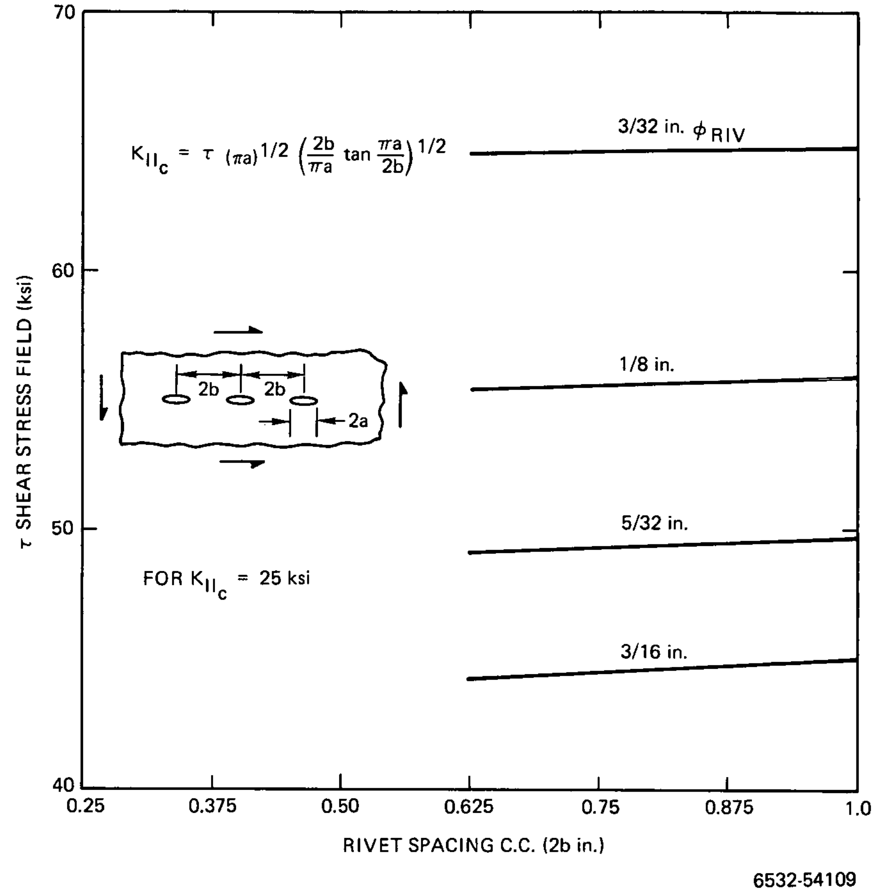

Figure 88. Allowable Shear Stress vs Rivet Spacing

Previous industry experience with Lockalloy has shown that care must be taken in the joining. From Reference 10, it is recommended that rivets should be centered at least 2.5 diameters from the nearest edge. Other recommendations are directed to maintaining minimum interference between the shank and the riveted material.

With careful joining and with the relatively lenient requirements on stress fields around rivet holes, inherent cracks, and inclusions, Lockalloy is considered to be acceptable material from the standpoint of fracture toughness.

H. FABRICATION STATUS

An order for Lockalloy was placed with the sole source, Kawecki Berylco Industries, Inc. (KBI) for fin members with a center saddle (Figure 89) for brazing the stainless-steel tubing and acting as micrometeoroid armor, and flat fin stock, Figure 90, to which a D-shaped, stainless-steel tube could be

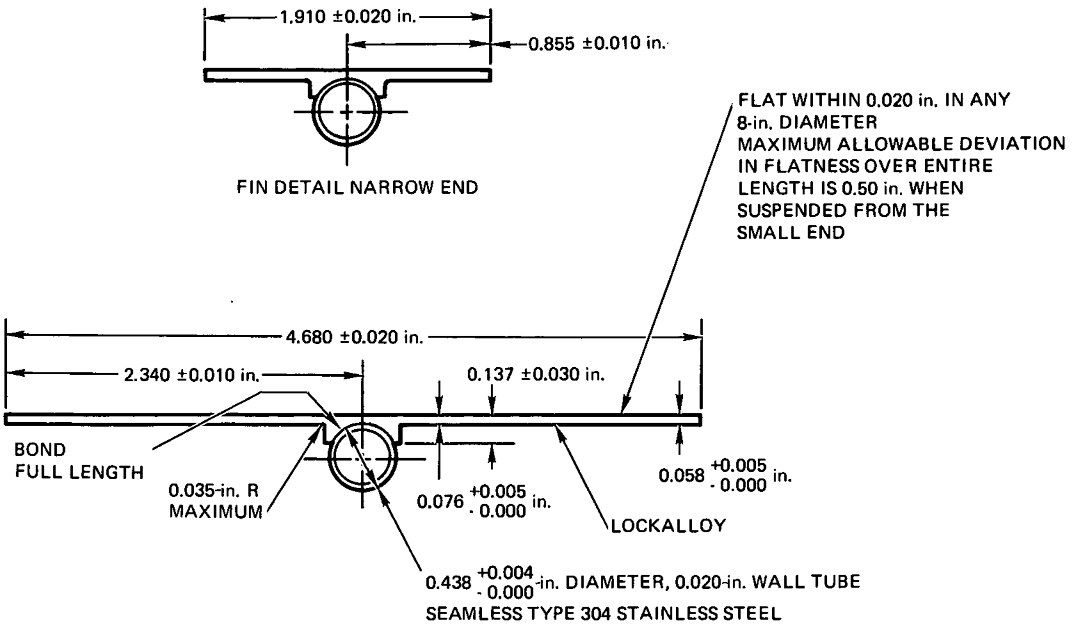

FIN DETAIL NARROW END

FIN DETAIL WIDE END

6532-54110

Figure 89. Fin Detail Wide End Reference Construction

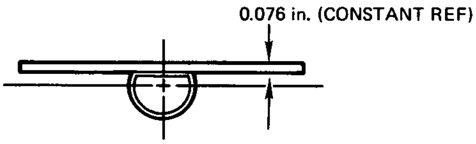

FIN DETAIL NARROW END

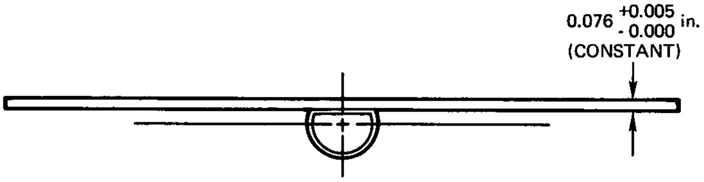

FIN CONSTRUCTION ALTERNATE 2
DIMENSION AND GEOMETRIC
CONTROLS IDENTICAL TO
ALTERNATE 1 EXCEPT AS NOTED

FIN DETAIL WIDE END

6532-54111

Figure 90. Fin Construction Alternate 2

brazed. KBI originally felt that lengthwise rolling, only, might increase the transverse ductility of the extruded material. An experimental rolling proved this to be untrue. There was no improvement in the transverse ductility. A decision was therefore made to use as-extruded material. Cross rolling could not be accomplished at KBI since their widest mill was 60 in. and the fin material was needed in finished 12-ft lengths.

Lockalloy is difficult to extrude and, to obtain flat surfaces, an as-extruded piece must be surface ground. Losses from the surface grinding normally amount of 0.010 to 0.015 in. in depth per surface. Furthermore, in the saddle design, the Lockalloy must be machined away from each side of the saddle since an extrusion to shape could not be accomplished within the framework of existing technology. Stock with a rectangular cross section could be extruded with subsequent milling to shape.

The initial purchase of Lockalloy was two pieces of extruded stock available at KBI which were 3 ft long and had a cross section of 0.3 in. by 1 in. This material was used for all of the brazing studies conducted at Atomics International.

1. Brazing Studies

a. Braze Alloy Selection

The fin-to-tube bond must have adequate initial strength, thermal conductivity, and stability. To achieve this, primary requirements for a braze alloy are:

1) The braze alloy must wet the surfaces to be joined;

2) The braze liquidus temperature must be less than the substrate melting temperature (1193°F);

3) The braze free-flow temperature must be less than the substrate melting temperature;

4) The molten braze must not erode the substrate excessively at the brazing temperature;

5) The unaged braze alloy must have good ductility in shear and under uniaxial and biaxial loading;

6) Aging must not harm the braze alloy, whether by development of Kirkendall voids, brittle intermetallics, gross dimensional instability,

crack propagation, or other defect, over the lifetime of 44,000 hours at 600°F with intermittent return to ambient;

7) The solidus temperature of the braze alloy or of any constituents of the braze alloy in interaction with any constituents of the substrate must be well above the 600°F operating temperature;

8) The diffusion rate of any braze or substrate constituent that might contribute to Kirkendall void or brittle phase development must be low at all operating temperatures;

9) The diffusion rate of any constituent leading to undesirable local composition effects must be low at the brazing temperature;

10) The braze alloy and the brazed component must have reasonable corrosion resistance both under operating conditions and under system assembly, storage, and test conditions;

11) Braze joint soundness must be easily determinable by standard nondestructive testing techniques and/or that in-batch reproducibility be sufficiently high that small-workload-fraction destructive analyses are permissible; and

12) The braze alloy must be brazeable by economically practicable techniques.

Examination of binary and ternary phase diagrams yields the potential aluminum alloy systems listed in Table 19, all with solidus temperatures below the melting point of aluminum. Further examination reveals the following deficiencies: (1) the literature reports brittleness and poor corrosion resistance for at least some of the Ag-Al alloys; (2) Al-Ca and Al-Th alloys are also expected to have poor corrosion resistance; and (3) the vapor pressures of calcium, magnesium, zinc and tellurium are excessive. Literature for the other alloy systems was examined, but except for Al-Si, there was apparently no wide spread use of any composition with the wanted 1040 to 1150°F solidus-liquidus range.

Examination of authoritative sources(11,12) and articles on brazing indicated only a few silver base brazing alloys (most containing undesirable cadmium and zinc), and a few aluminum-silicon brazing alloys (BAl-Si3 and BAl-Si4) and

TABLE 19

MELTING POINTS OF SELECTED ALUMINUM BINARY ALLOY EUTECTICS

Binary	Eutectic Composition (wt % Al)	Solidus (°C)
Ag-Al	28	558
Al-Au	3.92	525
Al-Ca	~28	545
Al-Ge	~45	423
Al-Cu	67.0	548
Al-Mg	~65	450
	~35	437
Al-Si	~88	577
Al-Zr	~5	382
Al-Te	~96	621
Al-Th	~76	~620
Al-Be	~98.5	644
(Al)		(660.2)

several aluminum casting alloys (Al + Mg, Cu, and/or Si) with solidus-liquidus temperatures in the nominal 1040 to 1150°F range and flow points of 1200°F or below.

b. Stainless-Steel Surface Conditioning

Aluminum is known to form undesirable embrittling intermetallic compounds with the iron in the stainless steel at operating temperatures. A titanium layer has been used effectively as an intermediate layer, but silicon tends to alloy with it, attacking the titanium severely, so that fabricators place a layer of silicon-free aluminum between the titanium layer and the BAl-Si4 braze.

In the preliminary tests performed at Atomics International, electron beam heating evaporation was employed to coat the cleaned stainless-steel joint surfaces with a nominal 0.001-in. layer of titanium. This coating method permitted very careful control of the substrate temperature (nominal 1450°F) and good bonding between the stainless-steel substrate and the titanium (at the nominal 10^{-5} torr chamber pressure). Some of the as-titanium-coated, stainless-steel surfaces were immediately coated with a 1- to 5-mil-thick layer of evaporated aluminum (Figure 91), with no pause and without breaking the chamber vacuum. With this technique, the fresh titanium surface was chemically active, and the aluminum bonded to it very well.

c. Test Sample Surface Cleaning

Careful, thorough pre-cleaning of specimen surfaces was very important in making consistently sound brazed joints between surfaces incorporating easily oxidized, chemically active elements such as aluminum, beryllium, and chromium. Specimen components were cleaned within 4 hours of vacuum brazing or vacuum encapsulation. The cleaning at AI was by a 1-min immersion of individual pieces in a 15% HNO_3, 3% HF bath at 130°F ± 10°F, followed by ultrasonic cleaning in distilled water, and acetone and alcohol rinsing.

d. Brazing Study Results

Initial brazing studies were conducted on 1100 aluminum in order to conserve the small quantity of Lockalloy which was available to the program. In some cases, the coupons consisted of 1100 aluminum brazed to Lockalloy so that the interaction between the BAl-Si4 braze and the two materials could be observed. Due to the cancellation of the program shortly after the initiation of the braze studies, only cursory results are available.

A preliminary test was run on a braze consisting of a Ag-Cu-Sn eutectic composition (54Ag-21Cu-25Sn). The composition was not commercially available, so a small melt was prepared. The material was so brittle at room temperature that it was impossible to prepare a foil for a braze test. Therefore, a combination of two foils was used that would give the proper composition during the brazing operation. The results of this test may be seen in Figure 92. It appeared that a considerable amount of tin diffused into the Lockalloy, as noted in the 19X photomicrograph, but a satisfactory bond was still achieved. Obviously the technique would be unsatisfactory from both a production and diffusion standpoint. At this point in the program, the decision was made to abandon all braze materials but BAl-Si4, due to the fact that all commercial brazing of Lockalloy had been done with BAl-Si4.

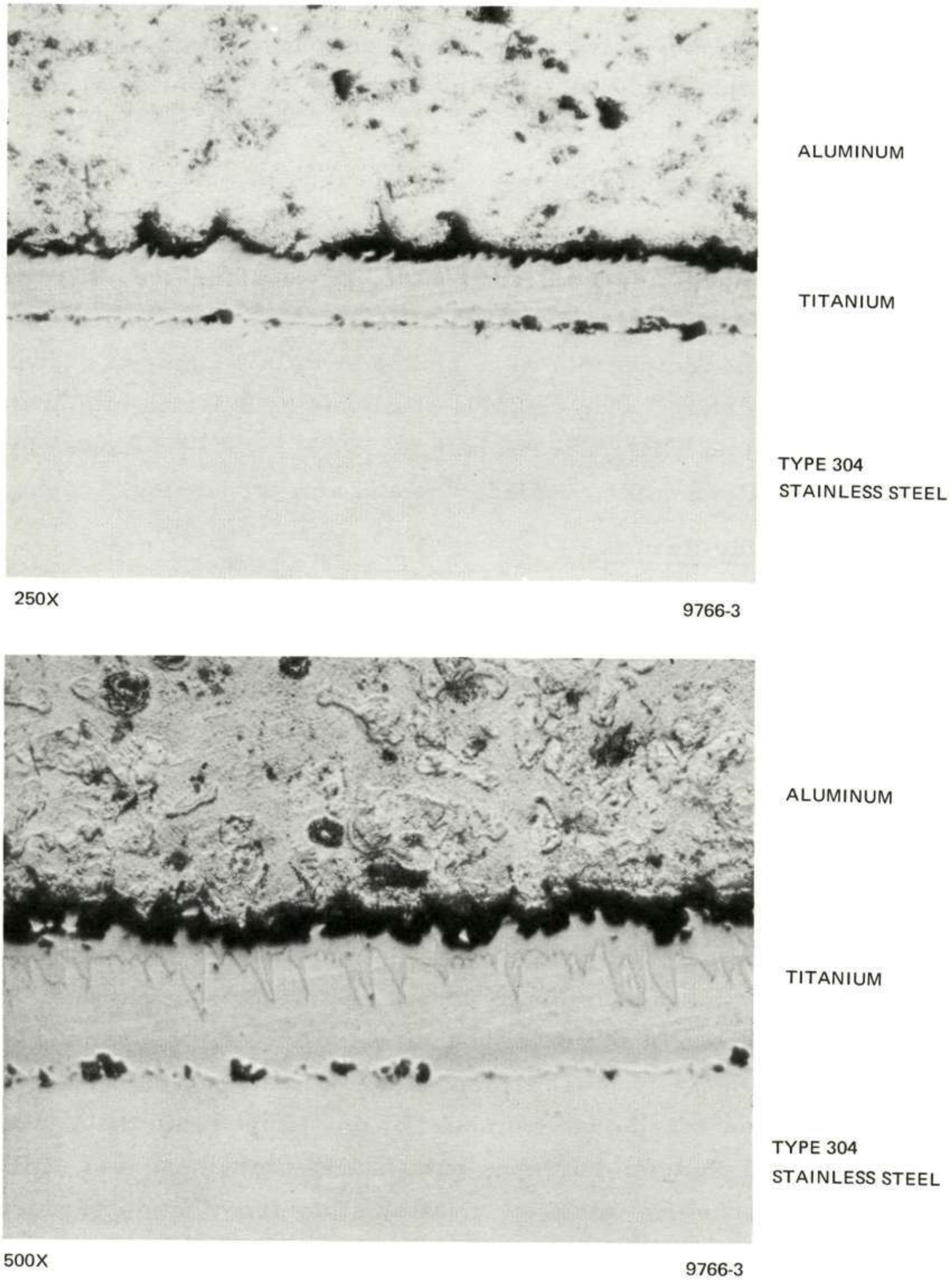

Figure 91. Vapor-Plated Titanium and Aluminum on Type 304 Stainless Steel

6532-54129

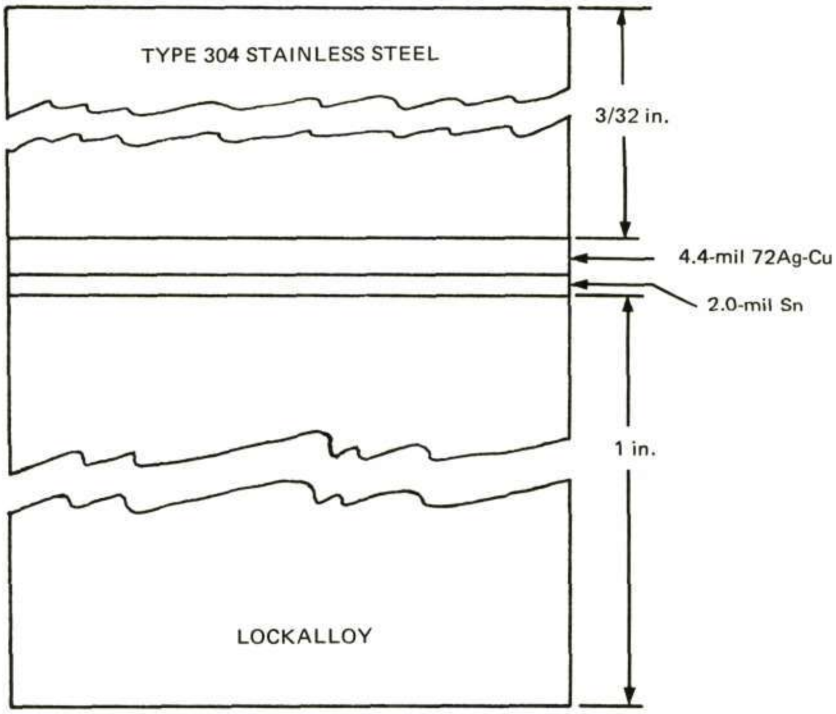

BRAZE SAMPLE ASSEMBLY

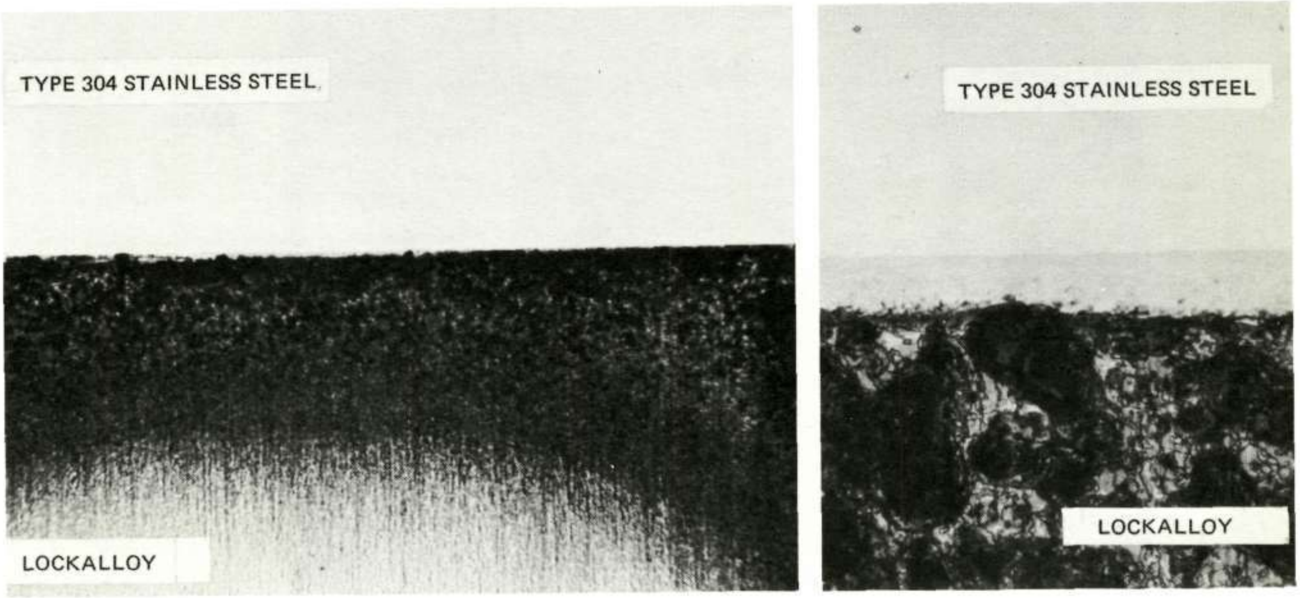

6532-54130

Figure 92. Ag-Cu-Sn Brazed Type 304 Stainless Steel – Lockalloy

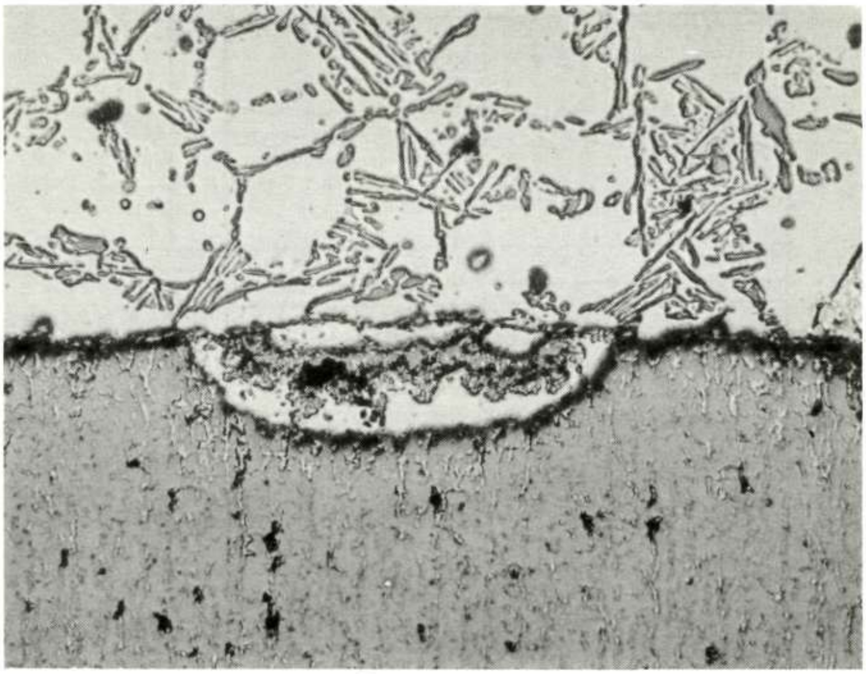

250X RUN NO. 12 9766-2

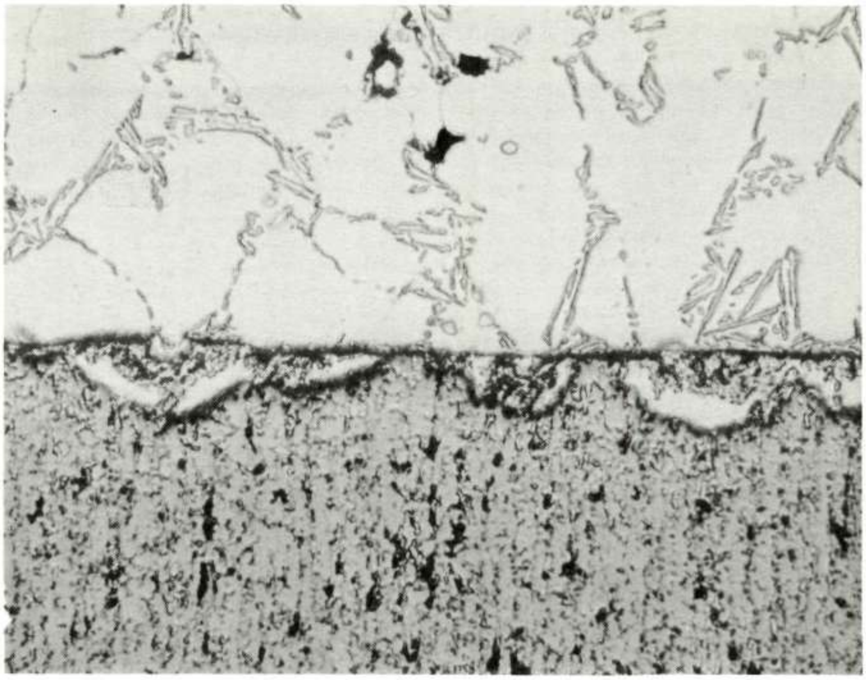

250X RUN NO. 11 9766-1

6532-54131

Figure 93. Vacuum-Brazed Lockalloy and BAl-Si4 Interface

Adequate wetting of Lockalloy and titanium-plated Type 304 stainless steel was achieved at 1150°F for 10 min in an evacuated capsule at a room temperature pressure of less than 10^{-5} torr. The cleaned stainless steel and Lockalloy samples sandwiching a 10-mil foil of BAl-Si4, were wired together for brazing. The contact pressure between the materials was therefore rather low. With higher contact pressure, brazing could undoubtedly be accomplished at a lower temperature, around 1100 to 1120°F. Due to program termination, photomicrographs of samples brazed at 1150°F are not available. Two earlier samples are shown in Figures 93 and 94. As will be noted in Figure 93, some erosion of the Lockalloy occurred at 1180°F for a 15-min braze cycle. Wetting of the Lockalloy surface was good. Figure 94 shows the interface between Lockalloy and 1100 aluminum when brazed under the same conditions. Again the erosion of the Lockalloy is noted along with interaction between the BAl-Si4 and the 1100 aluminum.

2. Lockalloy Procurement

The original order for Lockalloy called for extruded material which had been rolled lengthwise to improve the transverse ductility of the material. KBI ran a test and determined that the lengthwise rolling did not produce the desired increase in transverse ductility. At the same time, structural analysis of the material indicated that the transverse ductility of the as-extruded material was adequate for the design. Therefore the order was altered to purchase only extruded material. At the time the order was placed, KBI had only one extrusion die which could be used for the size members AI required, 4-3/4 in. wide by 0.076 in. thick. The die produced an extrusion, 3/8 in. thick by 5 in. wide. Since rolling was eliminated, it was necessary for a new die to be procured which could produce a thinner extrusion. The new extrusion was 3/16 in. thick by 5 in. wide. From this, the configuration, shown in Figure 90, could be machined. The entire shipment of material was received after the program was terminated so that no evaluation of the product was possible other than verification of the receival quantities.

I. EVALUATION OF THE LOCKALLOY RADIATOR

The characteristics that made Lockalloy attractive as the selected fin material were its physical and mechanical properties. It has low density,

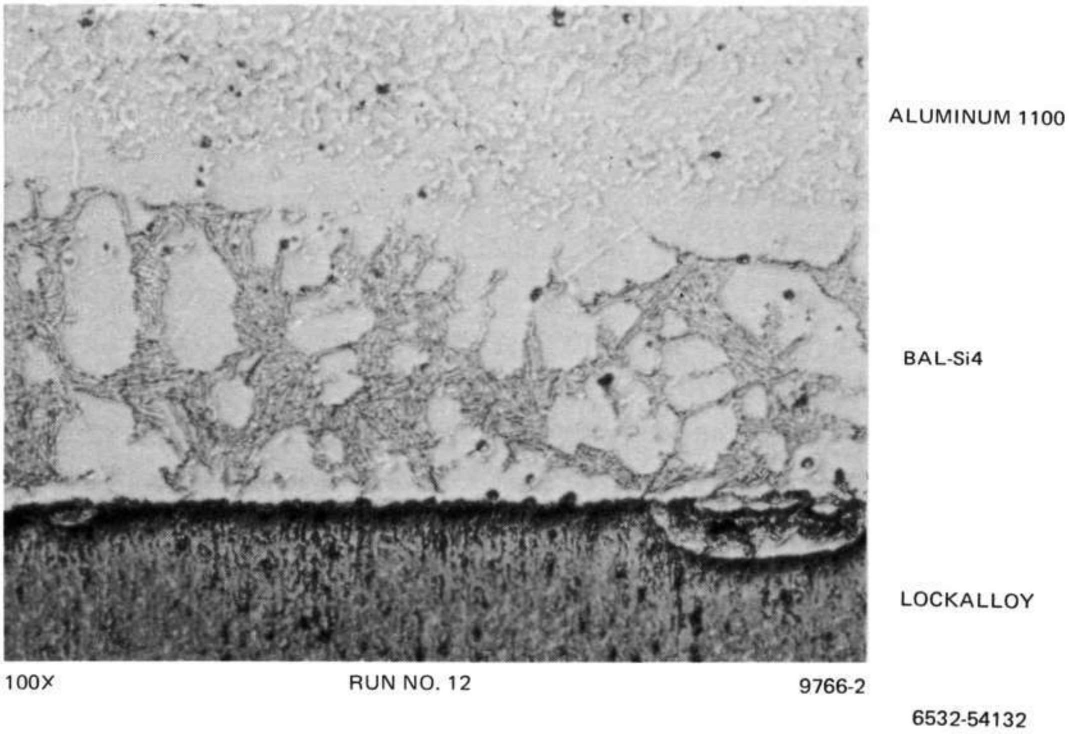

Figure 94. Vacuum-Brazed Lockalloy to Aluminum 1100 with BAl-Si4

moderately high thermal conductivity, high strength, high stiffness and, above all, its coefficient of thermal expansion is a close match to that of Type 304 stainless steel.

The design called for simplicity because of the relatively high cost of the raw material and subsequent fabrication. As the design evolved, it started as a circular tube in a Lockalloy extruded and machined saddle. It ended as a D tube brazed to a flat fin with a thin sheet of armor. The stiffness was sufficiently high with the D tube to allow the elimination of the leg of the T stringers with a corresponding weight reduction. Although a moderately light weight radiator could be produced, the necessity of fabricating the rings, stringers, and bracketing of stainless steel tends to offset the big advantage of the low density of Lockalloy. The final design weight was not excessive, however.

As noted, the close match of expansion coefficients caused a significant decrease in fabrication-induced stresses and those induced by thermal cycling. At operating temperature, the residual stresses were to be near negligible. The

c3

stresses caused by the 48 θ temperature ripple would be variable, and the effect cannot be determined without a better understanding of the creep of the material. Limited data indicate an improvement over aluminum in this respect.

Major weaknesses with Lockalloy are its high cost and production which requires considerable care due to its toxicity (because of its beryllium content). The braze has not been fully developed, although it was anticipated that a braze similar to those applicable to aluminum would be suitable. There would be a further probability of braze success since the expansion coefficients matched and local stresses would be lower.

The selection of Lockalloy eliminated the major problem associated with aluminum fins. Its uncertainties and disadvantages appeared small in comparison to aluminum and Lockalloy was, therefore, the reference material.

VII. ALTERNATE RADIATOR APPROACHES

Although Lockalloy 38 fins bonded to Type 304 austenitic stainless-steel tubes was selected as the reference radiator materials combination, several other combinations were considered. Each was considered on the basis of thermal performance, strength, fabricability, cost, weight, and thermal expansion mismatch.

The following sections describe the various alternates, their characteristics, their strong points and weaknesses, and the major reasons for ruling them out.

A. COPPER FIN RADIATOR

Copper has a high thermal conductivity and its coefficient of thermal expansion is a close match to that of stainless steel. It appeared then, to be a candidate for the radiator fin material. Thickness would not necessarily be dictated by thermal performance but rather by structural considerations. The thermal stresses due to any small differential in the coefficients of expansion (tube to fin) would not be significant and would not necessitate a symmetric configuration. The primary concerns associated with copper were its high density and relatively low strength at room temperature.

1. Configuration Selection

Copper was investigated as one of the alternative materials to be used in making the 5-kwe system thermal radiator fins. The coefficient of thermal expansion of many of the copper alloys is very close to that of the stainless-steel coolant tube material. This match of coefficients of thermal expansion would eliminate the problem of differential expansion at the fin and tube bond joint at elevated temperatures.

Copper has high thermal conductivity which would enable a relatively thin radiator fin to reject the required amount of thermal energy. It was hoped that this reduction in radiator fin thickness would more than compensate for the increased density of copper, relative to other materials, and thereby provide a net reduction in the total radiator system weight.

Copper also exhibits excellent workability and joinability at both hot and cold temperatures which would decrease the high cost of manufacturing inherent with other radiator fin materials.

Two radiator fin geometries were considered using copper as the fin material: a tapered fin with a minimum fin thickness of 0.020 in. and a fin with a constant fin thickness. A general schematic of each of these fin geometries is shown in Figure 95. The tapered symmetric fin and tube cross section was not considered for the copper radiator since differential expansion at the fin and tube bond is not a problem at elevated temperatures.

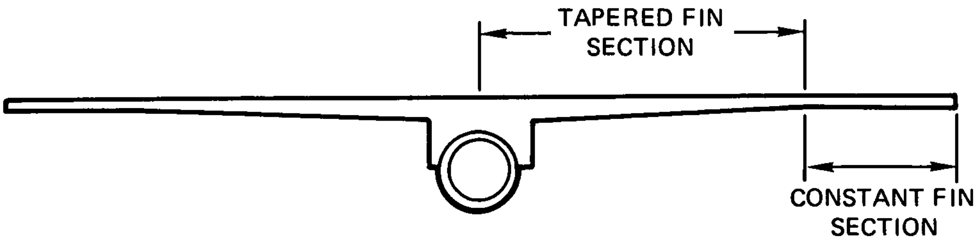

TAPERED ASYMMETRIC FIN AND TUBE CROSS SECTION

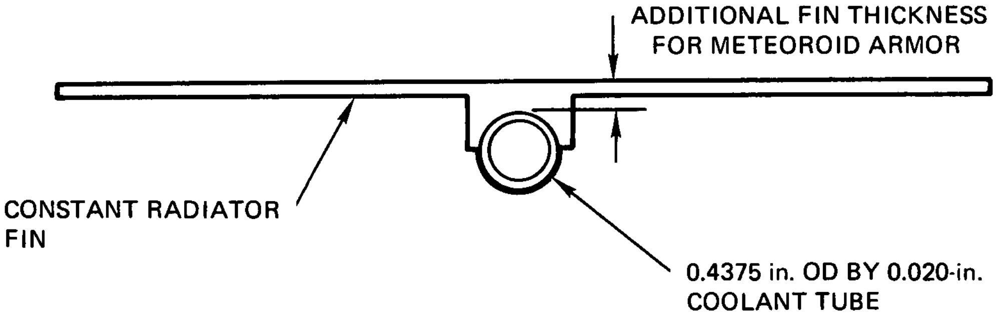

CONSTANT ASYMMETRIC FIN AND TUBE CROSS SECTION

6532-54112

Figure 95. General Schematics of the Asymmetric Taper and Constant Thickness Fin and Tube Cross Sections Considered for the Copper Radiator

A detailed analysis was performed on the two geometries shown in Figure 95 to establish the required configuration of each design. This analysis showed that the tapered fin and tube cross section is substantially lighter than the constant fin geometry that was required to reject the necessary thermal energy. A detailed discussion of this trade study is given in Section VII-A-3.

Three aspects of the copper radiator trade study were carried on simultaneously: thermal performance, structural analysis, and a detailed material selection. Copper-102 OFHC was initially selected as the candidate fin material due to its high thermal conductivity. This material was considered during both the thermal performance and structural analysis phases of the trade study.

The minimum weight fin cross section developed by the thermal performance studies had insufficient strength when evaluated as a structural support. Narloy-Z was therefore selected as the reference copper alloy on the basis of strength even though its thermal conductivity is approximately 80% of that of Cu-102.

Since the Cu-102 radiator concept was rejected as being too heavy, a reiteration of the thermal and structural analyses was not made using Narloy-Z as the fin material. The lower thermal conductivity of Narloy-Z would necessitate a thicker fin to reject the same amount of heat and would, therefore, be even heavier than the Cu-102 radiator.

2. Material Properties

Narloy-Z (Table 20), a copper base alloy containing a nominal 3 wt % Ag and 0.3 wt % Zr, was chosen as a reference material to study the design characteristics of a copper and Type 304 stainless-steel radiator.

TABLE 20

MECHANICAL AND PHYSICAL PROPERTIES OF NARLOY-Z

Property	Value at 75°F	Value at 600°F
Ultimate Tensile Strength (ksi)	40	31
Yield Strength (ksi)	22	18
Elongation (% in 4D)	35	33
Shear Modulus (psi x 10^6)	7	No data
Tensile Modulus (psi x 10^6)	18.5	15.8
Density (lb/in.^{3})	0.33	-
Thermal Conductivity (Btu/in./ft^2/°F-hr)	2232	2184
	Value in 75 to 200°F Range	Value in 75 to 600°F Range
Coefficient of Expansion (in./in. x 10^{-6})	9.6	9.9

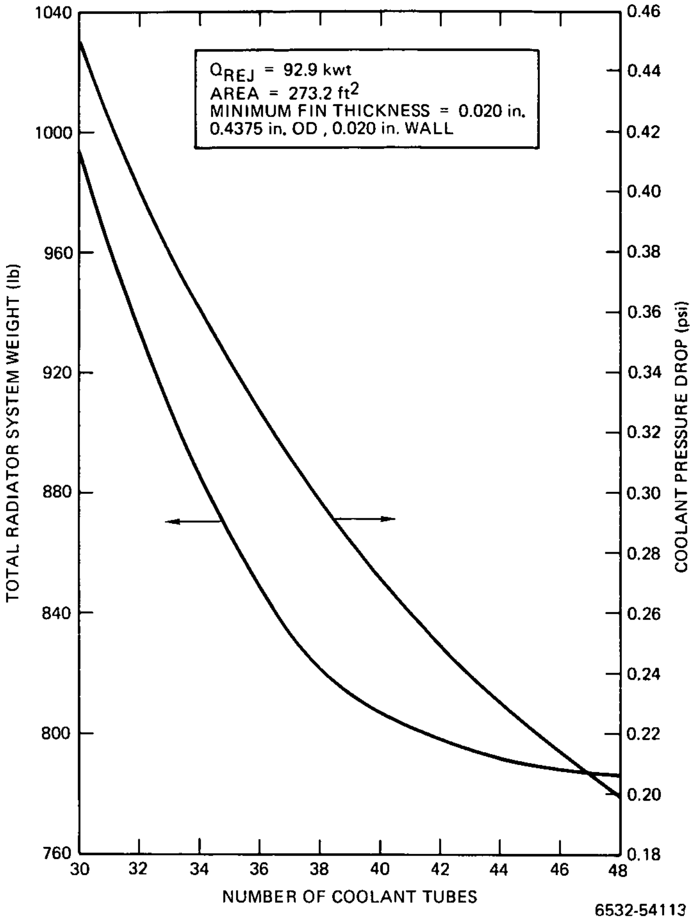

Figure 96

Tapered Copper and Stainless-Steel Fin, Radiator Weight and Coolant Pressure Drop vs Coolant Tube Number

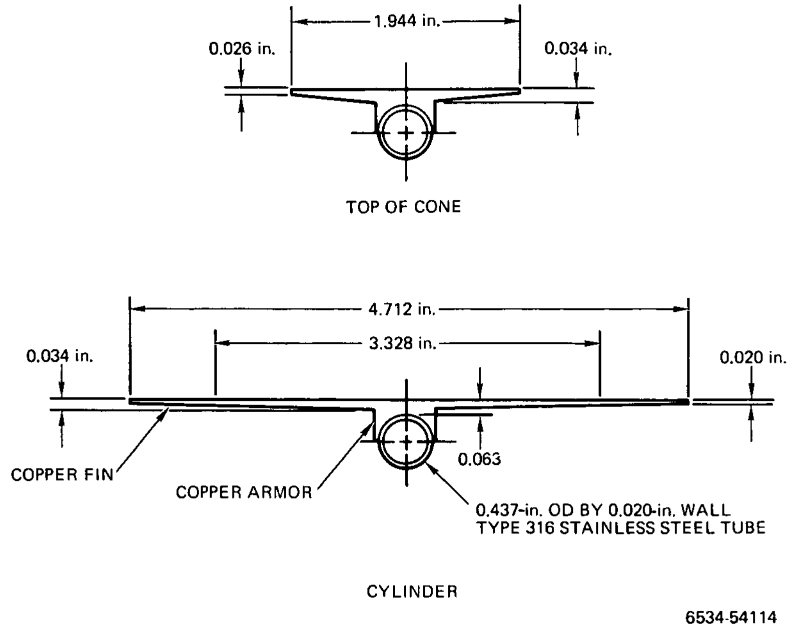

Figure 97. Tapered Copper Fin and Tube Cross Section

3. Thermal Performance Characteristics

Two radiator fin geometries were considered using Cu-102 in this analysis: a tapered fin with a minimum fin thickness of 0.020 in. and a fin with a constant thickness. Both fin geometries incorporated the asymmetric fin and tube radiator cross section. A 0.4375-in. OD coolant tube with a 0.020-in. wall thickness was used in both radiator cross section designs.

The Cu-102 fin material thermophysical properties and the radiator performance requirements are given in Table 21. Table 13 in Section VI gave the dimensions.

TABLE 21

COPPER-102 PROPERTIES, AND RADIATOR PERFORMANCE REQUIREMENTS AND DIMENSIONS

Parameter	Value
Copper-102 Properties	
Thermal Conductivity (Btu/hr-ft^2-°F/ft)	226
Density (lb/ft^3)	558
Meteoroid Material Cratering Coefficient, γR	2.00
Performance Requirements	
Net Power Rejected (kwt)	92.9
Inlet Temperature (°F)	590
Coolant Temperature Drop (°F)	144
Emissivity	0.9
Solar Absorptivity	0.5
Environmental Heat Input (Btu/ft^2-hr)	102

Figures 96 and 97 present the results of the calculations using a tapered Cu-102 radiator fin geometry. Figure 96 shows the total radiator system weight and the coolant pressure drop through the radiator as functions of the number of coolant tubes. From the results shown in Figure 96, it was concluded that 48 coolant tubes should be used in the copper radiator designs. The tapered fin copper radiator using 48 coolant tubes has a total system weight of approximately 788 lb. The coolant pressure drop through this radiator is 0.199 psi.

Figure 97 shows the typical fin and tube cross section dimensions for the Cu-102 tapered fin radiator using 48 coolant tubes. A fin root thickness of 0.034 in. is required to reject the 92.9 kwt. A total armor thickness of 0.063 in. is required for this design.

The tapered fin and tube cross section shown in Figure 97 was selected to be used as the copper radiator since it weighs substantially less than the radiator with a constant fin thickness.

4. Structural Characteristics

The structural evaluation of the copper fin radiator dealt primarily with its ability to sustain the launch loads. It was considered capable of sustaining gross operational conditions, brazing, and testing without the effect of thermal expansion mismatch. Had copper been maintained as the reference material, a more detailed thermal stress analysis would have been performed. Axial and circumferential gradients, sun shade effect, long-term creep, and low cycle fatigue analysis would have been evaluated.

Initially, the launch-induced loads were assumed to be equal to those of an aluminum fin radiator (Table 3, Figures 8 and 9). This assumption proved to be unconservative, however, since the system weight would be greater with the copper fins. With equal accelerations and increased radiator weight, the bending moments and shears in the lower stations would increase. It was estimated that the loads would be ≈ 6% greater on the copper structure.

The procedure for determining the structural capacity is similar to that used on other materials. The cross section with 0.100-in. armor, 0.034-in. hot end tapered to 0.020 in., and a saddle-mounted, 7/16-in. tube was analyzed. Although it was determined that this configuration with a 0.035-in. T splice would meet the launch requirements (Section IV-A), it was with a severe weight penalty. The tube, fin, splice, and armor assembly would weigh over 850 lb and the total radiator weight would approach 1000 lb.

A modification of the copper fin radiator was made where the copper is tapered from 0.034 in. at the hot end to a feather edge at the cold end of the fin and clad to a uniform thick stainless-steel sheet. The armor is reduced significantly by removing the saddle and incorporating a D tube. The strength of this configuration would not be limited to the copper yield strength. The analysis is based on the assumption that the copper would not carry a load but would provide sufficient stiffness to the stainless-steel cladding for it to work at its yield strength. The validity of that assumption is questionable; however, it was made to facilitate the analysis on a feasibility basis. The strength, then, is nearly the area of the stainless steel in the cross section, times its yield strength. This section with minimum practical cladding thickness of 0.010 in. was more than adequate but it too has a significant weight disadvantage. It had the further disadvantage of requiring a good contact bond between the copper and stainless-steel cladding. Copper was abandoned primarily on a weight consideration.

5. Copper Fin Radiator Evaluation

The strong points for copper were its high thermal conductivity, its thermal expansion rate close to that of stainless steel, and the proven methods of brazing. Although Narloy-Z was the probable copper alloy, much of the strength evaluation was based on Cu-102 OFHC copper properties. The cross section was basically the minimum that was required for thermal performance and it had insufficient strength with the Cu-102 OFHC alloy, but more than adequate strength when evaluated with Narloy-Z. In either case, however, the radiator weight approached 1000 lb representing a 20 to 25% increase in system weight. This was due to the high density of copper and was considered too great a weight penalty. The copper radiator was, therefore, considered unacceptable as a flight design component. It was given a potential rating, however, for a ground test radiator in the event the flight and ground test systems were to be of different designs. Copper could serve as a basis for testing all components of the system except the radiator.

B. STAINLESS-STEEL FIN RADIATOR

1. Configuration Selection

Stainless steel was chosen as an alternate radiator fin material because of its high strength and ease of attachment to the coolant tubes. Since both the coolant tubes and fin material would be stainless steel, the coefficients of thermal expansion of these components would be identical thereby eliminating the differential thermal expansion at high temperature.

The main disadvantages of using stainless steel as fin material are its high density and low thermal conductivity. Both of these properties lead to increased radiator system weight.

The asymmetric tapered fin and tube cross section was the only configuration considered for the stainless steel radiator since it is substantially lighter than the constant fin geometry. A thermal analysis was performed to determine the required dimensions of the stainless-steel radiator. This analysis showed that the total radiator system weight using stainless steel as the fin material would be approximately 8,000 lb.

2. Stainless-Steel Fin Radiator Evaluation

As expected, the analysis of a stainless-steel radiator showed high strength and virtually no problem with residual stresses. The low conductivity of stainless steel required extreme thickness and/or close tube spacing resulting in a heavy (8,000-lb) radiator. It was, therefore, given no further consideration as a candidate material for the radiator fin.

C. ALUMINUM BORON FILAMENT RADIATOR

1. Configuration Selection

Boron-fiber-reinforced aluminum was investigated as one of the alternate radiator fin materials because of its high strength, low weight and a coefficient of thermal expansion which can be tailored to match that of stainless steel.

The boron aluminum composite consists of laminations which are made by diffusion bonding alternate layers of aluminum foil and boron filaments. This type of laminated construction produces a high strength material very resistant to meteoroid impact damage.

Two radiator fin geometries were considered: a tapered fin with a minimum fin thickness of 0.020 in., and a fin with a constant thickness. A typical schematic of each of these fin geometries is shown in Figure 98. The tapered symmetric fin and tube cross-section was not considered for the boron aluminum radiator since differential thermal expansion at the fin-tube bond is not a problem at elevated temperatures.

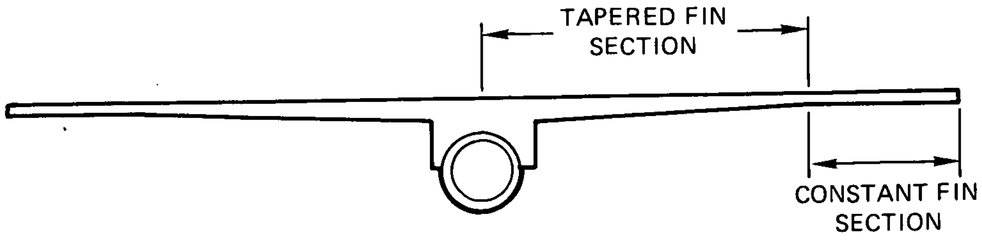

TAPERED ASYMMETRIC FIN AND TUBE CROSS SECTION

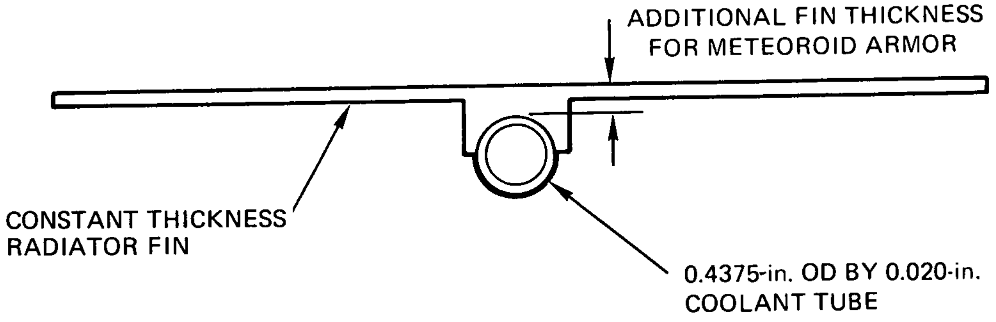

CONSTANT ASYMMETRIC FIN AND TUBE CROSS SECTION

6532-54115

Figure 98. Typical Schematic of the Asymmetric Tapered and Constant Thickness Fin and Tube Cross Sections Considered for the Boron Fiber-Reinforced Aluminum Radiator

A thermal analysis was performed to determine the required configuration of the two fin-tube cross sections shown in Figure 98. This analysis showed that the tapered fin-tube cross section design is substantially lighter than the constant fin geometry that was required to reject the necessary thermal energy. However, the cost of manufacturing the tapered fin geometry would be high. The fin and tube geometry with a constant fin thickness was therefore used as the reference boron-fiber-reinforced aluminum radiator.

A discussion of the thermal analysis of the boron aluminum radiator is given in Section VII-C-3. A description of the fabrication techniques used in the boron aluminum radiator is given in Section VII-C-5.

2. Material Selection

The primary materials selection consideration for the potential user of aluminum boron filament composites is that at present the manufacture of the materials is effectively a custom operation and very expensive. This is because there is no current short or intermediate range need for mass production capabilities for boron aluminum laminated plates. The nearest thing to volume production items are the 4-mil-diameter and the 5.6-mil-diameter tungsten cored boron monofilaments available from the several manufacturers and the so-called monolayer sheets available from the several secondary fabricators.

Monolayer sheets consist of a layer of parallel boron monofilaments sandwiched between and bonded to two thin layers of aluminum. Typical monolayer sheets contain 45 to 50 vol % boron fibers. According to representative secondary fabricators, this is an optimum boron fiber concentration, both from a sheet fabrication standpoint and a strength per unit weight standpoint. The monolayer sheets are stacked up and bonded to one another to form laminates. The properties of the monolayer sheet are highly orthotropic, i.e., anisotropic within the plane of the sheet, and so are many of the properties of the laminates despite a variety of choices for fiber orientation in the several layers of the laminate.

For most applications, very high laminate strength-to-weight ratios are essential, and virtually no spliced or broken fibers are permitted. This greatly increases the typical scrap loss from shearing each monolayer sheet prior to lamination, because the selvage is usually unusable and can represent up to 99% of initial sheet area if starting sheet size and finished laminate size and shape are not compatible.

Several types of boron-aluminum laminate plates appear worthy of at least preliminary consideration as space radiator fins. They are:

1) Thirty-five to thirty-seven vol % boron filament, with all filament axes oriented 90° from the coolant tube axes. For a 10-ft-long by 6-in.-wide plate, this type would cost about $350/lb in 200-lb quantities. Its thermal expansion along the tube length would match that of Type 304 stainless steel but would be only half as large (in the fin plane) at right angles to the tube. Pull out strength of rivet holes

along fins would be low for this material. The material is moderately well characterized.

2) Thirty-three vol % boron filament, with the axes of alternate layers of filaments running at 75 and 150° to the coolant tube axis. Plates of this type would cost about $425/lb in 200-lb quantities. Its axial coefficients of expansion would be similar to those of Type 1 material but its rivet hole pull out strength would be appreciably greater. Type 2 is substantially uncharacterized.

3) Sixteen vol % boron filament, with the axes of every third layer of filaments running at angles of 0, 60, and 120° to the coolant tube axis, or at angles of 0, 45, and 135° to the coolant tube axis. This material would cost about $460/lb in 200-lb quantities. The expansion properties in the plane of lamination should be equiaxial. Type 3 is virtually uncharacterized and the fiber content is low enough that there is some greater risk of deterioration of properties (filament breakage and delamination) with thermal cycling because of the limited fiber-matrix interface area and the marked differences in expansion coefficients of boron and aluminum. Impact damage characteristics of this laminate are unknown.

It would appear that radiators could be made using any of the three types of laminates as fin material but costs of materials, fabrication, and engineering property determinations would be high. The several physical mechanical property insufficiencies must also be evaluated. Methods by which radiators incorporating boron fiber-aluminum composite fins could be fabricated have been evaluated and are discussed in Section VII-C-5, below.

3. Thermal Performance Characteristics

An analysis was undertaken to determine the thermal radiator configuration for the 5-kwe reactor system using aluminum-boron filament as the radiator fin material. This analysis was made for the asymmetrical tapered and constant fin-tube cross sections. The coolant tubes used in this analysis had an outside diameter of 0.4375 in. and a 0.020-in. wall thickness.

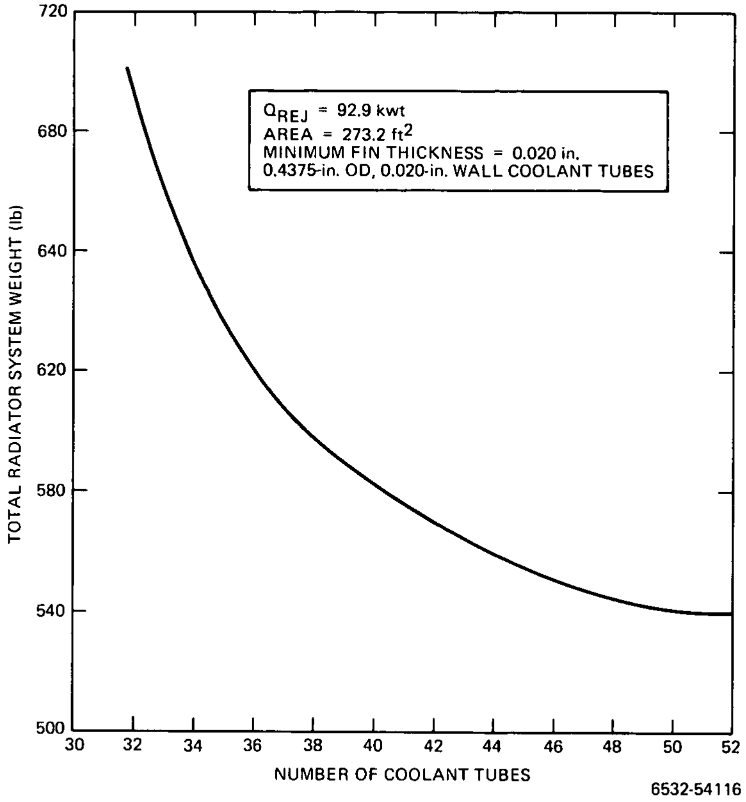

Figure 99. Tapered Aluminum-Boron Filament Fin, Radiator Weight vs Number of Coolant Tubes

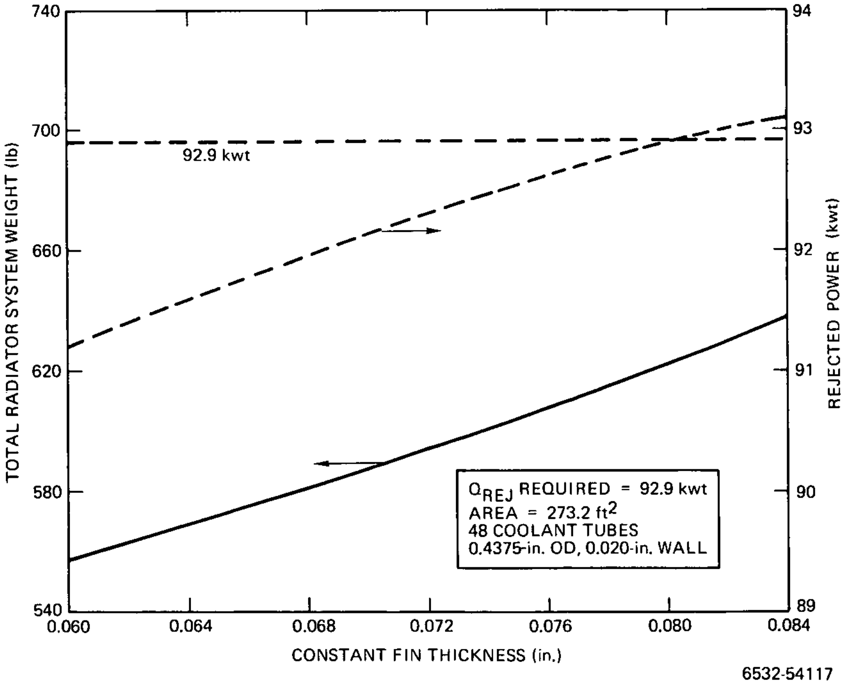

Figure 100. Constant Thickness Aluminum-Boron Filament Fin, Radiator Weight and Rejected Power vs Constant Fin Thickness

A thermal conductivity value of 88.0 Btu/hr/ft^2/°F-ft and a density of 161 lb/ft^3 was used for the aluminum-boron filament material. These property values are for the fin material with a 33% boron content. The thermal conductivity and density values will vary as a function of composition and filament orientation.

Figures 99, 100, and 101 present the results of the calculations using the aluminum-boron filament radiator fin material. Figure 99 shows the total radiator system weight as a function of the number of coolant tubes for a tapered fin-tube cross section. The minimum fin thickness for these cases was 0.020 in. From the results shown in Figure 99, 48 coolant tubes were chosen as the design value for the aluminum-boron radiator. The tapered asymmetric radiator fin using 48 coolant tubes has a maximum fin thickness of 0.099 in. and a total radiator system weight of 545 lb.

Figure 100 illustrates the aluminum-boron filament constant fin radiator system weight and rejected power as functions of constant fin thickness. Forty-eight coolant tubes were used in the constant fin cross section calculations. The power rejection capability of the radiator increases with increasing constant fin thickness. Figure 100 shows that a constant fin thickness of 0.080 in. is required to reject 92.9 kwt net power. This radiator configuration weighs approximately 622.3 lb.

Figure 101 shows the typical asymmetric aluminum-boron filament material fin-tube cross section dimensions using 48 coolant tubes with an OD of 0.4375 in. Due to the high cost of fabricating the tapered fin-tube cross section, as will be discussed in Section VII-C-5, the constant fin configuration shown in Figure 101 was used as the reference boron fiber-reinforced aluminum radiator design.

4. Aluminum Boron Filament Radiator Structural Characteristics

The characteristic of boron filament aluminum that made it attractive was its coefficient of thermal expansion. It is theoretically possible to induce any desired expansion rate (within tolerance) in any direction. It would be possible, then, to have the aluminum-boron fin with an expansion rate equal to that of the stainless-steel tube. There would be essentially no stress resulting from the

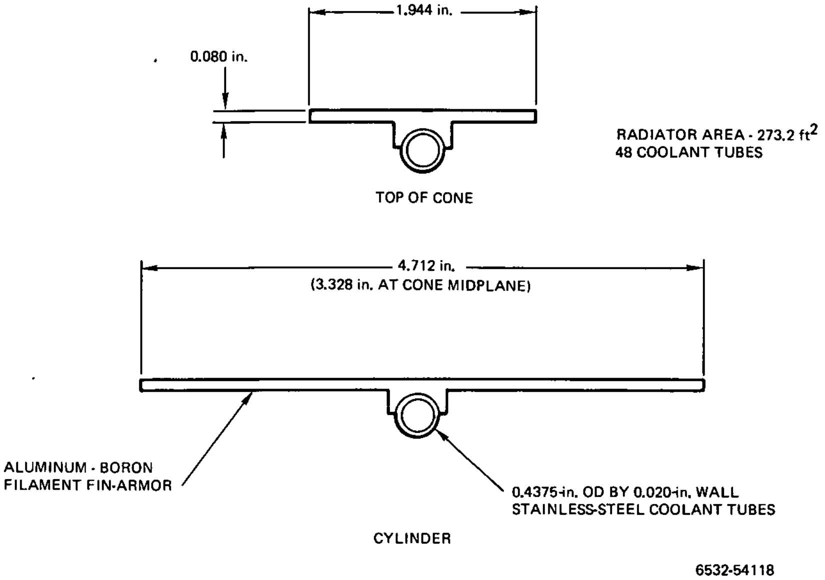

Figure 101. Constant Thickness Aluminum-Boron Filament Fin and Tube Cross Section

braze cycle or subsequent operational isothermal conditions. There would be the 48 θ stresses, however, but these would be in the range of 2,000-psi maximum. The significance could not be determined without creep and relaxation data.

The cold stresses, or launch-load stresses, could be handled without limitations. The strength of the aluminum-boron is equal to or greater than the 3003-T0 aluminum and its thickness would have been about the same. Thus, its strength would have been adequate.

5. Fabrication Status

a. Fin-to-Tube Bonding

Boron-aluminum composite fins can be joined to stainless-steel tubes by diffusion bonding or by brazing, e.g., with Al-12 Si (solidus ~960°F); but manufacturers recommend that the maximum temperature during fabrication or use be kept as far below 900°F as possible to avoid interaction between the boron and the aluminum, and to avoid loss of strength of the composite. This severely limits the bonding method and increases fabrication equipment cost. A proprietary (Rockwell International) diffusion bonding process might allow a maximum fabrication temperature of 850°F.

b. Tapering of Fins

Boron fibers are exceedingly hard and fins cannot be economically sawed to the required shape. They can be sheared to shape readily, providing good shearing practices are carefully followed, e. g., rigid maintenance of shear alignment.

c. Riveting of Fins

The proposed design rivets the fins to one another or to structural ribs. The poor pull-out strength of rivet holes in monodirectional laminates was mentioned in the materials selection section above (equivalent to that of 1100 aluminum). Riveting is a practical approach for use in fabricating boron aluminum composite materials into structures but the following special factors must be considered. The best way, and by far the lowest cost way, to produce the rivet holes is to punch them and the ream them to finish dimension. If tungsten carbide reamers are used, the reamer cost per hole will be about $5. If diamond reamers are used, the cost per hole will be about $1. If the undersized dressed down reamer can be used elsewhere, the effective cost per hole will be reduced further, but the riveting process will not be inexpensive.

6. Aluminum-Boron Filament Radiator Evaluation

The aluminum-boron filament material offered good thermal properties, strength, and a potential for a good thermal expansion match. It was also attractive because of its low density. Its use would have required considerable development, however, and fabrication costs would have been astronomical. Many uncertainties existed including the availability of the raw material. It was, therefore, abandoned as a candidate for the radiator fins.

D. MECHANICALLY ATTACHED LOCKALLOY FINS

1. Attachment Approaches

At the stage of development when the Lockalloy was selected as the fin material, there were uncertainties on the braze potential of Lockalloy to stainless steel. Although a brazed assembly would be more efficient and have lower thermal differentials, it was conceivable that a mechanically attached, riveted, fin-tube assembly could be made. Its practicality would be dependent on the ability to transfer heat from the tubes through a riveted joint to the fins. The conductivity would remain an uncertainty until tests were made. Tests would have to show the effect on conductivity of temperature, time, and repeated cycles of thermal excursions. It would also be necessary to show the effect of dynamic loading on the joint integrity.

2. Thermal Performance Characteristics

The riveted radiator fin-tube design discussed in Section VII-D-1 may impair radiator heat rejection capability by reducing the contact area between the coolant tube and radiator fin. An analysis was undertaken to determine the effect of reduced contact area between the coolant tube and fin material upon the asymmetric constant fin Lockalloy 38 radiator configuration. A thermal conductivity value of 92.5 Btu/hr-ft^2/°F-ft was used for the Lockalloy 38 fin material. This value is the approximate thermal conductivity for the fin material at 600°F. The coolant tubes used in this analysis had the D-shaped cross section discussed in Section VI-A with a flat side outside length of 0.4375 in. and a 0.020-in. wall thickness.

Figures 102, 103, and 104 present the results of the calculations for varied contact area between the coolant tube and radiator fin. Figure 102 shows the approximate temperature difference between coolant and fin root as a function of the percent contact area between the coolant tube and fin material.

A thermal analyzer program (TAP) model was developed to represent a typical fin cross section at the top of the conical portion of the reference radiator.

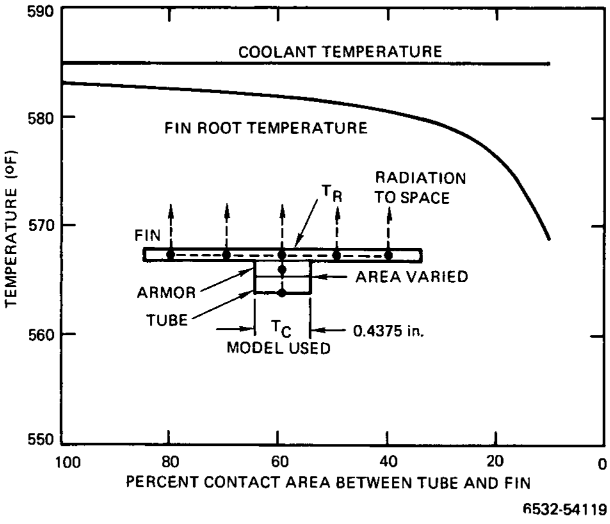

Figure 102.

Temperature Difference Between Coolant and Fin Root vs Percent Contact Area Between Tube and Fin

Figure 103.

Asymmetric Lockalloy 38 Radiator, System Weight and Constant Fin Thickness vs Percent Contact Area Between Tube and Fin

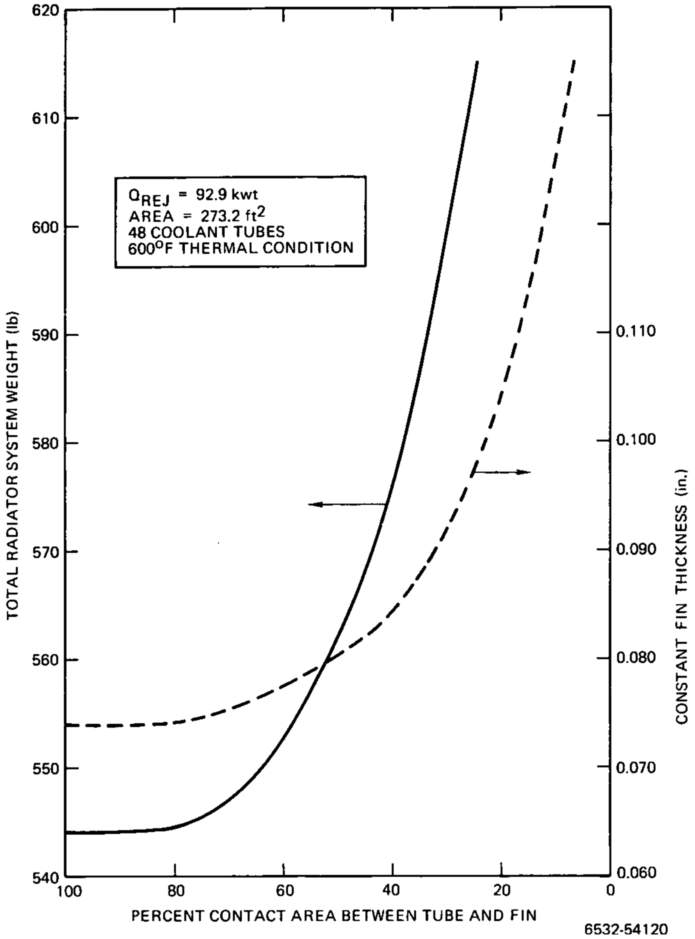

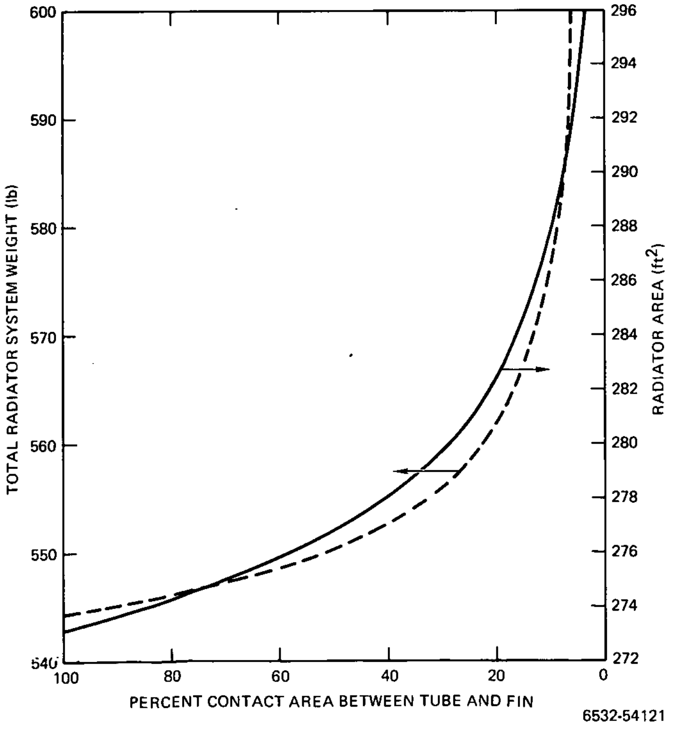

Figure 104.

Asymmetric Constant Thickness Lockalloy 38 Fin and Tube Cross Section Radiator System Weight and Surface Area vs Percent Contact Area Between Tube and Fin

The schematic of this model is also shown in Figure 102. As shown in Figure 102, the radiator fin-tube assembly was represented by three flat plates of unit length. The first plate simulated the 0.058-in.-thick by 1.944-in. wide Lockalloy radiator fin. This plate consisted of five nodes; each receives thermal input from the environment at a rate of 102 Btu/ft^2-hr and, in turn, rejects radiant energy to space. A second plate, consisting of one node, represented the 0.018-in.-thick Lockalloy 38 armor required for meteoroid impact protection. The third plate in the thermal model simulated a 0.4375-in. OD by 0.020-in., stainless-steel coolant tube. The node external to the coolant tube node represented the coolant temperature, T_C. This node was held at a constant temperature of 585°F as the heat transfer area between the tube and armor nodes was decreased. As the heat transfer area was decreased, the fin root temperature, T_R, decreased. As shown in Figure 102, the $T_C - T_R$ temperature difference is approximately 2°F with a 100% contact area. This temperature difference is not appreciably increased until the contact area is reduced to 40%. With a 40% contact area, the $T_C - T_R$ temperature difference is 4.4°F. With a 10% contact area, the $T_C - T_R \Delta T$ increases to approximately 16°F.

Figure 103 shows the influence of the increased ΔT between coolant and radiator fin root upon the total radiator system weight and constant fin thickness of the 273.2 ft^2 thermal radiator. As the percent contact area between tube and fin decreases, a thicker fin is required to reject a net power of 92.9 kwt. This increase in required fin thickness results in an increase in total radiator system weight. From Figure 103, it can be concluded that a decrease of 30% contact area will not have a large influence upon the radiator system weight. However, a contact area degradation of larger than 40 to 50% can only be compensated for by a large increase in radiator weight with the 273.2 ft^2 area.

Figure 104 presents the approximate radiator system weight and surface area as functions of the percent contact area between tube and fin. If the radiator area is increased slightly, radiator system weight does not increase significantly until the contact area between tube and fin is decreased to less than 40%.

3. Mechanically Attached Fins

One area of concern with Lockalloy fins and stainless-steel tubes dealt with metallurgical attachment. It was presumed that a braze method could be developed.

In the event a braze joint could not be achieved or could not serve thermally, a mechanically attached tube was considered. Figure 105 shows the proposed configuration.

The structural analysis will be similar to that of the brazed Lockalloy with respect to mechanical loads. The thermal stress analysis would be a function of the heat transfer relationship through the mechanical joint. The ability to transmit sufficient heat through the rivets can be enhanced by using relatively large rivet heads. Since complete contact is not necessary for thermal transmission, a relationship between percent contact and diameter of rivet contact area is needed. Percent contact is that part of contact if the tube were 100% brazed along the projected flow diameter (Figure 106).

The stress-free condition would be at room temperature since this would be the assembly temperature. The 48 θ stresses would be superimposed on the stresses associated with thermal mismatch. Although the latter would be no greater than the brazed assembly thermal mismatch stresses, the 48 θ stresses could be larger. These are dependent on the thermal transfer of the mechanical joint.

The thermal stress analysis was not completed.

4. Mechanically Attached Lockalloy Fin Evaluation

The riveted assembly shows most of the advantages of the brazed Lockalloy fin-tube assembly with respect to weight, strength, and simplicity. The inherent transverse clearances in the rivet holes would absorb some expansion differential resulting in lower thermal stresses than would exist in a brazed assembly. There is some uncertainty, however, regarding the conductivity of the riveted connection and the gradients could be more severe than could be tolerated. This approach would be maintained as an alternate but would be dependent on the outcome of joint conductivity tests.

E. SEPARATE RADIATOR

1. Configuration Approach

The decision to integrate the radiator with the structure was made at the outset of the program. It was based on experience gained on the SNAP 2 program

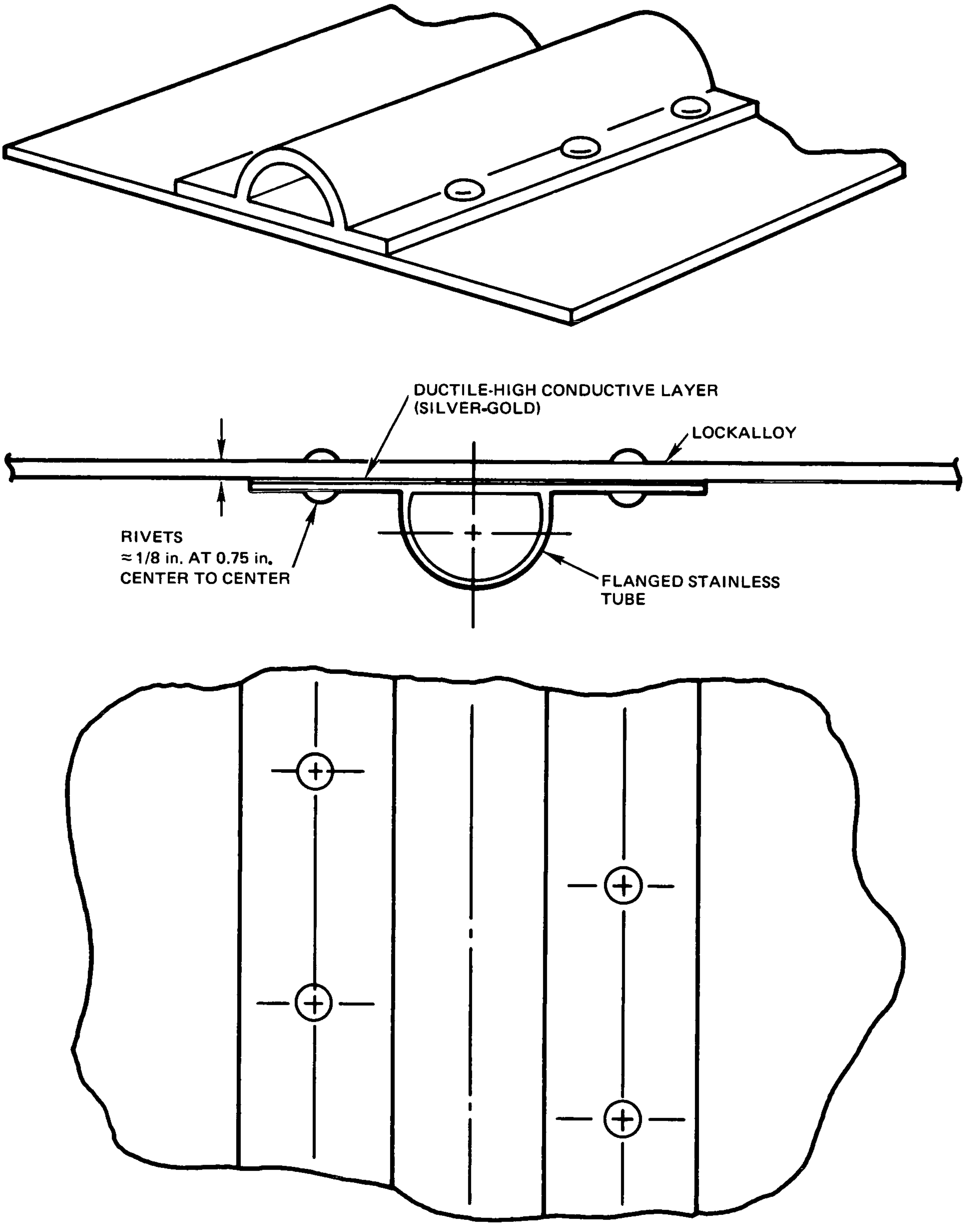

6532-54122

Figure 105. Mechanically Joined Lockalloy and Stainless Steel

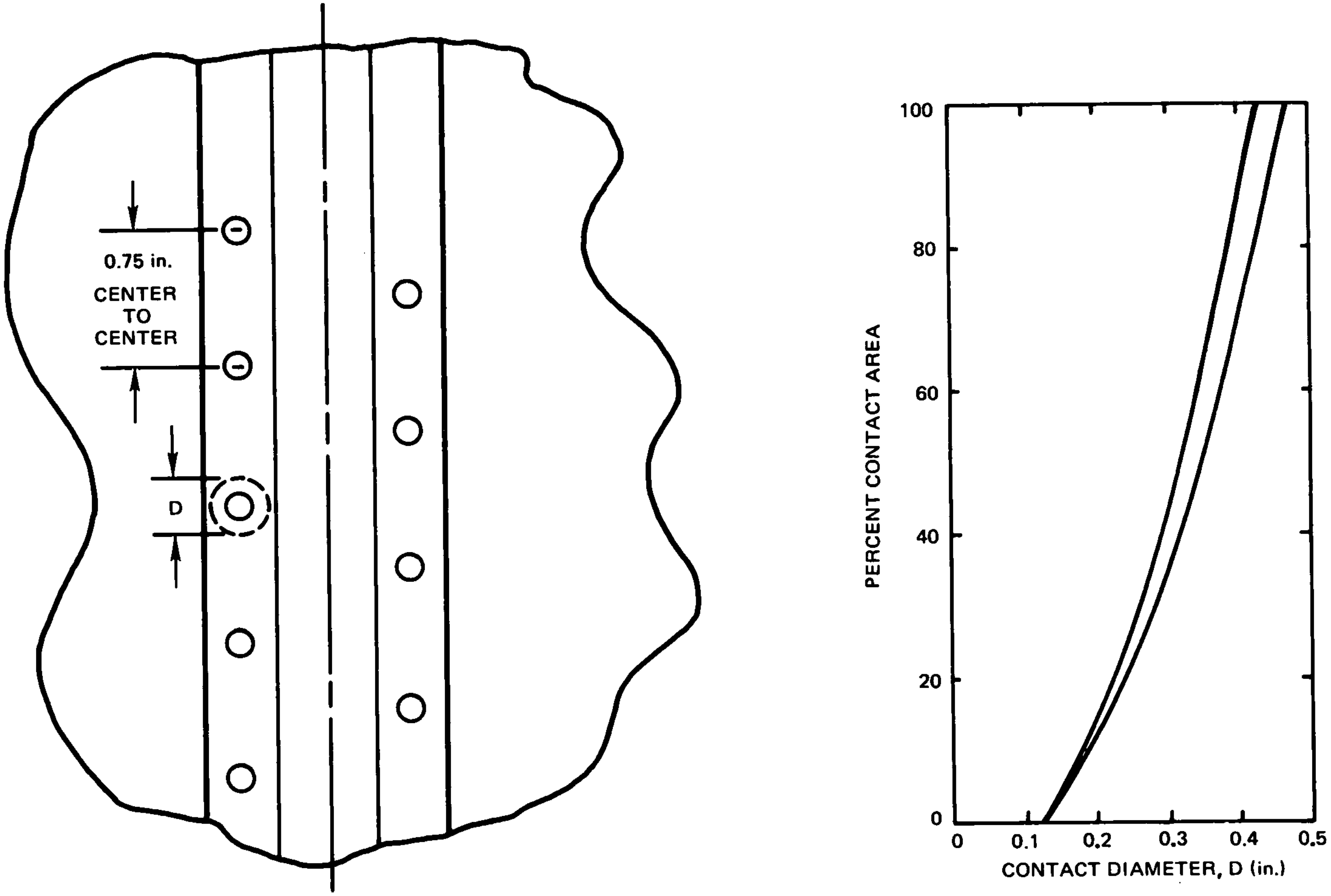

6532-54123

Figure 106. Contact Ratio, Mechanically Joined Lockalloy

and several NASA radiator programs. As the analysis progressed and showed that the aluminum radiator was unsuitable and that alternate materials and/or methods were required, the independent structure was considered. The method would have been similar to that used for the SNAP 10 system with the exception that the converters would not be located on the heat rejection tubes.

The configuration of the radiator would remain as a combined cone and cylinder with the same projected area as needed for an integral system but with allowances for spaces between adjacent fin segments. The structure would be of a semi-monocoque configuration whose function would be to sustain the launch loads and hold the configuration during operation and test. The radiator would consist of approximately 48 tubes, each with a dependent axial fin and each supported on the cone-cylinder structure. Provision would be made for the differential axial growth of the tubes with respect to the structure. The fin tube would be asymmetric and would be subjected to bowing depending on the thermal mismatch and the continuity of the fin. The points of attachment to the structure would be sufficiently rigid to prevent the tube from bowing. This would be accomplished by having them at or near frames. There would be axial slots at each support point progressively longer nearer the cold end. This would allow the hot tubes to grow with respect to the relatively cold structure.

This configuration has the advantage of divorcing thermally induced stresses from the structure. The fin could be either aluminum or Lockalloy. Local distortion of the fin caused by thermal mismatch would not affect the launch capability nor would the heat rejection capability be affected.

The significant objection to the independent radiator structure is its high weight. For most configurations of the integral type, the structure was dictated by thermal performance. Thus, it could be assumed that the tubes, NaK, and fins would have essentially the same weight for an independent radiator configuration as for the integral design. Then, that material required to sustain the loads and maintain configuration, is extra weight. Frames, splices, and bracketry will be similar on either system. An added weight would be the attachments of the tubes to the structure, and the mechanisms to allow the tubes to displace thermally during operation.

In spite of the weight disadvantage, the separate radiator system has been proved on SNAP 10A and offers a high degree of reliability.

2. Structural Analysis

The mechanical loads on the separate radiator structure are essentially the same as those on the integrated radiator. Based on its high strength-to-weight ratio, and experience on the SNAP 10A system, titanium 6AL4V was selected for the structural material for the study of feasibility.

A minimum section was selected as shown on Figure 107. The analysis shows the development of the column strength as a function of ring spacing and panel width. The configuration selected was shown to have a load capacity of 515 lb/in. as compared to an applied load of 230 lb/in. Thus, it proved to be more than adequate structurally.

The weight penalty associated with the separate radiator is shown to be approximately 250 lb which is 12 to 13% of the total system weight.

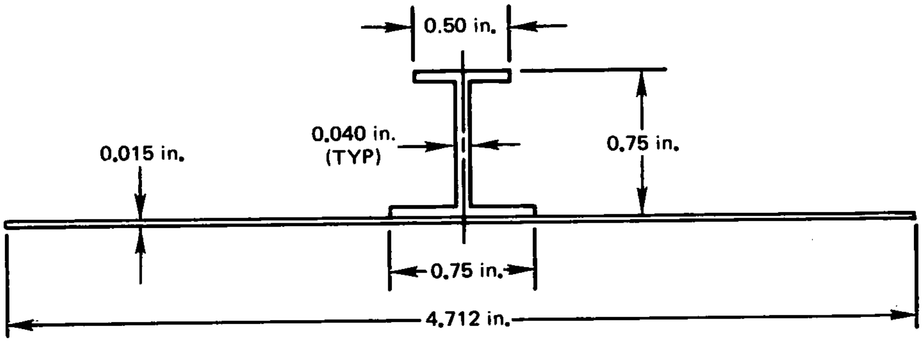

6532-54124

Figure 107. Separate Radiator Structure

3. Aluminum Fin Radiator Characteristics

The thermal performance requirements dictate the heat rejection surface dimensions of both the separate aluminum radiator and the integral radiator structure design. As discussed in Section V-F, the dimensions of the integral radiator, established by thermal requirements, are more than adequate to meet the structural needs of the 5-kwe reactor system.

The separate radiator design has the same vulnerable area as the radiator structure concept. The meteoroid armor requirements are therefore the same for both types of radiators.

To minimize bowing at elevated temperatures the separate aluminum radiator must also use the symmetric fin and tube cross section.

Because of these similarities and the fact that the thermal requirements for both radiators are identical, the fin and tube heat rejection surface dimensions are the same for both types of radiators. Therefore, the fin surface of the separate aluminum radiator will essentially be the same as the radiator structure design.

The symmetric tapered aluminum fin-tube cross section used as the radiator structure design is discussed in Section V-C-3. A schematic of the reference aluminum radiator is shown in Figure 15.

4. Lockalloy Fin Radiator Characteristics

The thermal performance requirements also dictate the design of the integral Lockalloy radiator structure. As discussed in Section VI-F, the radiator design that satisfies the thermal requirements is more than adequate to serve as a structural support for the 5-kwe reactor system.

Since the thermal requirements for the separate Lockalloy radiator are the same as for the integral design, the fin and tube heat rejection surface dimensions are the same for both types of radiators. Therefore, the separate Lockalloy radiator will be the same as the reference Lockalloy radiator structure described in Section VI-C-3. The thermal performance characteristics for the separate Lockalloy radiator are also the same as the reference Lockalloy radiator given in Section VI-E.

The thermal performance characteristics of the separate aluminum radiator are also the same as discussed in Section V-F for the reference integral aluminum radiator. The structural support weight for the separate radiator must be added to the fin, tube, and armor plus coolant weight in order to obtain the total separate radiator system weight. As described in Section VII-E-2, the total separate radiator system weight may be decreased by cutting out portions of the aluminum surrounding the coolant tube without appreciably affecting radiator performance. The aluminum armor removed from the outer surface of the coolant tube may be replaced by installing a bumper type armor system. However, the overall system weight savings will be small compared to the total system weight.

VIII. RESULTS

The radiator of the 5-kwe system progressed through a long series of changes and iterations. It was a multi-function component with its performance requirements resulting from the requirements of its interfaced components. It, therefore, had to be a compromise design.

The radiator structure's primary functions were indicated by its name. It was to serve as a heat rejection component and as the primary structure between the heavy masses of the reactor and shield assembly and the spacecraft (yet to be defined). Thermal requirements called for about 270 ft^2 and operating temperatures over 600°F. Structurally, it was required to provide support and separation of the massive components while subjected to the Titan-III launch environment, followed by 5 years of structural integrity in a space orbit. Alternately, it was required to support the system at 1.0 g for 5 years of ground tests.

The selection of aluminum bonded to stainless-steel tubes was based on previous radiator efforts and seemed to be a logical selection from the standpoint of fabricability, strength, and thermal performance. As the analysis continued, it became evident that the large difference in thermal expansion rate between the aluminum and the steel caused excessive strains and that an alternate design was needed.

The search for an alternate design stressed the need for matched expansion rates, high thermal conductivity, and low density. The resulting design was Lockalloy bonded to stainless-steel tubes. The tubes were to be D-shaped with the flat side bonded. Although bonding methods needed further development, the process appeared feasible, but a design incorporating a riveted fin and tube assembly was considered as a backup.

Lockalloy samples had been ordered and test plans were in progress to determine the several uncertainties including 600°F creep, cross axis fracture toughness, and rivet practice. Further development was planned for the bonding procedure.

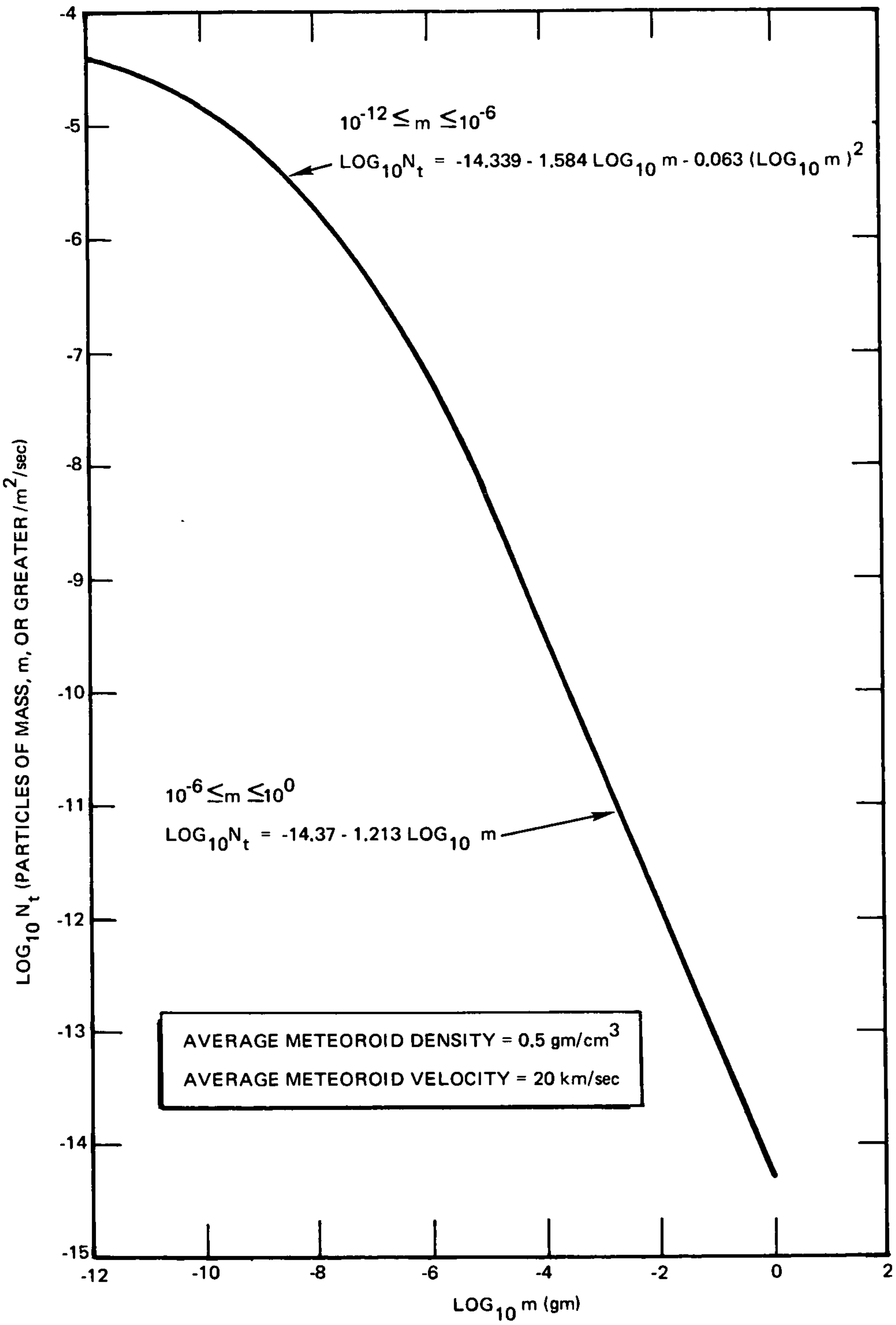

Figure 108. Average Cumulative Total Meteoroid Flux-Mass Model for 1 A. U.

APPENDIX
MICROMETEOROID DAMAGE ASSESSMENT CRITERIA

This appendix is intended to document the reference design micrometeoroid damage assessment criterion used on the 5-kwe reactor system thermal radiator.

The impact of a meteoroid on a space system can damage system components or radiator coolant tubes causing failure of subsystems. Armor must be provided to protect system components from critical damage by meteoroid impact.

The space vehicle meteoroid design criteria have been divided into two portions: (1) selection of the meteoroid environment model to be used, and (2) selection of the appropriate analytical methods to be used to assess meteoroid damage.

A. METEOROID ENVIRONMENT MODEL

A recent NASA monograph(13) has established the meteoroid environment model that should be used for engineering application to space missions in a near-earth orbit. The following meteoroid flux-mass model and the associated particle density and velocity values have been taken from Reference 13.

The average total meteoroid (average sporadic plus a derived average stream) environment is to be used for preliminary design and for mission periods that cannot be specified. This environment model encompasses only particles of cometary origin and is composed of sporadic meteoroids in the mass range between 10^{-12} and 1 gm, and stream meteoroids in the mass range, 10^{-6} to 1 gm. The characteristics of the average total meteoroid mass-flux model are as follows:

1. Particle Density

The mass density is 0.5 gm/cm^3 for all meteoroid sizes.

2. Particle Velocity

The average meteoroid velocity is 20 km/sec.

3. Flux-Mass Model

The average cumulative meteoroid flux-mass is shown in logarithmic form in Figure 108 and is described mathematically as:

$$\log_{10} N_t = -14.37 - 1.213 \log_{10} m \qquad \ldots (A\text{-}1)$$
$$\text{for } 10^{-6} \leq m \leq 10^{0}$$

and

$$\log_{10} N_t = -14.339 - 1.584 \log_{10} m - 0.063 \; (\log_{10} m)^2 \qquad \ldots (A\text{-}2)$$
$$\text{for } 10^{-12} \leq m \leq 10^{-6}$$

where

N_t = Number of particles of mass m or greater (m^2/sec)
m = Particle mass (gm)

Equation A-1 should be used for system design. Particles smaller than 10^{-6} grams will not penetrate aluminum sheets with a thickness greater than approximately 0.020 inches. Equation A-1 may be rewritten as:

$$N_t = \alpha m^{-\beta} \qquad \ldots (A\text{-}3)$$

where

$\alpha = 10^{-14.37} (gm^{\beta}/m^2\text{-sec})$

$\beta = 1.213$

B. METEOROID ARMOR EQUATION

The reference meteoroid armor equation that is being used to establish the amount of armor required to protect the fin-tube radiator assembly coolant tube from meteoroid impact was developed by Haller and Lieblein:(14)

$$\delta = \gamma_R a \left(\frac{\rho_p}{\rho_a}\right)^{1/2} \left(\frac{V_p}{C_a}\right)^{2/3} \left(\frac{6}{\pi \rho_p}\right)^{1/3} \left(\frac{E \alpha A_v t}{-\ln P_0}\right)^{1/3\beta} \left(\frac{2}{3n\theta\beta + 2}\right)^{1/3\beta} \left(\frac{T}{T_R}\right)^{1/6}$$

where

δ = Armor thickness

γ_R = Room temperature cratering coefficient

a = Rear surface damage thickness factor

ρ_p = Meteoroid average density (0.5 gm/cm^3)

ρ_a = Armor density

V_p = Meteoroid average velocity (20 km/sec)

C_a = Sonic velocity in armor

E = Armor earth shielding factor, 0.7631

α = Meteoroid flux constant ($10^{-14.37}$ gm^{β}/m^2-sec)

A_v = Vulnerable area

t = Mission time

P_0 = Design probability of no critical damage

n = Damage factor for oblique impact, 1.0

θ = Penetration constant, 0.667

β = Meteoroid flux constant, 1.213

T = Armor temperature

T_R = Room temperature

The meteoroid flux constants used in this equation from Reference 13 are:

$\alpha = 10^{-14.37} gm^{\beta}/m^2\text{-sec}$

$\beta = 1.213$

The values of V_p and ρ_p are also taken from Reference 13:

$V_p = 20$ km/sec

$\rho_p = 0.5$ gm/cm^3

The values of n and θ used in the armor equation were taken from Reference 15 as:

$n = 1.0$

$\theta = 2/3$

The oblique impact term in the armor equation, $[2/(3n\theta\beta + 2)]^{1/3\beta}$, then reduces to $[1/(1 + \beta)]^{1/3\beta}$.

The earth shielding factor, E, used in the armor equation may be calculated(16) as a function of orbital altitude, and is defined as the ratio of the shielded to unshielded flux (Figure 109):

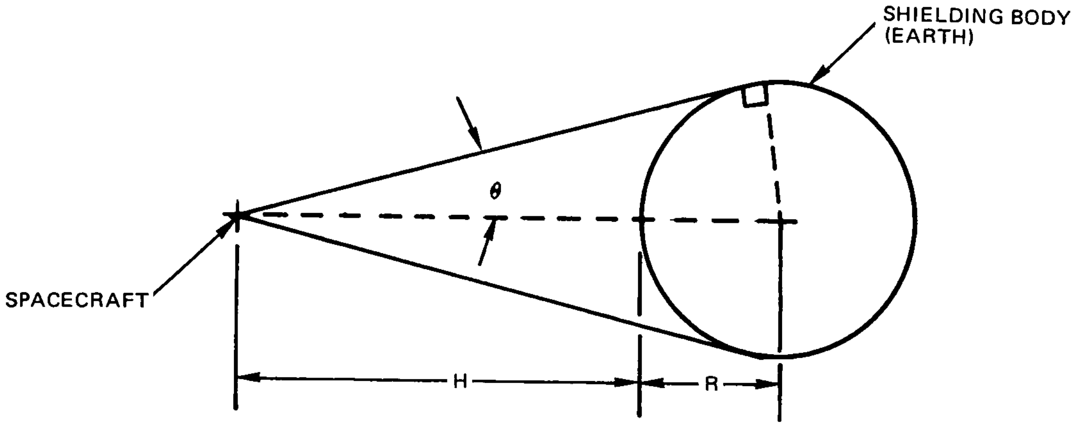

6532-54126

Figure 109. Earth Body Shielding Factor for Randomly Oriented Spacecraft

$$E = \frac{1 + \cos\theta}{2} = \frac{1 + 0.5242}{2} = 0.7621$$

where

$$\sin\theta = \frac{R}{R + H} = \frac{3444 \text{ n.mi}}{3444 + 600 \text{ (n.mi)}} = 0.8516$$

R = Radius of shielding body

H = Altitude above surface.

The γ_R values at elevated temperatures have been correlated to room temperature values by the $(T/T_R)^{1/6}$ term in the armor equation.

The cratering coefficient, γ_R, and the rear surface damage factor, a, in the meteoroid armor equation vary for different armor materials and as a function of temperature. Values for γ_R, taken from Reference 17, for various materials are given in Table 22. The method used to calculate the cratering coefficient of Lockalloy 38 is shown below:

The cratering coefficient of Lockalloy 38 was obtained by composition weighting the coefficients of Be and Al.

γ_R for Be = 2.28(8)

γ_R for Al = 1.70(9) ;

therefore, for Lockalloy,

$$\gamma_R = 0.62(2.28) + 0.38(1.70) = 2.06$$

TABLE 22

CRATERING COEFFICIENT VALUES FOR SELECTED MATERIALS

Target Material	Material Cratering Coefficient, γ_R
356-T51 Aluminum	2.15
7075-T6 Aluminum	2.00
2024-T6 Aluminum	1.70
Columbium - 1% Zirconium	1.81
Type 316 Stainless Steel	2.19
A-286	1.77
Inconel-718	1.85
Cobalt L-605	2.00
Vanadium	1.71
Tantalum	1.77
TZM-Molybdenum	2.00

The damage thickness factors, a, for incipient dimple, spall, and perforation for various materials are given in Table 23(18) at room temperature. The three modes of damage by meteoroid impact are defined as follows:

1) Dimple — The impacted surface is physically dented but the integrity of the rear surface is not disrupted.

2) Spall — The impacted surface may be partially penetrated and spallation may occur from the rear surface; however, the complete thickness of the material is not perforated.

3) Perforation — The complete thickness of the impacted material is physically perforated.

The damage thickness factors given in Table 23 were experimentally determined using flat plates as the target material. Impact studies using unlined aluminum 2024-T6 tubes have shown that the factors given in Table 23 for aluminum 2024-T6 are completely usable for single material (unlined) radiator tubes.

TABLE 23

DAMAGE THICKNESS FACTORS FOR INCIPIENT DIMPLE, SPALL, AND PERFORATION

Material	Damage Thickness Factor		
	Dimple	Spall	Perforation
Aluminum 2024-T6	2.5	2.3	1.7
Type 316 Stainless Steel	2.4	1.9	1.4
(A286)	~2.4	1.9	1.4
Columbium - 1% Zirconium	4.5	4.0	1.7
Inconel-718	~3.0	2.5	-
Cobalt L-605	~2.5	2.1	1.7

The presence of an inner liner was found to improve the damage resistance of radiator tubes. An inner liner although dimpled on the inside upon impact, prevented metal spalling into the tube.(15) The statement is made in Reference 17 that, in general, the inner surface integrity is not lost, even at complete closure of the tube by the liner. Values of the damage thickness factor as a function of dimple height produced in the liner are given in Figure 110 for cast aluminum armor over 0.028-in. stainless-steel liners of various inside diameters.(17) The solid line in Figure 110 is a summary of the experimental data

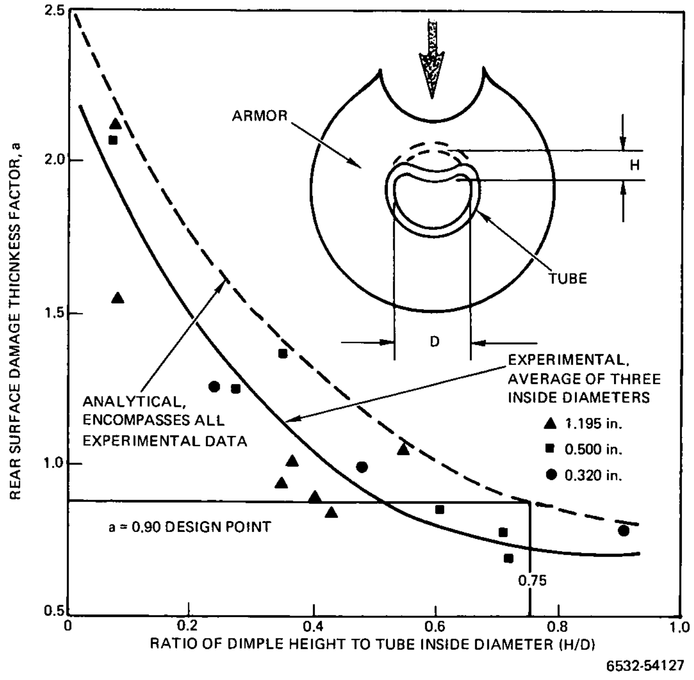

Figure 110.

Variation of Damage Thickness Factor with Tube Dimple Height for the three inside diameter tube sizes used in the study. The dashed line in Figure 110 has been drawn by the author to encompass all of the experimental data. It is recommended that the dashed line be used in engineering design. The use of the dashed line in Figure 110 will provide an armor thickness that will be somewhat conservative for a given dimple ratio.

In using Figure 110, however, it is implied that the damage thickness factor is not dependent upon the type of bond existing between the tube liner and the armor material. As stated in Reference 17:

> "Recently obtained data into lined aluminum tubes with various types of bonds indicate that the type of bond between liner and armor has very little effect on the liner damage."

It is therefore concluded that Figure 110 may be used in designs where an integral bond exists between the stainless-steel liner and the armor material. Using the dashed line in Figure 110 with a dimple ratio of 0.75, the damage thickness factor was found to be 0.9.

The armor equation was used to determine the required thickness of Lockalloy armor that must be provided to protect the front side of the thermal radiator coolant tubes. Figure 68 shows Lockalloy armor thickness as a function of the noncritical damage probability. The critical mode of damage for the radiator coolant tubes is that there be a 0.99 probability that the tube will not receive a 0.75 dimple upon impact. As shown in Figure 68, a 0.076-in. thickness of Lockalloy will be required. This must be the total material thickness between the outer edge of the coolant tubes and the outer surface of the radiator fin.

Figure 69 illustrates the location and dimensions of the meteoroid armor relative to the reference radiator fin-tube cross section.

Figure 111 shows the manner in which meteoroid impact to the outer surface of the reactor system can damage the inside surface of the radiator coolant tubes or other internal components. A primary meteoroid impacts and penetrates the outer surface of the system. Upon impact, the primary particle is fragmented and dispersed over a larger cone angle inside the reactor structure. The fragments of the primary particle plus spallation from the meteoroid puncture, in turn, strike interior surfaces of the system. In this way, the primary impacted surface serves as a bumper for the interior components.

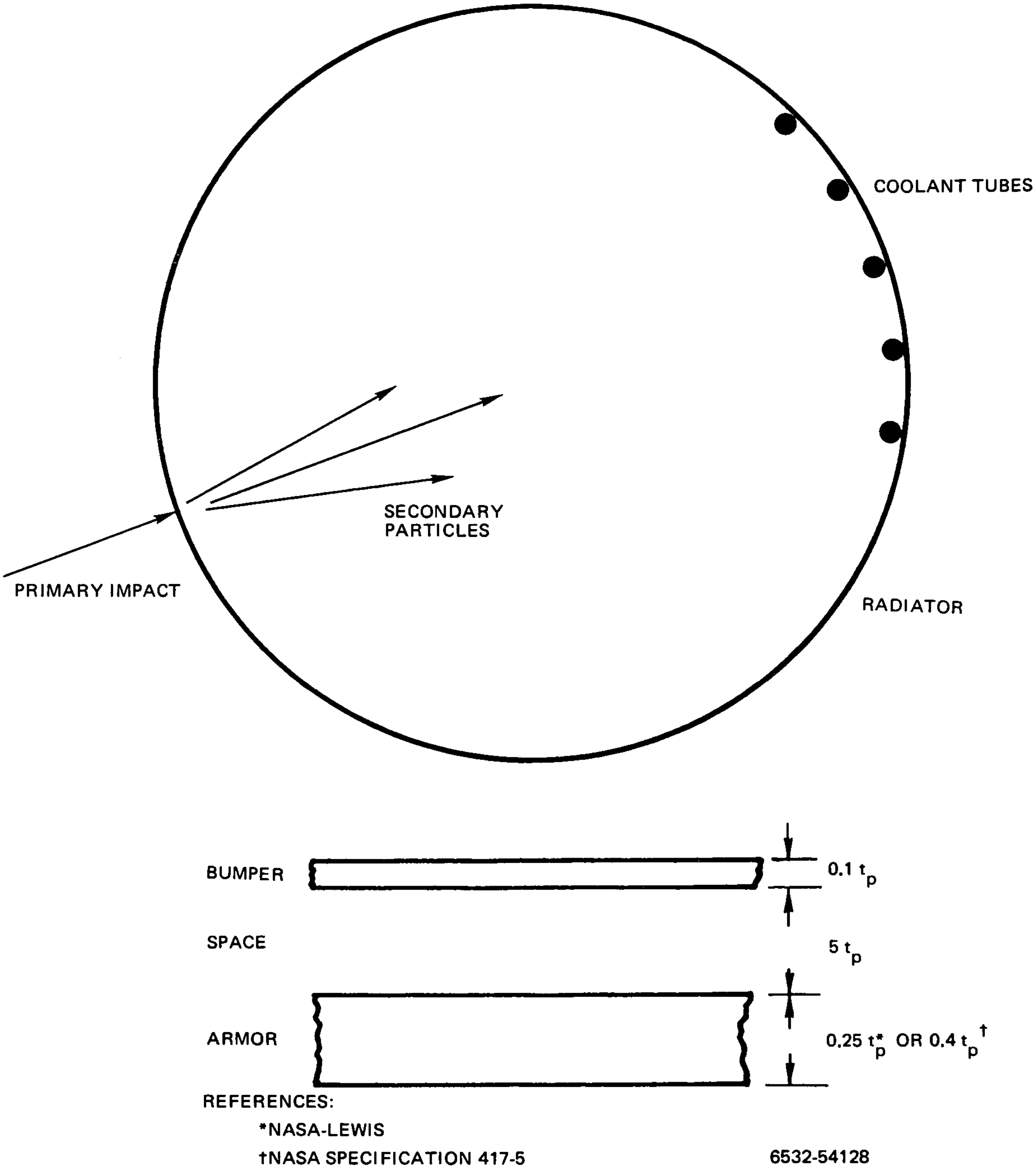

Figure 111. Bumper Effect Upon Primary Meteoroid Impacts

As shown in Figure 111, a bumper type armor system will be effective if it has the following dimensional characteristics:

Bumper thickness = 0.1 t_p

Secondary armor = 0.25 to 0.40 t_p

Space between bumper and secondary armor $>5\ t_p$

where

t_p = single plate armor thickness.

The range on the secondary armor thickness requirements have been obtained from two references. NASA-Lewis(19) specifies that the secondary armor thickness should be 0.25 t_p. An additional source(20) suggests that the secondary armor thickness should be 0.4 t_p.

Figure 70 gives the single plate stainless-steel thickness and the secondary armor thickness requirements for a 30 ft^2 vulnerable area as a function of the noncritical damage probability. The critical event for these calculations was also a 0.99 probability of not receiving a 0.75 dimple. This critical event was used since most of the internal system components are composed of piping. These components have a stainless-steel wall thickness of at least 0.020 in. A secondary armor thickness of 0.020 in. provides a noncritical damage probability of 0.998 when the 0.25 t_p relation is used as suggested by NASA-Lewis.(14)

REFERENCES

1. E. Miller, W. Carroll, and R. Klemmn, "Program for the Development of Space Radiator Surfaces," NA-61-802, July 18, 1961

2. K. Kieder, E. Miller, and M. Hagen, "Further Development of a Thermal Radiation Control Coating for Use on SNAP Vehicles," NA-62-622, June 8 1962

3. J. R. Crosby and M. A. Perlow, "SNAP 10A Thermal Control Coatings," AIAA Paper No. 65-652, AIAA Thermophysics Specialist Conference, Monterey, California

4. "Titan-III Performance Handbook," Martin-Marietta Corporation, Denver, Colorado

5. D. B. Mackay, Design of Space Powerplants (Prentice-Hall, Inc., New York), 1963

6. W. Jost, Diffusion in Solids, Liquids, and Gases (Academic Press, Inc., New York), Third Printing, 1960

7. F. R. Shanley, Strength of Materials (McGraw-Hill Book Company, New York), 1957

8. J. H. Deidrich, I. J. Loeffler, and A. R. McMillan, "Hypervelocity Impact Damage Characteristics in Beryllium and Graphite Plates and Tubes," NASA TN D-3018, 1965

9. N. Clough, J. H. Diedrich, and S. Lieblein, "Results of Hypervelocity Impacts Into Space Radiator Materials," NASA-TMX-52142, October 1965

10. "Lockalloy Usage on Minuteman-III," D2-3A1 and CD2-4A1 PBCS Body Sections, NR-72-V-84

11. H. R. Brooker and E. V. Beatson, "Industrial Brazing," in Welding and Metal Fabrication (Iliffe and Sons, Ltd., London, England), 1953

12. T. Lyman, Ed., Metals Handbook, Vol 1, "Properties and Selection of Metals," 8th Ed., American Society for Metals, Metals Park, Novelty, Ohio, 1961

13. D. J. Kessler, "Meteoroid Environment Model-1970 (Interplanetary and Planetary," NASA-Space Vehicle Design Criteria (Environment), NASA-SP 8038, October 1970

14. H. C. Haller and Seymour Lieblein, "Analytical Comparison of Rankine Cycle Space Radiators Constructed of Central, Double, and Block-Vapor Chamber Fin-Tube Geometries," NASA-TN-D-4411, February 1968

15. I. J. Loeffler, S. Lieblein, and N. Clough, "Meteoroid Protection for Space Radiators," ARS Space Power Systems Conference, Santa Monica, Calif., September 25-28, 1962

16. B. G. Cour-Polais, "Meteoroid Environment Model-1959 (Near Earth to Lunar Surface)," NASA Space Vehicle Design Criteria (Environment), NASA-SP-8013, March 1969

17. N. Clough, S. Lieblein, and A. R. McMillan, "Crater Characteristics of 11 Metal Alloys Under Hypervelocity Impact Including Effects of Projectile Density and Target Temperature," NASA-TN-D-5135, April 1969

18. N. Clough, S. Lieblein, and A. R. McMillan, "Dimple, Spall, and Perforation Characteristics of Thin Plates of Nine Materials Under Hypervelocity Impact," NASA-TND-5625, January 1970

19. Memorandum: Meteoroid Protection Criteria for Space Radiators; To: Space Power Systems Division, NASA-Lewis Research Center; From: Chief V/STOL Engine Branch, Airbreathing Engines Division, October 7, 1966

20. "Specification for SNAP 8 Meteoroid Protection for Space Systems, Revision A," NASA 417-5, May 25, 1964